Universität Bremen

Dissertation

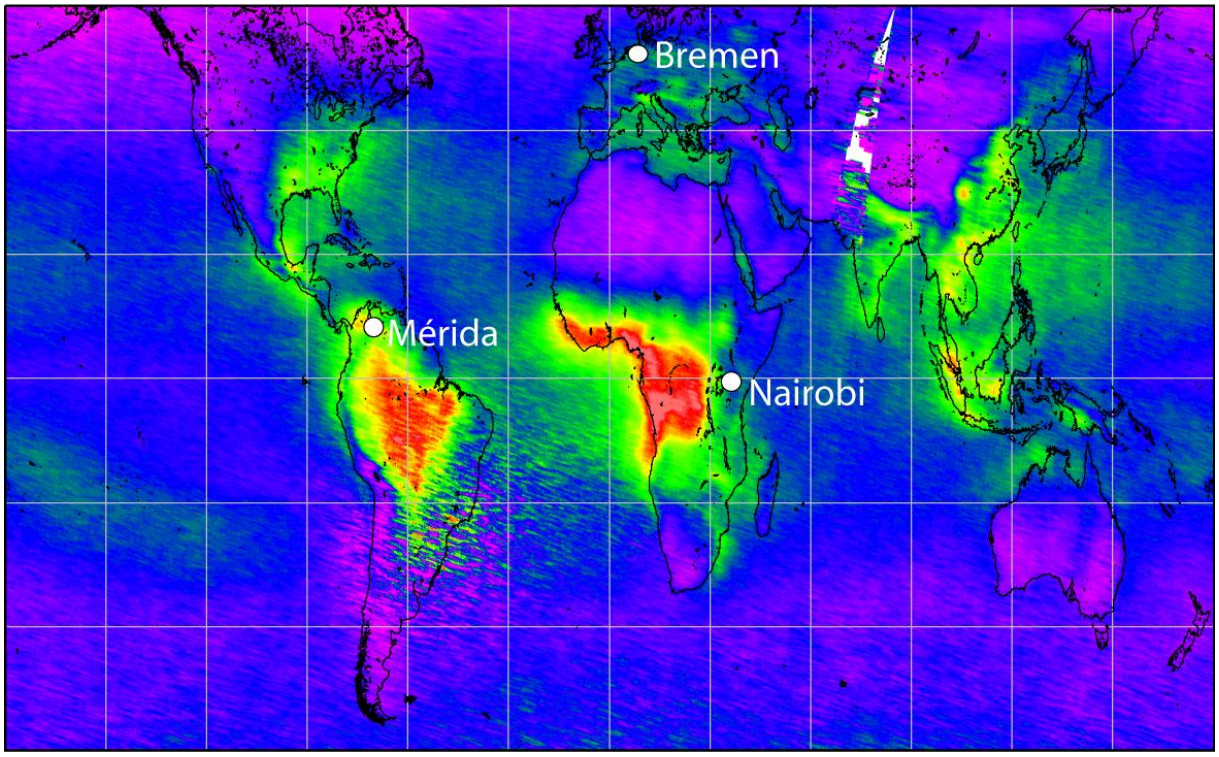

The retrieval of oxygenated volatile organic compounds by remote sensing techniques

zur Erlangung des Grades

Doktor der Naturwissenschaften

- Fachbereich Physik und Elektrotechnik -

Folkard Wittrock

Gutachter: 1. Prof. John P. Burrows

2. Prof. Otto Schrems

Eingereicht: 3. Januar 2006

Tag des mündlichen Kolloquiums: 19. Mai 2006

Zusammenfassung

Diese Arbeit beschreibt globale Messungen des Spurengases Formaldehyd abgeleitet von Streulichtspektren im ultravioletten Spektralbereich der Satelliteninstrumente GOME und SCIAMACHY sowie bodengestützter MAX-DOAS-Geräte. Die Auswertung erfolgte mittels der Methode der Differenziellen Optischen Absorptionsspektroskopie (DOAS). Ergänzend präsentiert die Arbeit die ersten Messungen des Spurengases Glyoxal mit den genannten Instrumenten im sichtbaren Spektralbereich. Es wurden neue Algorithmen entwickelt und beschrieben, welche die Ableitung von vertikalen Säulen aus den Satellitenmessungen ermöglichen. Für die Bodengeometrie wurde ein Weg gefunden, Profilinformationen für die troposphärischen Absorber abzuleiten. Mithin trägt die Arbeit wesentlich zu einer Verbesserung des Verständnisses über die Chemie der Troposphäre bei. Sie ermöglicht eine bessere Abschätzung der Quellen und Senken von Kohlenwasserstoffen und damit ein exakteres Verständnis der troposphärischen Ozonchemie. Eine Reihe von Fallstudien illustriert insbesondere die Bedeutung biogener Emissionen für die Gesamtverteilung der flüchtigen organischen Verbindungen. Vergleiche mit Ergebnissen eines globalen Atmosphärenmodells zeigen in vielen Regionen unseres Planeten nur eine mäßige Übereinstimmung. Dies spiegelt den derzeit nur begrenzten Kenntnisstand über die sehr komplexen physikalischen und chemischen Prozesse in der Troposphäre wieder.

Abstract

This work describes global measurements of the trace gas formaldehyde derived from stray light spectra in the ultraviolet region measured by the satellite instruments GOME and SCIAMACHY along with ground-based MAX-DOAS instruments. The analysis was carried out using the method of the Differential Optical Absorption Spectroscopy (DOAS). The work complementarily presents the first measurements of the trace gas glyoxal in the visible wavelength region. New algorithms to derive vertical columns of the satellite instruments are developed and described. For the ground-based geometry a way was found to derive profile information for the tropospheric absorbers. This work therefore contributes fundamentally to an improvement in the understanding of the chemistry of the troposphere. It offers the opportunity to obtain a better estimate on the sources and sinks of hydrocarbons in the atmosphere. Particularly, a number of case studies illustrate the significance of biogenic emissions and of biomass burning for the global distribution of the oxygenated volatile organic compounds. A comparison with results from a global atmosphere model shows only a moderate agreement in many regions of the earth. This reflects the limited state of knowledge at present about the very complex physical and chemical processes in the troposphere.

Schlagwörter:

Atmosphäre, Formaldehyd, Glyoxal, DOAS, MAX-DOAS, biogene Emissionen, VOC

Keywords:

atmosphere, formaldehyde, glyoxal, DOAS, MAX-DOAS, biogenic emissions, VOC

Contents

Widmung

Diese Arbeit widme ich meiner Familie. Sie war auch in schwierigen Zeiten immer für mich da.

List of Acronyms

AATSR	**A**dvanced **A**long **T**rack **S**canning **R**adiometer (ATSR)
AERONET	**AE**rosol **RO**botic **NET**work
agl	**a**bove **g**round **l**evel
AMAXDOAS	**A**irborne **M**ulti-**AX**is **DOAS**
AMF	**A**ir **M**ass **F**actor
AOD	**A**erosol **O**ptical **D**epth
asl	**a**bove **s**ea **l**evel
ASM	**A**zimuth Scanner Module
ASTAR	**A**rctic **S**tudy of **T**ropospheric **A**erosol and **R**adiation
ATSR	**A**long **T**rack **S**canning **R**adiometer
AU	**A**rbitrary **U**nits
AVHRR	**A**dvanced **V**ery **H**igh **R**esolution **R**adiometer
AWI	**A**lfred-**W**egener-**I**nstitute for Polar and Marine Research, Bremerhaven and Potsdam, Germany
BAMF	**B**lock **A**ir **M**ass **F**actor
BAS	**B**ritish **A**ntarctic **S**urvey
BREAM	**BRE**mian **A**dvanced **M**AX-DOAS Retrieval Algorithm
BREDOM	**BRE**mian **DO**AS network for atmospheric **M**easurements
CCD	**C**harge-**C**ouple **D**evice
CDIPI	**C**ombined **D**ifferential-**I**ntegral Approach involving the **P**icard **I**terative Approximation
CEA	**C**ommissariat à l'**E**nergie **A**tomique, French Atomic Energy Commission
CFC	**C**hloro**F**luoro**C**arbon
CNRS	**C**entre **N**ational de la **R**echerche **S**cientifique, French National Center for Scientific Research
CTM	**C**hemical **T**ransport **M**odel
DANDELIONS	**D**utch **A**erosol and **N**itrogen **D**ioxide **E**xperiments for va**LI**dation of **O**MI a**N**d **S**CIA-MACHY
DOAS	**D**ifferential **O**ptical **A**bsorption **S**pectroscopy
DOD	**D**ifferential **O**ptical **D**epth
DSC	**D**ifferential **S**lant **C**olumn
DSCD	**D**ifferential **S**lant **C**olumn **D**ensity

DTM	**D**igital **T**errain **M**odel
ECMWF	**E**uropean **C**entre for **M**edium-Range **W**eathe**F**orecasts
EDGAR	**E**mission **D**atabase for **G**lobal **A**tmospheric **R**esearch
ENSO	**E**l **N**iño / **S**outhern **O**scillations
ENVISAT	**ENVI**ronmental **SAT**ellite
ERA40	**E**CMWF **R**eanalysis of Meteorological D**A**ta
ERS-2	Second **E**uropean **R**emote-Sensing **S**atellite
ESA	**E**uropean **S**pace **A**gency
ESM	**E**levation **S**canner **M**odule
EU	**E**uropean **U**nion
FORMAT	European Project "FORMAldehyde as a Tracer for oxidation in the troposphere"
FRESCO	**F**ast **RE**trieval **S**cheme for **C**loud **O**bservables
FTIR	**F**ourier **T**ransform **I**nfrared **S**pectroscopy
FTS	**F**ourier **T**ransform **S**pectrometer
FWHM	**F**ull **W**idth **H**alf **M**aximum
GACP	**G**lobal **A**erosol **C**limatology **P**roject
GCM	**G**eneral **C**irculation **M**odel
GEIA	**G**lobal **E**missions **I**nventory **A**ctivity
GEOS-CHEM	Global 3D chemical transport model from Harvard University
GODIVA	European Project "GOME Data Interpretation, Validation and Application"
GOME	**G**lobal **O**zone **M**onitoring **E**xperiment
GOMETRAN	Radiative Transfer Model for GOME
HITRAN	**HI**gh Resolution **TRAN**smission
HWHM	**H**alf **W**idth **H**alf **M**aximum
IASB/ BIRA	**I**nstitut d'**A**éronomie **S**patiale de **B**elgique, Belgium
IFU	see IMK-IFU
ILO	**I**nternational **L**abour **O**rganization
IMK-IFU	**I**nstitut für **M**eteorologie und **K**limaforschung - Atmosphärische Umweltforschung, Garmisch-Partenkirchen, Germany
INCA	**IN**teraction **C**himie – **A**érosols, Chemistry and Aerosol Model coupled to LMDz
INCHEM	Website for "Chemical Safety Information from Intergovernmental Organizations"
INDOEX	International field experiment "Indian Ocean Experiment "

IPCS	**I**nternational **P**rogramme on **C**hemical **S**afety
IRR	**I**nfra-**R**ed **R**adiometer
ITCZ	**I**nter**T**ropical **C**onvergence **Z**one
IUP	**I**nstitut für **U**mwelt**p**hysik (Institute of Environmental Physics), University of Bremen
JRC	**J**oint **R**esearch **C**entre
KNMI	Royal Netherlands Meteorological Institute
LIDAR	**LI**ght **D**etection **A**nd **R**anging
LMDz	**L**aboratoire de **M**étéorologie **D**ynamique (LMD) **z**oom, General Circulation Model
LOS	**L**ine **O**f **S**ight
LOWTRAN	**LOW** Resolution **TRAN**smission
LT	**L**ocal **T**ime
MARS	**M**érida **A**tmospheric **R**esearch **S**tation
MAX-DOAS	**M**ulti-**AX**is DOAS
MBL	**M**arine **B**oundary **L**ayer
MBO	2-**M**ethyl-3**B**uten-2-**O**l
MEGAN	**M**odel of **E**missions of **G**ases and **A**erosols from **N**ature
MICROTOPS	Commercial 5 channel hand-held ozonometer for measuring total ozone column
MINOS	International Field experiment "**M**editerrenean **IN**tensive **O**xidant **S**tudy"
MIPAS	**M**ichelson **I**nterferometer for **P**assive **A**tmospheric **S**ounding
MODIS	**MOD**erate Resolution **I**maging **S**pectroradiometer
MPI	**M**ax-**P**lanck-**I**nstitut
MWS	**M**icro**W**ave **S**ounder
NASA	**N**ational **A**eronautics and **S**pace **A**dministration
NDSC	**N**etwork for the **D**etection of **S**tratospheric **C**hange
NDVI	**N**ormalised **D**ifference **V**egetation **I**ndex
NILU	Norwegian Institut for Air Research
NIWA	**N**ational **I**nstitute of **W**ater and **A**tmospheric Research, New Zealand
NMHC	**N**on-**M**ethane **H**ydro**C**arbons
NOAA	**N**ational **O**ceanic and **A**tmospheric **A**dministration
OD	**O**ptical **D**epth
OHP	**O**bservatoire de **H**aute-**P**rovence, France
OMI	**O**zone **M**onitoring **I**nstrument

p	pressure
PBL	**P**lanetary **B**oundary **L**ayer
PMD	**P**olarisation **M**onitoring **D**evice
POET	European Project "Precursors of Ozone and their Effects in the Troposphere"
PROMOTE	**PRO**tocol **MO**ni**T**oring for the GMES Service **E**lement
PSI	Paul-Scherrer-Insitute, Switzerland
PVU	**P**otential **V**orticity **U**nit
QUILT	European Project "Quantification and Interpretation of Long-Term UV-Visible Observations of the Stratosphere"
RAMAS	**R**adiometer for **A**tmospheric **M**easurements **A**t **S**ummit
RETRO	European Project "REanalysis of the TROpospheric chemical composition over the past 40 years"
RMS	**R**oot **M**ean **S**quare
RTM	**R**adiative **T**ransfer **M**odel
SAA	**S**outhern **A**tlantic **A**nomaly
SAOZ	**S**ysteme d'**A**nalyze par **O**bservation **Z**enithale, French network of zenith-sky DOAS instruments operated by CNRS
SC	**S**lant **C**olumn
SNR	**S**ignal-to-**N**oise **R**atio
SOF	**S**olar **O**ccultation **F**lux: A mobile FTIR system
SZA	**S**olar **Z**enith **A**ngle
SCIAMACHY	**SC**anning **I**maging **A**bsorption SpectroM**e**ter for **A**tmospheric **C**artograp**HY**
SCIAmini	Small version of SCIAMACHY, former name for GOME
SCIATRAN	Radiative Transfer Model for SCIAMACHY
T	Temperature
TEMIS	**T**ropospheric **E**mission **M**onitoring **I**nternet **S**ervice
TM4	Global 3D chemical transport model from KNMI, as TM5 but without zoom-option
TOMS	**T**otal **O**zone **M**apping **S**pectrometer
TROPOZ	International field experiment "**TROP**ospheric **OZ**one"
UNEP	**U**nited **N**ations **E**nvironment **P**rogramme
UPS	**U**ninterruptible **P**ower **S**upply
UV	**U**ltra**V**iolett
VC	**V**ertical **C**olumn

vis	visible
VMR	**V**olume **M**ixing **R**atio
VOC	**V**olatile **O**rganic **C**ompound
VOD	**V**ertical **O**ptical **D**epth
VRS	**V**ibrational **R**aman **S**cattering
WFN	**W**eighting **F**unction
WHO	**W**orld **H**ealth **O**rganization
WMO	**W**orld **M**eteorological **O**rganization

List of Figures

List of Tables

Introduction

That beautiful, warm, living object looked so fragile, so delicate, that if you touched it with a finger it would crumble and fall apart.

James Irwin, Apollo 15 Astronaut

In the last decades it has become more and more obvious, that mankind is endangering the habitability of its own biosphere. Most of the potential risks for our environment are forced by human activities and are mediated through the chemistry and physics of the atmosphere:

- air pollution resulting from industrial combustion and biomass burning
- changes in the oxidation capacity of the lower atmosphere due to anthropogenic and changing biogenic emissions
- global warming as a consequence of the increasing emissions of greenhouse gases
- acidic precipitation
- changes in precipitation and cloud coverage
- climatic impact of changes in land use (e.g. tropical deforestation)

The first time that atmospheric science came into the focus of the public interest happened in the 80s of the last century after the discovery of the ozone hole above Antarctica [Chubachi, 1984; Farman et al., 1985]. This caused concern, because the ozone layer protects life on earth against harmful ultraviolet radiation of the sun. A slight decrease of ozone was expected in the scientific community from the publications by Molina and Rowland [1974] and Cicerone et al. [1974]. They had shown that anthropogenic release of halogen containing compounds could lead to ozone destruction by catalytic cycles. However values of ozone far below 200 Dobson Units (DU) were entirely unforeseen.

This dramatic development has made clear, that our environment is in an extremely delicate balance of physical, chemical, and biological processes. Furthermore we became aware that our knowledge on their connections is marginal.

As a consequence atmospheric science was intensively subsidised since then to develop new observational platforms, to model the future behaviour of the atmosphere, to understand the historic development of climate, to monitor anthropogenic and natural emissions as well as to collect knowledge for policy makers to facilitate their decisions.

Without doubt it is a positive example in human history that consolidated scientific findings have led to international laws, which banned the use of chlorofluorocarbons (CFCs) and halons (bromine containing fully halogenated organic compounds) in industry (The Montreal Protocol on Substances that Deplete the Ozone Layer as adjusted and/or amended in London, 1990, Copenhagen, 1992, Vienna, 1995, Montreal, 1997 and Beijing 1999). At the present time there is a possibility that the ozone layer will recover to before 1980s status until the end of this century [WMO, 2003]. The Kyoto Protocol to the United Nations Framework Convention on Climate Change which was put into force on 16 February 2005 is another sign for an improved practice with our natural resources. But although some statements in the general public leave the impression that the scientific fundamentals of atmospheric and climate problems have been essentially solved, I am not convinced that the underlying

issues have been adequately addressed. This scepticism is not about whether or not man-made change of climate and atmospheric chemistry exists, it is rather about what the impacts are going to be. This thesis might be a small step to a better understanding of our environment.

The main focus of this work is the observation of the trace gas formaldehyde (HCHO) in the atmosphere. Formaldehyde plays an important role in atmospheric chemistry. It is a major intermediate in oxidation of hydrocarbons, a good tracer for photooxidation and thereby for emissions from fossil fuel combustion, biogenic sources, and biomass burning.

Formaldehyde in the atmosphere has been measured on an occasional, i.e. campaign or regular basis for several decades (e.g. [Platt and Perner, 1980]). This includes several types of sampling and analytical methods including measurements from both urban and remote locations. With the GOME (Global Ozone Monitoring Experiment) instrument on the European satellite ERS-2, formaldehyde measurements from space have become possible for the first time. Several independent studies have shown the feasibility of the HCHO retrieval from GOME data, and regions with elevated HCHO concentrations have been identified in the data and linked to biogenic isoprene emissions, biomass burning and also pollution (e.g. [Thomas et al., 1998; Chance et al., 2000; Wittrock et al., 2000]).

The HCHO retrieval algorithm applied in this study has partially been developed in the framework of the European GODIVA and FORMAT projects, but a number of open questions remained to be solved to obtain more quantitative results. Important issues include improvements of the spectral fitting routines, determination of the atmospheric light path and correction of cloud and aerosol effects. For satellite measurements, validation of the results is essential, but up to this work only few attempts have been made to validate HCHO columns retrieved from satellite spectra [Ladstätter-Weißenmayer et al., 2003; Palmer et al., 2003; Martin et al., 2004].

Quite recently, another trace gas has come into the focus of the scientific community: Glyoxal or CHOCHO. It has been measured using the Long-Path DOAS technique in Mexico City [Volkamer et al., 2005]. Glyoxal is formed from the oxidation of several volatile organic compounds. Since for glyoxal – in contrast to formaldehyde – direct emissions are believed to be small, the authors suggest that global observations of this minor trace gas might help to identify photochemical hot spots in the earth's atmosphere.

The overall objectives of this work are

- to obtain a better knowledge of the concentrations and distribution of formaldehyde and glyoxal in the troposphere globally,
- to provide the possibility to validate satellite measurements of formaldehyde and glyoxal,
- to compare measured and modelled formaldehyde,
- to use global models together with satellite measurements to achieve a better understanding of the global distribution and role of HCHO and CHOCHO as tracers of fossil fuel combustion, biogenic emissions and biomass burning.

In order to accomplish these objectives algorithms for the retrieval of HCHO and CHOCHO from different observation platforms were developed for this thesis. Numerous radiative transfer calculations have been carried out to obtain tropospheric vertical columns for diverse meteorological conditions. Temporal and spatial variations are shown and possible sources identified. Another important step in passive remote sensing described within this work is the progress from ground-based zenith-sky observations to multi-axis measurements (MAX-

DOAS). This technique has enabled us to validate findings from satellite observations and to study the behaviour of important trace gases in the troposphere on a local scale. A new retrieval method has been developed to derive profile information from the MAX-DOAS results. This is illustrated on formaldehyde and glyoxal and validated for nitrogen dioxide.

The outline of this work is as follows: At first an overview on the fundamentals of atmospheric dynamics and chemistry is given with the main focus on the HCHO chemistry (chapter 1). The next section is on the different instruments and data sets used (chapter 2). Basics of the absorption spectroscopy which is the main method applied in this work are introduced in chapter 3. Chapter 4 describes the theory of the radiative transfer for the atmosphere necessary for a proper interpretation of remote sensing data. Chapter 5 illustrates the retrieval algorithms, while in chapter 6 the results are presented. This thesis closes with a summary and gives an outlook (chapter 7).

1 The Atmosphere

The atmosphere is a thin layer of air that separates the earth's surface from outer space. This envelope is attracted to the earth by gravitation. It features numerous properties essential for life on the earth: It protects the surface from harmful solar radiation, it provides a blanket that elevates the surface temperature, it is responsible for the redistribution of water and heat, it provides life with oxygen and it acts as a sink for harmful gaseous compounds. In the following paragraphs those properties important to the understanding of this work are described. General remarks on the atmosphere and the chemistry therein are mainly based on selected chapters in [Brasseur et al., 1999; Wayne, 2000; Lutgens and Tarbuck, 2001], and on material found in the internet (e.g. from the Department of Atmospheric Physics, University Toronto and Wikipedia). Details on the properties and the chemistry of formaldehyde and glyoxal are available from e.g. the International Programme on Chemical Safety (IPCS) website. The IPCS is a collaborative venture of the World Health Organization (WHO), the United Nations Environment Programme (UNEP) and the International Labour Organisation (ILO).

1.1 Structure and Composition of the Atmosphere

In general, the atmosphere is separated into four regions, very different in their dimension, thermodynamics, chemistry, and dynamics. This partition is best reflected by the atmospheric vertical temperature profile whose points of inflection are used to distinguish these regions (Figure 1-1). Starting from the ground, they are called the troposphere, the stratosphere, the mesosphere and the thermosphere, and the boundaries separating them the tropopause, the stratopause and the mesopause.

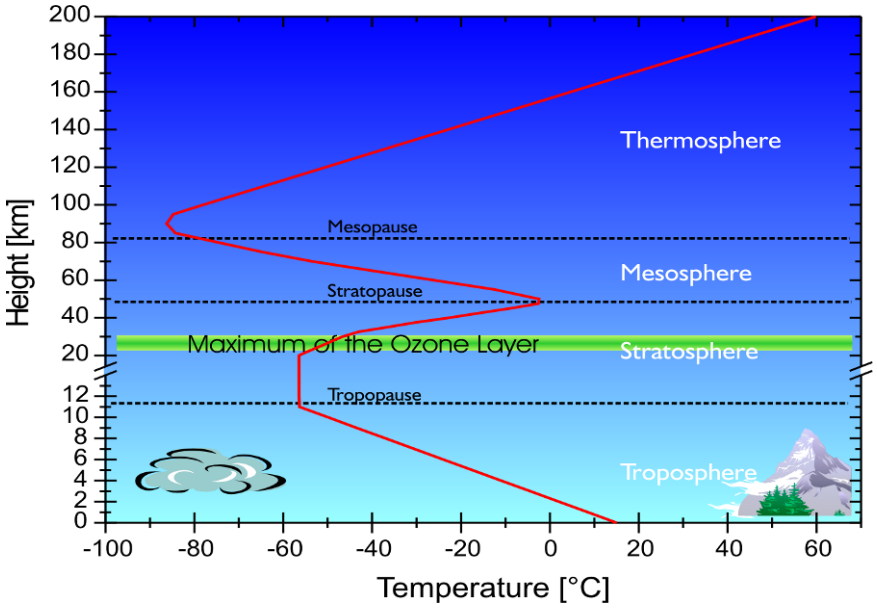

Figure 1-1: Vertical profile of the temperature between the surface and 100 km altitude as defined in the U.S. Standard Atmosphere. Note that the tropopause level represents midlatitude conditions.

The atmospheric thermal structure is caused by a combination of dynamic and radiative transfer processes. The troposphere is heated from the ground, which absorbs solar radiation and releases electromagnetic waves in the infrared. The temperature of the air in this region decreases roughly linearly with altitude, at an adiabatic lapse rate of about 5 to 7 K km^{-1}. The tropopause, situated between 8 km (at high latitudes) and 18 km (at the equator) with some seasonal variation, marks the end of this linear decrease and the beginning of the stratosphere. This

layer contains most (approximately 85 percent) of the atmospheric ozone. The presence of ozone is indispensable for life on earth, as it absorbs the dangerous components of incoming ultraviolet radiation. As a result, the stratosphere heats up which causes a positive temperature gradient. The temperature peaks at the stratopause at approximately 50 km in altitude, then decreases linearly again in the mesosphere as ozone heating diminishes. The region of the atmosphere above the mesopause is called the ionosphere or thermosphere and is quite different from the three lower regions because it cannot be treated as an electrically neutral medium. The structure is strongly influenced by the charged particle wind from the sun (solar wind), which is in turn governed by the level of solar activity. In addition very short-wave (high energetic) solar radiation ionises the molecules and atoms to form a plasma of free electrons and ions that interact with the earth's magnetic field.

The word troposphere stems from the Greek *tropos* for turning or mixing which emphasises the fact that in this region convective processes dominate over radiative processes. The troposphere is indeed marked by large convective activity. Parcels of warm air travel upwards to the tropopause, carrying water vapour and forming clouds as they cool down. The troposphere contains the bulk of atmospheric water vapour, the majority of clouds and most of the weather, both on a global and a local scale. Since pressure decreases exponentially with altitude it also holds more than 80 percent of the total mass of the atmosphere. Most importantly, however, it is in contact with the earth's surface and therefore interacts directly with other climate subsystems, such as the biosphere (the land and vegetation), the hydrosphere (the oceans), the cryosphere (the ice caps), the lithosphere (the topography), and most of all with the human world. The region of the troposphere where surface effects are important is called planetary boundary layer (PBL).

Table 1: Main compounds in dry tropospheric air.

Constituents	*Volume Mixing Ratio*	*Major Sources*
N_2 (Nitrogen)	78.08%	Biological
O_2 (Oxygen)	20.95%	Biological
Ar (Argon)	0.93%	Inert
CO_2 (carbon dioxide)	345 ppm_V	Combustion, Biosphere
O_3 (ozone)	10 ppm_V	Photochemical
CH_4 (methane)	1.6 ppm_V	Biogenic, Anthropogenic
N_2O (nitric oxide)	350 ppb_V	Biogenic, Anthropogenic
CO (carbon monoxide)	70 ppb_V	Photochemical, Anthropogenic
CFCs 11-12	0.2-0.3 ppb_V	Anthropogenic

The most abundant chemical constituents of dry air are nitrogen N_2 (78 percent by volume) and oxygen O_2 (21 percent by volume). These gases as well as the noble gases comprise very long lifetimes and, consequently, are well-mixed throughout the lowest three regions of the atmosphere (called also homosphere). Minor constituents, such as carbon dioxide, water vapour, methane, ozone, and many others despite their much lower concentrations and shorter lifetimes play an essential role in all aspects of atmospheric physics and chemistry: E.g. they influ-

ence the transmission of solar and terrestrial radiation, they determine the oxidising capacity of the atmosphere and, as a result, the atmospheric lifetime of biogenic and anthropogenic trace gases. Table 1 provides the average tropospheric abundance of a selected number of species. Note that the gases of interest in this work, namely formaldehyde, glyoxal and nitrogen oxides, have mixing ratios expressed in ppt_V or ppb_V.

1.2 General Circulation of the Atmosphere

In general the earth's atmosphere is set into motion because of the unequal heating of the earth's surface which results in pressure differences. The tropics receive more heat than the poles since the solar rays are almost perpendicular to the earth and the cross-sectional area of the solar rays striking the earth's surface is smaller at the equator. Another reason is that the thickness of the atmosphere which the solar rays must pass through is greater at the poles than at the equator. Therefore, more of the radiation is attenuated at the poles than at the equator. This produces a meridional circulation of air.

If the earth would not rotate we would only have a single circulation cell in each hemisphere. This classical model has been proposed by George Hadley in 1735. In the 1920s, a three-cell circulation model was introduced, taking into account the fluid motion on a rotating sphere (see Figure 1-2). Because the circulation pattern between the equator and roughly 30° latitude north and south resembles the earlier single-cell model, the name Hadley cell is generally applied to both. The second cell between 30° and 60° latitude is denoted as the Ferrel cell, while the third one between 60° latitude and the pole calls Polar cell. "The areas of general subsidence between 20° and 35° latitude with weak winds are called the horse latitudes. In each hemisphere, the equatorward flow from the horse latitudes deflected by the Coriolis force forms the trade winds" (NE wind in the northern hemisphere, SE in the southern hemisphere). "Convergence of the trade winds from both hemispheres near the equator produces a region of very light winds called the doldrums. The circulation between 30° and 60° latitude (north and south) results in the prevailing westerlies. The area where the cold polar easterlies clash with this warm westerly flow of the midlatitudes is referred to as the polar front which forms an important meteorological region." (from http://wps.prenhall.com/esm_lutgens_atmosphere_8/4/1030/263868.cw/index.html)

If the earth had a uniform surface, two zonally (latitudinally) oriented belts of high and three of low pressure would exist: the equatorial low with ascending warm and moist air, also referred to as the intertropical convergence zone (ITCZ) since it is the region where the trade winds converge (seen as a broad band of clouds near to the equator from space), the subtropical high, at about 20° to 35° on either side of the equator, the subpolar low, situated at about 50° to 60° latitude, and the polar high, close to the earth's poles. In the reality of a rather irregular distribution of water and land with orographic features, the only true zonal pattern of pressure exists along the subpolar low in the Southern Hemisphere. At other latitudes, particularly in the Northern Hemisphere where there is most of the landmass, the zonal pattern is replaced by semipermanent cells of high and low pressure.

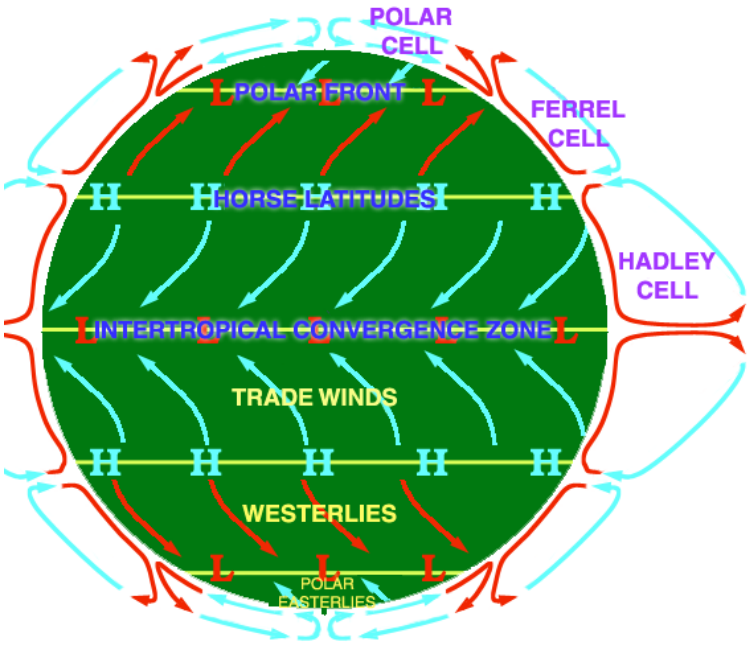

Figure 1-2: The general pattern of the circulation in the troposphere. In principal the earth's weather results from the interactions of three large circulation cells: the Hadley, the Ferrel and the Polar Cell. In addition, this sketch shows the various upwelling and subsidence zones between them. Chemical constituents are redistributed in the atmosphere by these transport processes. (This image is licensed under the Creative Commons Attribution ShareAlike License v. 1.0: http://creativecommons.org/licenses/by-sa/1.0/)

1.3 Troposphere-Stratosphere Exchange

The exchange through the tropopause is an important process in the redistribution of trace gases in the atmosphere. E.g. on the one hand ozone destroying CFCs are transported into the stratosphere but on the other hand also the stable reservoir species are removed from this layer. Stratospheric intrusions of ozone where they occur are dramatic events that strongly impact on the tropospheric ozone column density, locally. However it was found that photochemical production of O_3 on a global scale, driven by nitrogen oxides from anthropogenic sources, ultimately dominates the tropospheric O_3 budget (e.g. [Crawford et al., 1997]). That the lowermost stratosphere will be sometimes perturbed with air from tropospheric processes has been shown by several studies: Convective injection of biomass burning events from large scale boreal fires into the lowermost stratosphere was demonstrated by e.g. [Fromm and Servranckx, 2003; Fromm et al., 2005]; deep convection pumping boundary layer air without significant dilution to the tropopause region were investigated by [Hauf et al., 1995; Fischer et al., 2003; Scheeren, 2003].

In section 1.1 the boundary between the troposphere and the stratosphere has been defined as the temperature minimum. In order to consider exchange processes it is useful to employ a dynamic definition of the tropopause. For this the two parameters potential temperature and Ertel's potential vorticity need to be explained:

For an air parcel with temperature T and pressure p that is adiabatically – without gain or loss of heat – compressed to the surface pressure p_0 the potential temperature θ is given by:

$$\theta = T \cdot \left(\frac{p_0}{p} \right)^{\frac{R}{c_p}} \tag{1.1}$$

where c_p is the specific heat capacity of the gas and R the universal gas constant. The potential temperature is conserved in adiabatic processes. Lines with the same potential temperature are called isentropes. These are essentially horizontal in the atmosphere. Due to this fact isentropes qualify as good vertical coordinates and adiabatic displacements can be illustrated on two-dimensional planes with the same potential temperature.

Ertel's potential vorticity named after the German meteorologist Hans Ertel is defined as:

$$P = \left(\zeta_\theta + f \right) \left(-g \cdot \frac{\partial \theta}{\partial p} \right) = \text{const} \tag{1.2}$$

where ζ_θ is the component of the relative vorticity normal to the isentropic surfaces, f is the planetary vorticity which is just the local vertical component of the vorticity of the earth owing to its rotation, g is the acceleration due to gravity, and $\frac{\partial \theta}{\partial p}$ represents the effective depth, i.e. the distance between potential temperature surfaces measured in pressure units. The units of P are K kg^{-1} m^2 s^{-1} which is equivalent to PVU (potential vorticity unit). According to equation (1.2) the potential vorticity is conserved following the motion in an adiabatic, frictionless flow. A derivation and a detailed discussion of the individual parameters can be found in the book by Holton [1992].

Comparison with the temperature and height distribution of the atmosphere yields a climatological, dynamic tropopause: In the tropics, it is defined by the 380K isentrope and outside the tropics the surface of constant potential vorticity of 2 PVU is used.

The location of the exchange through the tropopause is given by the Brewer-Dobson-Circulation illustrated in section 1.2: Transport of tropospheric air into the stratosphere mainly takes place in the tropics and contrariwise in middle and high latitudes: The vertical flux across the tropopause in the tropics is thought to be caused by cumulonimbus clouds that penetrate into the stratosphere by convection. The cross tropopause exchange in the mid-latitudes is dominated by tropopause folding connected to frontogenesis in the vicinity of the jet stream: The dynamical tropopause - defined in terms of Ertel's potential vorticity – intrudes deeply into the troposphere. At the edge of the tropopause folding small-scale mixing occurs. The exchange through the tropopause in both directions is associated to short-lived atmospheric structures.

1.4 Interaction between Ocean and Atmosphere

Winds are a driving force of ocean currents because energy is passed from moving air to the water through friction. As a consequence, a relationship exists between the oceanic circulation and the general atmospheric circulation. In general, in response to the circulation associated with the subtropical highs and as a result of the Coriolis force, ocean currents form clockwise vortices in the Northern Hemisphere and counterclockwise vortices in the Southern Hemisphere. Ocean currents play a major role in maintaining the earth's heat balance. The most prominent example is the moderating effect of the North Atlantic Drift, which is an extension of the Gulf Stream. The same amount of energy is transported towards the North Pole by oceanic and atmospheric circulation. In addition

to producing surface currents, winds can also cause vertical water movements. Upwelling, the rising of cold, nutrient-rich water from deeper layers, is a wind-induced vertical movement. It is characteristic for the eastern shores of the oceans, e.g. along the coasts of West Africa, Peru, and California. Landmasses near to these coastlines are characterised by a climate with very low precipitation. The aridity is intensified due to the chilling of the cold water and air masses become very stable without the upward movement that creates clouds.

Other triggers of ocean currents are surface heating and freshwater input (precipitation plus rivers minus evaporation) which determine the salinity distribution in the ocean. In contrast to the atmosphere, heating of the ocean surface stabilises the water column and prevents rapid replacement of the warm top layer (18°C on average) and the deep water (3°C on average). Therefore, exchange of surface and deep water is limited to some localised polar regions. The resulting thermohaline circulation is very important over long timescales (e.g. glacial cycles).

Perturbations of the oceanic circulation influence the conditions in the atmosphere and therefore all biogeochemical cycles over great distances. E.g. the El Niño refers to episodes of massive ocean warming along the coasts of Ecuador and Peru that replace the cold Peruvian current. These events are part of the global circulation and related to a seesaw pattern of atmospheric pressure between the eastern and western Pacific called the Southern Oscillation. The last very strong El Niño event (1997–1998) was responsible for a variety of weather extremes in many parts of the world and will be briefly investigated in chapter 6. When surface temperatures in the eastern Pacific tend to be colder than average, a La Niña event is triggered. A typical La Niña winter results in colder than normal air over the Northwest Pacific and the northern Great Plains while warming the major part of the rest of the United States.

From a chemical point of view, there is another coupling between ocean and atmosphere through the exchange of trace gases across the air-sea interface. This transfer is mainly controlled by two sometimes competing factors of the temperature: Warming of surface waters releases trace gases such as CO_2, but also affects the biological productivity, which converts dissolved trace gases into other substances. Details of these processes are highly uncertain. For most trace gases, it is unknown whether the ocean is a source or a sink.

1.5 Interaction between Biosphere and Atmosphere

It is a well-known fact that the biosphere is important to the global atmospheric chemistry as a source and a sink for many compounds (see Figure 1-3). Although the determination of such fluxes has been examined for several decades, the uncertainties remain large. The structure of the terrestrial biosphere is controlled by the interaction of climate with the patterns of soils and topography. Usually, climate patterns are reflected in productivity, with warmer regions having higher productivity and up to orders of magnitude higher emission of trace gases. This has brought the tropics into the focus of atmospheric science. One example which is of particular importance for this study are large quantities of hydrocarbons such as isoprene (C_5H_8) released by the foliage of the vegetation in productive ecosystems (see section 1.6.1). The isoprene emission rate has been investigated only for a few hundred out of approximately 240.000 living species (see http://www.es.lancs.ac.uk /cnhgroup/iso-emissions.pdf). Most of the rates reported in the literature do not account for differences in physiological activity. More recent studies include growth conditions, photosynthesis, stomatal conductance and other measurements (e.g. in [Rottenberger et al., 2004; Rottenberger et al., 2005]). This illustrates quite impressive one of the great challenges for atmospheric chemistry and also for global change science, namely the need to extrapolate the impact of biogeochemical processes from the scales of a few microns, at which the processes actually occur, to the global scale.

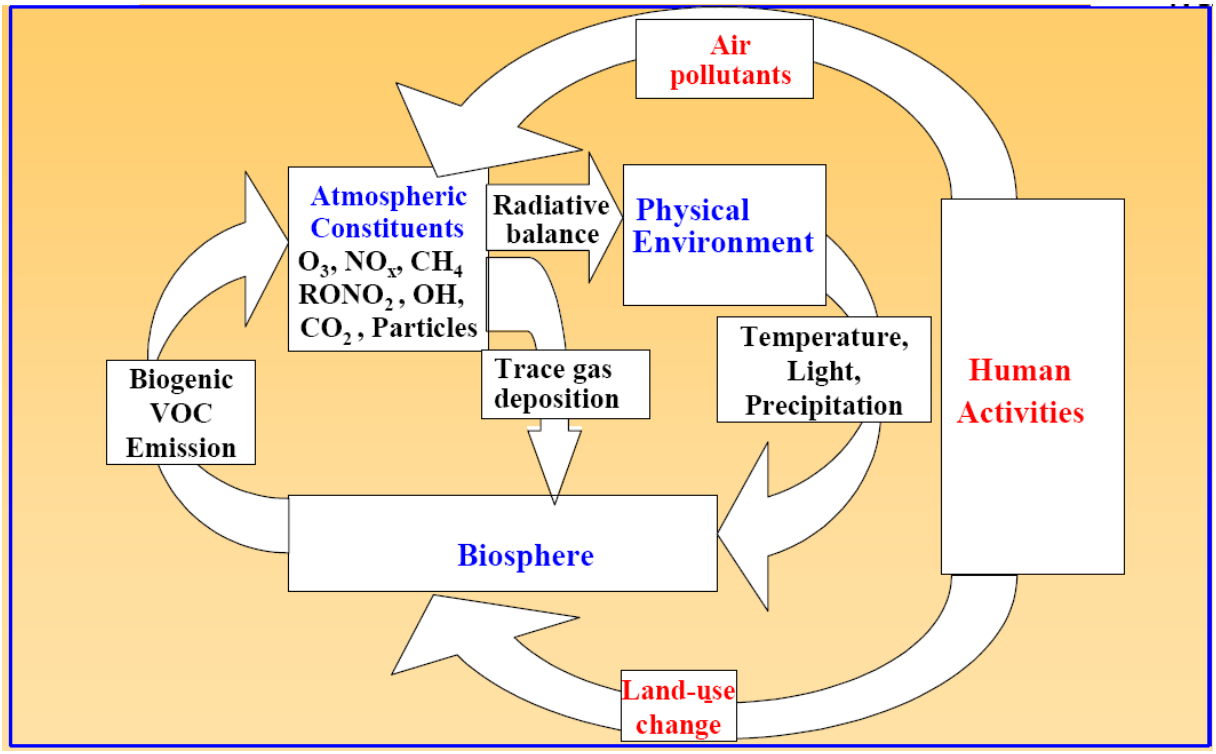

Figure 1-3: This scheme illustrates the coupling between biosphere, atmospheric chemistry, human activities and climate (from Guenther [2003]).

1.6 Tropospheric Chemistry

As mentioned above, in addition to nitrogen, oxygen, inert gases, carbon dioxide and water vapour the air contains many trace gases which influence our atmospheric system. Natural sources of these constituents include volcanic eruptions, forest fires and biogenic emissions. Anthropogenic sources comprise industrial activities, fossil fuel combustion, biomass burning, emissions from livestock and agriculture, emissions and deposition resulting from changes in land usage. The troposphere is dominated by reactions involving ozone and other oxidants, e.g. hydroxyl / peroxy radicals, and nitrogen oxides, which are of significance for the self-cleaning power of the atmosphere. Besides the chemical conversion to non-polluting constituents, such as H_2O or O_2, there are two other removal processes: dry and wet deposition. With the help of dry deposition gases are absorbed by plants, water or soil. This effect is circumstantial since it often only applies to gases in the boundary layer on a local scale. The wet deposition removes species that have a sufficient solubility in water. Many gases released to the troposphere are insoluble but their oxidation leads to polar species, which are often soluble.

The capability of the atmosphere to oxidise trace species emitted into it is referred to by the term oxidation capacity. The radicals determining this capacity in descending order of importance are (adapted from http://www.atmosp.physics.utoronto.ca/people/loic/chemistry.html):

- "The hydroxyl radical OH. Hydroxyl is a short-lived free radical and by far the most effective scavenger in the troposphere. It is the main oxidant for CO, CH_4 and higher hydrocarbons, H_2S (hydrogen sulphide) and SO_2 (sulphur dioxide).
- The nitrate radical NO_3. At night, this radical takes over from hydroxyl as the dominant oxidant in the atmosphere: Hydroxyl is formed by photolysis and its concentration peaks during daytime while NO_3 does not survive sunlight.

- The oxygen atom O(^{1}D). This excited state of the oxygen atom produced by the photolysis of ozone has the ability to oxidise unsaturated hydrocarbons and other gases containing a double bond such as CS_2 and COS in the upper troposphere.
- Peroxy and hydroperoxy radicals HO_2 and RO_2 (where R is an alkyl). HO_2 and RO_2 are strongly linked with hydroxyl in the oxidation cycle. They are not as efficient as hydroxyl, but react with themselves to form H_2O_2, an important oxidant in cloud droplets.
- Hydrogen peroxide H_2O_2. This reacts very efficiently in cloud droplets and oxidises a number of trace gases, in particular sulphur dioxide. Highly soluble, it also accounts for a large part of the excess acidity in rain.
- Ozone, O_3. Ozone reacts directly with many species of biogenic origin.

Together, these oxidants determine the lifetime and the abundance of trace species in the troposphere, acting as atmospheric regulators. The reverse is also true: The abundance of trace species determines the oxidising capacity of the atmosphere because an increase in the emission of a given pollutant reduces the amount of its principal oxidant. The resulting positive feedback may even lead to an increase of other pollutants. This underlines the importance of a stable oxidising capacity in the troposphere."

The primary source of OH is the photolysis of ozone at wavelengths shorter than 320 nm followed by reaction with water vapour:

(R 1) $$O_3 + h\nu \rightarrow O_2 + O(^1D)$$

(R 2) $$O(^1D) + H_2O \rightarrow 2OH$$

Note that only a small fraction (about 1-10 percent depending on humidity) of the excited oxygen O(^{1}D) reacts with water vapour to form hydroxy radicals. The remaining part is quenched through collision with unreactive molecules (M) to its ground state (^{3}P) which quickly recombines with molecular oxygen to form ozone. Thus there is not a significant loss of ozone (e.g. [Kuhlmann, 2001] and references therein).

In the presence of a sufficient amount of nitrogen oxides (NO_x= NO+NO_2) e.g. in urban areas, the oxidation of hydrocarbons and carbon monoxide in the atmosphere can lead to ozone production. The simplest such reaction scheme, is the oxidation of carbon monoxide (CO):

(R 3) $$OH + CO \rightarrow H + CO_2$$

(R 4) $$H + O_2 + M \rightarrow HO_2 + M$$

(R 5) $$HO_2 + NO \rightarrow OH + NO_2$$

(R 6) $$NO_2 + h\nu \rightarrow NO + O$$

(R 7) $$O + O_2 + M \rightarrow O_3 + M$$

(R 8) $$\text{net } CO + 2O_2 + h\nu \rightarrow CO_2 + O_3$$

The radicals OH and HO_2 (HO_x) as well as the oxides of nitrogen NO_x are not affected by this reaction sequence. Such a catalytic cycle is characteristic for many reaction schemes in atmospheric chemistry. The number of times that the reaction sequence 3 to 7 is repeated (the so-called chain length) depends on reactions that remove either HO_x or NO_x.

The main terminating reaction for NO_x is:

(R 9) $$OH + NO_2 + M \rightarrow HNO_3 + M$$

Nitric acid (HNO_3) is a well soluble substance but not very reactive. Thus, there is a high probability of depositing and being lost from the atmosphere before it can release back the NO_2.

HO_x radicals can also directly react with ozone:

(R 10) $$HO_2 + O_3 \rightarrow OH + 2O_2$$

(R 11) $$OH + O_3 \rightarrow HO_2 + O_2$$

Reaction 10 competes with reaction 5. Hence, the availability of NO_x is an important factor in determining whether net production or destruction of ozone prevails. The threshold between high and low NO_x is about 40 ppt_V.

The oxidation of methane is another major reaction scheme in the troposphere. It also serves as an example of HCHO activity in atmospheric photochemistry. Under high NO_x conditions one has ([Crutzen and Lovelock, 1983] and references therein):

(R 12) $$CH_4 + OH \rightarrow CH_3 + H_2O$$

(R 13) $$CH_3 + O_2 + M \rightarrow CH_3O_2 + M$$

(R 14) $$CH_3O_2 + NO \rightarrow CH_3O + NO_2$$

(R 15) $$CH_3O + O_2 \rightarrow HCHO + HO_2$$

(R 16) $$HO_2 + NO \rightarrow OH + NO_2$$

(R 17) $$2(NO_2 + h\nu) \rightarrow 2(NO + O)$$

(R 18) $$2(O + O_2 + M) \rightarrow 2(O_3 + M)$$

(R 19) $$CH_4 + 4O_2 \rightarrow HCHO + H_2O + 2O_3 \text{ net}$$

Again the net reaction is catalysed by the abundance of HO_x and NO_x. Under low NO_x conditions, the reaction of CH_3O_2 with HO_2 can compete with reaction 14:

(R 20) $$CH_3O_2 + HO_2 \rightarrow CH_3O_2H + O_2$$

The formed hydroperoxide CH_3O_2H can again photolyse or react with OH:

(R 21) $$CH_3O_2H + h\nu \rightarrow CH_3O + OH$$

which is rapidly followed by reaction 15 to form HCHO.

The latter reaction is:

(R 22) $$CH_3O_2H + OH \rightarrow CH_2O_2H + H_2O$$

which is followed by

(R 23) $$CH_2O_2H \rightarrow HCHO + OH$$

Because these reactions tend to destroy HO_x, these radicals will be reduced under low NO_x conditions. The resulting formaldehyde, which is not removed heterogeneously, undergoes photolysis or reaction with OH to produce CO, H_2, and HO_2:

(R 24) $$HCHO + h\nu \rightarrow CO + H_2$$

(R 25) $$HCHO + h\nu \rightarrow CHO + H$$

(R 26) $$HCHO + OH \rightarrow CHO + H_2O$$

The products of reactions 25 and 26 rapidly react with molecular oxygen:

(R 27) $$CHO + O_2 \rightarrow CO + HO_2$$

and reaction 4, which yields a link to the CO cycle (reactions 3 to 8).

Since CH_4 and CO are readily available even in remote areas, ozone production from these hydrocarbons is limited by the availability of NO_x. On the other hand these cycles provide the background source of formaldehyde. In the next section the general properties of formaldehyde and the different sources will be described.

1.6.1 Formaldehyde

Formaldehyde (HCHO) is also known as methanal, methylene oxide, oxymethylene, methylaldehyde, oxomethane, and formic aldehyde and is the simplest member of the aldehydes. It is used in large amounts in a variety of chemical manufacturing processes and is produced principally by the vapour-phase oxidation of methanol. At room temperature, formaldehyde is a colourless gas but with a strong pungent, irritating odour. It is highly reactive, readily undergoes polymerisation, is highly flammable, and can form explosive mixtures in air. Formaldehyde is soluble in water, alcohols, and other polar solvents. "As a reactive aldehyde, formaldehyde can undergo a number of self-association reactions, and it can associate with water to form a variety of chemical species with properties different from those of the pure monomolecular substance. These associations tend to be most prevalent at high concentrations of formaldehyde; hence, data on properties at high concentrations are not relevant to dilute conditions" (from. INCHEM). Formaldehyde is harmful to health for levels higher than 0.5 ppm_V. It is extremely irritating to the mucous membranes. Exposure to formaldehyde irritates the eyes, nose, and throat, and can cause skin and lung allergies. Higher levels can cause throat spasms and a build-up of fluid in the lungs. Formaldehyde can cause an asthma-like allergy. Repeated exposures may cause bronchitis, with symptoms of cough and shortness of breath. Formaldehyde is classified as a 'probable human carcinogen'.

Indoor sources of formaldehyde include direct sources such as cigarette smoke [Baek and Jenkins, 2004], fireplaces, cooking [Lee et al., 2002], and outgassing from building materials and consumer products such as wood panels, latex paints, new carpets, textile products, and resins [Hedberg et al., 2002]. In some countries, there are regulations to control emissions from building materials and furnishings, since these are recognised as the major sources of elevated concentrations of formaldehyde in indoor air. Levels up to several hundred ppb_V were reported [Baez et al., 2004].

In the atmosphere, formaldehyde occurs naturally and is the product of many natural processes like the oxidation of methane (see above) and other non-methane hydrocarbons (e.g. [Finlayson-Pitts and Pitts, 1986]). The background level of HCHO in remote areas is about 0.3 – 1 ppb_V (e.g. [Burrows et al., 1991; Slemr et al., 1996; Junkermann and Stockwell, 1999; Weller et al., 2000; Singh et al., 2004]). Formaldehyde is also directly emitted into the atmosphere by combustion of fossil fuels and biomass (e.g. [Anderson et al., 1996; Geiger et al., 2002] and [Holzinger et al., 1999; Yokelson et al., 1999; Andreae and Merlet, 2000]). In anthropogenically polluted areas, HCHO was found in peak levels up to 70 ppb_V (e.g. in Los Angeles or Mexico City [Grutter et al., 2005]). As shown above formaldehyde is an important intermediate in the atmospheric formation of carbon monoxide, CO, and carbon dioxide (CO_2) and its removal by wet and dry deposition processes can reduce the flow of carbon to these species. The photolysis of HCHO, its reaction with hydroxyl (OH) or its reaction with a nitrate radical at night leads to the perhydroxyl radical (HO_2) formation and subsequently, and more importantly, to stronger oxidants like OH and ozone [Logan et al., 1981]. HCHO may be taken up by atmospheric water where it deposits with precipitation or participates in aquatic reactions with species like dissolved SO_2 or OH (e.g. [Chameides and Davis, 1983]). Ocean surfaces are thought to be sinks for HCHO [Thompson and Zafiriou, 1983]. However,

it may be released to the atmosphere through snow and ice chemistry [Riedel et al., 1999; Sumner et al., 2002], or through the photochemical degradation of dissolved organic matter and biological processes [Zhou and Mopper, 1997]. Formaldehyde indirectly influences chlorine chemistry. Therefore it is likely that HCHO plays a major role in the development of tropospheric ozone depletion episodes during polar sunrise [Rudolph et al., 1999]. HCHO plays a role in HO_x chemistry and in ozone production as a source of HO_2 and hence NO_2.

In summary, it is believed that most of the global formaldehyde is a product of hydrocarbon or volatile organic compound (VOC) oxidation. Because of the short lifetime of HCHO of a few hours [Arlander et al., 1995] one can assume that it is highly correlated with the emission field of the precursor compounds [Palmer et al., 2003], which is important for the interpretation of the results in chapter 6. In particular Isoprene (C_5H_8) and monoterpenes (general formula $(C_{10}H_{16})_n$) are reactive VOCs which are emitted into the atmosphere by vegetation in large quantities. The magnitude of isoprene emissions on a global scale is of the same order as methane and twice as high as anthropogenic VOC emissions [van Aardenne et al., 2001] but there is a large uncertainty on the real numbers (see Table 2 and section 1.5). The lifetimes of isoprene and monoterpenes are small. Considering both day and night, the lifetimes of isoprene range from 1.5 to 3 hours. For α-pinene, an important monoterpene, the lifetime can range from as little as 5 minutes to 3 hours [Kesselmeier and Staudt, 1999]. Monoterpenes emitted by plants generally "contain at least one unsaturated carbon-carbon bond, and often have one or more rings in their structure. In the case of α-pinene, one of these rings contains just four carbon atoms, which introduces strain in some of the carbon-carbon bonds and consequently, increases the reactivity of the molecule" [Sanderson, 2002, p. 2]. Both, the short lifetime of HCHO and most of the emitted VOCs, might help to improve the current emission inventories by means of global observations of formaldehyde. A first attempt has been made using GOME observations above North America by [Palmer et al., 2003]. Clearly, HCHO measurements together with observations of other photochemically active species, for example NO_2, are powerful tools in testing our understanding of ozone production, hydrocarbon oxidation and, in general, the oxidising power of the atmosphere represented by O_3 and OH, but for this, long-term and in particular quality controlled data sets are necessary. This is one of the major aims of this study.

Table 2: Global natural VOC emission rate estimates [Tg C yr^{-1}] from different studies, from Kesselmeier and Staudt [1999]

	Isoprene	*Monoterpenes*	*Other reactive VOCs*	*Other VOCs*	*Total*
[Went, 1960]					175
[Rasmussen and Went, 1965]					432
[Robinson and Robbins, 1968]					480
[Zimmermann, 1979]	350	480			
[Rasmussen and Khalil, 1988]	452				
[Warneck, 1988]					>800
[Dignon and Logan, 1990]	450				
[Taylor et al., 1990]	175	143			
[Turner et al., 1991]	285				
[Mueller, 1992]	250	147			
[Allwine et al., 1992]	420	128		279	827
[Guenther et al., 1995]	503	127	260	260	1150

1.6.2 Glyoxal

Glyoxal (CHOCHO) is also known as ethanedial, diformyl, ethanedione, biformal, and oxal. Glyoxal can undertake rotational isomerisation between the planar *cis* and *trans* conformations (see Figure 1-4), with trans-glyoxal being the more stable isomer (see INCHEM).

Figure 1-4: Structure of the glyoxal. Left: *trans*-, right *cis*- glyoxal.

Glyoxal is the smallest α-dicarbonyl compound. It is a colourless to yellow liquid with a faint odour. It is also miscible with water. Glyoxal is harmful by inhalation and may cause sensitisation by skin contact and is irritating to eyes and skin. It is used as a chemical intermediate in the production of pharmaceuticals and dyestuffs. It is also industrially employed as a cross-linking agent in the production of a variety of polymers, such as textiles.

Furthermore, glyoxal is used as a biocide and as a disinfecting agent and is contained in many products, such as cleansers used for the disinfection of surfaces.

In the atmosphere, there are several sources of glyoxal: It is formed during the oxidation of hydrocarbons in particular of aromatic hydrocarbons [Volkamer et al., 2001], in analogy with formaldehyde both from biogenic and anthropogenic sources. Figure 1-5 illustrates hydroxyl radical reaction schemes showing glyoxal as a minor second- or third-generation oxidation product of isoprene and 2-methyl-3buten-2-ol (MBO) which is emitted in high levels from pines. Furthermore, this figure comprises information on the possible ratios between CHOCHO and HCHO (here about 0.04 for isoprene and 0.1 for MBO).

Lee et al. [1998] have reported mean levels of 0.07 ppb_V glyoxal in the boundary layer of a rural site which were thought to originate from isoprene rather than from anthropogenic emissions. Spaulding et al. [2003] found lower values of about 0.03 ppb_V above a ponderosa pine plantation in California. Biomass burning and domestic as well as residential log fires will release glyoxal in addition to other aldehydes [Ho and Yu, 2002]. Another recognised source of glyoxal is traffic emissions and the subsequently formed photochemical smog, which gives rise to the formation of this compound. Direct vehicle emissions are believed to be small [Volkamer et al., 2005]. During the day, photolysis and reaction with OH determine its lifetime which was found to be less than 2 hours for overhead sun conditions.

In summary, measurements of glyoxal are quite sparse and most of them from urban areas. Nevertheless, they can lead, in conjunction with measurements of formaldehyde and other photochemical species like NO_2, to a better understanding of VOC chemistry and source strengths.

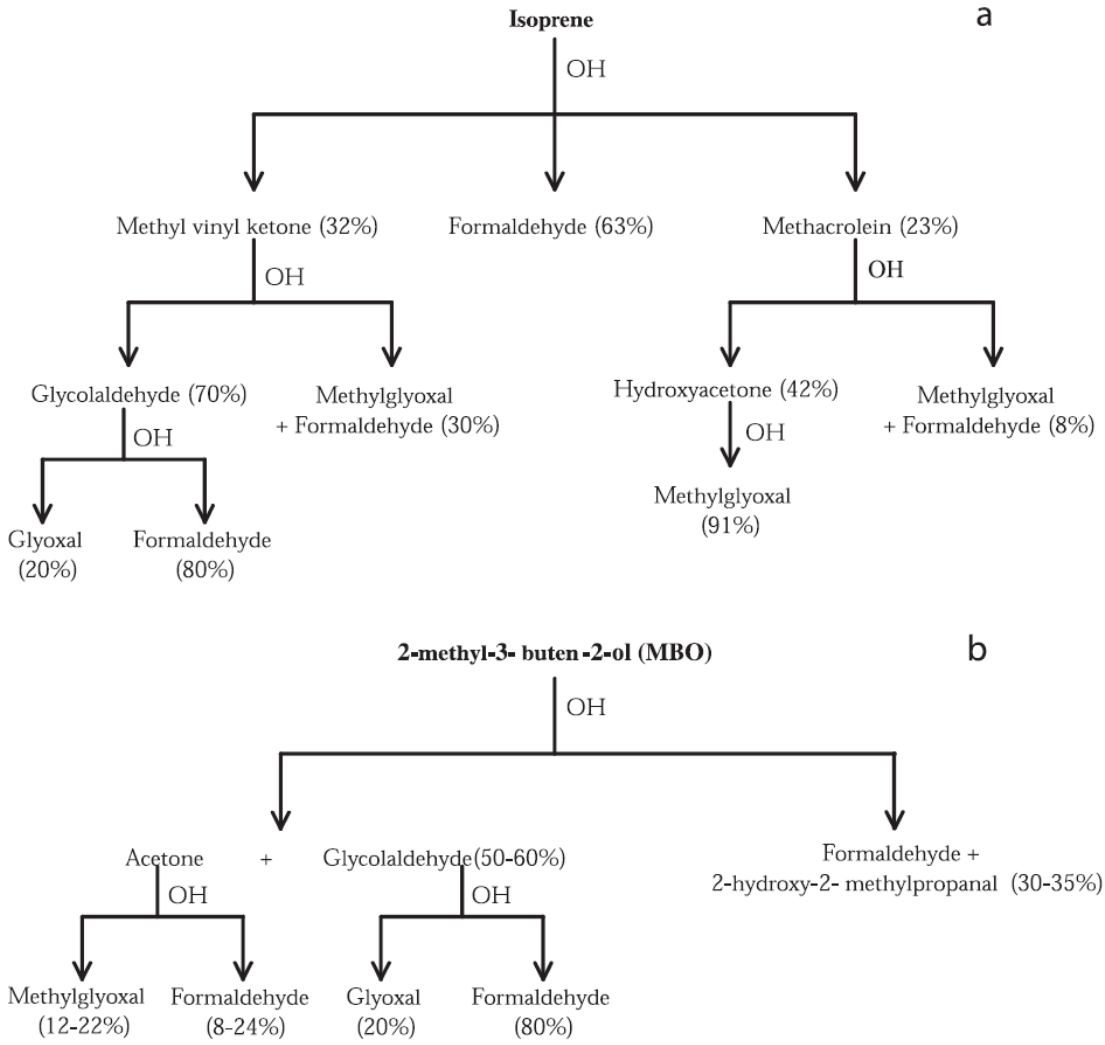

Figure 1-5: Hydroxyl radical reaction schemes for (a) isoprene, and (b) 2-methyl-3-buten-2-ol (MBO), from Spaulding, et al. [2003]. From that CHOCHO to HCHO ratios between 0.04 and 0.1 can be derived.

2 Instruments

This chapter describes, in the first three sections, the instruments used to derive the data for retrieving atmospheric HCHO and CHOCHO columns by means of the DOAS method. The latter will be discussed in the next chapter 3. One characteristic, all these instruments have in common, is that they measure light scattered by the earth's atmosphere in the ultraviolet (UV) and visible (vis) range as illustrated in Figure 2-1. In the fourth section, all instruments from which supplementary data have been utilised are introduced briefly. Instrumental shortcomings will be discussed in detail in Section 5.1.

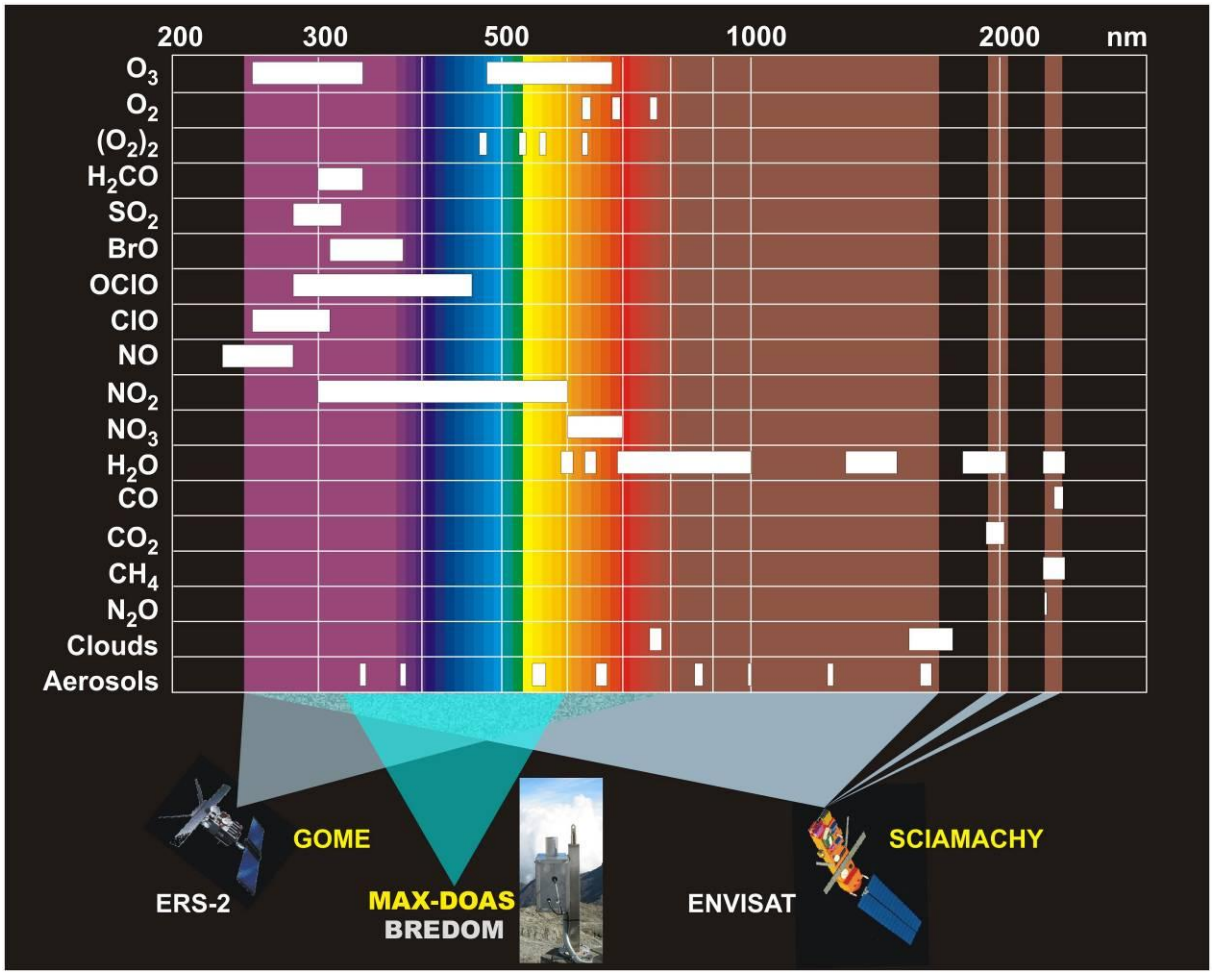

Figure 2-1: The wavelength range covered by the UV/vis instruments used in this study (GOME, SCIAMACHY, and MAX-DOAS) together with spectral regions where the major trace gases are typically analysed.

2.1 Global Ozone Monitoring Experiment (GOME)

The Global Ozone Monitoring Experiment (GOME) aboard the second European Remote Sensing satellite (ERS-2) is successfully monitoring the earth atmospheric composition since its deployment in space in April 1995 ([Burrows et al., 1997] and references therein). GOME is the first European passive remote sensing instrument operating in the ultraviolet, visible, and near infrared wavelength regions. Primary data products are vertical columns of ozone and nitrogen dioxide. Advanced products include vertical profiles of ozone and columns of bromine oxide, chlorine dioxide, and other minor trace gases as well as tropospheric NO_2 columns (e.g. [Burrows and Chance, 1992; Eisinger and Burrows, 1998; Hegels et al., 1998; Richter et al., 1998; Wagner and Platt,

1998; Hoogen et al., 1999; Wittrock et al., 1999; Chance et al., 2000]). In June 2003, the tape recorder on ERS-2 permanently failed, and since then, only those GOME measurements are available that can be directly recorded by a ground receiving station, reducing the coverage by about 70 percent.

The GOME instrument was proposed in 1988 by John P. Burrows and Paul Crutzen as a small scale version (SCIAmini) of the Scanning Imaging Absorption Spectrometer for Atmospheric Cartography (SCIAMACHY, see 2.2). GOME is observing the atmosphere in nadir viewing geometry only with four spectral channels, as opposed to eight channels for SCIAMACHY. In addition, GOME performs a direct solar irradiance measurement once per day and in order to enhance coverage of the polar regions the line of sight can be tilted under an angle towards this region (polar view). The latter data however are not used in this thesis.

2.1.1 The GOME instrument

The GOME instrument is a double monochromator which combines a predisperser prism, a channel-separator prism and in each of the four optical channels a holographic grating as dispersing elements. The four channels comprise the wavelength intervals 237-316 nm, 311-405 nm, 405-611 nm and 595-793 nm (see Table 3). A schematic diagram of the GOME optical layout is shown in Figure 2-2. Irradiance and radiance spectra are sampled with four linear Reticon silicon-diode arrays with 1024 spectral elements each – so-called pixels. In order to reduce the dark current, Peltier elements attached to the diode arrays and connected to passive deep space radiators cool the detectors to about -40ºC.

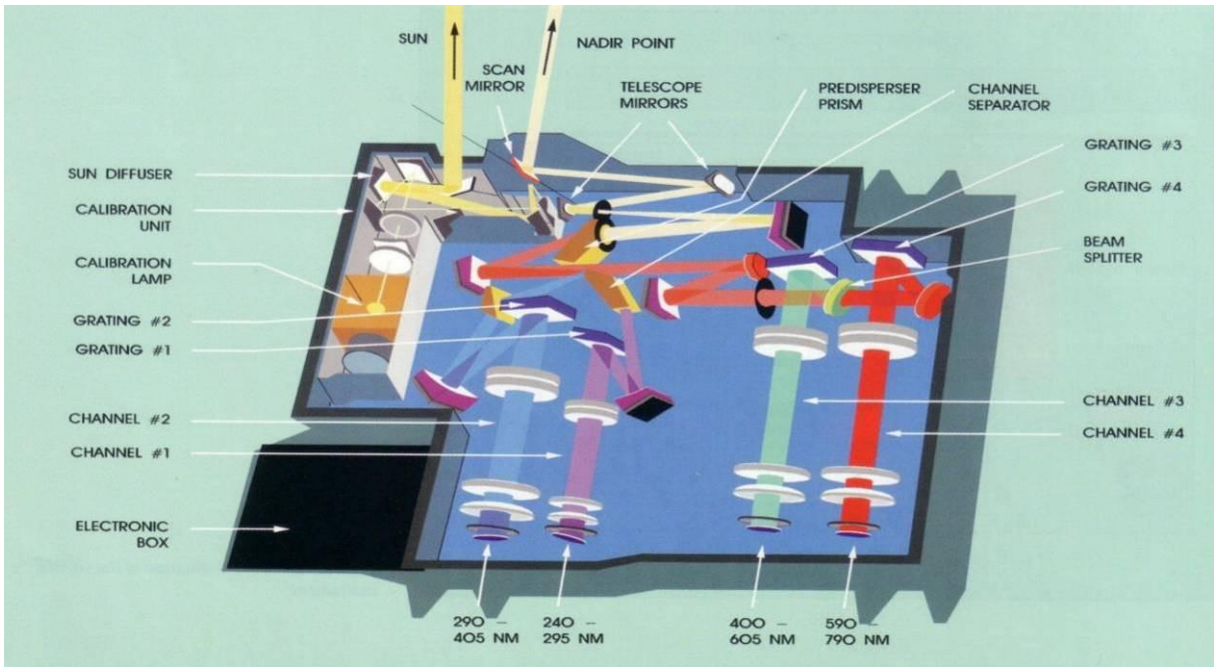

Figure 2-2: Functional block diagram of the GOME spectrometer optical system [ESA, 1995]

Except for the scan mirror at the nadir view port, all parts of the instrumental set-up are fixed. Spectra are recorded simultaneously from 240 nm to 790 nm. The light which reaches the predisperser prism is split into two branches. The first one is recorded with three broadband polarisation monitoring devices (PMD), which approximately cover the spectral range in the optical channels two to four: 300-400 nm, 400-580 nm and 580-750 nm, respectively. The PMDs measure the amount of light under an instrument-defined polarisation angle to facilitate correction of the instrument polarisation sensitivity in the level 0 (raw data) to level 1 (calibrated spectra) con-

version. The second, moderately wavelength dispersed beam is focused by a parabolic mirror into the channel separation prism.

The calibration unit adjacent to the spectrometer comprise of the sun-view-port and a compartment housing a platinum-neon-chromium hollow cathode discharge lamp. The solar radiation is attenuated by a mesh (20 percent transmission) and directed via a diffuser plate (wet-sanded aluminium plate with chromium/aluminium coating) onto the entrance slit of the spectrometer. As a result of residual periodic structures on the diffuser, spectral artefacts are present in the solar irradiances recorded by GOME which depend on the illumination angle and therefore on the seasonally varying position of ERS-2 relative to the sun [Richter and Wagner, 2001].

2.1.2 GOME Viewing Geometries

The ERS-2 satellite moves in a retrograde, sun-synchronous, near polar orbit at a height of about 795 km. The maximum scan width in the nadir viewing is 960 km and global coverage is achieved within three days (after 43 orbits), the orbit repeating time being 35 days. The local crossing time at the equator is 10:30 AM for the descending node. An across track scan sequence consists of four ground pixel types called East, Nadir, West, and Backscan with typically 1.5 seconds integration time each as indicated in Figure 2-3. In the UV part of channel 1 (Channel 1A) and beyond 85° solar zenith angle, integration times are longer to compensate for lower light intensities.

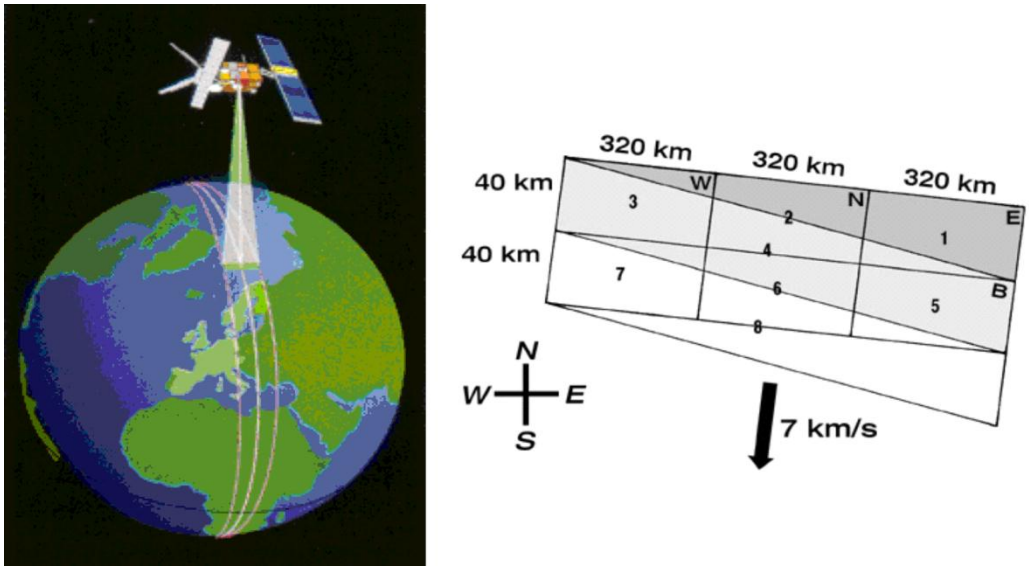

Figure 2-3: The illustration to the left shows the nadir looking GOME instrument onboard ERS-2. In addition, the scan geometry is shown for two successive scan sequences. The forward scan consists of East (E), Nadir (N), and West (W) pixels (320 x 40 km^2 each) and is followed by a Backscan (B) (light grey). The satellite is moving from North to South crossing the equator at 10:30 local time. The local overpass time changes with latitude. The difference is about one hour between 53°N (11.00 LT) and 53°S (10.00 LT). This can have an impact on observations of photochemically active species as in this study. Usually, every tenth day GOME is measuring in a narrow swath mode having a spatial resolution of 80 x 40 km^2 for the forward scans but consequently at reduced spatial coverage (see Figure 6-15).

The PMDs are readout sequentially every 93.75 msec, which implies that for a nominal East-West scan (4.5 sec) forty-eight PMD measurements are collected for each wavelength region. Using the maximum possible scan width of 960 km, each PMD covers an area of 40×20 km² on the surface. This qualifies the PMD measurements for detecting rapid changes in the observed surface reflectivity and cloudiness during scanning.

Table 3: Fact sheet on GOME onboard ERS-2 – channel 2 is applied in this study for the HCHO retrieval [ESA, 1995; Burrows et al., 1999].

Channel	*Wavelength [nm]*	*Integration Time [s]*	*Spectral Resolution [nm]*	*Polarisation Measurement Device (PMD)*
1A	237-283	12	0.20	
1B	283-316	1.5	0.20	
2	311-405	1.5	0.17	1
3	405-611	1.5	0.29	2
4	595-793	1.5	0.33	3

2.2 Scanning Imaging Absorption Spectrometer for Atmospheric Cartography (SCIAMACHY)

The SCIAMACHY (SCanning Imaging Absorption spectroMeter for Atmospheric CartograpHY) is a spectrometer designed to measure sunlight, transmitted, reflected and scattered by the earth's atmosphere or surface in the ultraviolet, visible and near infrared wavelength region (240 nm – 2380 nm) at moderate spectral resolution (0.2 nm – 1.5 nm) [Bovensmann et al., 1999]. SCIAMACHY was launched on ENVISAT into orbit on March 1st, 2002 and has an equator crossing time of 10 AM which is about half an hour earlier than GOME. As mentioned above, SCIAMACHY is an enhanced version of the GOME instrument, but in many respects, the two experiments are quite similar. The absorption, reflection and scattering characteristics of the atmosphere are determined by measuring the extraterrestrial solar irradiance and the upwelling radiance observed in different viewing geometries: In addition to the nadir measurements implemented in GOME, SCIAMACHY also performs solar and lunar occultation measurements and limb scans. From these measurements, column amounts and to some extent also vertical distributions of O_3, BrO, OClO, SO_2, HCHO, NO_2, CO, CO_2, CH_4, H_2O, N_2O, pressure (p), temperature (T), aerosol properties, radiation, cloud cover and cloud top height can be retrieved [Afe et al., 2004; Buchwitz et al., 2004; Noel et al., 2004; Richter et al., 2004; Buchwitz et al., 2005; Frankenberg et al., 2005; von Savigny et al., 2005]. A special feature of SCIAMACHY is the combined limb-nadir measurement mode which allows determining the tropospheric column amounts of several trace gases with better accuracy than with the nadir mode only.

2.2.1 The SCIAMACHY Instrument

The ENVISAT satellite with SCIAMACHY flies like ERS-2 in a sun-synchronous, near polar orbit at a height of about 800 km. The maximum scan width in the nadir-view is 960 km and global coverage is achieved within six

days (after 86 orbits), the orbit repeating time being 35 days. SCIAMACHY consists of three basic parts: the optical unit, the electronic unit, and the radiant cooler. In contrast to GOME, the instrument contains two scan mirrors in the light path: one at the front of the elevation scanner module (ESM) and one at the front of the azimuth scanner module (ASM). In nadir mode, only the ESM mirror is used to scan in the east-west direction (across track). When looking at the limb, both mirrors are used to perform the azimuth scan (east-west direction) as well as the elevation scan (up-down direction). A telescope mirror produces a focus on the entrance slit of the spectrometer. Afterwards, a predisperser prism of the spectrometer separates the collimated light into three spectral bands which are split into 8 different channels. A grating located in each channel further disperses the light which is then focused on eight detector arrays (each with 1024 pixel). As in the GOME instrument, the predisperser is used as a Brewster window to extract a small fraction of the light polarised perpendicular to the instrumental optical plane (parallel to the entrance slit). The polarised light is distributed to the PMDs (see Table 4).

Table 4: Fact sheet on SCIAMACHY [Burrows et al., 1995; Bovensmann et al., 1999] – channels 2 and 3 are used in this study for the retrieval of formaldehyde and glyoxal, respectively. The integration times are different for different spectral bands, so that the ground pixel size for a certain trace gas column depends on the spectral band it is retrieved from. In the case of HCHO and CHOCHO one has typically 0.5 sec (pixel size 30 km along track and 60 km across track). For spectral fitting of HCHO in this study four pixels were averaged yielding a spatial resolution of 60 x 120 km^2.

Channel	*Spectral Range [nm]*	*Spectral Resolution [nm]*	*Polarisation Measurement Device (PMD)*
1	240 - 314	0.24	
2	309 - 405	0.26	0
3	394 - 620	0.44	1
4	604 - 805	0.48	2
5	785 - 1050	0.54	3
6	1000 - 1750	1.48	4
7	1940 - 2040	0.22	
8	2265 - 2380	0.26	5

2.2.2 SCIAMACHY viewing geometries

SCIAMACHY performs measurements in nadir, limb, and solar/lunar occultation geometry (see Figure 2-4). In nadir mode, the atmospheric volume beneath the spacecraft is observed, scanning an area on ground corresponding to a maximum swath width of 30 km along track by 960 km across track. The edge of the swath width has a line of sight (LOS) varying from 0° to a maximum of about 30.9° which has to be taken into account for radiative transfer modelling (see section 5.2.2).

In the limb mode, the spectrometer slit is projected parallel to the horizon in flight direction by a combination of the ASM and the ESM mirrors. The ASM mirror scans the atmosphere through different tangent heights from 0 to 100 km in horizontal (azimuth) direction; whereas, appropriate movement of the ESM mirror results in a vertical (elevation) scan direction. A typical limb scan cycle comprises 34 horizontal scans at different tangent heights, starting 3 km below the horizon. One of the main issues for these limb observations is the accuracy with which the tangent heights can be reconstructed. The requirements on the knowledge of orientation and position of the spacecraft are particularly strict for limb-viewing instruments, because of the large distance between the satellite and the sampled air volume (about 3000 km). For instance, an angular difference of only 1 arcmin translates to a tangent height difference of about 1 km [von Savigny et al., 2005]. The individual spatial resolution is typically 240 km within a 960 km swath width in the horizontal direction across track.

About 7 minutes after a measurement in the limb mode has been carried out, the same atmospheric volume is measured in the nadir mode. In principle, this feature, called limb-nadir-matching, permits to separate the tropospheric trace gas amounts from the total column for a variety of atmospheric trace gases. Up to now, this has been accomplished for NO_2 (see e.g. PROMOTE, PROtocol MOniToring for the GMES Service Element).

Occultation measurements are performed using the ASM and ESM mirrors with the sun or moon in the full view of the instrument. SCIAMACHY selects a target, the sun or the moon and tracks it as soon as it appears above the horizon and until the line of sight reaches a maximum tangent height of 100 km. Spectra of the source radiation transmitted through the atmosphere are recorded during the complete sequence.

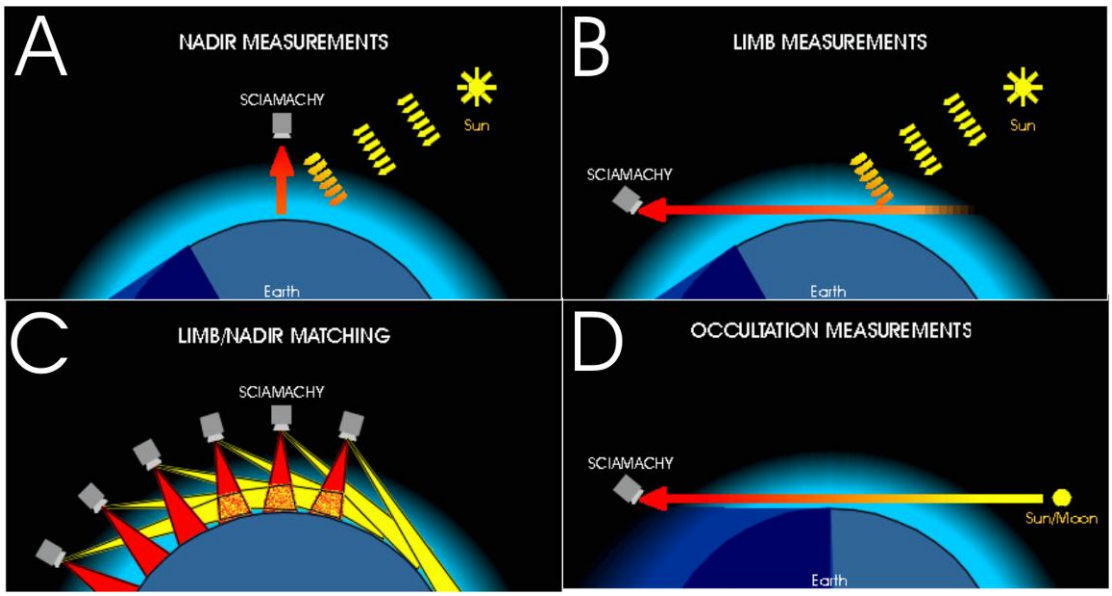

Figure 2-4: Measurement modes from SCIAMACHY: Only measurements using the nadir mode (A) have been used in this study.

2.3 Bremian DOAS Network for Atmospheric Measurements (BREDOM)

The BREDOM is a ground-based network of high quality UV/visible spectrometers for atmospheric observation that has been set up by the Institute of Environmental Physics (IUP), University of Bremen. BREDOM was proposed in 2001 by John P. Burrows to extend the existing DOAS sites operated by the IUP Bremen (Ny-Ålesund and Bremen) to low latitudes. The most important aim is to provide long-term, continuous measurements of a number of stratospheric and tropospheric species at latitudes ranging from the Arctic to the equator focussing on satellite validation. The instruments used for the network are NDSC-qualified ([Roscoe et al., 1999; Vandaele et al., 2005]), and a close co-operation exists with the NDSC and other DOAS networks (from the University of Heidelberg, the IASB, NIWA) and the SAOZ network of the CNRS, adding to the global atmospheric observation system.

The stations of the BREDOM are given in Table 5. The distribution of the stations is designed to provide a latitudinal cross-section covering Arctic, mid-latitude and tropical regions. This is particularly useful for satellite validation like SCIAMACHY, as a broad range of atmospheric situations (summer / winter; high / low ozone, NO_2, H_2O; vortex / non vortex conditions; changing albedo, cloud cover, ...) and also of different measurement conditions (high / low solar elevation) is covered. In addition, the network is also well-suited for studies of stratospheric ozone loss, bromine loading and tropospheric pollution. In particular in tropical regions, biogenic and biomass burning emissions and lightning produced NO_x as well as troposphere to stratosphere exchange (see section 1.3) can lead to large tropospheric ozone concentrations.

Table 5: Permanent BREDOM sites

Station	*Latitude*	*Longitude*	*Status*	*Wavelength coverage*
Ny-Ålesund	79°N	12°E	operational since spring 1995	320 – 565 nm
Bremen	53°N	8°E	operational since spring 1993	320 – 720 nm
Merida	8°N	71°W	operational since spring 2004	320 – 410 nm
Nairobi	1°S	36°E	operational since summer 2002	320 – 565 nm

One of the lessons learned from the validation of GOME data is the need for measurements at low latitudes (e.g. in [Ladstätter-Weißenmayer et al., 1996]). Compared to Northern mid-latitudes and the polar regions, the density of measurement stations at low latitudes is sparse and routine zenith-sky measurements of halogen oxides and other minor trace species are not performed at all. However, such measurements are needed for several reasons: First of all, the tropical regions are of paramount importance for the atmosphere as a whole as most of the vertical transport to the stratosphere takes place at these latitudes (see section 1.3). Therefore, satellite measurements at low latitudes are of particular interest, and validation of these data has a high priority. In addition, the specific measurement conditions at these latitudes, namely high sun and short light path through the atmosphere are particularly challenging for the satellite instrument. If these data can be validated with good accuracy, many error sources can be minimised that are also important for data taken at other latitudes. For example, GOME measurements of minor trace species are subject to varying offsets that could be corrected if appropriate ground-truth would be available at low latitudes.

All stationary instruments of the network are measuring continuously. That is at Ny-Ålesund only outside of the polar winter from mid of February to mid of October. Using the zenith-viewing direction for stratospheric species and the horizon viewing measurements for tropospheric retrievals, stratospheric column amounts of the trace gases Ozone, NO_2, BrO and OClO are retrieved routinely, and tropospheric columns and profiles of NO_2, HCHO, IO, CHOCHO and H_2O can also be determined.

A BREDOM travelling instrument has participated in several campaigns e.g. at OHP (NDSC campaign June 1996, [Roscoe et al., 1999]), Kaashidhoo (INDOEX campaign February and March 1999, e.g. [Burkert et al., 2003]), the Po valley (FORMAT campaign July/August 2002 and August/September 2003, [Heckel et al., 2005]), Andøya (NDSC campaign February/March 2003, [Vandaele et al., 2005]) and Cabauw (DANDELIONS campaign June/July 2005). Some of the data obtained during these campaigns will be presented in this study.

2.3.1 The MAX-DOAS instrument

One major aim of this thesis was to redesign the 'classical' zenith-sky DOAS in order to provide information also on the tropospheric amounts of the absorbers.

The standard set-up as used for several decades (e.g. [Noxon, 1975; Solomon et al., 1987]) has its highest sensitivity in the stratosphere, in particular during twilight. This is the result of the large enhancement in stratospheric light path at dawn and dusk combined with a relatively short tropospheric path. When measurements at twilight are analysed relative to noon measurements as often is the case, the tropospheric contribution effectively cancels as long as concentrations do not vary over time. However, in the presence of clouds, tropospheric absorbers can contribute significantly to the signal [Erle et al., 1995; Platt et al., 1997; Pfeilsticker et al., 1998; Wagner et al., 1998; Pfeilsticker et al., 1999; Winterrath et al., 1999] but they are difficult to quantify as the exact light path is not known.

The sensitivity of the instrument towards tropospheric signals can be strongly increased by pointing the telescope to the horizon instead of the zenith. Depending on tropospheric visibility, the light path in the lower layers can become very long. At the same time, the light path through the stratosphere is in good approximation independent of the instrument pointing. Thus, by taking measurements at different viewing directions, vertical profiles with several pieces of information in the troposphere can be retrieved as discussed in chapter 5.3.

The instrumental challenge was therefore to change the existing instruments in a way that allows both zenith-sky and horizon measurements in a fully automated way both in very cold and hot climates over long periods of time.

After successful tests in April 1998 in Ny-Ålesund and during the INDOEX campaign on the Maldives (February/March 1999) [Wittrock et al., 1999], the set-up which is now used at all BREDOM stations was developed in co-operation with Sixten Fietkau [Fietkau, 2006] and Thomas Medeke [Medeke, 2006]. It facilitates not only zenith-sky observations, but also measurements at lines of sight from -5° (for mountain sites) to 30° above the horizon. The viewing directions are selected by a computer controlled mirror inside the telescope housing as described below, providing a rugged and versatile set-up.

All stations of the BREDOM network are now equipped with Multi-Axis Differential Optical Absorption Spectroscopy (MAX-DOAS) instruments. These instruments are basically UV/visible spectrometers observing scattered light in different viewing directions.

The instruments consist of at least one grating spectrometer equipped with a cooled CCD (charge-couple device) detector and a separate telescope unit connected to the main instrument via a quartz fibre bundle. The spectrometer is temperature stabilised to avoid wavelength drifts. Although the installed CCD is a two-dimensional detector, it is operated in full vertical binning for optimal signal-to-noise ratio and to avoid problems with pixel-to-pixel variation on the chip. The quartz fibre bundle efficiently depolarises the incoming light and also provides flexibility for the instrument set-up. The telescope unit (see Figure 2-5 below) has two viewing ports, one to the zenith and one to the horizon. The viewing direction or line of sight (LOS) is selected via a motorised mirror. In the lower part of the housing, two calibration lamps (a mercury-cadmium line lamp and a white light source) are integrated for calibration measurements. To limit the field of view of the instrument, a small lens is installed in front of the quartz fibre bundle. To prevent direct sunlight from entering the telescope, additional shades are mounted on both the zenith and the horizon ports (not shown in the figure).

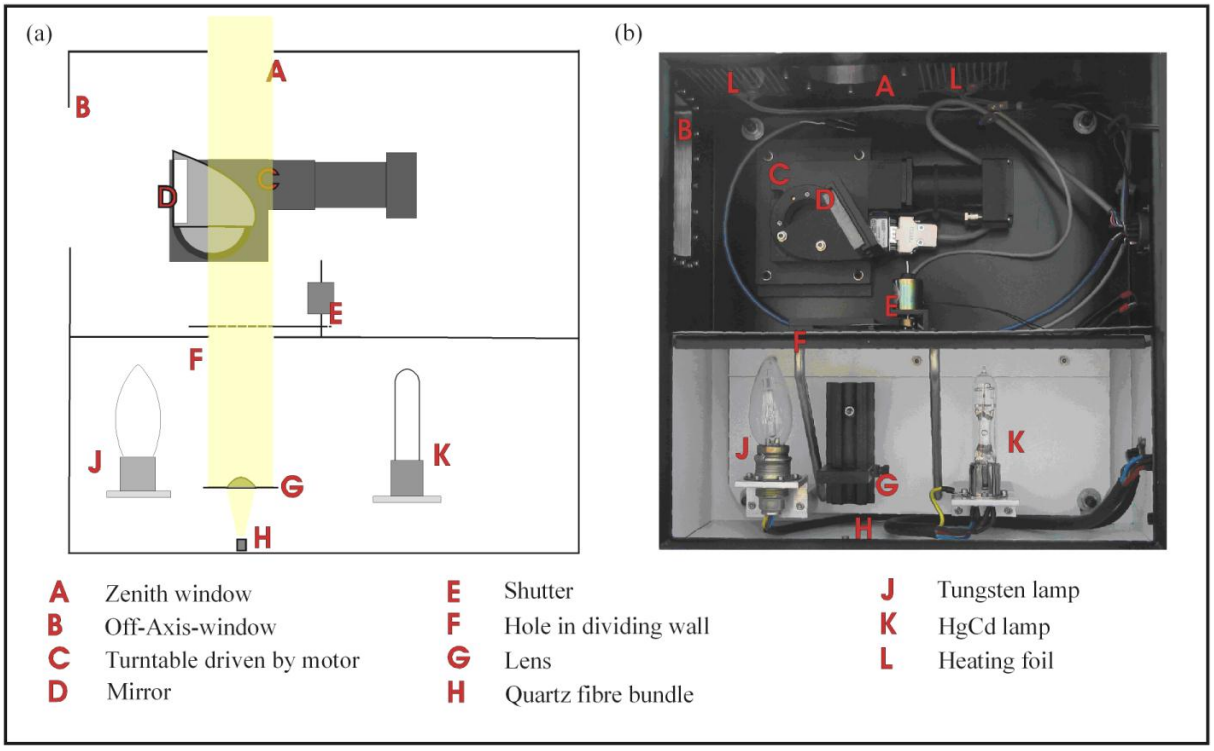

Figure 2-5: Schematic (left) and photo (right) of the telescope used for the BREDOM instruments.

During operation, the instrument scans sequentially several viewing directions from the horizon to the zenith, taking about 1 minute of measurements in each direction. The angle selection depends on location and the focus of the measurements. The integration times are automatically chosen from a test measurement and increase towards twilight. At night, calibration measurements (line lamp for wavelength calibration, white light source for throughput monitoring, dark measurements for dark current characterisation) are taken. As the calibration unit can be separated by a shutter, the calibration is also possible during polar day.

To optimise spectral coverage and resolution, three of the four BREDOM stations (Bremen, Ny-Ålesund and Nairobi) are equipped with two spectrometers, one for the UV and one for the visible part of the spectrum. The instruments share the telescope unit through a quartz fibre bundle that splits into two ends on the spectrometer side.

2.3.1.1 Stratospheric Observations (zenith-sky DOAS)

For stratospheric observations, usually, the zenith viewing direction is applied. If the species of interest is known to be negligible in the troposphere, any viewing direction can be used and measurements towards the bright part of the sky have been used in some studies of e.g. OClO in Antarctica to improve the signal [Arpag et al., 1994; Miller et al., 1997]. The sensitivity of the instrument is largest at twilight as a result of the long light path in the stratosphere. This is illustrated below in the Figure 2-6, where a simplified light path is shown for high and for low sun.

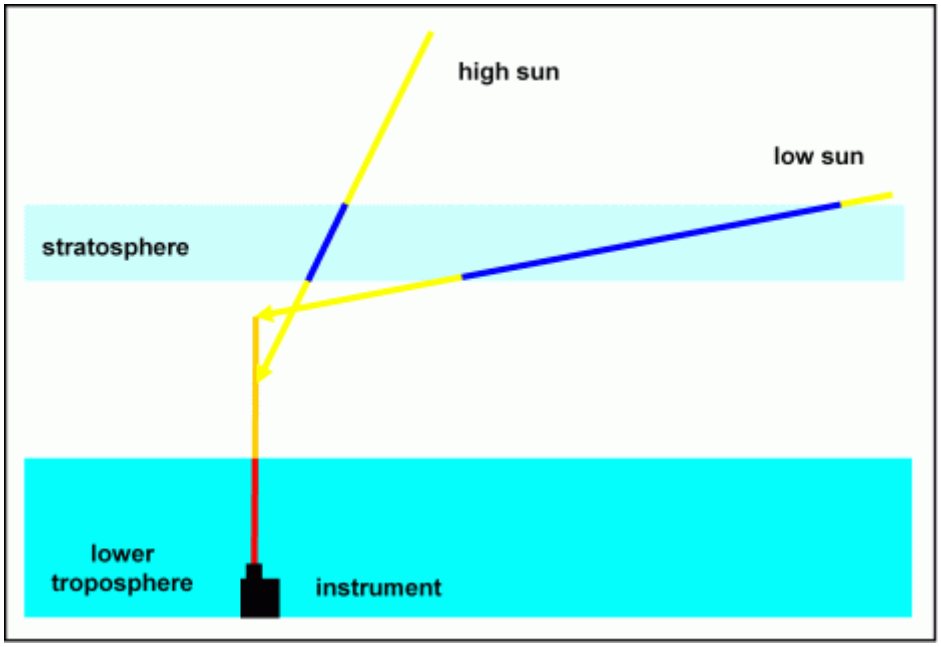

Figure 2-6: Sketch of a zenith-viewing measurement. Towards high solar zenith angles (low sun) the effective light path through the stratosphere is increasing.

In the real atmosphere, the situation is more complex as a result of the curvature of the atmosphere, refraction and the effects of multiple scattering (see section 4.1). However, the basic idea remains and measurements of stratospheric constituents are therefore based on comparison of data taken at dawn and dusk with a reference taken around noon. If the instrument is stable enough, a background spectrum from another day can be used to improve consistency or signal (important for high latitudes where the range of solar zenith angles (SZA) available is small during some times of the year).

An interesting aspect of the above sketch is that the light path in the lower troposphere (red) is the same for measurements at high and low sun. Thus, a constant tropospheric contribution will cancel when comparing noon and twilight measurements of the same day, making the measurements even more adequate for stratospheric research. However, if the tropospheric concentrations vary over the day or if the tropospheric light path changes e.g. due to clouds, the stratospheric measurements can be affected.

While sensitivity is highest at twilight, this time of measurement is not always desirable for other reasons: Many atmospheric species of interest undergo rapid photochemistry, and concentrations can change strongly during twilight making interpretation difficult. On the other hand, in combination with model calculations, such changes can provide additional information on the chemistry of the absorber. For satellite validation, the searched quantity is the column at time of overpass, and this is often not at twilight. For such cases, the measurements must

either be interpolated (possibly using a chemical model) or a reduced sensitivity of the ground-based measurement at higher sun has to be accepted.

2.3.1.2 Tropospheric Observations (MAX-DOAS)

For tropospheric observations, the MAX-DOAS instruments use the measurements pointing to the horizon. As illustrated in the Figure 2-7, the light path through the upper atmosphere (dark blue, above the scattering point) does not depend on viewing direction, while in the lowest atmospheric layers, the light path (dark red) increases as the viewing direction approaches the horizon.

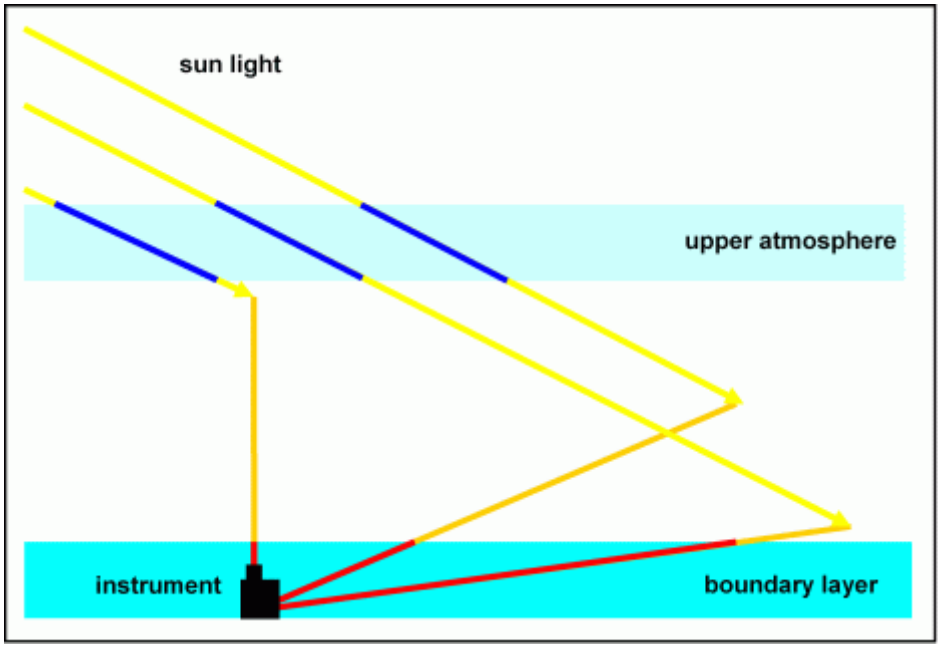

Figure 2-7: Sketch of a horizon-viewing measurement. With smaller elevation angles the effective light path through the lower layers in the atmosphere is increasing, while the path through the stratosphere remains constant.

The length of the light path in the lowest layers depends on the geometry (i.e. the elevation angle or line of sight) but also on the mean free path of the photon. In the sketch, the scattering point is above the surface layer and the light path is determined by geometry only. If scattering probability increases e.g. at higher aerosol loading or for measurements in the UV (more Rayleigh scattering), the last scattering point is closer to the instrument and the light path for the lowest viewing directions reduces. In the extreme case (fog, snow fall), there is no difference in the light path. An important boundary condition for the interpretation of the measurements is the assumption, that horizontal gradients can be neglected. In real measurements, this is not always the case and results can become ambiguous with respect to whether a signal variation results from vertical or from horizontal changes [Heckel, 2003].

As the vertical sensitivity is a function of elevation angle, the combination of all measurements can be used to retrieve vertical profiles of absorber concentrations which is one of the major aims of this study (see section 5.3). The vertical resolution of such profiles depends on the number of viewing directions, SZA, aerosol loading and surface albedo but is in the order of 3 to 5 layers for the lower troposphere. For such an inversion, a good estimate of the aerosol optical depth and vertical distribution is needed. This can be retrieved from measurements of species with well-known vertical distribution such as O_2 or O_4, and in fact aerosol optical depth is another output

of the inversion algorithm. If data are taken not only for different elevation angles, but also at various azimuth angles, information on the aerosol phase function and thus aerosol composition can also be obtained [Wagner et al., 2004].

For satellite validation, the tropospheric column is often the quantity of interest. This can be determined from the ground-based measurements either by integrating the retrieved profile or - more quickly - by using a viewing direction of 30°/18° elevation where the last scattering point is assumed to be above the layer with high concentrations of the trace gas of interest.

2.3.2 BREDOM Sites

2.3.2.1 Ny-Ålesund (79°N, 12°E)

In 1995, a DOAS instrument was set up in cooperation with the Alfred-Wegener-Institute for Polar and Marine Research, Bremerhaven in the NDSC building at Ny-Ålesund in Svalbard [Wittrock et al., 1995]. This measurement station is part of the primary Arctic NDSC station. Polar night prevails from mid of October to mid of February, solar elevation angles change rapidly in spring and fall and there is polar day in summer. The focus of the measurements at this site is on stratospheric chemistry in arctic regions, in particular ozone chemistry. As a result of its geographical location, Ny-Ålesund experiences both time periods with the polar vortex located above the station, and situations when non-vortex air is probed.

A second issue addressed by the Ny-Ålesund measurements is polar tropospheric halogen chemistry, in particular bromine chemistry. Depending on the meteorological conditions, air masses from the polar ice cap are transported to Ny-Ålesund, and episodes of rapid ozone destruction in the boundary layer (low ozone events) can be observed frequently in spring. For further information on results obtained from measurements at this site, see e.g. [Wittrock et al., 1996; Wittrock et al., 1997; Martinez et al., 1999; Wittrock et al., 2000; Mueller et al., 2002; Oetjen, 2002; Sinnhuber et al., 2002; Tornkvist et al., 2002; Wittrock et al., 2004].

Originally, the DOAS instrument in Ny-Ålesund was a simple zenith-viewing telescope with a grating spectrometer using a 1024 pixel cooled Reticon diode array as a detector. The telescope of the instrument is integrated in a skylight, allowing all the other components to be inside the building.

In spring 1999, a flip mirror was integrated in the telescope, facilitating alternating zenith-sky and off-axis (horizon viewing) measurements. The latter were directed towards the fjord, and had an elevation angle of 4°. With this viewing geometry, the light path through the troposphere is strongly enhanced, increasing the sensitivity of the measurements towards tropospheric absorbers such as BrO.

In spring 2002, the telescope was replaced by an improved version, allowing sequential measurements in up to 4 directions above the horizon (3°, 6°, 10° and 18°) and to the zenith with a motorised mirror. At the same time, the spectrometer and detector were replaced by a new system using a CCD detector to decrease noise at low sun. In March 2003, a second spectrometer with a CCD was installed to extend the observed wavelength range to the visible spectral range. Both spectrometers are connected to the same telescope.

2.3.2.2 Bremen (53°N, 9°E)

Since early 1993, DOAS zenith-sky measurements are continuously performed from the roof of the Physics Department at the University of Bremen. In 1994, a second instrument was added to separate the UV and visible parts of the spectrum, thereby improving the detection limits in the UV.

Bremen is a typical mid-latitude location close to the North Sea. In winter and spring, it is occasionally influenced by polar air masses, but usually is situated well out of the polar vortex. In spite of the frequent supply of clean air from the sea, measurements are affected by both local pollution from the nearby motorway, coal fired power plants and an incinerating plant, and regional pollution by steel industry. Therefore, tropospheric NO_2 concentrations are usually high and very variable. In contrast, tropospheric ozone concentrations rarely exceed the warning limits and are usually much lower than in other industrialised regions.

The current instrument in Bremen consists of two grating spectrometers, one for the UV (320 - 420 nm), and the second one for the visible spectral range (400 - 720 nm). Both spectrometers are equipped with cooled CCD detectors and are temperature stabilised to minimise the spectral drift. In January 2004, the instrument was relocated to the new building of the Institute of Environmental Physics, Bremen. Since then, it is equipped with the MAX-DOAS telescope described in section 2.3.1. For further information on results obtained from measurements at this site see e.g. [Eisinger et al., 1997; Richter et al., 1999].

2.3.2.3 Mérida (8°N, 71°W)

A new atmospheric measurement station (MARS) has been established in cooperation with the Physics Department of the University of Mérida and the Forschungszentrum Karlsruhe in the vicinity of the city Mérida, Venezuela in March 2004. This station uses the advantage of the high altitude site Pico Espejo (4765 m) for measurements with a DOAS instrument and a microwave sensor. The Pico Espejo is accessible with the world's highest cable car. Additional instruments (LIDAR, FTIR and UV-A/B spectrometers) will also be deployed at the nearby Instituto Astrofisico at 3600 m altitude by the Alfred-Wegener-Institute, Bremerhaven and the University of Bremen.

The Pico Espejo station is characterised by its high altitude (in fact it is the highest station for atmospheric measurements on the globe), facilitating stratospheric measurements in a tropical region that is largely unperturbed by tropospheric pollution and the large tropospheric water vapour burden usually found at these latitudes. Therefore it is an ideal site for both stratospheric research and the validation of satellite instruments such as GOME, SCIAMACHY and MIPAS. Using the off-axis measurements of this DOAS instrument it is also possible to investigate trace gases in the free troposphere, and to study the effects of long-range transport of pollution e.g. from the fires in Southern America.

The DOAS instrument in Mérida is located inside the MARS station building. It comprises again a temperature stabilised grating spectrometer equipped with a cooled CCD detector and covers the spectral range 320 to 410 nm. Unfortunately, a spectrometer for the visible part of the light is not available at this site hence preventing the detection of CHOCHO. The instrument is connected to a telescope, which is located outside the building, with a quartz fibre bundle and a number of electrical and control connections. The telescope is that one described in section 2.3.1. The off-axis port is directed to the South towards the Llanos (see Figure 2-8). The instrument is fully automated and can be controlled remotely through an internet connection to Bremen. To ensure continuous operation during power failures, it is connected to an UPS (uninterruptible power supply) shared with the microwave instrument.

Figure 2-8: The view from space of Venezuela and Colombia. The red dot marks the position of the measurement site within the Venezuelan Andes. The arrow denotes the viewing direction of the instrument towards the Llanos, a very flat area (prairies) with biomass burning mainly from January to March. Beyond that and south of the Orinoco river the tropical rain forest starts. (www.worldwind.com)

2.3.2.4 Nairobi (1°S, 37°E)

In July 2002, a DOAS instrument was installed on the UNEP (United Nations Environment Programme) headquarter building in Nairobi, Kenya. Nairobi is a tropical high altitude (1798 m) site that is strongly affected by local urban pollution (Nairobi has more than 2.5 million inhabitants) and sometimes by transport of air masses from biomass burning regions.

Unlike the meteorological station at nearby Mount Kenya, this site is not ideal for stratospheric measurements, but rather has a focus on tropospheric pollution in tropical regions.

The DOAS instrument in Nairobi is located in a temperature controlled office room inside the UNEP building. It has the same main feature than the set-ups described above. The off-axis port of the telescope is directed to the South (see Figure 2-9) towards a forest and downtown Nairobi behind it. In January 2004, a second spectrometer covering the visible part of the spectrum was added to the instrument which allows the detection of CHOCHO.

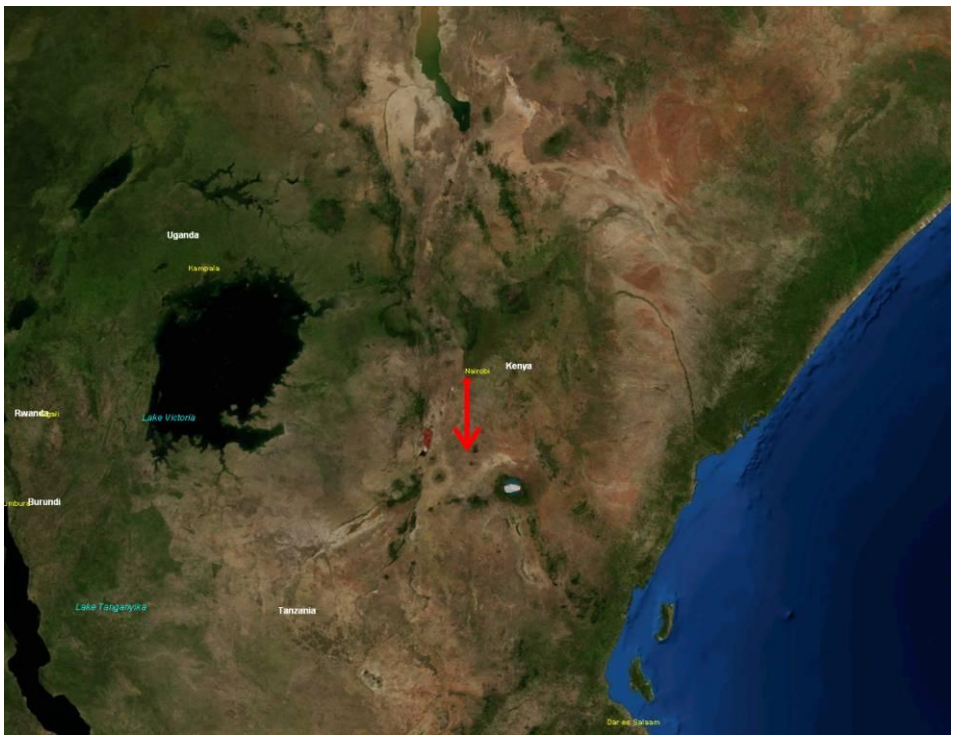

Figure 2-9: The view from space of Kenya, Uganda and Tanzania. The red dot marks the position of the measurement site within Kenya. The arrow denotes the viewing direction of the instrument towards the South. (www.worldwind.com)

2.3.2.5 Temporary Sites

All temporary sites were equipped with at least one spectrometer covering the UV range (320 – 410 nm) and sometimes also with a second one for the visible range and the MAX-DOAS telescope described in section 2.3.1. Usually, supplementary instrumentation e.g. for meteorological parameters were available at these sites. Only those sites are shown here from which data sets have been analysed within this study.

2.3.2.5.1 Summit (72°N, 38°W)

A MAX-DOAS instrument was operated at the Summit research station in the interior of Greenland from July 2003 to March 2005. This station is located at a very special high altitude (3200 m) Arctic site characterised by low temperatures, very low water vapour column and a clean troposphere.

The focus of the measurements was stratospheric chemistry, although some interesting tropospheric chemistry is also taking place on and within the snow. With its year-round snow and ice cover, Greenland is also a very interesting site for satellite validation and the study of albedo effects on the data retrieval.

The DOAS instrument at Summit was located inside a measurement container shared with the RAMAS microwave instrument which is also operated by the IUP Bremen [Golchert et al., 2005]. The telescope on top of the container was heated to avoid snow accumulation.

2.3.2.5.2 Zugspitze (47°N, 11°E)

Due to logistical reasons it was not possible to set up the Mérida instrument before spring 2004. Hence, this instrument was installed near to the top of the Zugspitze in the Schneefernerhaus, Germany before. Measurements were carried out in the wavelength range from 320 to 410 nm from January to June 2003. The telescope

was located on a balcony of the Schneefernerhaus with the off-axis port directed to the Southwest into a valley near to Garmisch-Partenkirchen. Even though the altitude of this site is about 2.650 m, it is frequently influenced by polluted air from the nearby urban Munich region.

2.3.2.5.3 Alzate (46°N, 9°E)

During two large measurement campaigns within the European FORMAT project, one in summer 2002 and a second in autumn 2003, MAX-DOAS measurements of HCHO and NO_2 were carried out with the Bremen campaign instrument. The FORMAT (Formaldehyde as a tracer of photo oxidation in the Troposphere) project was an EU funded three-year project focussing on measuring, modelling and interpreting HCHO in the heavily polluted region of the Po-Valley in Northern Italy (see Figure 2-10). Its most important objective was to improve and validate techniques which are used to measure formaldehyde.

The instrument was located in a container near to rural Alzate about 50 km north of Milan, which is one of the most polluted areas on the globe. The MAX-DOAS telescope was installed on the roof of the container and directed to the Southwest. The first campaign was mainly focussed on intercomparison of different measurement techniques, which provided the opportunity to validate our instrument and furthermore the retrieval algorithms with other experiments installed at the same site [Heckel, 2003; Heckel et al., 2005]. Unfortunately, only spectra in the UV were measured which prevents the retrieval of CHOCHO from this data set.

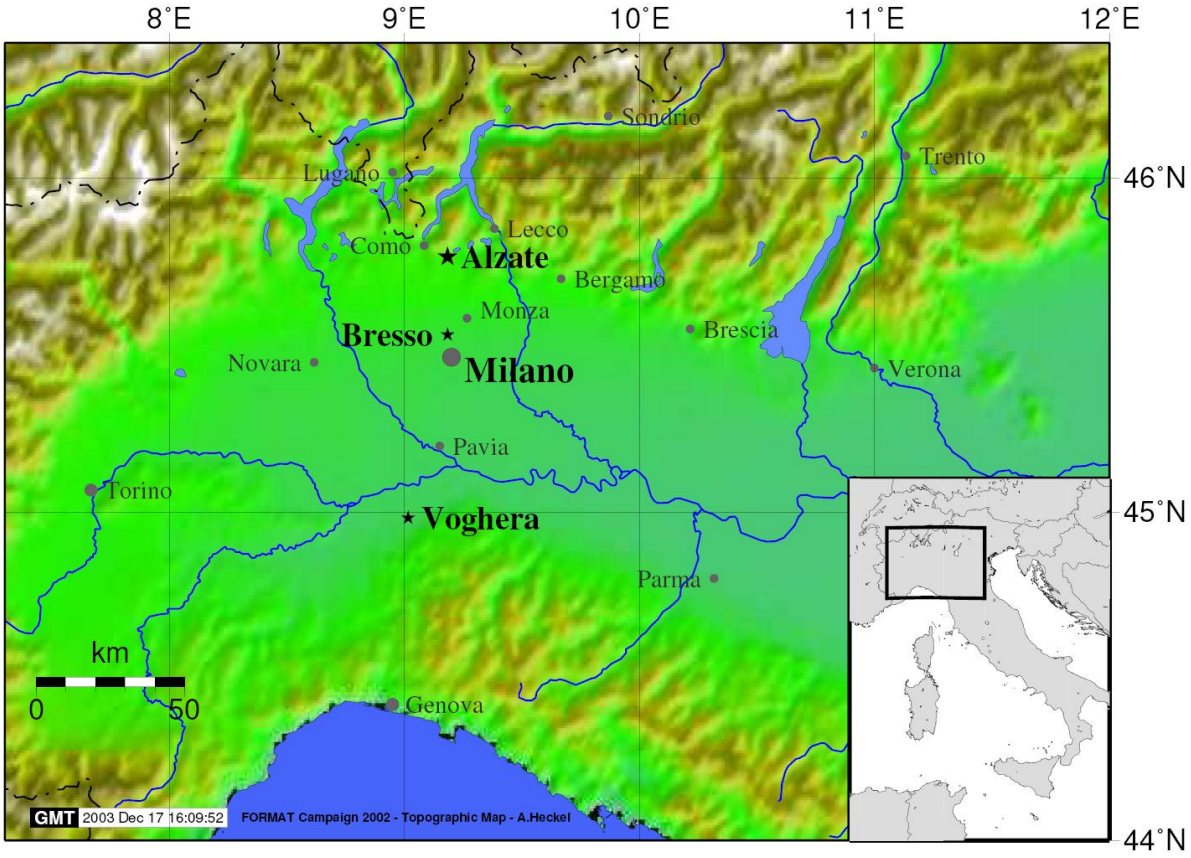

Figure 2-10: Map of the measurement area, showing the Po-Valley in northern Italy. The location of the measurements presented here was Alzate, 50 km north of Milan. Within the frame of the FORMAT campaigns in 2002 and 2003 additional instruments were placed in Bresso and close to Voghera (from Heckel et al. [2005]).

2.3.2.5.4 Cabauw (52°N, 5°E)

As part of the DANDELIONS project, MAX-DOAS measurements of different trace gases have been carried out in Cabauw, Netherlands from May 9 to July 17, 2005. DANDELIONS (Dutch Aerosol and Nitrogen Dioxide Experiments for vaLIdation of OMI and SCIAMACHY) is a Dutch national project. The overall objective is the validation of OMI, SCIAMACHY and AATSR (see section 2.4.1) measurements of aerosols and NO_2 over the Netherlands. One additional objective is to verify the quality of ground-based MAX-DOAS observations by the intercomparison of different set-ups and by comparison to a NO_2 LIDAR experiment. The site in Cabauw comprises, besides the usual meteorological experiments, a 213 m high mast built for investigation on relations between the state of the atmospheric boundary layer, land surface conditions and the general weather situation for all seasons. Cabauw is a rural site but close to the cities of Utrecht and Rotterdam. It is operated by the Royal Netherlands Meteorological Institute (KNMI). The following Table 6 shows some of the participating instruments, partly used in this study for the interpretation of the MAX-DOAS data.

The Bremian MAX-DOAS experiment was located inside a container with the telescope fixed to a small mast outside. The off-axis port was directed to the Southwest parallel to a street with usually low traffic about 50 metres away.

Table 6: Overview on instruments, which have participated in the DANDELIONS field campaign from May to July 2005.

Instrument	*Group*	*Products*
MAX-DOAS	IUP Bremen	NO_2 (HCHO, CHOCHO)
MAX-DOAS	IUP Heidelberg	NO_2
MAX-DOAS	IASB/BIRA Brussels	NO_2
NO_2-LIDAR	KNMI	NO_2
***in situ* monitor**	KNMI	NO_2 near to the surface
SCIAMACHY		NO_2 (CHOCHO, HCHO), absorbing aerosol index
OMI		NO_2, aerosol optical depth
Boundary layer LIDAR	KNMI	aerosol extinction
ozone and radio sondes	KNMI	T, p, relative humidity, ozone

2.4 Supplementary Data Sets

This section describes briefly the experiments and their data sets, which have been used in chapter 5.4 and 6 to interpret the results from the DOAS observations.

2.4.1 ATSR-II and AATSR

The Along Track Scanning Radiometer (ATSR, see e.g. http://earth.esa.int/ers/atsr/) consists of two instruments, an Infra-Red Radiometer (IRR) and a Microwave Sounder (MWS). The ATSR instruments were designed to provide the following types of data and observations:

- Sea surface temperature with an absolute accuracy of better than 0.5 K with a spatial resolution of 50 km and under conditions of up to 80 percent cloud cover.
- Images of surface temperature with 1 km resolution and 500 km swath, relative accuracy about 0.1 K.

The IRR uses spectral channels which are very similar to those on recent NOAA meteorological satellites, with many improvements in accuracy. The ATSR-2 and Advanced ATSR (AATSR) instruments are developments from the original experimental ATSR-1 instrument which, in addition to the ATSR-1's infrared channels, carry extra channels in the visible at 0.55µm, 0.67µm and 0.87µm for vegetation remote sensing and an according calibration system. The ATSR-2 instrument, launched in April 1995, is currently flying as part of the payload of the ESA ERS-2 satellite (together with GOME), while AATSR is part of ESA's ENVISAT platform (together with SCIAMACHY).

"The major purpose of AATSR is to provide continuity of the crucial sea surface temperature data sets which have been produced by ATSR-1 and ATSR-2. Therefore, the key scientific parameters which were optimised for ATSR are retained for AATSR: Details of the scan, the optical system, the basic spectral bands (see Figure 2-11), the thermal calibration system, spatial resolution and swath have been kept as close as possible to those of the original instrument to ensure continuity." (from http://earth.esa.int/ers/eeo4.10075/ERS1.5.html)

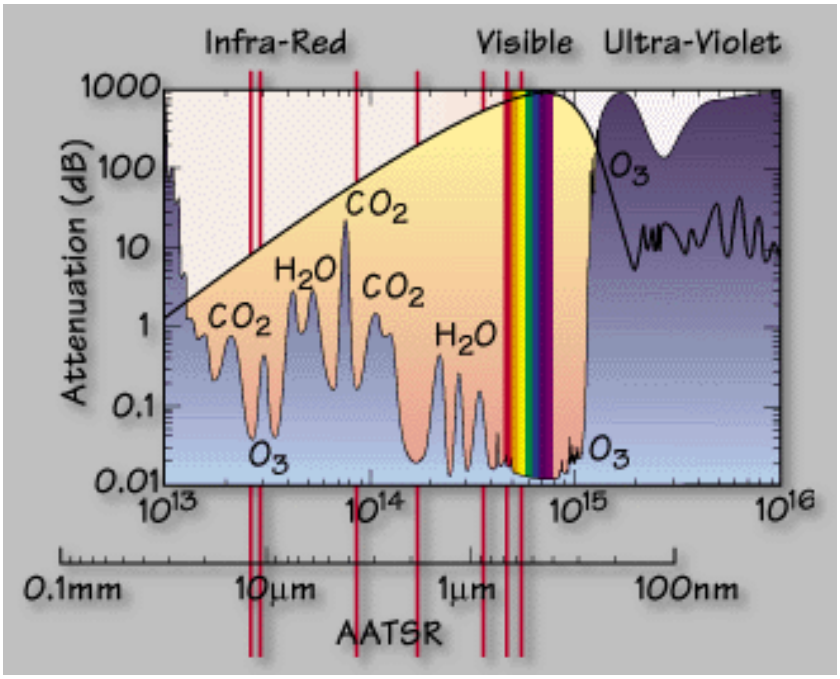

Figure 2-11: Spectral coverage of the AATSR instrument onboard ENVISAT (source ESA).

In this study, the fire product using the ATSR fire algorithms was used [Arino et al., 1995; Goloub and Arino, 2000; Simon et al., 2004]. This algorithm utilises the ATSR night time radiation data from the bands at 1.6 µm, 3.7 µm, 11.0 µm, and 12.0 µm to detect hot spots on the surface. In algorithm 2 which has been used here a hot spot is detected, if the temperature of the measured radiation at 3.7 µm is larger than 308 K. The detection capabilities depend on the fire temperature, and can be estimated as follows: 0.1 ha at 600K to 0.01 ha at 800K, for a background temperature of 300K. The temperature of the fire and the area alight are not taken into account in the processing. The spatial resolution is given as 1 km.

The advantages of the ATSR fire product are:

- Due to night time detection there are no artefacts caused by solar reflection.
- High radiometric sensitivity allows detection of small fires, too.

Known limitations:

- ATSR frames overlap (some fires might be detected twice).
- Sometimes warm surfaces will be counted as fires.
- Global underestimation of the hot spot number because of the solely night time detection.

The following Figure 2-12 shows averaged fire counts as detected by ATSR-2 from 1997 to 2001.

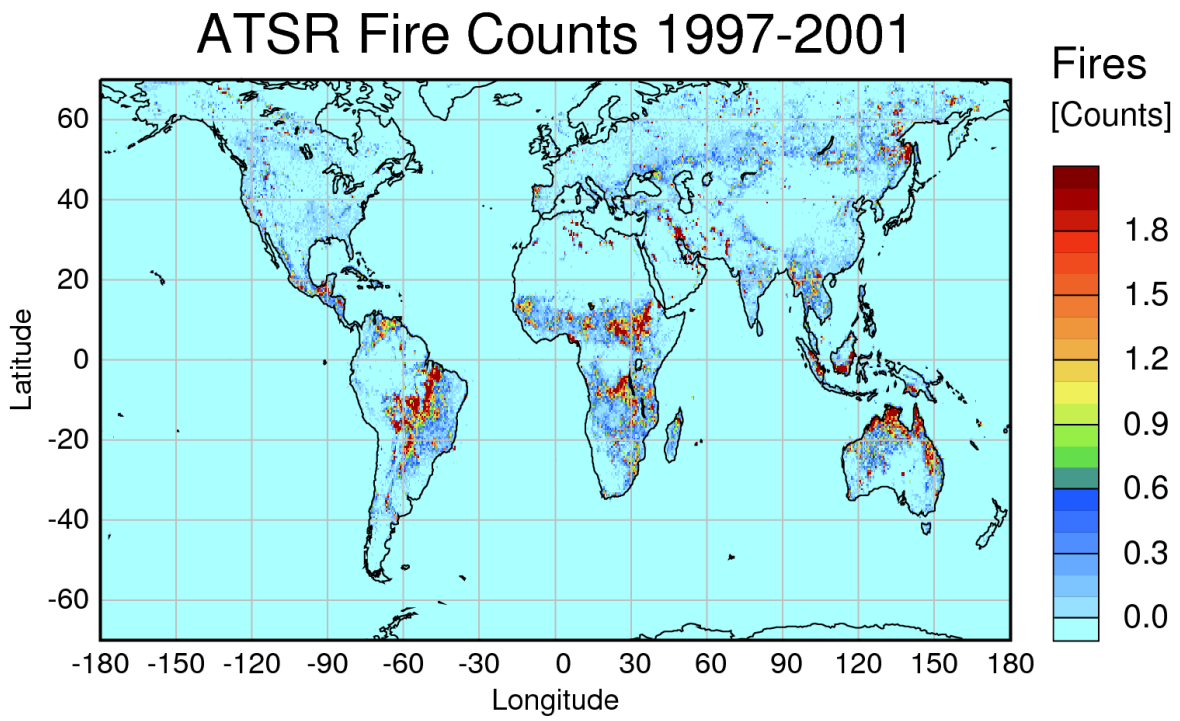

Figure 2-12: Mean fire counts per month obtained from ATSR-2 from 1997 to 2001. The data have been averaged after gridding the original monthly data sets to a 0.5° x 0.5° spatial resolution. Main burning areas are regions with wooded grassland and woodland (according to the classification of the Global Land Cover Facility, University of Maryland). The ATSR detects also flames from anthropogenic activities like oil drilling (e.g. in Arabia and the North Sea).

2.4.2 AVHRR and MODIS

On the NOAA-7, NOAA-9, and NOAA-11 satellites, the Advanced Very High Resolution Radiometer (AVHRR, see e.g. http://geo.arc.nasa.gov/sge/jskiles/top-down/OTTER/OTTER_docs/AVHRR.html) sensor has measured

emitted and reflected radiation in five channels (bands) of the electromagnetic spectrum: a visible (0.58 to 0.68 µm) band that is used for daytime cloud and surface mapping; a near-infrared (0.725 to 1.1 µm) band used for surface water delineation and vegetation cover mapping; a mid-infrared (3.55 to 3.93 µm) band used for sea surface temperature and night time cloud mapping; a thermal infrared (10.5 to 11.5 µm) band used for surface temperature and day and night cloud mapping; and another thermal infrared (11.5 to 12.5 µm) band also used for surface temperature mapping. The Moderate Resolution Imaging Spectroradiometer (MODIS, see http://daac.gsfc.nasa.gov/MODIS/index.shtml) sensor onboard TERRA and AQUA satellites have quite similar features and were in operation for the years 2001 to 2005.

The first AVHRR channel is in a part of the spectrum where chlorophyll causes considerable absorption of incoming radiation, and the second channel is in a spectral region where spongy mesophyll leaf structures lead to considerable reflectance. This contrast between responses of the two bands can be shown by a ratio transform; i.e., dividing one band by the other. Several ratio transforms have been proposed for studying different land surfaces. The Normalised Difference Vegetation Index (NDVI) is one such ratio, which has been shown to be highly correlated with vegetation parameters such as relative biomass and greenness [Chen and Brutsaert, 1998; Boone and Galvin, 2000]. If sufficient ground data is available, the NDVI can be used to calculate and predict primary production, dominant species, and grazing impact and stocking rates [Diallo and Diouf, 1991; Oesterheld and DiBella, 1998; Ricotta and Avena, 1998]. It is also highly correlated with climatic variables, such as the El Niño Southern Oscillation (ENSO, see section 1.4) [Li and Kafatos, 2000] and precipitation.

In order to identify regions with the potential for biogenic emissions, data for the normalised differential vegetation index (NDVI) have been utilised in this study (see section 5.4). The equation to calculate the NDVI is:

$$NDVI = \frac{I_{IR} - I_{red}}{I_{IR} + I_{red}} \tag{2.1}$$

where I_{IR} is the intensity in the infrared and I_{red} the intensity in the visible. The NDVI index values can range from -1.0 to 1.0, but vegetation values typically range between 0.1 and 0.7. Higher index values are associated with higher levels of healthy vegetation cover, whereas clouds and snow will cause index values near zero, making the vegetation appear less green.

The NDVI from the following satellite sensors have been used in this study:

- NOAA AVHRR – bands 1 (0.58-0.68 µm) and 2 (0.72-1.00 µm)
- Terra MODIS – bands 1 (0.62-0.67 µm) and 2 (0.841-0.876 µm)

The following Figure 2-13 shows an example of the NDVI obtained from the AVHRR instrument.

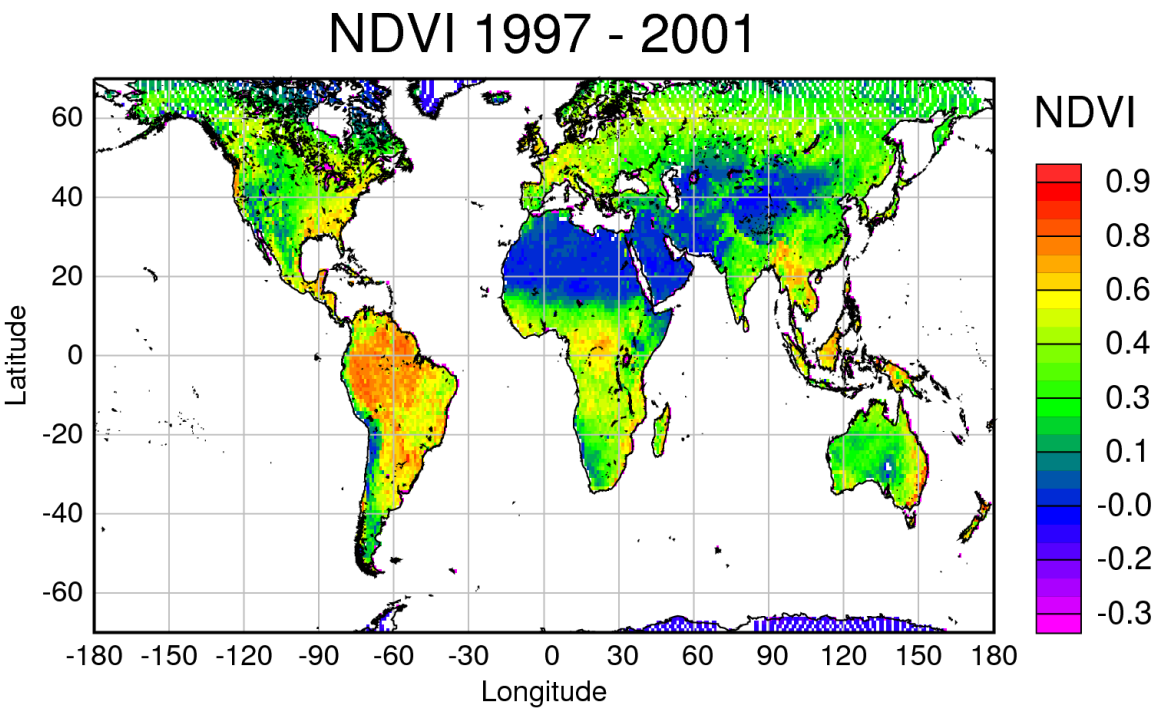

Figure 2-13: Averaged NDVI calculated from AVHRR data from 1997 to 2001. Regions with high greenness such as tropical rain forests in South America and Africa have values above 0.7.

Another parameter measured by the AVHRR and MODIS sensor which is utilised in this study is the aerosol optical depth (AOD) at 550 nm above oceans (see section 5.4). The algorithm to derive the AOD is described in detail in [Mishchenko et al., 1999; Geogdzhayev et al., 2002; Mishchenko et al., 2003; Geogdzhayev et al., 2004]. In general, the same channels as for the NDVI are used in the algorithm assuming spherical aerosols with a power-law size distribution. The refractive index is wavelength independent and includes some aerosol absorption.

3 Absorption Spectroscopy

Absorption spectroscopy is a widely used technique for measurement of atmospheric trace gases. Beginning in the 1920s with the work of Dobson et al. [1929] this method has been further developed and employed to a variety of different target species, observation geometries and instrumental platforms. In the following the fundamentals of spectroscopy and in particular absorption spectroscopy will be briefly described. In addition, the characteristics of the sun as light source are discussed in section 3.1. Section 3.2 introduces the DOAS equation, while in 3.3 different aspects of the reference or background spectrum are considered. The chapter closes with a short overview on the Ring effect in section 3.4.

The absorption of light is applied to analyse matter in spectroscopic measurements. Every substance features a characteristic emission and absorption spectrum. Solid or liquid materials have a continuous spectrum. For gases, continuous as well as discrete spectra with sharp spectral lines can be observed. These lines can be so close together that they only appear as discrete lines when they are observed with an instrument with very high resolution. Otherwise, they seem to be continuous why they are called bands. Those bands are present in the spectra of molecules since the lines due to electronic transitions are superposed by lines that are caused by energy changes from the movement of the atomic nuclei and by rotation.

There are three categories of energy transitions, respectively spectral lines in molecular spectra:

1. Electronic structures: The electrons of molecules can be excited into different energy levels. Transitions between those levels require light of the visible and the ultraviolet spectral range.
2. Vibrational structures: For every electronic energy level several vibrational states exist which are caused by the movement of the atomic nuclei relative to each other. The distances between those energy levels correspond to wavelengths from microwaves to the far infrared spectrum.
3. Rotational structures: The complete molecule can be excited to a rotation around an axis. This causes the vibrational energy levels to split into a number of rotational states with transitions in the infrared spectrum.

According to Planck's law, a body emits a continuous spectrum of light depending on its temperature. Light can also be emitted when the atoms or molecules relax from an excited state. In absorption spectroscopy, a material is placed into the path of rays of a light source with a continuous spectrum. By means of the positions of the discrete absorption lines or bands in the spectrum, the absorber can be identified and by means of the magnitude of the absorption, the amount present in the light path can also be quantified.

In this study, the method of the differential optical absorption spectroscopy (DOAS) is applied to scattered sun light to characterise the absorption of trace gases in the earth's atmosphere. Here, differential means that only the high frequency part of the spectrum is analysed. Hence only gases with sufficiently narrow spectral lines can be detected; e.g. Ozone or NO_2. The observed structures are mainly caused by vibrational transitions on top of electronic transitions.

DOAS can be employed to a variety of applications in the remote sensing of the atmosphere as well as in laboratory experiments (e.g. [Deters et al., 1996; Orphal et al., 2000; Martin et al., 2004; Volkamer et al., 2005]). In the atmosphere the evaluation of direct as well as scattered light is possible with DOAS. As direct light sources the sun, the moon (e.g. [Schlieter et al., 1997; Wagner et al., 2000]) and several stars [Roscoe et al., 1994] can be observed in occultation but also artificial light sources for so-called Long-Path measurements close to the ground

are employed (e.g. [Platt and Hausmann, 1994; CamyPeyret et al., 1996; Lorenzen-Schmidt et al., 1998; Pundt et al., 2005]). Scattered light can be detected in several viewing geometries from the ground both in zenith and off-axis direction (e.g. [Brewer et al., 1973; Noxon, 1975; Mount et al., 1987; Richter, 1997; Leser et al., 2003; Wittrock et al., 2004]), from aircrafts (e.g. [Pfeilsticker and Platt, 1994; Wang et al., 2005]), balloon (e.g. [Renard et al., 1997; Ferlemann et al., 1998]), and satellite (e.g. [Chance et al., 1997; Hegels et al., 1998; Richter et al., 2004]).

In this work, scattered light from the sun is observed from space and by ground-based multi-axis instruments. In the next chapter, the basic features of this light source are described.

3.1 The Sun as a light source

The gaseous body of the sun consists mainly of hydrogen but also of protons and helium. The energy that is released in the form of solar radiation is created by nuclear fusion in the interior of the sun. There, four protons unite to one helium atom. By means of electromagnetic radiation in the inside and by convection further outside, this energy is transported to the surface of the sun.

The part of the sun visible by the earth is called photosphere. This photosphere is not the surface of the sun but a thin layer of the solar atmosphere with a temperature of about 5800 K. The photosphere can be regarded as a blackbody which emits a continuous spectrum according to Planck's law. The spectrum of the sun comprises wavelengths from the long radio waves to the gamma radiation. The maximum of the spectral intensity is located in the visible range, more precisely at about 460 to 480 nm. 43 percent of the overall radiation is emitted in visible, 49 percent in near infrared and 7 percent in ultraviolet wavelengths (see Figure 3-1).

Already the extraterrestrial spectrum of the sun displays strong absorption lines which are named Fraunhofer lines after their discoverer Joseph von Fraunhofer. These absorptions result from atoms and ions in the photosphere and the outer parts of the chromosphere. Many of the Fraunhofer lines are considerably stronger than most of the absorption lines in the earth's atmosphere in particular in the visible and ultraviolet wavelength region beyond 300 nm (see Figure 3-1).

The radiation from the sun varies with time e.g. due to the occurrence of sunspots. These are dark regions in the photosphere marked by relatively low temperatures (3000 – 5000 K) and intense magnetic activity. Sunspot activity varies with a frequency of about eleven years. This is the so-called solar cycle. The variability of the solar irradiance due to this phenomenon depends strongly on the wavelength region. While it is for light less than 150 nm more than 100 percent, the effect beyond 300 nm is quite small (less than 1 percent).

The above description of the sun is mainly based on material from the book by Philips [1992].

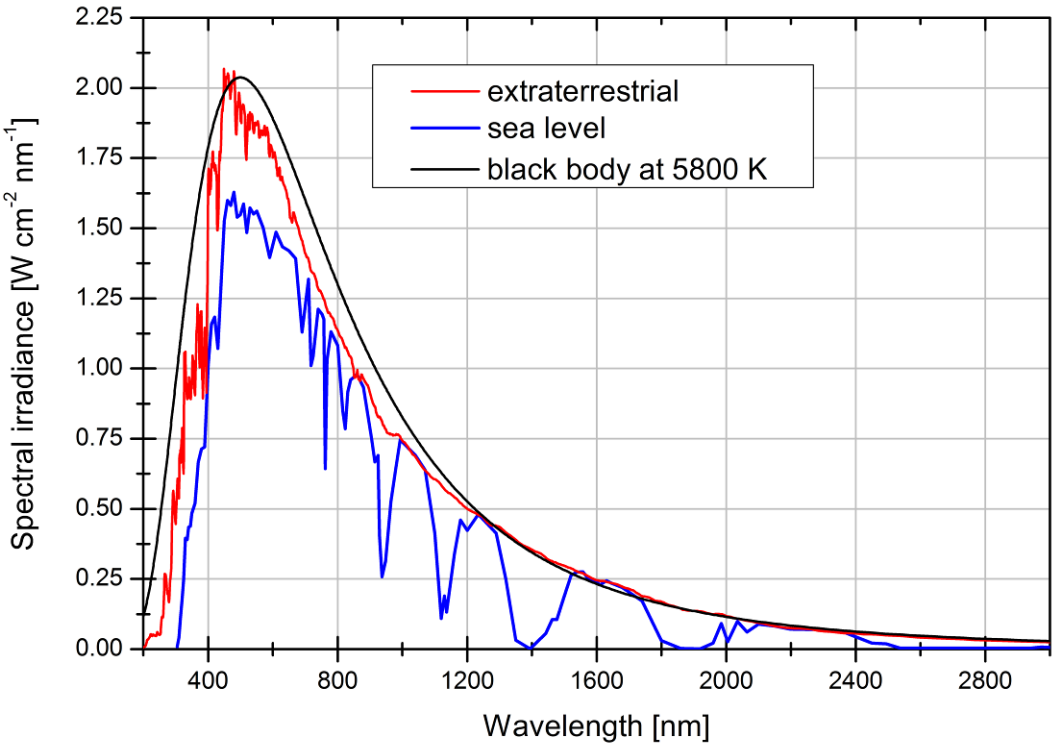

Figure 3-1: The spectrum of solar radiation outside the earth's atmosphere and at sea level (calculated for US Standard atmosphere at 30° SZA) compared to the black body radiation at 5800 K. The atmospheric absorption features are mainly due to O, O_2, O_3, H_2O and CO_2. Minor trace gases like those analyzed in this study are indiscernible in this illustration.

3.2 DOAS equation

While passing through matter, the intensity I of radiation at a given wavelength λ is attenuated according to the *Beer-Lambert-Bouguer law* (This law was independently discovered – in various forms – by Pierre Bouguer in 1729, Johann Heinrich Lambert in 1760 and August Beer in 1852):

$$I(\lambda) = I_0(\lambda)\exp\left[-s\rho\sigma(\lambda)\right] \tag{3.1}$$

where I_0 is the incident intensity, s is the path length, ρ is the number density and σ the absorption cross-section at a given wavelength. This equation has to be modified for the atmosphere since the atmosphere is a mixture of many different absorbers i. Also scattering on molecules, water droplets and aerosols have to be considered. These effects also decrease the intensity of the light. In addition the number density of an absorber is height dependant. The absorption cross-section of a gas depends on temperature and on pressure in the atmosphere and consequently also on the height. This results in:

$$I(\lambda) = I_0(\lambda)\exp\left[-\int ds \sum_i \rho_i(s)\cdot\sigma_i(\lambda,s)\right] \tag{3.2}$$

where the integral is taken along the light path s through the atmosphere.

In general, three different scenarios of scattering in the atmosphere are distinguished:

1. Elastic scattering on molecules in the air (diameter ~10^{-10} m) is described by the Rayleigh theory which is valid for particles with a diameter that is small compared to the wavelength of the incident light. The scattering cross-section σ_{Ray} is proportional to λ^{-4}.

2. The diameter of aerosols (~ 1 µm) and water droplets (~10 µm) is in the same range as the main wavelengths from the sun. Then the incident radiation is elastically scattered. From Mie theory elastic scattering cross-sections are derived as: $\sigma_{Mie} \approx \lambda^{-k}$ with *k* between 0 and 2.

3. Raman scattering is an inelastic scattering on molecules in the air which causes the so-called Ring effect. This effect is described in section 3.4.

Consequently, the complete Beer-Lambert-Bouguer law for a measurement in the atmosphere can be expressed as follows:

$$I(\lambda) = I_0(\lambda)\exp\left[-\int ds \begin{Bmatrix} \sum_i \rho_i(s)\sigma_i(\lambda,s) \\ +\rho_{Ray}(s)\sigma_{Ray}(\lambda,s) \\ +\rho_{Mie}(s)\sigma_{Mie}(\lambda,s) \\ +\rho_{Ring}(s)\sigma_{Ring}(\lambda,s) \end{Bmatrix}\right] \tag{3.3}$$

where I_0 is the extraterrestrial sun spectrum, $\rho_{i,Ray,Mie,Ring}$ is the number density of the absorbers or the scattering particles, $\sigma_{i,Ray,Mie,Ring}$ the scattering or absorption cross-sections for the absorber *i*, and Rayleigh, Mie, and Raman scattering. If the concentrations of the absorbers and scatterers are unknown, this equation cannot be solved for the atmosphere since the contributions of the single processes cannot be separated. In order to derive the quantities of interest (the absorber concentrations), some assumptions have to be applied:

1. The height dependency of the absorption cross-sections σ_i will be neglected. This is possible when in the retrieval cross-sections are applied which are recorded for the temperature and pressure that is present in the height of the absorber layer. Thus, the summation and the integral in equation (3.3) can be exchanged. The resulting quantity is called slant column density *SC* :

$$SC_i \equiv \int \rho_i(s) \cdot ds \tag{3.4}$$

   and is the total amount of the absorber *i* per unit area integrated along the light path.

2. The Ring effect will be treated as an additional absorber according to Solomon et al. [1987] (see chapter 3.4).

3. At this point the so-called DOAS concept is introduced into the derivation. The absorption cross-sections are separated into two parts σ_i' and σ_i^0, that are fast and slowly varying with the wavelength, respectively:

$$\sigma_i = \sigma_i' + \sigma_i^0 \tag{3.5}$$

4. The components with the low frequency variations like the absorption cross-section σ_i^0 and the Rayleigh and Mie scattering which follow simple power laws are substituted by a polynomial *P*:

$$P = \sum_p a_p \lambda^p \tag{3.6}$$

5. Together this yields:

$$I(\lambda) = I_0(\lambda) \exp\left[-\sum_i \sigma_i'(\lambda) SC_i - \sum_p a_p \lambda^p \right] \tag{3.7}$$

6. For the application to measurements the logarithm of this equation is used:

$$\ln I(\lambda) = \ln I_0(\lambda) - \sum_i \sigma_i'(\lambda) SC_i - \sum_p a_p \lambda^p \tag{3.8}$$

or

$$\tau(\lambda) = -\ln\left[\frac{I(\lambda)}{I_0(\lambda)} \right] = \sum_i \sigma_i'(\lambda) SC_i + \sum_p a_p \lambda^p \tag{3.9}$$

where τ is the optical depth.

With known reference spectrum I_0 and known differential absorption cross-sections σ_i', the slant column densities SC_i of the different trace gases and the coefficients a_p of the polynomial can be retrieved by the means of a linear least squares fit [Richter, 1997]. Equation (3.8) is the so-called DOAS equation.

The slant column densities SC_i derived from the DOAS retrieval are usually converted into vertical column densities (VC_i) which are defined as the vertically integrated trace gas concentration:

$$VC_i \equiv \int \rho_i(h) \cdot dh \tag{3.10}$$

where h is the altitude.

This conversion can be achieved by geometric calculations for observations of direct light e.g. from the moon [Schlieter, 2001]. For measurements of scattered light, as those used here, one has to take the different light paths (the *effective* light path) through the atmosphere into account, which requires the application of radiative transfer models. This aspect is illustrated in the next chapter 4.

It should be noted that equation (3.8) is restricted to weak absorptions which is valid in this study. Otherwise, it cannot be assumed that the measured differential optical depth τ' is proportional to the mean slant column density S_i (e.g. [Platt et al., 1997; Marquard et al., 2000]):

$$\frac{\tau_i'}{\sigma'} \neq SC_i \tag{3.11}$$

3.3 Reference spectrum

For the satellite measurements presented in this study the solar radiance spectra recorded by GOME and SCIAMACHY respectively are used as the reference I_0. Thus the DOAS retrieval yields the absolute slant column density SC_i in this case (see Figure 3-2).

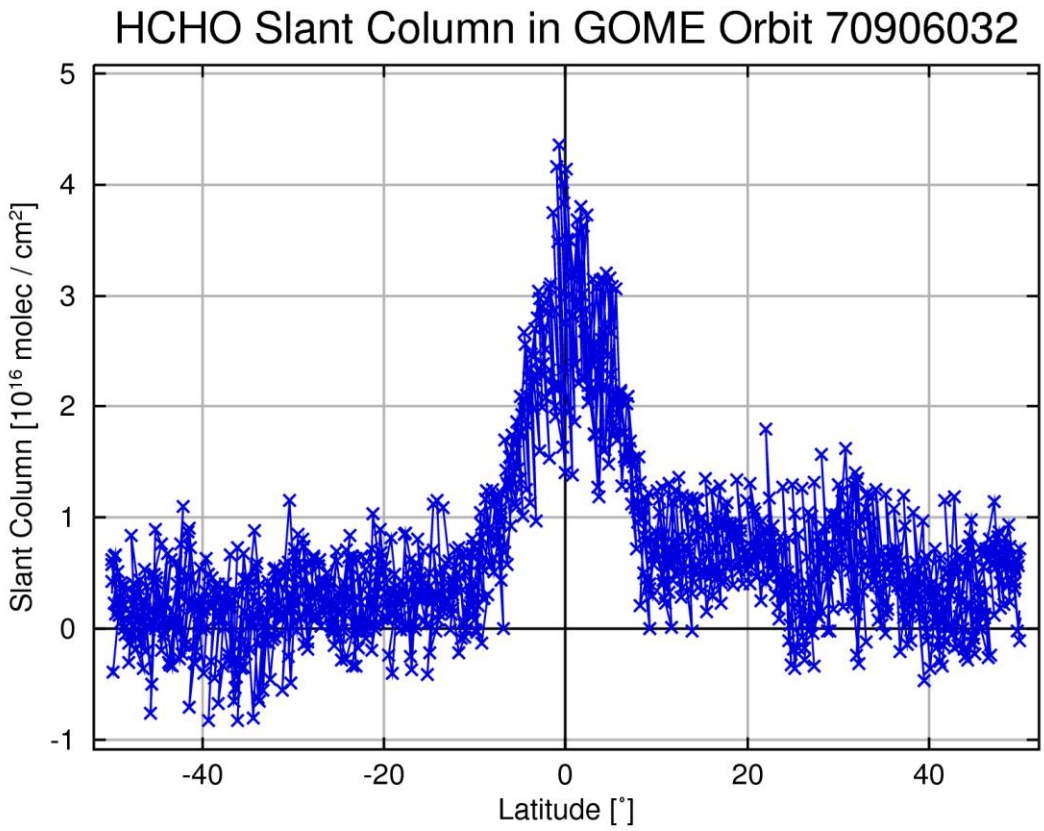

Figure 3-2: Absolute slant columns for formaldehyde in GOME orbit 70906032.

On the other hand, for ground-based applications it is not possible to record an extraterrestrial solar spectrum with the same instrument. Instead, a zenith spectrum taken at the smallest solar zenith angle on the day of measurement or a specific spectrum from a selected day is used as reference. Using a reference recorded with the same instruments leads to the compensation of all multiplicative instrumental features. However, there is an unknown amount of atmospheric absorption already present in the reference spectrum which has to be accounted for. For all viewing directions of the MAX-DOAS measurements, in general the noon zenith spectrum I_0^{NZ} is used as reference.

Thus, the DOAS equation has to be restated for ground-based applications:

$$\frac{I(\lambda)}{I_0^{NZ}(\lambda)} = \exp\left[-\sum_i \sigma_i'(\lambda)\left(SC_i - SC_i^{NZ}\right) - \sum_p a_p \lambda^p\right] \tag{3.12}$$

which yields the differential slant column densities $DSC_i = SC_i - SC_i^{NZ}$ (see Figure 3-3).

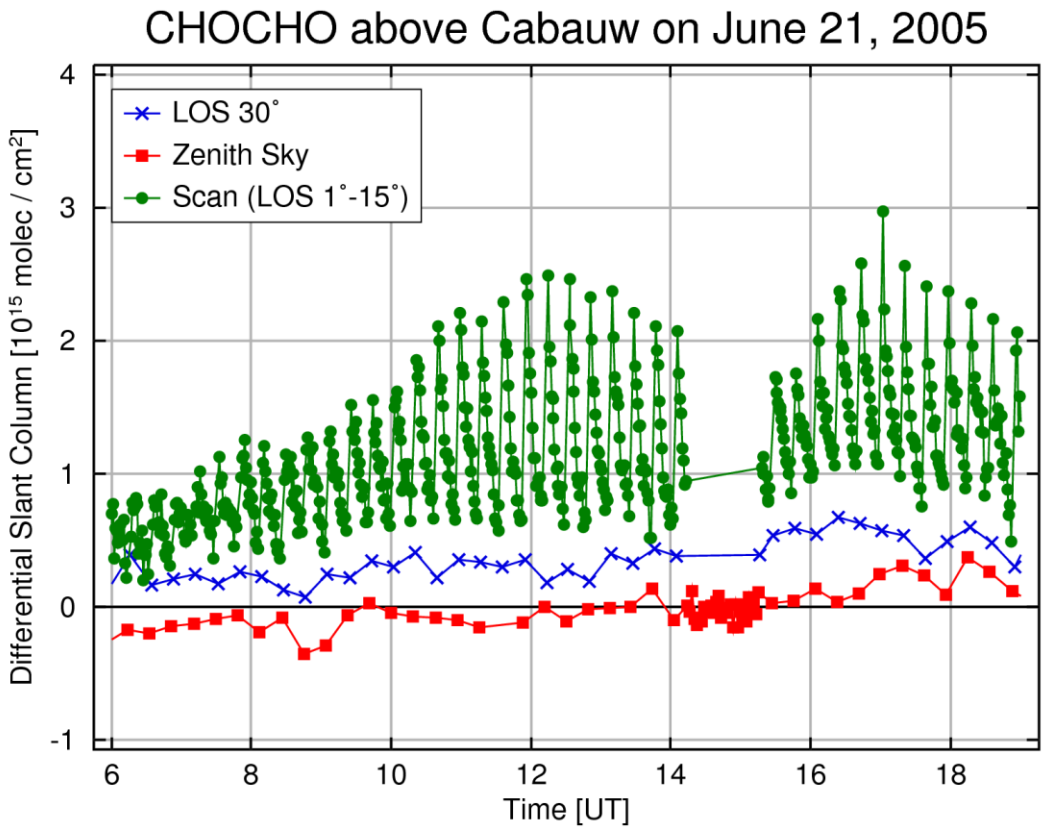

Figure 3-3: Differential slant columns for glyoxal above Cabauw for different lines of sight (LOS – the angle of the viewing direction above the horizon). As reference the noon zenith-sky spectrum (11:30 UT) was taken. In case the off-axis port is directed towards the sun, only zenith-sky measurements are carried out to avoid damage of the optical components.

3.4 Ring effect

Comparisons of scattered and direct sun light exhibit a difference in the depth of the Fraunhofer lines: For scattered light, those lines are less pronounced. This effect was first observed by Grainger and Ring [1962] and was consequently named Ring effect. This filling-in of the Fraunhofer structures is widely accepted to occur due to inelastic rotational Raman scattering on molecules (e.g. [Fish and Jones, 1995; Joiner et al., 1995; Vountas et al., 1998; Stam et al., 2002]).

Classically, the Raman effect can be explained as follows: Light with a frequency much higher than the frequencies of the rotation or vibration of the movement of the nuclei falls onto the molecule. At the same time the light induces a dipole moment by moving the electron cloud in the pulse frequency of the incoming wave. This oscillating electronic dipole can again emit electromagnetic waves with the exciter frequency (elastic Rayleigh scattering) or waves with a different energy and consequently different frequency (inelastic Raman scattering). This gain or loss of energy is connected to a change in the rotational or vibrational state of the molecule. This effect can be observed in a simple experiment: Molecules exposed to monochromatic light feature, in the scattered light spectrum, some equidistant lines next to the Rayleigh line at the exciting frequency. The distance between those Stokes or Anti-Stokes lines corresponds to the distances of the vibrational and rotational energy levels (see also Figure 3-4).

Besides the filling-in of the Fraunhofer lines, of course, also the absorption structures caused by the earth's atmosphere are modified. This is called the molecular Ring effect which can lead to an underestimation of the slant column densities.

In the data retrieval the Ring scattering cross-section is treated as an absorption cross-section. Consequently a 'slant column' of the Ring is obtained in the least square fit of the DOAS equation (see section 5.1.3).

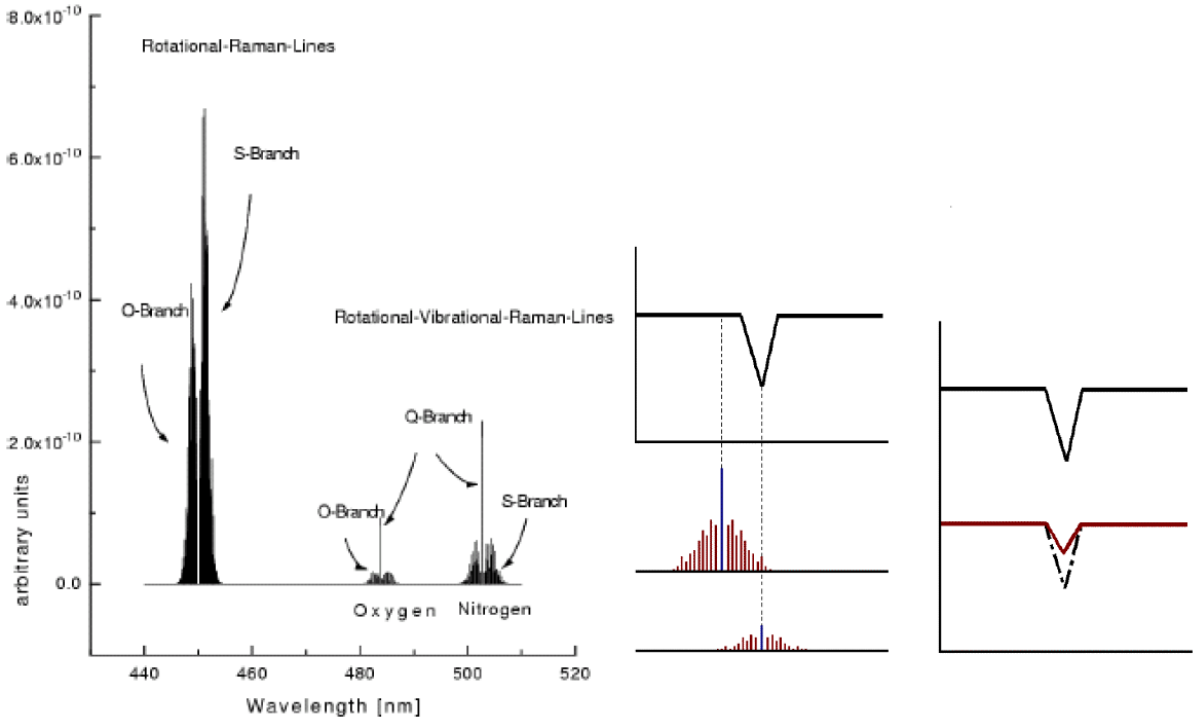

Figure 3-4: Ring Effect: Raman scattering from outside and inside of the Fraunhofer lines leads to a reduction of the intensities in the line centres (from Kühl [2005]).

4 Radiative Transfer

For the analysis and further interpretation of the results obtained by applying the DOAS equation (3.8) to UV/vis measurements, the air mass factor concept has been developed (e.g. [Noxon, 1975; Solomon et al., 1987; Perliski and Solomon, 1993]). The air mass factor (*AMF*) is defined as the ratio of the effective optical path through the atmosphere, i.e. the ratio of the slant column *SC* to the vertical column *VC*:

$$AMF(\theta,\varphi,\vartheta,\lambda) \equiv \frac{SC(\theta,\varphi,\vartheta,\lambda)}{VC} \tag{4.1}$$

This definition implies that the AMF contains all information about the viewing geometry (where θ is the solar zenith angle, φ the relative azimuth, and ϑ the elevation angle of the line of sight) and all the meteorological parameters which might have an impact on the effective light path. In order to calculate the AMF, a radiative transfer model (RTM) is required. In this study, the RTM SCIATRAN (e.g. [Rozanov et al., 1997; Rozanov et al., 2002]) developed at the Institute of Environmental Physics, University of Bremen is used and will be described in the next section.

4.1 Radiative Transfer Model SCIATRAN

The solar radiation is modified by various effects in the atmosphere: Photons are absorbed by molecules or they are elastically scattered on molecules and aerosols. For inelastic scattering, not only the direction of the radiation is changed but also the energy and consequently the wavelength. Changes in the ground albedo as well as clouds result in modification of the multiple scattering. Considering refraction causes rays to deflect to the denser medium, i.e. into the direction of the ground. Emission can be neglected since it takes mainly place in the infrared spectrum.

The diffuse radiance *I* from the sun in the earth's atmosphere at the location $\boldsymbol{r}$ into the direction $\boldsymbol{e}_s$ is described by the radiative transfer equation that accounts mathematically for the above mentioned effects. In its general, coordinate-independent form it can be written as:

$$\frac{dI(\boldsymbol{r},\boldsymbol{e}_s)}{ds} = -\alpha(\boldsymbol{r})I(\boldsymbol{r},\boldsymbol{e}_s) + \alpha(\boldsymbol{r})B(\boldsymbol{r},\boldsymbol{e}_s) \tag{4.2}$$

Equation (4.2) is a partial differential equation of first order. The left hand side is the change in radiation over a path length *s*. The first term on the right hand side describes the attenuation of the radiation due to absorption and scattering. The extinction coefficient α presents the sum of the absorption and the scattering coefficient. The second term accounts for the gain by scattering where *B* is the source function. This equation can only be solved when a coordinate system is defined.

The procedure for the full-spherical radiative transfer model SCIATRAN [Rozanov et al., 2000] is as follows. Two coordinate systems are required: One which describes the location $\boldsymbol{r}$ globally and another one for the local direction of $\boldsymbol{e}_s$. For the global orientation spherical coordinates are applied with the point of origin in the centre of the earth and the z-axis always pointing into the direction of the sun. The coordinates are defined as $\boldsymbol{r} = (r, \Psi, \Phi)$. The direction at $\boldsymbol{r}$ is described by two angular variables $\boldsymbol{e}_s = (\theta, \varphi)$. Here, the z-axis is perpendicular to the surface.

In order to solve the radiative transfer equation in the described coordinate systems it is converted into an integral form. For that, both sides of equation (4.2) are integrated along a characteristic s_c which is a line - this line of sight is bent due to refraction - between the location $\boldsymbol{r}$ and the top of the atmosphere or the ground. Only the diffused radiation I_{dif} will be considered:

$$I_{dif}(\boldsymbol{r},\boldsymbol{e}_s) = I_{dif}^0 e^{-\tau_0} + \int_0^{s_c} ds\alpha e^{-\tau(s)} B_{ES} + \int_0^{s_c} ds\alpha e^{-\tau(s)} B_{MS} \tag{4.3}$$

The meaning of the three terms on the right hand sight is:

1. The first component describes the diffuse radiation I_{dif}^0 at the end of the characteristic s_c. Depending on the viewing geometry this is the upper or lower limit of the atmosphere. The diffuse radiation also accounts for the ground albedo.

   In general, the optical density τ is given by:

   $$\tau = \int ds\alpha(s) \tag{4.4}$$

   In equation (4.3) is τ_0 the optical density along the complete line of sight. Overall, the first term of the radiative transfer equation describes the extinction on the line of sight.

2. The second term represents the gain through single-scattering of the direct light beam into the direction of the line of sight. This is described by the source function B_{SS}:

   $$B_{SS}(\boldsymbol{r},\gamma_R) = \frac{\omega(\boldsymbol{r})}{4} F_0 P(\boldsymbol{r},\gamma_R) \exp\left(-\int_0^{s_T} ds\alpha(s) \right) \tag{4.5}$$

   with γ_R is the angle between the solar ray and the line of sight. This angle varies under refraction. The single-scattering albedo ω expresses the ratio of scattering to the overall extinction. The incident solar flux at the top of the atmosphere is πF_0. The phase function P describes the weighting of the scattering in the direction of the angle γ_R. The exponent is again the optical density but this time along the sun beam through the atmosphere to the point of scattering and after that along the line of sight.

3. The fraction which is gained through diffuse radiation is described in the third term. The source function B_{MS} of the multiple-scattering is given by:

   $$B_{MS}(\tilde{\boldsymbol{r}},\tilde{\theta},\tilde{\varphi}) = \frac{\omega(\tilde{\boldsymbol{r}})}{4\pi} \int_0^{2\pi} d\hat{\varphi} \int_0^{\pi} d\hat{\theta} \sin\hat{\theta} P(\tilde{\boldsymbol{r}},\gamma) I_{dif}\left(\tilde{\boldsymbol{r}},\hat{\theta},\hat{\varphi}\right) \tag{4.6}$$

   The coordinates with tilde represent the global or local coordinates somewhere on the line of sight. These can be calculated from the original coordinates $\boldsymbol{r}$ and $\boldsymbol{e}_s$ [Rozanov et al., 2000]. The angle γ is the scattering angle.

In general the source function is given by:

$$B = B_{SS} + B_{MS} \tag{4.7}$$

Since the source function B_{MS} for multiple-scattering is a function of the wanted diffuse radiation I_{dif} an iterative scheme is applied to solve this radiative transfer equation. Rozanov et al. [2001] are using the Picard iterative approximation. As a first guess for the intensity the radiation field for a pseudospherical atmosphere is calculated with the previous model version GOMETRAN [Rozanov et al., 1997]. Pseudospherical means that for the diffuse radiation field the atmosphere is assumed to be plane-parallel but for the attenuation of the direct and the single-scattered radiation the sphericity of the atmosphere is considered. In GOMETRAN the radiative transfer equation in its integro-differential form (equation (4.2)) is transformed into a system of equations by separating the angular variables. This system is solved using the method of the finite-differences. The solution is used to calculate the source function B_{MS}. After only a few iterations convergence is reached. The first two terms in equation (4.3) are calculated separately since they are independent of the iteration.

The spherical version of SCIATRAN applied in this work is the so-called CDIPI-version (*Combined Differential-Integral Approach involving the Picard Iterative Approximation*).

4.2 Calculation of air mass factors

The AMF is calculated by running the model SCIATRAN twice: First, the intensity is calculated with the absorber *i* of interest, second, without. Then the AMF is derived by applying the equation:

$$AMF_i\left(\theta,\varphi,\vartheta,\lambda\right)=\frac{1}{VOD_i}\ln\left(\frac{I_{-i}\left(\theta,\varphi,\vartheta,\lambda\right)}{I_{+i}\left(\theta,\varphi,\vartheta,\lambda\right)}\right) \tag{4.8}$$

where I_{+i} and I_{-i} are the intensities with and without the absorber *i*, θ is the solar zenith angle, φ the relative azimuth, and ϑ the elevation angle of the line of sight. The vertical optical density VOD_i from the ground to the top of atmosphere h_0 is defined by:

$$VOD_i\left(\lambda\right)\equiv\int_0^{h_0}dh\rho_i\left(h\right)\sigma_i\left(\lambda,h\right) \tag{4.9}$$

where *h* is the altitude, ρ is the number density of the absorber and σ the absorption cross-section at a given wavelength.

Again, equation (4.8) is only valid for an optically thin atmosphere: The effective light path has to be the same for an atmosphere with as well as without the absorber. In addition it should be noted that for the calculation of the AMF the shape of the trace gas profile must be known.

This approach to calculate the AMF was utilised in this study for analysing the satellite data (see section 5.4) and for most of the sensitivity studies presented in section 5.2.

4.3 Calculation of block air mass factors

Block air mass factors are defined as the AMF for one single, thin layer *j* in the atmosphere. This implies that the radiative transfer within this layer is independent from the absorber density in this and in the adjacent ones [Palmer et al., 2001]. Then equation (4.1) can be rewritten as:

$$SC(\lambda)=\sum_j BAMF_j\left(\lambda\right)\cdot VC_j \tag{4.10}$$

where VC_j is the individual column for each layer j and dependence on θ, φ and ϑ has been omitted.

The block air mass factors $BAMF_j$ are calculated in a somewhat different way than the total AMF. SCIATRAN is able to compute weighting functions for absorbers, aerosols and some other parameters. These weighting functions give the *absolute* change in intensity for a *relative* change of 100 percent of a parameter. For an optically thin atmosphere, the weighting functions can be easily converted into $BAMF_j$ for each individual layer:

$$BAMF_j(\lambda) = -\frac{WFN_j^I(\lambda)}{I_0(\lambda) \cdot \sigma(\lambda) \cdot \rho_j} \tag{4.11}$$

where WFN^I is the intensity weighting function, I_0 is the absolute intensity at the top of the atmosphere, σ is the absorption cross-section of the absorber of interest, ρ_j is the air density at layer j.

Similar approaches have been introduced in recent studies (e.g. [Palmer et al., 2001; Martin et al., 2002; Eskes and Boersma, 2003; Bruns et al., 2004; Nüß, 2005]. Block air mass factors were applied for the first time to MAX-DOAS observations of atmospheric trace gases (see section 4.3) within this study.

5 Data analysis

This chapter describes the algorithms developed in this study to retrieve tropospheric formaldehyde and glyoxal from ground-based and satellite measurements. The individual steps involved in analysing the spectral data obtained from the different instruments are discussed in the first section. This includes the spectral DOAS fitting to generate the slant column densities for both trace gases. In section 5.2 a number of sensitivity studies are described which have been carried out to characterise the influence of different meteorological parameters on the radiative transfer for both, satellite and ground-based observations. Section 5.3 introduces the profile retrieval algorithm BREAM developed for MAX-DOAS observations within this thesis, while in 5.4 the implementation of more-dimensional AMF-tables for the satellite retrieval is treated. This chapter closes with considerations on the error of the data products.

5.1 Spectral fitting

An overview is presented, which comprises the aspects that are relevant for the DOAS fitting (see section 3.2 for the mathematical background) of both satellite and ground-based data in this study. This includes general reflections on e.g. the wavelength range for the DOAS fit but also the handling of instrumental shortcomings like polarisation features in satellite observations.

5.1.1 Absorption cross-sections

The quality of the retrieval of the slant columns of the different compounds depends strongly on the quality of the reference absorption cross-sections used in the fitting procedure. This is particularly valid for the wavelength calibration as well as for the absolute cross-section values. Both have been significantly improved in recent years, e.g. by using Fourier Transform Spectroscopy (FTS) for the measurements (e.g. [Fleischmann et al., 2004; Volkamer et al., 2005]) and in recording the cross-sections for various temperatures (e.g. [Voigt et al., 2001]). The latter permits provision for the temperature dependency of the absorption of trace gases in the DOAS retrieval: Usually two absorption cross-sections, one for low, the other for high temperatures are included in equation (3.8). This is recommended at least for ozone in the UV since the temperature dependency not only scales the absorption bands but also leads to appearance or disappearance, respectively, of bands.

In general, there are two options for the absorption cross-sections utilised for the DOAS analysis:

1. Using high accuracy high spectral resolution cross-sections (see above) and convolving them with the instrumental slit function: That is the way the ground-based data are analysed in this study, since laboratory measurements of trace gases of interest with the field instrument are not available. The slit function is usually measured once per day using the mercury-cadmium lamp inside the calibration unit of the MAX-DOAS telescope (see section 2.3.1).
2. Using cross-sections measured with the instrument itself: In the case of GOME and SCIAMACHY, Ozone and NO_2 have been measured at several temperatures with high accuracy. The use of these cross-sections is recommended and has been implemented here for the analysis of the satellite data. Due to some systematic inaccuracies in the wavelength assignment, GOME cross-sections have to be shifted slightly in the analysis.

The number and also the species types of the absorption cross-sections included into the fitting procedure depends on the wavelength region chosen which will be discussed in the next section (5.1.2). An overview on the cross-sections employed is given in Table 7.

Table 7: References on cross-sections used in this study. For information on Ring and vibrational Raman scattering (VRS) see section 5.1.3.

Instrument / *Absorber*	*GOME*	*SCIAMACHY*	*BREDOM*
O_3	[Burrows et al., 1999] (wavelength corrected)	[Bogumil et al., 2003]	[Bogumil et al., 2003]
NO_2	[Burrows et al., 1998] (wavelength corrected)	[Bogumil et al., 2003]	[Vandaele et al., 2002]
BrO	[Wilmouth et al., 1999]	[Fleischmann et al., 2004]	[Wilmouth et al., 1999]
O_4	[Greenblatt et al., 1990] (wavelength corrected)	[Greenblatt et al., 1990] (wavelength corrected)	[Greenblatt et al., 1990] (wavelength corrected)
H_2O	[Rothman et al., 1992]	[Rothman et al., 1992]	[Rothman et al., 1992]
HCHO	[Meller and Moortgat, 2000]	[Meller and Moortgat, 2000]	[Meller and Moortgat, 2000]
CHOCHO	not applicable	[Volkamer et al., 2005]	[Volkamer et al., 2005]
Ring	[Vountas et al., 1998]	[Vountas et al., 1998]	[Vountas et al., 1998]
VRS	[Vountas et al., 2003]	[Vountas et al., 2003]	not necessary

5.1.2 Wavelength region

In order to decide on a specific wavelength region for the DOAS retrieval of a certain species, one has to find the best compromise between a couple of boundary conditions:

1. Using the strongest differential absorption lines of the species of interest.
2. Few other absorbing compounds in the wavelength region.
3. Little correlation between different cross-sections.
4. Avoiding strong Fraunhofer lines.

The following two figures (Figure 5-1 and Figure 5-2) present an overview on the cross-sections for the trace gases relevant within this thesis.

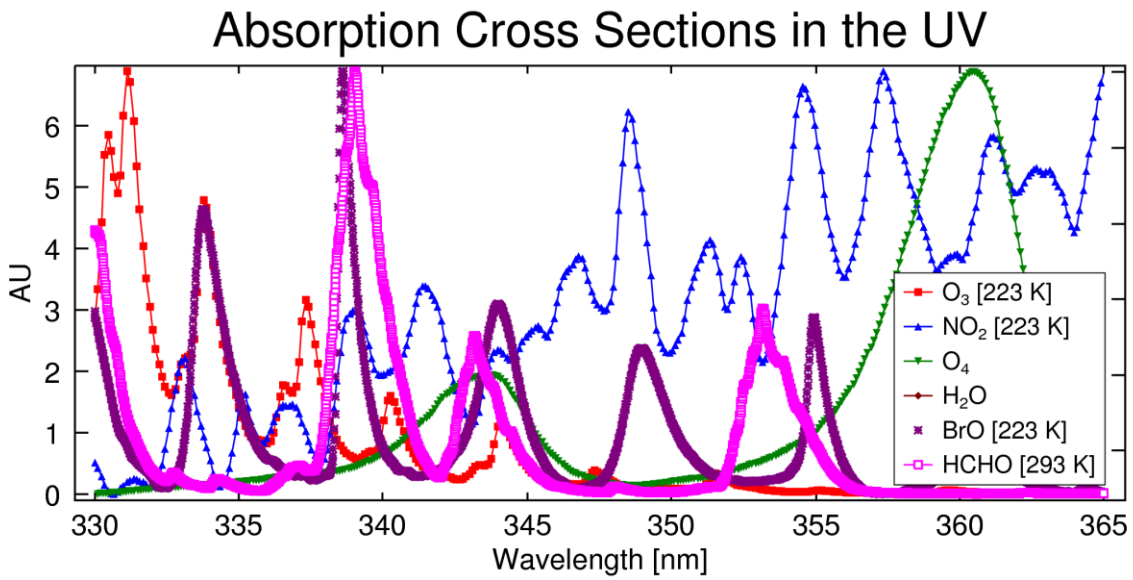

Figure 5-1: Absorption cross-sections in the UV wavelength region: All trace gases relevant for the formaldehyde retrieval. The cross-sections are shown with the spectral resolution of the SCIAMACHY instrument.

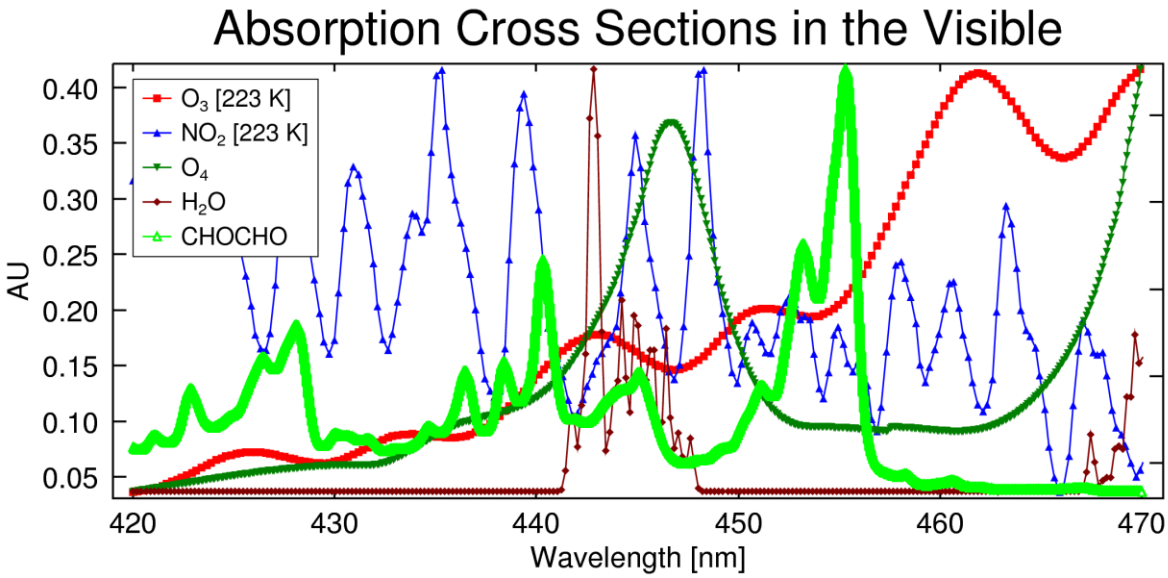

Figure 5-2: Absorption cross-sections in the visible wavelength range: All trace gases relevant for the glyoxal retrieval. The cross-sections are shown with the spectral resolution of the SCIAMACHY instrument.

All absorption cross-sections are shown in vacuum wavelengths and scaled to the highest value in the selected wavelength region. Since these trace gases are present at very different amounts in the atmosphere the following Table 8 shows realistic values of the differential optical density (DOD), i.e. a typical slant column (SC) for a solar zenith angle of 60° multiplied by the differential absorption cross-section (σ') to illustrate which absorber dominates the absorption feature.

Table 8: Typical values for slant column, differential absorption cross-section and differential optical density in the wavelength regions utilised in this study (for 60° SZA).

Trace Gas	*SC (UV) [molec/cm²]*	*σ′ (UV) [cm²/molec]*	*DOD (UV)*	*SC (vis) [molec/cm²]*	*σ′ (vis) [cm²/molec]*	*DOD (vis)*
Ozone	$1 – 3 \cdot 10^{19}$	$2 \cdot 10^{-21}$	0.02 – 0.06	$1 – 3 \cdot 10^{19}$	$1 \cdot 10^{-22}$	0.002 – 0.006
NO_2	$10^{16} – 10^{17}$	$1.5 \cdot 10^{-19}$	0.0015 – 0.015	$10^{16} – 10^{17}$	$4 \cdot 10^{-19}$	0.004 – 0.04
O_4	1000 – 5000 [10^{40}molec²/cm⁵]	$3 \cdot 10^{-6}$ [10^{-40}cm⁵/molec²]	0.003 – 0.015	1000 -10.000 [10^{40}molec²/cm⁵]	$6 \cdot 10^{-7}$ [10^{-40}cm⁵/molec²]	0.0006 – 0.006
BrO	$5 \cdot 10^{13} – 1.5 \cdot 10^{14}$	$2 \cdot 10^{-17}$	0.001 – 0.003	–	–	–
H_2O	–	–	–	$1 \cdot 10^{22} – 5 \cdot 10^{23}$	$5 \cdot 10^{-27}$	$5 \cdot 10^{-5}$ – 0.0025
HCHO	$5 \cdot 10^{15} – 3 \cdot 10^{16}$	$7 \cdot 10^{-20}$	0.00035 – 0.0021	–	–	–
CHOCHO	–	–	–	$5 \cdot 10^{14} – 3 \cdot 10^{15}$	$5 \cdot 10^{-19}$	0.00025 – 0.0015
Ring	0.1 – 1	0.07	0.007-0.07	0.1 – 1	0.008	0.0008 – 0.008

Table 8 points out that the dominant 'absorbers' in the UV are ozone and the Ring effect while in the visible, nitrogen dioxide and water vapour are the most important. The expected absorption features for the trace gases of interest in this study – formaldehyde and glyoxal – yield differential optical densities one to two orders of magnitude smaller than the dominant absorbers. This underlines the need to very carefully selected retrieval settings in order to obtain the best sensitivity for the fitting of HCHO and CHOCHO.

5.1.2.1 Formaldehyde

The formaldehyde molecule shows a pronounced spectral structure at wavelengths between 270 and 357 nm. Since the ozone absorption is getting very large below 335 nm the three absorption bands between 337 and 357 nm were selected for the retrieval in this study (see Figure 5-1). They correspond to the lower-most vibrational transitions at the visible end of the energetically lowest (first) electronic transition (n $\rightarrow \pi^*$) around 303 nm [Dieke and Kistiakowsky, 1934]. The uncertainty of the absolute cross-section applied here has been quoted to be about five percent [Meller and Moortgat, 2000].

In order to avoid the high correlation between HCHO and BrO absorption features in the spectral range from 337 to 346 nm it is essential to add the absorption band of HCHO at 353 nm. As pointed out in section 5.1.8 this is currently not feasible for the SCIAMACHY measurements.

5.1.2.2 Glyoxal

The glyoxal molecule exhibits three pronounced absorption band systems in the visible wavelength region between 420 and 460 nm. The most prominent one is that at 455 nm: $\tilde{A}^1A_u - \tilde{X}^1A_g\left(\pi^* - n\right)$. Since the Ring effect is significantly increasing for wavelengths below 433 nm the absorption feature around 428 nm was not considered in the CHOCHO retrieval presented here. During this study it became clear that the water vapour cross-section [Rothman et al., 1992] is not sufficiently accurate and leads to significant permanent features in the residual (see Figure 5-8). A better water vapour cross-section is not available, but fortunately this feature is in-between the glyoxal bands and should not influence the retrieved CHOCHO slant column. However, there is a need for a more reliable absorption cross-section of water vapour in this spectral region.

The uncertainty of the absolute cross-section of glyoxal applied here has been quoted to be about five percent [Volkamer et al., 2005].

5.1.3 Ring effect

As pointed out in section 3.4 the optical depth of the Fraunhofer lines for scattered sunlight is reduced due to inelastic rotational Raman scattering, mainly by the molecules N_2 and O_2, called Ring effect [Grainger and Ring, 1962]. Due to the large abundance of molecular nitrogen and oxygen in the atmosphere, the Ring effect can cause spectral structures of up to a few percent optical thickness (especially in the UV region, i.e. in the HCHO fitting window), which is then one or two magnitudes larger than the optical densities of the trace gases of interest retrieved by DOAS (see Table 8 in section 5.1.2). The Ring effect is even more important for satellite measurements where the direct sunlight which contains the original unattenuated Fraunhofer lines is used as reference spectrum. Thus, for an accurate retrieval, an optimal correction of the Ring effect is essential. Here, the required cross-section is calculated by the radiative transfer model SCIATRAN (see chapter 4) which simulates the rotational Raman scattering on oxygen and nitrogen molecules in the atmosphere [Vountas, et al., 1998].

A similar effect examined in this study is the vibrational Raman scattering (VRS) by liquid water. That this process might have an impact on DOAS retrievals from satellite observations was proposed the first time in Wittrock et al. [1999]. In the following Vountas et al. [2003] have quantified the VRS by implementing a simple ocean reflectance model (according to [Sathyendranath and Platt, 1998; Vasilkov et al., 2002]) into the radiative transfer model SCIATRAN. In case of the BrO retrieval, deviations up to 30 percent depending on water type and solar zenith angle were found. Dinter [2005] has carried out a sensitivity study on the possible influence of VRS on the HCHO retrieval and found a very small impact. This has been scrutinised here and an example of the results is shown in Figure 5-3. For both SCIAMACHY and GOME HCHO retrieval the deviation is less than three percent on average and therefore VRS is not included in the standard formaldehyde retrieval from the satellite instruments.

In addition, possible consequences of VRS on the CHOCHO retrieval were checked. Here, inclusion of the VRS cross-section in the analysis introduces large offsets into the retrieval results even above land. Thus, VRS was not accounted for in the standard glyoxal retrieval.

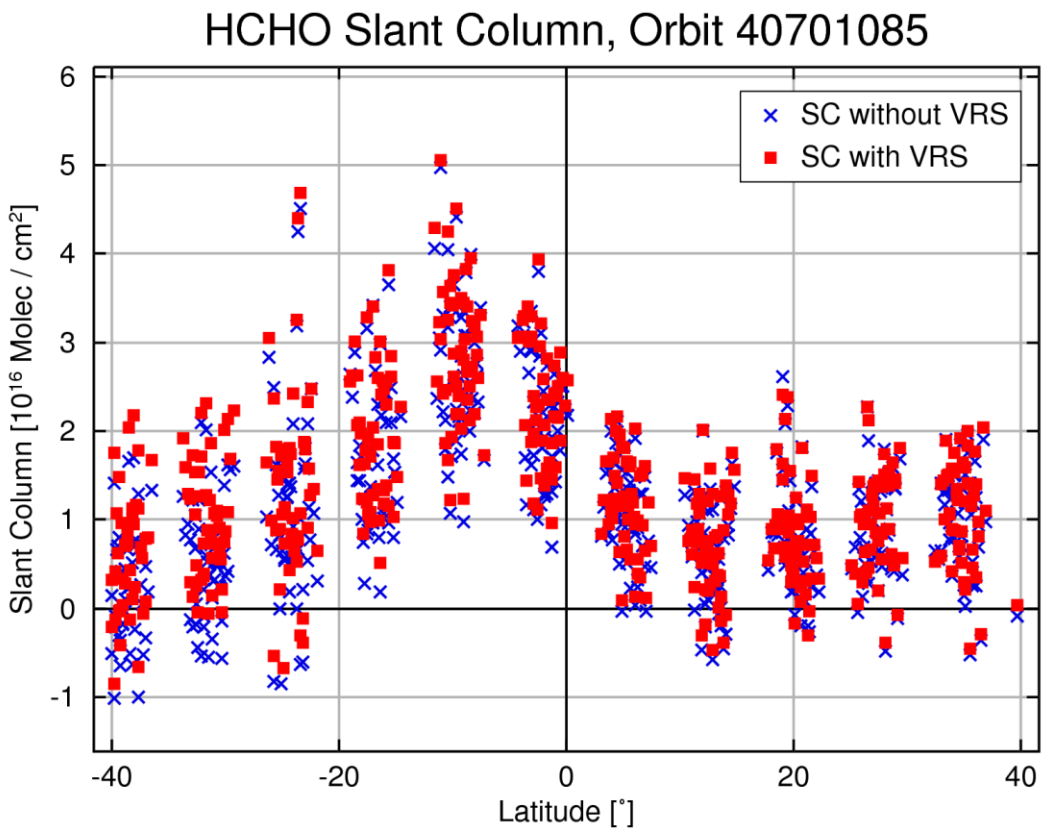

Figure 5-3: Fit results for HCHO from SCIAMACHY observations with and without taking into account vibrational Raman scattering.

5.1.4 Doppler shift of solar irradiance

As mentioned in section 2.1 and 2.2, GOME and SCIAMACHY irradiance measurements are not performed through the nadir viewing port, but rather via a diffuser plate. They are conducted in flight direction while the satellites leave the dark part of the orbit. Therefore, the solar measurements suffer from a Doppler shift, which is about 0.008 nm in the UV wavelength region. The nadir measurements are not Doppler shifted as they are orthogonal to the movement of the satellite; as a result, there is a distinct spectral shift between radiance and irradiance measurements of both GOME and SCIAMACHY which is a problem for the self-calibration of the DOAS measurements (see section 3.3) as discussed in the next section 5.1.5.

5.1.5 Sampling

As a result of last minute changes in the optical layout of GOME, the spectral resolution in the UV channels is slightly better than expected. While this gives sharper spectra with more details, it also reduces the number of measurements per FWHM (full width half maximum) of the slit function. In fact, the sampling of the slit function is now less than two for some spectral regions, violating the Nyquist theorem [Nyquist, 1928] and recommendations by Roscoe et al. [1996] making a perfect reconstruction of the signal impossible. This does not have an effect if all data are taken on the same grid, but once they have to be interpolated, errors cannot be avoided. Unfortunately, the spectral shift between radiance and irradiance measurements (see section 5.1.4) makes interpolation of one of the two necessary, and as a result, strong high frequency residual structures appear in all GOME fits using the solar spectrum as a background.

There are three possibilities to treat the undersampling problem:

1. Smoothing of all spectra (loss of information), see section 5.1.14.
2. Using earth-shine instead of irradiance measurements as background (loss of zero absorption in the background).
3. Simulating the effect of the undersampling and applying a correction function [Slijkhuis et al., 1999; Chance et al., 2005].

All three methods can be applied with the available fitting software, the latter being the one used in this study. However, in all fits some residuals of the undersampling remain. For SCIAMACHY, undersampling is less of a problem but still noticeable. The ground-based measurements use a sampling ratio of at least 6 and therefore are over-, and not undersampled. Roscoe et al. [1996] have proposed a sampling of at least 4.5 to fit trace gases without interpolation errors.

5.1.6 Diffuser plate structures

In addition to the problems described in section 5.1.4, a second effect of the diffuser plate used in the GOME measurements of the irradiance became apparent when several years of data became available [Richter and Wagner, 2001]. When comparing the seasonal variation of NO_2 columns above Bremen, some patterns that are not related to the normal seasonal variation of NO_2 are visible. The effect depends strongly on the wavelength region used for the fit (completely different patterns are observed for the fit in the UV and in the visible) and can result in deviations up to 50 percent in tropical regions for many absorbers. It turned out that this effect acts as a constant offset on the slant columns and not on the vertical columns. Using one fixed solar background spectrum instead of the usual daily one solves the problem indicating that the solar irradiance spectra are the source of the effect. The most probable explanation is the systematic variation in the azimuth angle between the diffuser and the sun as a function of season in combination with a pronounced angle dependence in the wavelength dependence of the diffuser reflectivity. The latter has been measured for the SCIAMACHY ESM diffuser which is similar to the one used in GOME and it has been confirmed, that the effect is significant. In response to this problem, a second diffuser (on the back of the ASM, see section 2.2.1) was added to SCIAMACHY briefly before launch which does not exhibit such problems.

There are several ways of compensating this effect:

1. Using one fixed background spectrum: But over time, instrumental aging increases the errors in the analysis and introduces drifts (see also section 5.1.7).
2. Using an earth-shine spectrum as background: But this introduces the uncertainty of the absorber amount in the background-spectrum.
3. Correcting the measurements by subtracting the amount measured over a specific region (e.g. a reference sector in the Pacific) and adding the expected value (for example from model predictions): But this introduces a priori assumptions in the analysis.

None of the three approaches is ideal and the method chosen depends on the particular problem. In this study approach three was selected for the following reasons:

- One aim of this study is to provide a consistent data set for the whole GOME time series since 1995. This forbids the first approach.

- Even if the other attempts have similar limitations, the third one is easier to handle because there is not a risk of unexpected features in the selected background spectra.

Consequently, a region in the Eastern Pacific (10°S to 10°N, 180°W to 140°W) was chosen, where one can assume only background concentrations for both, formaldehyde and glyoxal. In the case of formaldehyde the background value was set to $3x10^{15}$ molec/cm^2 for the slant column according to measurements from Heikes et al. [2001], that for glyoxal was chosen to be 1 $x10^{14}$ molec/cm^2.

5.1.7 Etalon

Contrary to prior expectations, the GOME instrument is subject to strong etaloning on the detectors. This is caused by residual water vapour on the satellite that is forming growing ice layers on the detectors. Interference in this layer creates sinusoidal structures in the spectra that have amplitudes of several percent and occur at wavelengths that are comparable to those of ozone in the Chappuis bands. The effect is particularly strong after switching off the coolers which is necessary from time to time because of instrumental problems of the satellite or GOME. But even several months after the restarting of the coolers the etalon structures are still changing.

There are two options to deal with the etalon

1. Using background spectra that are timewise as close as possible to the measurement spectra.
2. Using a high degree polynomial in the DOAS retrieval (see equation (3.8)) to correct for changes in etalon.

In this study, both methods are applied since it became obvious that the polynomial chosen in the beginning (degree 3) introduces offsets in the GOME HCHO results for the measurements since 1999. This is most probable due to the etalon effect or to degradation (see section 5.1.6). Therefore a higher polynomial of 5 has been chosen to correct this. In addition daily sun spectra were used for the retrieval whenever possible. Because one should expect similar problems with the SCIAMACHY instrument the same polynomial was applied to the SCIAMACHY HCHO retrieval. In the CHOCHO fitting window a polynomial of degree 3 was found to be sufficient to avoid any etalon effects.

The ground-based instruments have not shown any etalon structures on the detectors. However, the mirror used to scan the off-axis directions was identified to introduce broad-band signatures into the spectra. This has been accounted for in using a polynomial of degree 5 in the HCHO fit and degree 3 in the CHOCHO fit, respectively (see section 5.1.13).

5.1.8 Polarisation correction

As all optical instruments, GOME and SCIAMACHY have a different sensitivity towards light polarised parallel to the optical axis as towards light polarised perpendicular to this axis. Primarily, this sensitivity is changing slowly with wavelength and is not of concern for the DOAS retrieval. However, some components of the instrument exhibit sharp changes in sensitivity for the different polarisations, and introduce wavelength dependent signatures in the measured spectra if not corrected. The most prominent of those is the dichroic that is separating channels two and three in both satellite instruments. The basic philosophy of the polarisation correction in the satellite instruments is, that they measure the light as it comes from the atmosphere, and that the polarisation degree is determined using the PMDs and some other information. Using pre-flight calibration measurements, the effects of polarisation are calculated using the so called *eta* and *chi* functions (Figure 5-4), and then corrected in the spectra. Unfortunately, the dichroic has changed over time, in particular due to outgassing, and the pre-

flight calibration curves do not longer apply. As a result, the effects of polarisation cannot be corrected completely, and all attempts to do so have introduced additional artefacts.

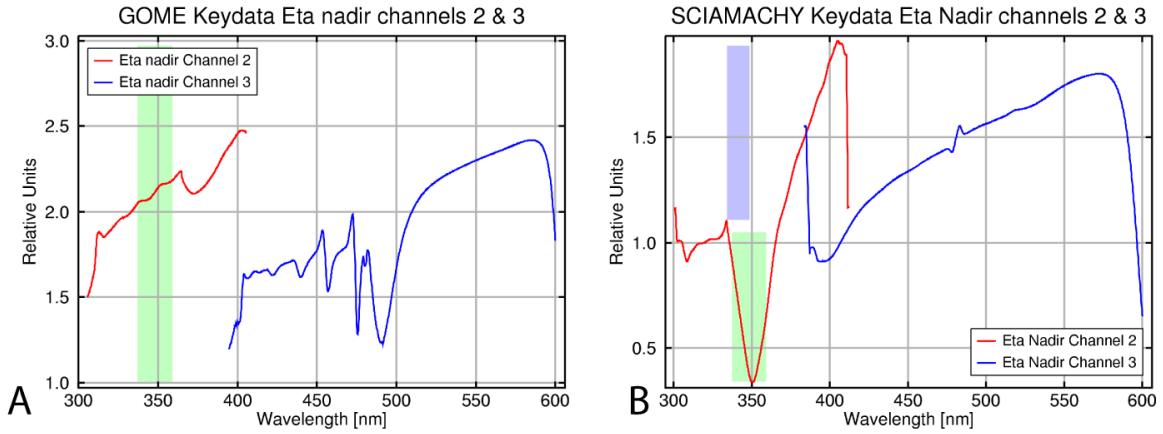

Figure 5-4: Polarisation response functions (*eta*) for GOME (A) and SCIAMACHY (B) in the spectral channels 2 and 3 relevant for this study. The proposed HCHO fitting window is marked in green. Due to the strong anomaly at 350 nm a UV-shifted window (marked in blue) was chosen for the SCIAMACHY HCHO retrieval.

So far, a good way to deal with this problem has not been found, and in general, those wavelength regions exhibiting the polarisation structures have to be avoided for fitting weak absorbers. This is the case for the HCHO retrieval in SCIAMACHY as well as for the CHOCHO retrieval in GOME. While a slightly UV-shifted window similar to that chosen by Afe [2005] for BrO was applied to SCIAMACHY channel 2 spectra to derive HCHO, up to now a successful approach could not be found to analyse CHOCHO in the channel 3 from GOME.

The ground-based instruments do not have any problems with polarisation features since the quartz-fibre bundle used to transmit the light from the telescope to the spectrometer efficiently depolarises the incoming light (see section 2.3.1).

5.1.9 Solar I_0-correction

When using the DOAS equation, the implicit assumption is made, that using intensities and cross-sections convolved with the same slit function is appropriate. However, this is not strictly true: the DOAS equation is only valid for a very narrow slit function. In reality, there is a difference between applying the convolution before or after the absorption. This difference depends strongly on the spectral structures of the light source; for a smooth light source, the effect is small, for the solar spectrum, which has strong Fraunhofer lines in the UV and visible part of the spectrum, the effect is significant for strong absorbers having highly structured spectra (e.g. [Johnston, 1996; Richter, 1997; Wagner, 1999]).

This effect is called I_0-effect. A correction can be applied to the data by observing the effect on synthetic spectra. For ground-based measurements of BrO, this can make a difference of up to 30 percent at 90° SZA [Aliwell et al., 2002]. In the case of the measurements presented here, the I_0-effect can usually be neglected, as most measurements are taken at smaller SZAs and/or were carried out in the visible with less structured spectra. Case studies yielded deviations always less than 5 percent. Therefore all results presented here were calculated without considering the I_0-effect.

5.1.10 Wavelength dependence of air mass factor

The light path through the atmosphere (and thereby the air mass factor) depends on scattering and absorption, and therefore on wavelength (see section 1). In general, one of the basic assumptions in the DOAS analysis is that it is possible to separate the spectral analysis from the simulation of the light path. Consequently, only one air mass factor is necessary for the whole fit. However, strictly speaking, a separate air mass factor is necessary for each wavelength. For strong absorptions, this is a significant effect and has to be accounted for in the analysis by using cross-sections that are weighted with the appropriate wavelength dependent air mass factor [Richter, 1997]. This effect can be neglected because in general data for SZAs less than 80° were analysed in this study.

5.1.11 Stray light correction

Every spectrometer exhibits a specific level of stray light. Therefore in the results presented here a stray light correction has been applied. Usually the stray light correction simulates the effect of a constant and sometimes also a linearly changing offset in the measurements. Even if stray light is a simple function in intensity, it is complex in optical thickness as

$$\ln\frac{I+c}{I_0} \neq \ln\frac{I}{I_0} + \ln(c) \tag{5.1}$$

but in first approximation

$$\ln\frac{I+c}{I_0} \approx \ln\frac{I}{I_0} + \frac{c}{I_0} \tag{5.2}$$

where I is the measured intensity, I_0 the background intensity and c the assumed offset (stray light).

Therefore, if stray light correction is applied, an additional cross-section is created from the current spectrum I having the form c_M/I, where c_M is the maximum value of I in the selected spectral window multiplied by an empirical factor. A factor of the order of 0.03 is usually appropriate, and in general, the magnitude of this factor does not have a large impact on the results. In addition, a second correction term was used to change the value of c_M linearly.

The stray light correction has proven to be useful for the results presented here, and can correct not only instrumental stray light but also inaccuracies in the Ring correction and other atmospheric effects like the vibrational Raman scattering in liquid water which is described in section 5.1.3.

5.1.12 Fraunhofer Calibration

Although all spectra are pre-calibrated to the fitting (using the on-board spectral line lamp for the satellite instruments and the mercury-cadmium-lamp inside the telescope for the ground-based BREDOM instruments), the accuracy of the wavelength attribution is not better than 0.03 nm in many parts of the spectrum. This small error is large enough to introduce uncertainties in some fitting windows in particular in the UV (formaldehyde) and a better spectral calibration is preferred. This can be achieved by aligning the background spectrum to an external Fraunhofer atlas measured with high accuracy and at high spectral resolution. In this study spectral calibration on the Kurucz Fraunhofer atlas was selected [Chance and Spurr, 1997]. This calibration also takes care of the necessary correction of the Doppler shift for the satellite spectra (see section 5.1.4).

5.1.13 Polynomial

In principle, the polynomial should correct for the wavelength dependence of Mie and Rayleigh scattering only. Therefore a low order polynomial (smaller or equal to 4) should be appropriate. However, in practice the polynomial also corrects for changes in detector etalon (see section 5.1.7), inaccuracies in the instrument calibration or deficiencies in the knowledge of broadband absorption spectra (e.g. O_4 and liquid water). Therefore, in some cases polynomials of larger order have to be applied. In this study a polynomial of degree 5 was chosen for the HCHO retrieval and a polynomial of degree 3 in the case of CHOCHO.

5.1.14 Smoothing and averaging

Two types of averaging techniques can be applied to the measurements: averaging over time and averaging over wavelength. When averaging over time, consecutive measurements are averaged to improve the signal-to-noise-ratio (SNR), but spatial and/or temporal resolution is lost. For random noise (e.g. photon noise from the detectors) this type of averaging increases the precision of the measurements with the square root of the number of averaged spectra. In this study the GOME spectra were not averaged. In order to reduce the scatter of the SCIAMACHY data the spectra were averaged to a spatial resolution of 120 km across track and 60 km along track. Usually, the ground-based data are averaged during the recording process over one minute for each viewing direction [Oetjen, 2002].

A second type of averaging is the spectral averaging, where intensities from neighbouring wavelengths are averaged. This procedure is usually referred to as smoothing of the spectra. When spectra are smoothed before the fitting, the fit residuals are decreased significantly. However, the values at the individual wavelengths are no longer independent, and as a result the accuracy of the fit does not improve. Therefore, spectral smoothing is generally not recommended for the DOAS fit and has not been applied to any of the results presented here.

5.1.15 Clouds

In particular for satellite instruments, clouds have quite dramatic impact on the measured intensity. As the integration time of the instrument cannot be adjusted, it is set in such a way, that even the brightest clouds do not lead to detector saturation. Therefore, only cloudy situations (or measurements above ice) use the full dynamic range of the instrument, whereas all other measurements use rather low signals. This implies, that measurements over clouds have a better signal to noise ratio, and might not be fully comparable to measurements over cloud-free scenes. Also, because of the spectral dependence of Mie scattering, instrumental stray light from the visible part of the spectrum might be a problem in the UV for cloudy scenarios. Another effect of clouds is a significant change in Ring effect, as Raman scattering is proportional to the Rayleigh scattering, and in the case of scattering from clouds the relative contribution of Rayleigh scattering is much smaller than for a cloud-free scene. Also, the different spectral distribution of the photons will change the shape of the apparent Ring spectrum. In order to avoid the limitations mentioned here a cloud criterion has been applied for all satellite measurements presented in this study: Only pixels having cloud coverage less than 20 percent were utilised.

Clouds also have a large impact on air mass factors. This is investigated in section 5.2.2.5.

5.1.16 Spatial aliasing

In the satellite instruments, diode array detectors are used in the spectroscopic channels. Although the read-out of such detectors is fast, it still takes some time during which the satellite moves ahead and the scene on the ground

is changing. As those parts of the array that have not yet been read out continue to integrate signal, spatial changes in intensity will be reflected in spectral changes in signal. This effect can be observed at the edge of clouds or ice fields as apparent jumps in the spectra measured by GOME and SCIAMACHY. In most cases, the changes will be small and varying smoothly with wavelength, and therefore do not have an effect on the DOAS analysis. However, in principle, they can introduce noise into the measurements.

5.1.17 Surface albedo

Nadir viewing satellite instruments observe not only photons scattered in the atmosphere, but also photons reflected on the ground. This does not simply have an influence on the overall intensity, but also on the spectral distribution. Some surfaces exhibit an albedo that changes smoothly with wavelength, but others show clear spectral signatures, that can interfere with the trace gas retrieval in DOAS. Unfortunately, very little is known about the spectral dependence of surfaces, in particular at the relatively high spectral resolution of GOME and SCIAMACHY. This point is of particular importance in the visible part of the spectrum, where chlorophyll [Bracher et al., 1999] and liquid water [Pope and Fry, 1997] have significant features.

For the retrieval of CHOCHO from SCIAMACHY these problems have been investigated in detail. After first tests in CHOCHO fitting it became clear that water regions are quite problematic for the chosen algorithm. In particular, scenes with very clear water (e.g. in the Southern Pacific, see Figure 5-5) yield unreasonable negative results for the CHOCHO slant columns. In order to investigate the reason for that unexpected behaviour, pixels above these regions with and without clouds have been averaged and then the ratio $I_{cloud}/I_{nocloud}$ was calculated.

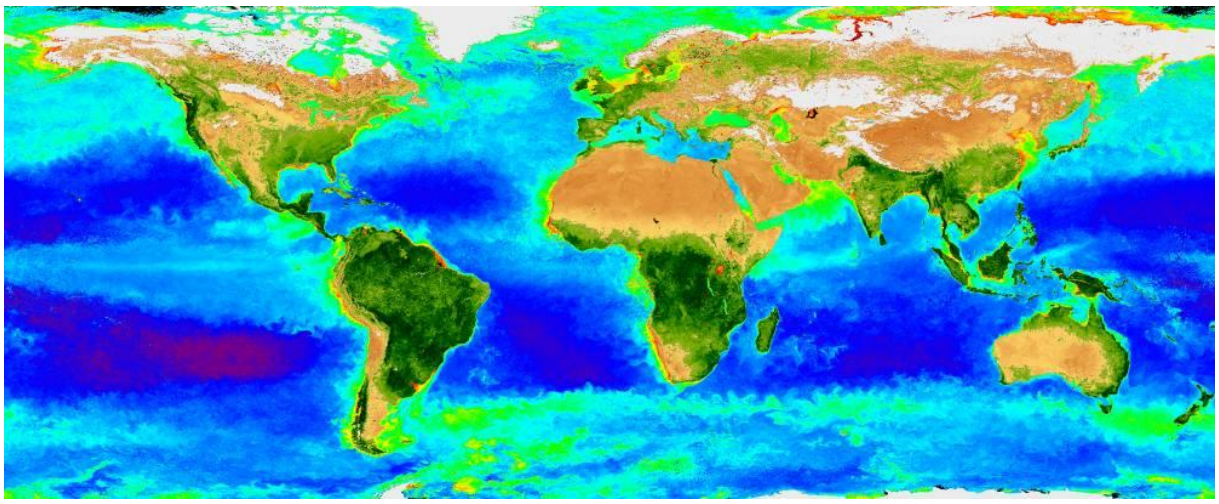

Figure 5-5: Composite of MODIS chlorophyll data from February 2005. Dark blue or violet colours indicate regions with very clear water where the SCIAMACHY CHOCHO fit fails.

The ratio is shown in Figure 5-6 along with the differential absorption coefficient of liquid water [Pope and Fry, 1997]. From this plot it is clear that the absorption of liquid water can influence the DOAS retrieval. One way to fix the problem is to add either the liquid water absorption or the residual from the clear water scenario into the DOAS fitting procedure. When doing this, the slant columns above clear water got more reasonable but the fitting results above the continents became rather unstable. Therefore all results on SCIAMACHY CHOCHO presented in chapter 6 are derived neglecting the problems above water.

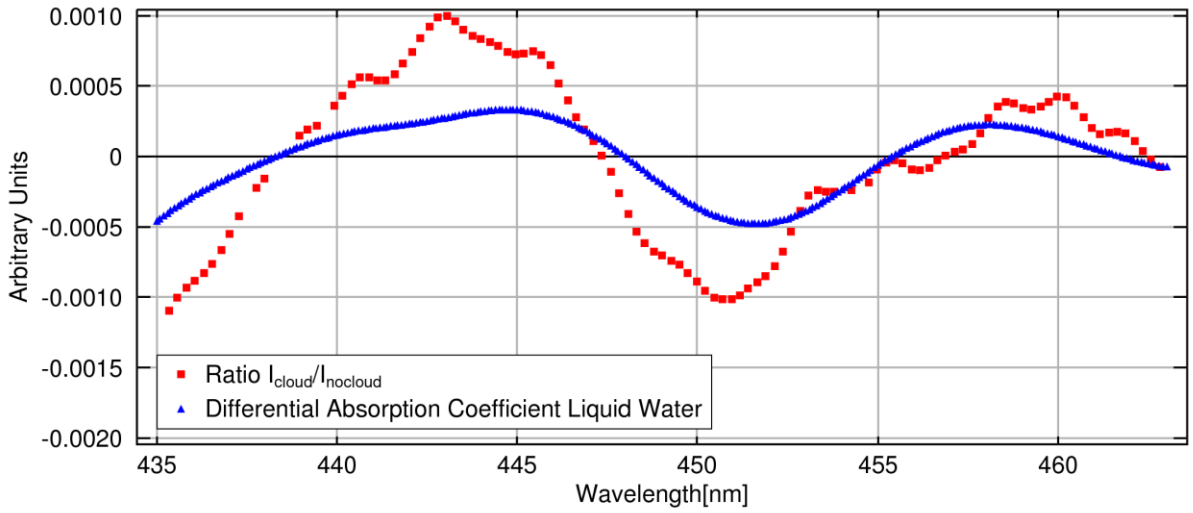

Figure 5-6: Comparison of the differential absorption coefficient of liquid water with structures obtained by investigating cloudy and non-cloudy pixels above clear water regions.

5.1.18 Southern Atlantic Anomaly

In the Southern Atlantic, close to the coast of Brazil, the Van Allen radiation belt has a fault about 200 km from earth's surface and particles from the sun reach the upper atmosphere. In this region, satellite measurements are subject to spikes and other anomalies, and large errors occur in the data, in particular for weak absorbers. This problem is addressed by selecting the data by its chi-square and accepting the data gaps in this region. Chi-square is a measure of the quality of the DOAS retrieval. An example of the global chi-square pattern is given in Figure 5-7. Because the signal-to-noise ratio is smaller in channel 2 SCIAMACHY data, this data gap is larger in SCIAMACHY HCHO data sets as in those from GOME.

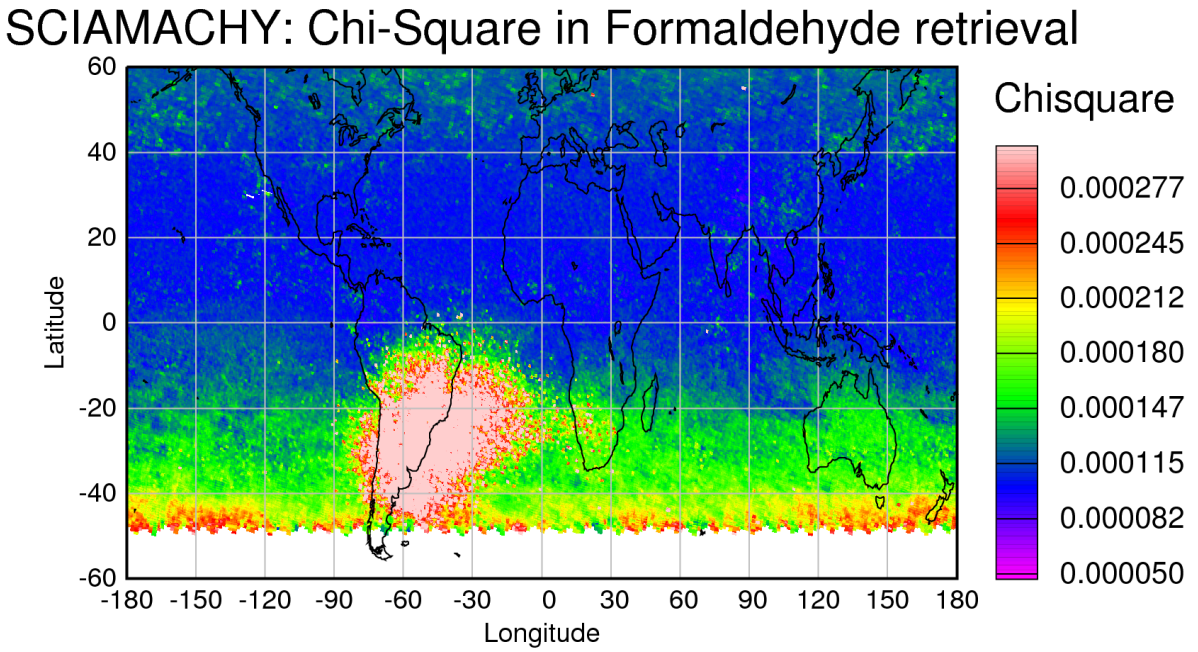

Figure 5-7: Chi-square from the SCIAMACHY HCHO retrieval for July 2004. The fault in the Van Allen belt induces strong noise into the DOAS results. In addition, the chi-square increases with higher solar zenith angles in the southern hemisphere.

5.1.19 Overview on retrieval settings

As a consequence of the different aspects and boundary conditions detailed in sections 5.1.1 to 5.1.18 a set of standard retrieval parameters was derived which is summarised in the following tables (Table 9 and Table 10). Due to the anomaly in the polarisation response function (see section 5.1.8) the sensitivity of SCIAMACHY to the HCHO absorption features is significantly reduced. Similar problems in GOME channel 3 prevent the retrieval of CHOCHO from GOME up to now.

It should be noted that the typical detection limit given in the tables refers to the slant column *SC* of one single spectrum. For the ground-based measurements, the detection limit for the vertical column is enhanced as a result of large air mass factors and the possibility to average over several spectra.

The following Figure 5-8 shows examples of the fitting of both, formaldehyde and glyoxal for the various instruments. It also illustrates that in addition to the formaldehyde glyoxal has been clearly identified in scattered light spectra for the first time. All graphs show the residual after removing all contributions with the exception of the trace gas of interest in conjunction with the scaled laboratory reference spectrum.

Table 9: Formaldehyde fitting parameters and obtained fit quality.

HCHO Fitting Parameters	*GOME*	*SCIAMACHY*	*BREDOM*
Wavelength range	337.5 – 359 nm	334.3 – 348.5 nm	335 – 357 nm
Polynomial	5	5	5
Stray light	Two terms	Two terms	Two terms
Absorber	Ozone (two temperatures), NO_2, BrO, HCHO, O_4, Ring	Ozone (two temperatures), NO_2, BrO, HCHO, Ring	Ozone (two temperatures), NO_2, BrO, HCHO, O_4, Ring
Background	Daily solar irradiance	Daily solar irradiance	Daily zenith-sky noon
Undersampling corr.	Yes	Yes	No
Wavelength calibration	Kurucz	Kurucz	Kurucz
Typical residual at 60° solar zenith angle [DOD]	0.0007	0.001	0.0003
Detection limit (SC) [molec/cm^2]	$1.4 \cdot 10^{16}$	$2 \cdot 10^{16}$	$6 \cdot 10^{15}$

Table 10: Glyoxal fitting parameters and obtained fit quality.

CHOCHO Fitting Parameters	*SCIAMACHY*	*BREDOM*
Wavelength range	436 – 457 nm	436 – 457 nm
Polynomial	3	3
Stray light	Two terms	Two terms
Absorber	Ozone, NO_2, O_4, CHOCHO, H_2O, Ring	Ozone, NO_2, O_4, CHOCHO, H_2O, Ring
Background	Daily solar irradiance	Daily zenith-sky noon
Undersampling correction	No	No
Typical residual at 60° solar zenith angle [DOD]	0.0005	0.0005
Detection limit (SC) [molec/cm^2]	$1 \cdot 10^{15}$	$1 \cdot 10^{15}$

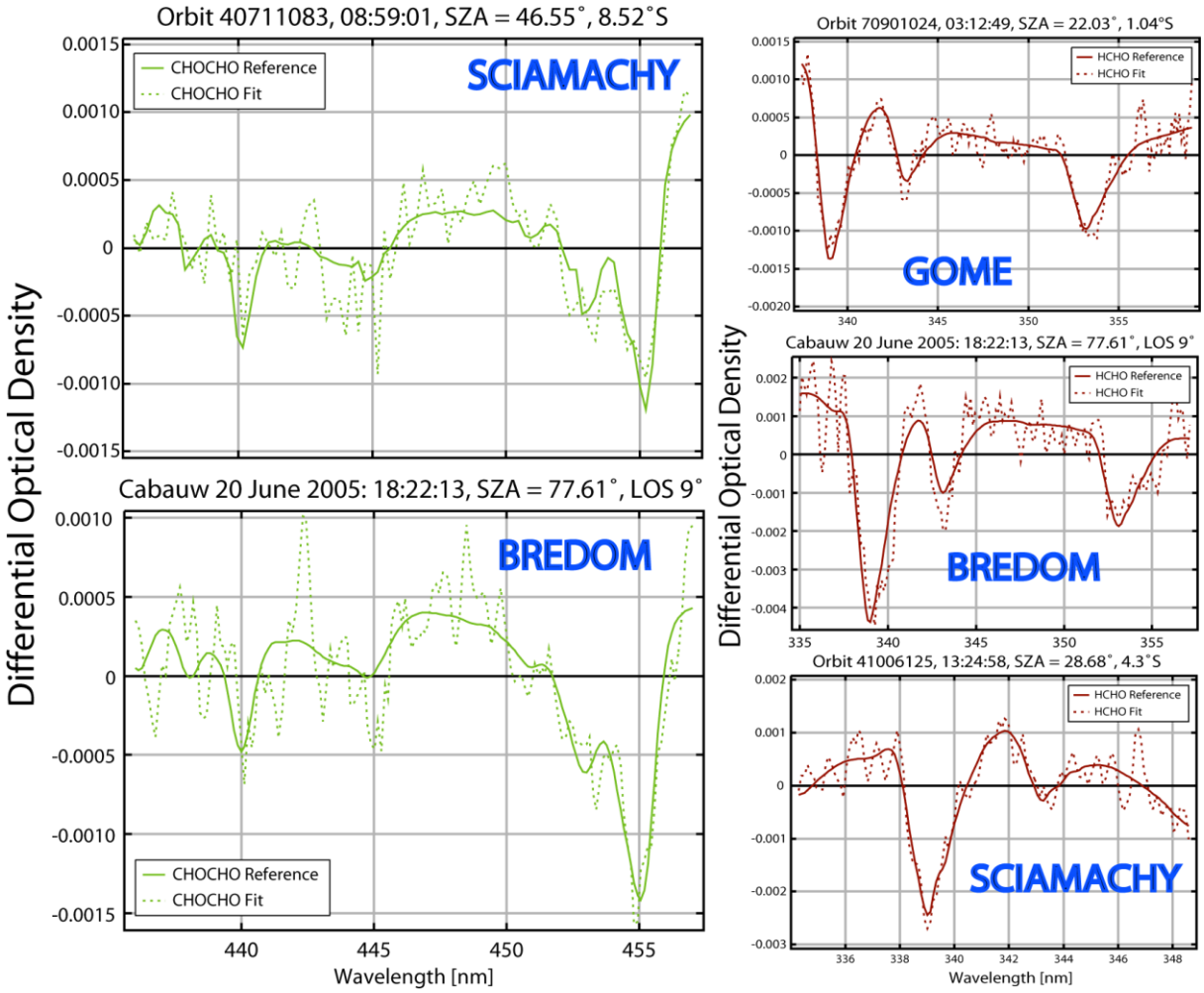

Figure 5-8: Examples of the laboratory (thick lines) and observed (dashed lines) fit spectra for glyoxal (left) and formaldehyde (right) using the different instrumental platforms. Large residual structures in the CHOCHO retrieval between 442 and 448 nm are due to an incomplete removal of water vapour absorption.

5.2 Sensitivity studies for radiative transfer

When modelling the radiative transfer in the atmosphere, a number of parameters have to be set to realistic values. The most important ones are the viewing geometry, the position of the sun, wavelength, and the vertical profiles of absorbers, of pressure and of temperature. However, surface albedo and the atmospheric aerosol loading also have an impact on the results. Here the influences of those parameters are investigated and quantified for both, ground-based and satellite observations.

5.2.1 Radiative transfer modelling studies for ground-based observations

For the investigation on the different parameters of the radiative transport the model SCIATRAN (section 4.1) in its full-spherical version was applied. Most of the following work (section 5.2.1.1.1 to 5.2.1.1.5) was carried out in the framework of the European projects QUILT and FORMAT and has been published in *Atmospheric Chemistry and Physics* [Wittrock et al., 2004; Heckel et al., 2005]. In addition an intercomparison exercise between six different radiative transfer models including the calculation of AMFs under different conditions for the multi-axis geometry was organised as part of the QUILT project [Hendrick et al., 2005].

5.2.1.1 Sensitivity studies for O_4

O_4 is a powerful indicator for the radiative conditions in the atmosphere. Its vertical profile is determined by pressure and temperature and therefore can be computed from meteorological data. Thus, the value of O_4 is threefold:

1. Validation of the radiative transfer model: Using realistic input parameters for the meteorological conditions should enable the model to calculate O_4 differential slant columns similar to those observed with the MAX-DOAS instrument. This was confirmed for SCIATRAN in several studies [Rozanov, 2001; Wittrock et al., 2004].
2. Sensitivity studies such as presented in the following subsections can illustrate the influence of specific parameters on the radiative transfer in a very intuitive way since in contrast to other absorbers the profile and therefore the vertical column of O_4 is exactly known.
3. The comparison of modelled and measured O_4 slant columns in principle yields information on parameters influencing the radiative transfer and thus, can be used to retrieve this parameter. This is in particular true for the aerosol (see section 5.2.1.1.4) where complementary measurements are usually sparse. The usage of this piece of information is illustrated later in section 5.3 where the profile retrieval from ground-based observations is described.

In Ny-Ålesund (see section 2.3.2.1) at least weekly profiles for the absorber ozone and daily temperature and pressure profiles of the atmosphere are available through ozone soundings and radiosondes, respectively, providing the opportunity to get realistic input data for the radiative transfer calculations. Above the burst height of the balloon the profiles are continued by values from a model climatology provided by the MPI for Chemistry, Mainz [Brühl and Crutzen, 1992]. These profiles are used as meteorological input for the radiative transfer model. In the following sections, the influence of multiple scattering, the relative azimuth, surface albedo, aerosols and of the refraction on the O_4 AMF and the resulting vertical column are investigated with model data. Such sensitivity studies are necessary to determine which parameters need to be known to which extent in order to derive realistic vertical columns from the measurements. The results are presented in the form of a ratio between a reference air mass factor AMF_{Ref} of a standard scenario with the air mass factor AMF obtained with one of the above mentioned parameters changed. This ratio indicates the error in the vertical column that is introduced when setting the respective parameter to an inappropriate value.

For the reference AMF, the atmospheric profile from 3 April 2002 was used and a Fraunhofer reference spectrum taken at 60° SZA in the zenith direction was assumed. All calculations shown have been executed at 370 nm (the centre of the O_4 fitting window in UV applications), an albedo of 0.5, a background arctic aerosol (see Figure 5-15) and full multiple scattering and refraction. It is important to note that the sensitivity studies are presented in the form in which the AMF will be applied to the actual measurement. Therefore, not the absolute AMF but rather the difference in AMF between a horizon measurement and the background zenith measurement at 60° SZA is used for the comparison with the reference scenario. This relative quantity sometimes has a larger sensitivity to changes in model parameters than the absolute AMFs giving a better estimate for the real measurement situation.

5.2.1.1.1 Multiple scattering

For a qualitative interpretation of MAX-DOAS measurements, simple geometric considerations with the help of a simple single scattering approach have been used sometimes to estimate the air mass factors (e.g. in [Hön-

ninger and Platt, 2002]). However, in the troposphere multiple scattering cannot be ignored, and using a single scattering approximation introduces large errors. This is illustrated in Figure 5-9 where for an elevation angle of 6° the underestimation of the vertical column increases from a few percent at high sun to more than 50 percent at low sun depending on the relative azimuth. As it is expected, the influence of multiple scattering increases with decreasing elevation angle (not shown here). The reason for the large impact of multiple scattering is twofold: On the one hand, the air mass factor for the zenith-sky measurement increases with multiple scattering, thereby decreasing the difference between horizon and zenith measurement. On the other hand, the air mass factor for the horizon viewing mode is slightly increased by multiple scattering for high sun, but clearly decreased at low sun. The combination of both effects results in the behaviour shown in Figure 5-9.

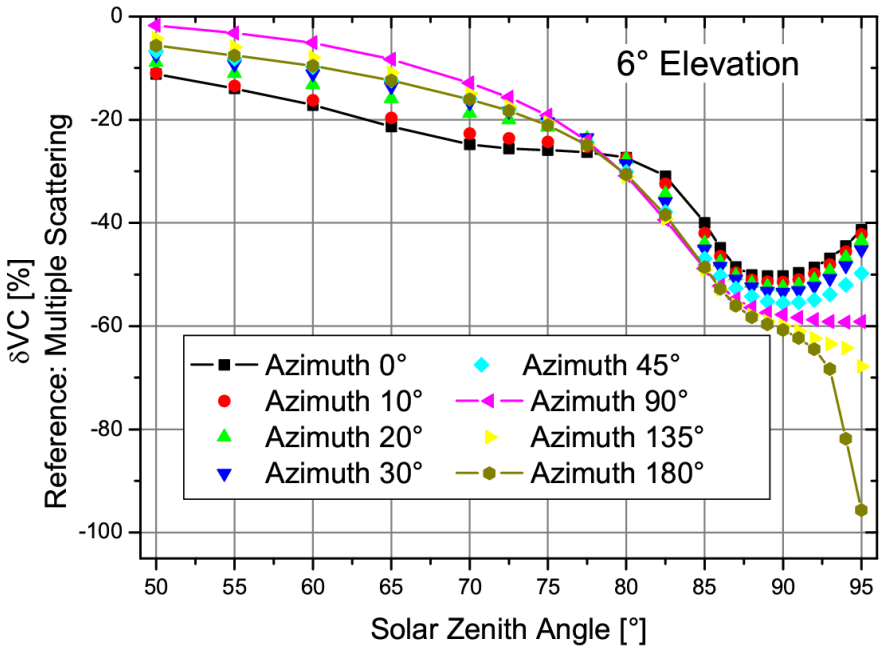

Figure 5-9: Effect of neglecting multiple scattering on the vertical column of O_4. For an elevation angle of 6° the vertical column will be underestimated, if only single scattering is taken into account for the air mass factor.

5.2.1.1.2 Relative azimuth

When analysing the O_4 columns measured under different elevation angles on a clear day, it is apparent that the values do not only depend on solar zenith angle as is the case for zenith-sky measurements but also vary with the relative azimuth angle. This becomes apparent from Figure 5-10, which shows measurements of differential slant columns (DSCs) from 26 April 2003. As the instrument is pointed towards the NNW, the relative azimuth varies over the day, and morning and afternoon measurements taken at the same SZA differ significantly.

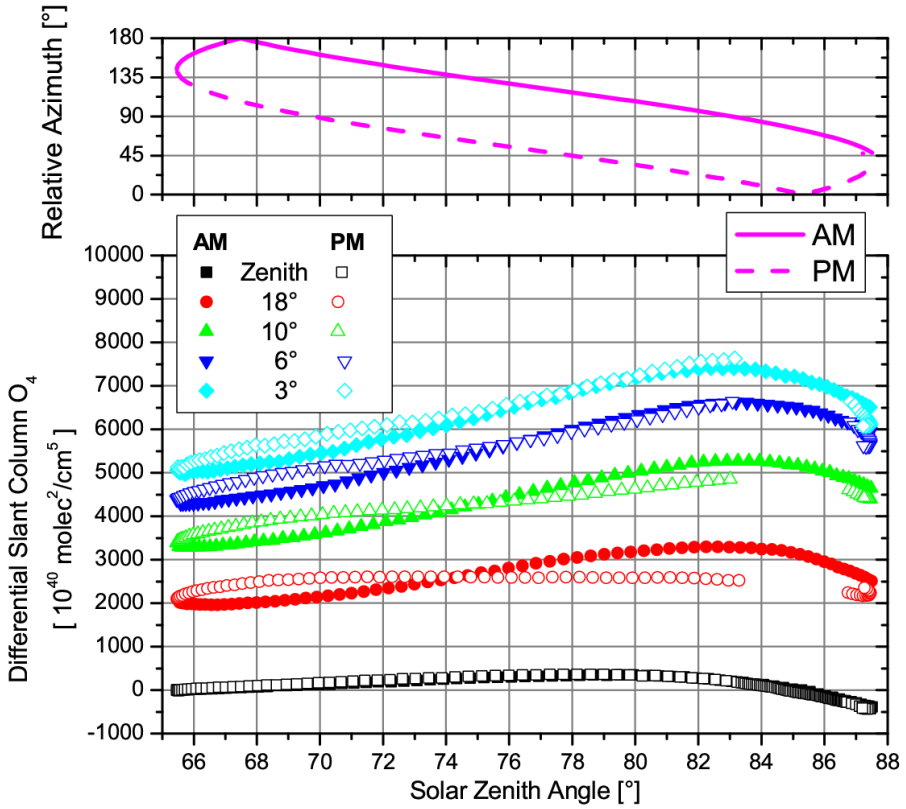

Figure 5-10: Diurnal variation of the measured O_4 DSCs on 26 April 2003. As background the zenith-sky noon spectrum from the same day was used. On this very clear day (only thin clouds in the late evening), the azimuthal dependency of the measured O_4 is clear. There is a gap in the off-axis measurements in the late afternoon to avoid direct sunlight.

In order to evaluate the impact of the relative azimuth between measurement direction and the sun, air mass factors have been calculated for different elevation angles (3°, 10° and 18°) and then sorted accordingly to the relative azimuth. The main effect is that the AMF is significantly smaller when looking towards the sun, in particular for higher elevation angles (see Figure 5-11). This is a result of the strong forward peak in Mie scattering which reduces the effective light path in this geometry. The effect on the difference between the horizon AMF and the zenith AMF can become quite large as shown in Figure 5-12. Here, the error of the vertical columns is shown that is introduced when using a deviating azimuth instead of the correct relative azimuth of 90° in the AMF calculations. The azimuth effect is relevant for all elevation angles, and is largest for higher elevations and a small relative azimuth. For all azimuth angles pointing away from the sun, the error is smaller than 10 percent for SZAs less than 93°. From the results of this test one can conclude, that it is preferable to point a horizon viewing instrument away from the sun, and that it is essential to take into account the correct azimuth in the AMF calculation.

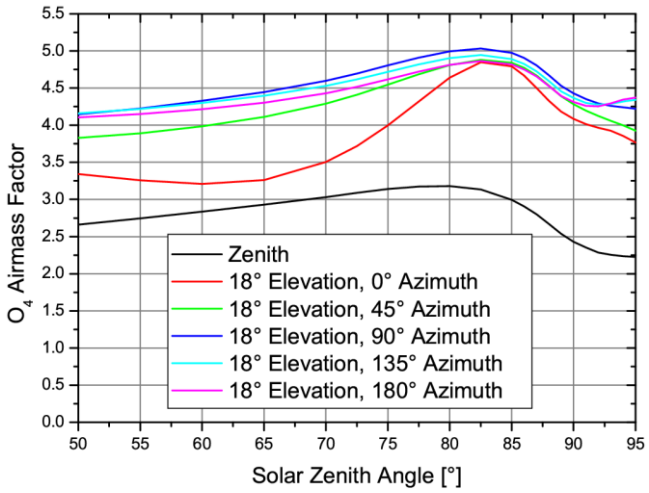

Figure 5-11: Absolute air mass factors for O_4. Pointing the instrument towards the sun (0° relative azimuth) leads to decreasing differences between horizon and zenith-sky AMF.

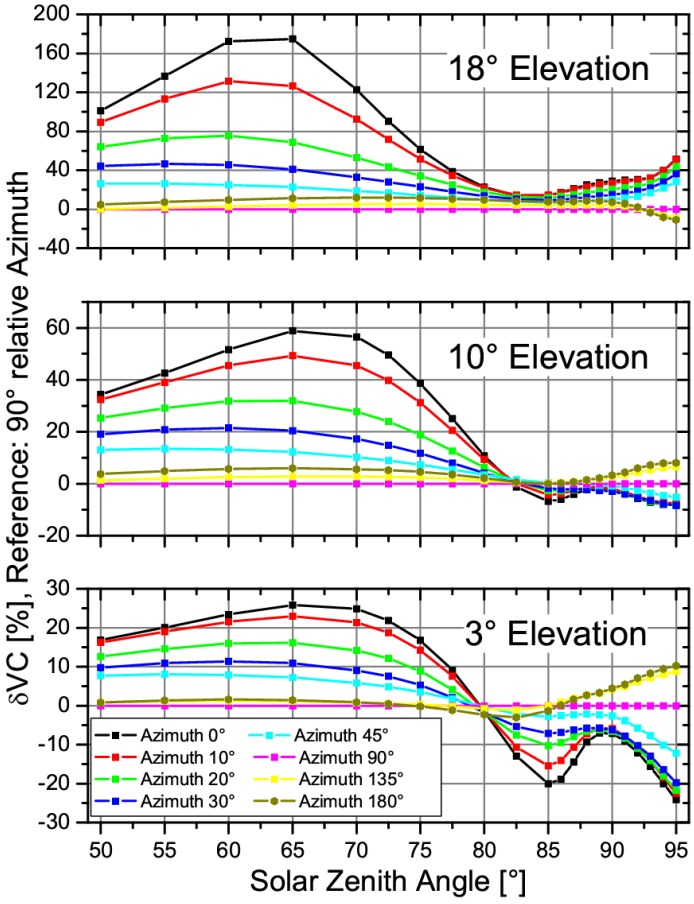

Figure 5-12: Effect of the relative azimuth angle on the calculated VC. Shown is the error introduced in the vertical column of O_4 if an azimuth angle different from the 90° of the reference case is used in the air mass factor calculation.

5.2.1.1.3 Albedo

Surface albedo changes have a significant impact on the intensity of the diffuse radiation field close to the surface. At most of the BREDOM sites (Bremen, Mérida, Ny-Ålesund), quite different albedo values can be found depending on season and viewing direction, for example, when comparing snow-covered ground and open water. To study the impact of albedo on the AMF, calculations with the albedo of freshly fallen snow (0.9) and a very small albedo (0.01) are compared to a medium albedo of 0.5. For an elevation angle of 3° the vertical column will be underestimated when a too small albedo is assumed and overestimated when the albedo is too high (Figure 5-13). At an elevation of 18° the same trend can be observed for the directions pointing away from the sun. For the direction towards the sun, i.e. 0° azimuth, using a wrong albedo has a big impact on the vertical column. For relative azimuths larger than 45°, the error introduced by using an inappropriate albedo is generally less than 20 percent.

Figure 5-14 shows the relative AMF, i.e. the difference between the actual AMF and the AMF of midday at 60° SZA. As can be seen the difference is decreasing with increasing albedo. This results in a higher relative sensitivity of the off-axis measurements for a small albedo which at first glance is surprising. The reason for this unexpected behaviour is not so much the effect of high albedo on the low elevation measurements but an increased sensitivity of the zenith-sky viewing direction. For high albedo the number of photons scattered close to the ground is larger, making the zenith-sky measurements more sensitive to absorption in the troposphere. This reduces the difference in AMF between horizon and zenith-sky viewing directions. In summary, the impact of albedo changes on the AMF is significant, in particular, when looking towards the sun. Good albedo estimates are needed for the analysis (or have to be derived from the measurements themselves) and again it is simplifying the analysis if the telescope is pointed away from the sun.

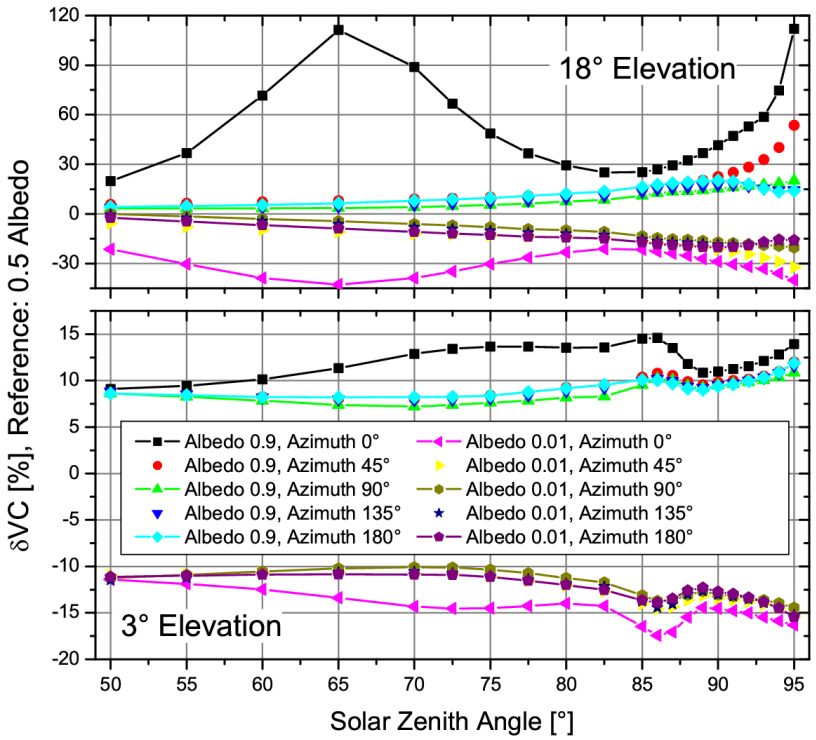

Figure 5-13: Effect of the albedo on the calculated VC. Shown is the deviation introduced in the vertical column of O_4 if an albedo different from 0.5 of the reference is used in the air mass factor calculation.

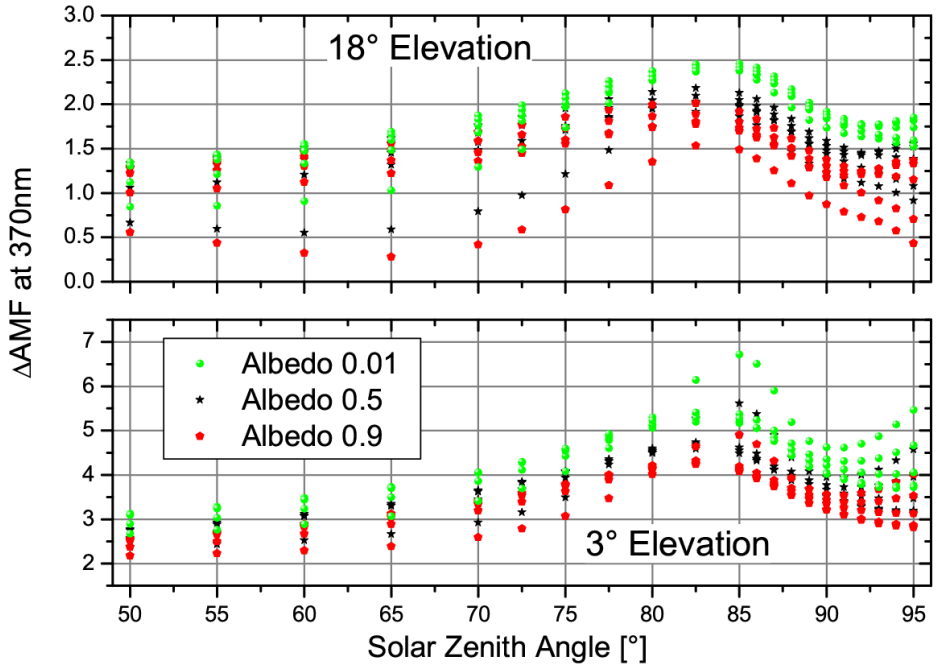

Figure 5-14: Differences of AMF for O_4 calculated with different albedos. All relative azimuth angles from previous figures are plotted but for clearness not indicated with extra symbols. All AMFs are related to the zenith-sky AMF at 60° solar zenith angle. Although absolute AMFs are getting larger for increasing albedo, the inverse behaviour is true for AMF differences between off-axis and zenith-sky.

5.2.1.1.4 Aerosols

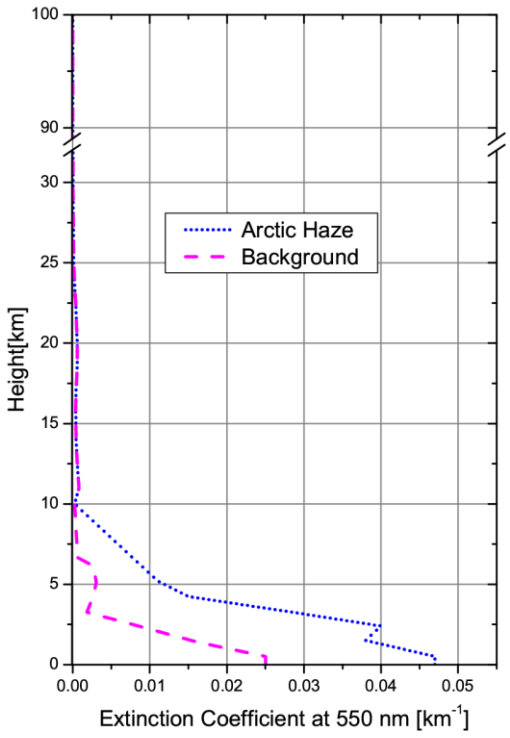

Figure 5-15: Profiles of the aerosol extinction coefficient at 550 nm used for AMF calculations shown in Figure 5-16.

The optical properties of aerosols are determined by their composition, their shape and the relative humidity. For the impact on the AMFs, the vertical distribution of the aerosols also plays an important role. In general, increasing the aerosol extinction reduces the light path for the lower viewing directions but has little impact on the zenith directions thereby reducing the difference in tropospheric absorption path for the different viewing directions. For the sensitivity studies, a simplified vertical extinction profile based on measurements in Svalbard during the ASTAR-Campaign 2000 was used [Rathke et al., 2002; Treffeisen et al., 2004; Yamanouchi et al., 2005]. In the troposphere, a marine aerosol type was chosen, aged volcanic aerosol for the stratosphere and above that meteoric dust. The standard extinction coefficient is shown in Figure 5-15. The relative humidity was set to 50 percent in the lowermost 5 km of the atmosphere. In this study, only the total extinction was changed: The background scenario is compared with very strong extinction as would be observed in an arctic haze event and with no aerosols at all, i.e. zero extinction coefficient throughout the whole atmosphere. The results are shown in Figure 5-16 for three elevation angles.

For the lowest elevation, the light path increases with decreasing extinction, and using a high aerosol scenario instead of the standard scenario will lead to a 10 percent overestimation of O_4. Similarly, using a Rayleigh atmosphere in the air mass factor calculations will lead to a 10 to 20 percent underestimation of the real column. For higher elevations, the sensitivity to aerosols decreases, but azimuth effects are more important. In particular, the 0° azimuth direction (pointed towards the sun) is very sensitive to changes in the aerosol extinction mainly because the air mass factor for this direction is very close to the one of the zenith-sky background measurement (see Figure 5-11).

It was shown, that MAX-DOAS observations are quite sensitive to the aerosol content even in remote areas. Thus, O_4 slant columns can be used to retrieve aerosol parameters (see section 5.3), assuming that the other important boundary conditions for the radiative transfer calculations (e.g. the surface albedo) are well-known. This result has initiated the idea to include an aerosol retrieval in the MAX-DOAS evaluations (see section 5.3).

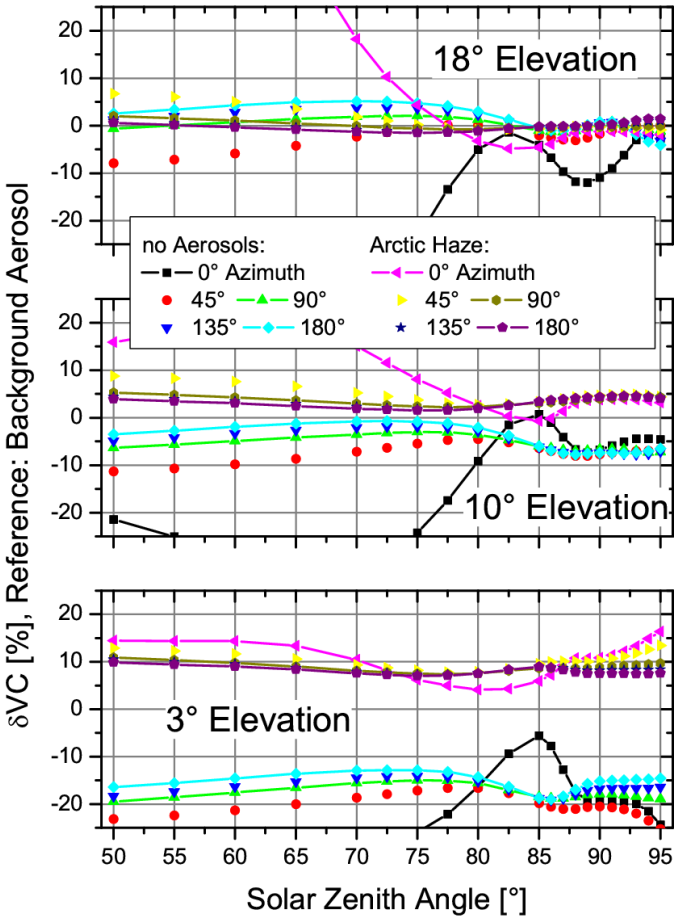

Figure 5-16: Effect of the aerosol extinction profile on the calculated vertical column. Shown is the error introduced in the vertical column of O_4 if aerosol scenarios different from the background aerosol of the reference are used in the air mass factor calculation.

5.2.1.1.5 Refraction

As a result of refraction in the atmosphere, the solar disc can be seen during dusk and dawn for some time even when it is geometrically below the horizon. In the SCIATRAN model, including refraction in the horizon view-

ing geometry is computationally expensive, and therefore the effect of neglecting refraction on the AMF was evaluated. As can be seen in Figure 5-17, the error in the vertical would be well below 1 percent at SZAs smaller than 80° depending on viewing geometry (elevation and azimuth) and increases for larger SZAs. Thus, in this study refraction is of minor importance because vertical columns and/or profiles from HCHO and CHOCHO have been analysed for smaller SZA.

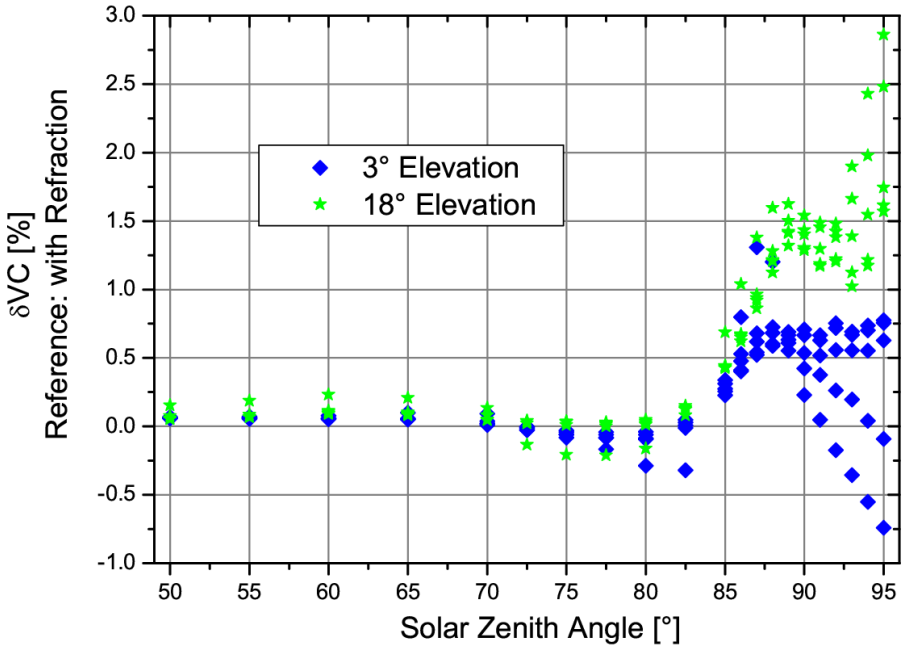

Figure 5-17: Effect of neglecting refraction on the calculated VC. Only for solar zenith angles larger than 85° the introduced errors are larger than 0.5 percent.

5.2.1.1.6 Conclusion

The results of the model studies for O_4 show, that multiple scattering cannot be ignored, whereas refraction has only a minor impact on the results. The relative azimuth between sun and viewing direction has a significant effect and has always to be taken into account, in particular when the instrument is not pointed away from the sun and/or for measurements at high latitudes. The effect is more pronounced when the realistic case of a zenith-sky background spectrum with non negligible O_4 content is considered. Both, aerosol extinction and surface albedo can have a large effect on the air mass factors, and determining these parameters is crucial for a quantitative retrieval. The albedo can be adequately determined through weather observation or web camera pictures whereas the aerosol scenario persists to be an element of uncertainty. However, the measurements from different lines of sight can be used to get aerosol information which is one motivation for the development of the MAX-DOAS retrieval algorithm described in section 5.3. In all sensitivity studies, only one parameter was changed at a time to simplify interpretation. However, some of the parameters are clearly not independent from each other, and for example the effect of surface albedo might vary with aerosol extinction. Also, absorbers with a different vertical profile like formaldehyde and glyoxal will not behave exactly as O_4 does. However, the qualitative behaviour will be similar, and O_4 has the advantage of providing the opportunity to validate the model results as stated above.

5.2.1.2 Vertical resolution

Another set of sensitivity studies has been performed to investigate the possible information content on the vertical resolution which can be derived from MAX-DOAS measurements of tropospheric trace gases like HCHO and CHOCHO. One example of the different studies is described in the following using data obtained during the FORMAT campaigns in Alzate, Italy (see section 2.3.2.5.3). *In situ* measurements have shown that the boundary layer near Milan is sometimes split into two sublayers. To answer the question, whether stratification like this could be detected by the MAX-DOAS instrument, air mass factors have been calculated for three different HCHO profiles shown in Figure 5-18 (left). The integrated vertical column for each profile was kept constant to guarantee the comparability. The relative differences for the AMF compared to the AMF for one homogenous layer (profile 1) are shown in Figure 5-18 (right). Deviations in the range of 10 to 20 per cent should be detectable also in experimental data. This result was the main motivation to develop the profile retrieval algorithm described in section 5.3.

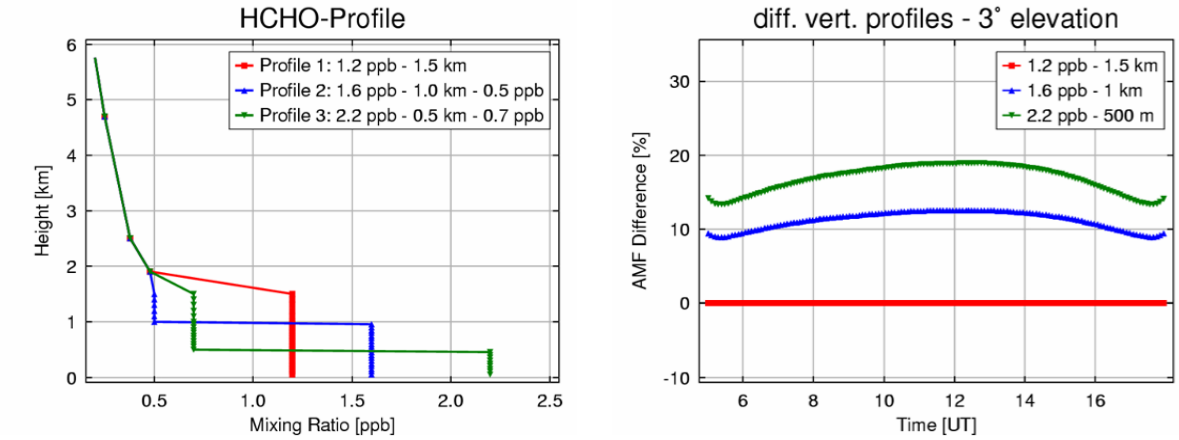

Figure 5-18: Left: different assumed vertical HCHO mixing ratio profiles used for the AMF calculation. Right: Relative differences between the AMFs (for 3° elevation) calculated for the selected profiles. The differences between the sensitivities for the different profiles clearly indicate the potential of the MAX-DOAS measurement for profile retrieval which has been realised and described in section 5.3.

5.2.2 Radiative transfer modelling studies for satellite observations

While AMFs can easily be computed with high accuracy by radiative transfer models such as SCIATRAN, it is not obvious what to use for the input parameters such as absorber profile, aerosol content, and albedo, and thus the error budget of the trace gas columns is dominated by the uncertainties of the AMFs. Similar to what has been done for the ground-based viewing geometry (see section 5.2.1) the following sections investigate the impact of those parameters on the radiative transfer and thus on the results of the trace gas retrieval for space-based observations. It is out of the scope of the following section to give a full review on the radiative transfer for spaceborne observations. Here, only the most realistic scenarios are considered. A very comprehensive description of radiative transfer model results for satellite observations of NO_2 which is retrieved in a similar wavelength range as CHOCHO one can find in Nüß [2005].

5.2.2.1 Vertical Absorber Profile

Usually, the sensitivity of nadir measurements in the UV/visible spectral domain decreases strongly towards the surface (see e.g. Figure 5-24). To compensate for this effect, the vertical distribution of the absorber must be

known, an information which cannot be derived from the satellite measurements themselves (with the exception of ozone in the stratosphere, e.g. [Muller et al., 2003; Tellmann et al., 2004]) .

From the MAX-DOAS measurements at the BREDOM permanent and campaign sites and from literature, different types of HCHO profiles have been identified ([Schmidt and Lowe, 1982; Arlander et al., 1995; Junkermann and Stockwell, 1999; Kesselmeier et al., 2000; Heikes et al., 2001; Frost et al., 2002; Fried et al., 2003; Kormann et al., 2003; Singh et al., 2004; Heckel et al., 2005], see also section 5.4) and utilised to investigate the impact of the profile on the satellite AMF (see Figure 5-19). In the case of CHOCHO no profile information is available neither from observations nor from modelling. However, as glyoxal has a similar fate as HCHO in terms of sources and sinks in the troposphere the same vertical distribution is assumed. It is important to note that only the shape of the profile is needed, whereas the absolute amount does not have an impact on the air mass factor within a very large concentration range. Therefore, volume mixing ratios of several ppb_V for CHOCHO are unlikely but do not affect the AMF calculation.

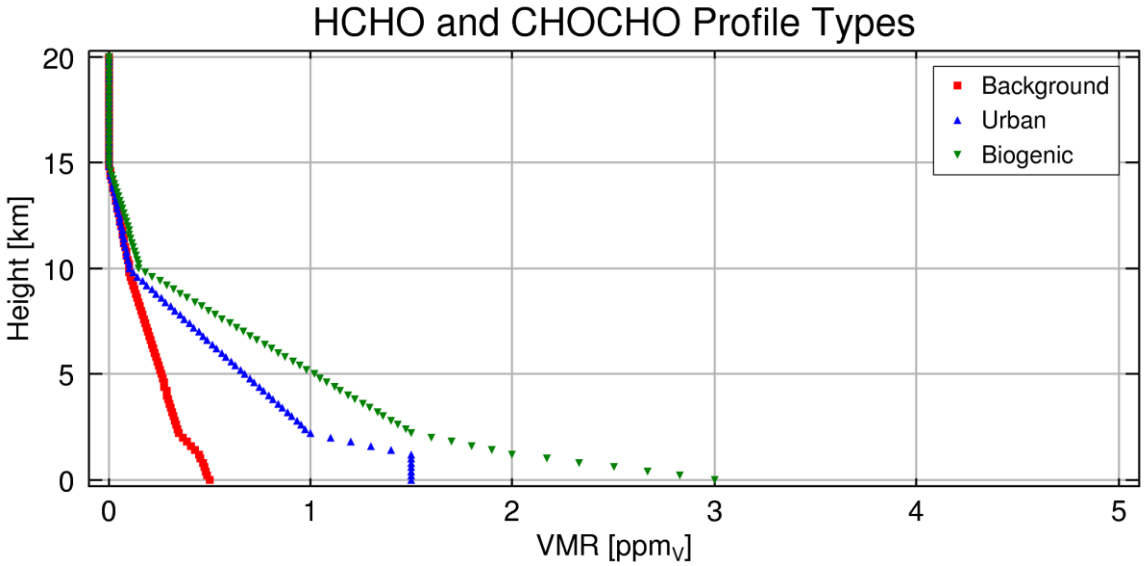

Figure 5-19: Profile types utilised to calculate the satellite AMF for formaldehyde and glyoxal in this section and in section 5.4.

At first glance the profiles look quite similar. However, the biogenic profile peaks close to the ground based on findings from e.g. [Kesselmeier et al., 2000], while the other profiles show a more or less constant volume mixing ratio (VMR) in the boundary layer. In general, there is agreement between measurements and model predictions (e.g. [Martin et al., 2004]) that the volume mixing ratio of HCHO is decreasing with altitude. It should be noted that under certain conditions, e.g. rapid convective transport due to biomass burning, other profile shapes are imaginable. But observations of that are sparse. Consequently, the focus here will be on the most likely scenarios.

Figure 5-20 shows the AMF for both, HCHO and CHOCHO assuming the aforementioned profiles, an albedo of 0.06, a rural aerosol type, a ground level of 0 km and a visibility of 10 km. These settings are used in the following as standard. In general, the sensitivity in the UV is between 20 percent and more than 100 percent lower for small and for large SZAs, respectively, compared to the visible. This is mainly caused by the wavelength dependency of the Rayleigh scattering. Actually, that means that the detection limit for CHOCHO in higher latitudes is much better than for HCHO (in terms of differential optical density) at least for low albedo. The devia-

tions between the different profile types are comparatively small but nevertheless reach 20 percent for the difference of the background and the biogenic profile at higher SZAs and should not be neglected. Since the fraction of the trace gas amount in the boundary layer is highest for the biogenic profile this yields the smallest AMF. It should be noted here that in case of NO_2, the profile is of greater importance for the interpretation of the satellite measurements (e.g. [Nüß, 2005]). This is caused by the higher variability: Anthropogenic sources yield a large peak near to the ground while e.g. thunderstorms generate NO_2 high up in the troposphere. In addition, NO_2 exhibits a longer lifetime compared to HCHO and CHOCHO which boosts the relevance of transport and the associated more complex vertical profiles.

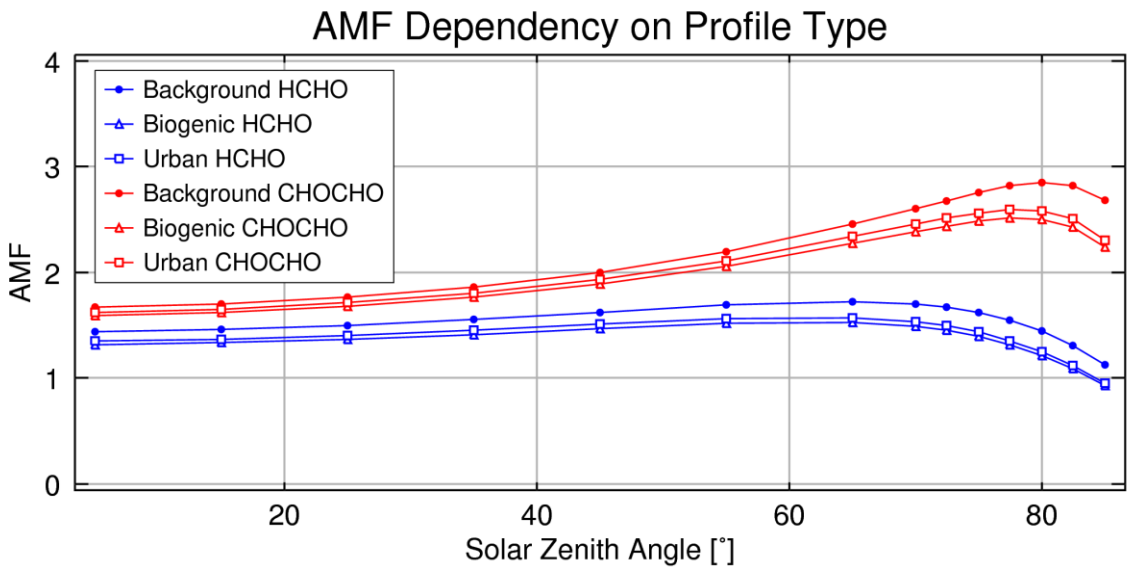

Figure 5-20: AMF in the visible (446 nm, CHOCHO) and the UV (336 nm, HCHO) for different profile types.

5.2.2.2 Surface Elevation

Surface elevation plays a role in air mass factor calculation which is exemplarily illustrated in the following Figure 5-21. The differences are caused by several partly conflicting processes: On one hand, the amount of surface-reflected photons is larger for raised ground. On the other hand, the fraction of photons reflected by the atmosphere is increasing with the thickness of the air mass.

In general, spaceborne observations are more sensitive to trace gases in the boundary layer above high altitude regions (e.g. Mexico City) than to regions at sea level. The deviation is from 3 up to 30 percent increasing with SZA. The relative importance is comparable for the UV and the visible.

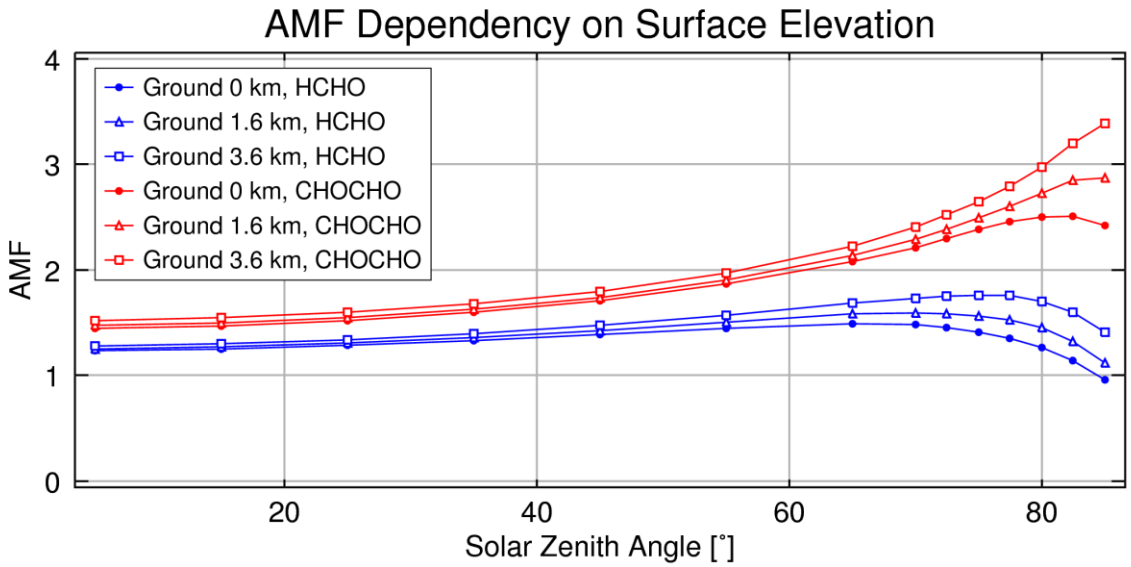

Figure 5-21: AMF in the visible (446 nm, CHOCHO) and the UV (336 nm, HCHO) for different surface elevations and in this case a low aerosol content (visibility 23 km) in the boundary layer assuming the standard profile shape.

5.2.2.3 Surface Albedo

The sensitivity of satellites to the lower troposphere depends strongly on the surface albedo caused by the different fraction of photons reflected back to the satellite, at least under conditions where the aerosol optical depth is not too large. This makes the parameter albedo the single most important one for the interpretation of satellite measurements of HCHO and CHOCHO.

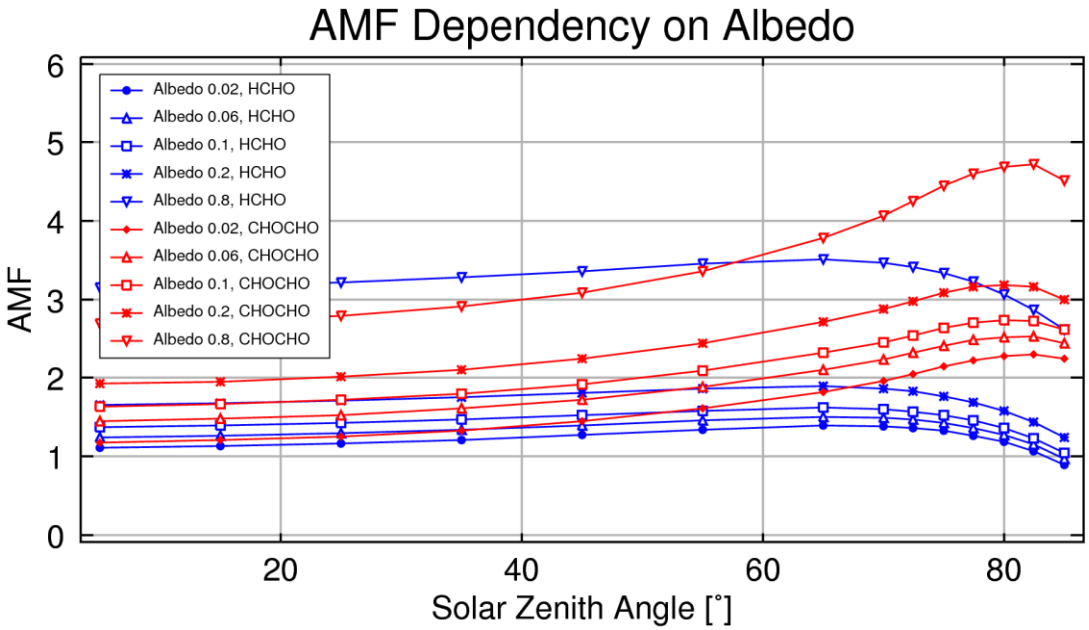

Figure 5-22: AMF in the visible (446 nm, CHOCHO) and the UV (336 nm, HCHO) for different albedos assuming the standard profile shape.

In the UV, the difference between the AMF for e.g. snow (0.8) and that for water surfaces (0.05) is more than 200 percent while in the visible deviations up to 150 percent occur. The relative differences are quite independent of the SZA mainly determined by the profile shape. Since the fraction of light passing the lower parts of the atmosphere is decreasing with larger SZAs, the fraction of reflected photons is also getting smaller. This has particularly an impact on the AMF for profiles with a peak near to the surface.

Overall, a good estimate is needed for surface albedo at the wavelengths used for the retrieval as a function of location and season. Such a database has been derived from GOME data by Koelemeijer et al. [2003] and from TOMS measurements by Tanskanen et al. [2003]. In this study, the first one is used in the visible, the latter one in the UV (see section 5.4).

5.2.2.4 Aerosols

The effect of aerosols on HCHO columns measured by satellite is twofold: HCHO within or below an aerosol layer will be seen with reduced sensitivity. HCHO situated above a reflecting aerosol such as a maritime type will be seen with enhanced sensitivity (see Figure 5-23). Therefore, it is useful to know the vertical distribution of aerosols and also the composition, as absorbing and reflecting aerosols will have different effects on the radiative transfer.

Here the impact of aerosols on satellite observations is investigated using the LOWTRAN database [Shettle and Fenn, 1976]. This database uses three different aerosol types (rural, urban and maritime). The extinction is defined by the visibility (50, 23, 10, 5, and 2 km). The relationship between the total extinction and the visibility for the human eye is given by the empirical *Koschmieder* equation:

$$V = \frac{3.912}{\varepsilon_{total}} \tag{5.3}$$

where V is the visibility in km and ε_{total} the total extinction at 550 nm. It should be noted that even though this equation comprises the total extinction ε_{total}, the visibility is dominated by the aerosol content. A pure Rayleigh atmosphere has a visibility of about 300 km (see e.g. http://irina.eas.gatech.edu/lectures/Lec26.html).

The following Figure 5-23 shows the satellite AMF for the urban and maritime aerosol having different visibilities. The optical properties of the rural aerosol are quite similar to those of the maritime type and therefore not shown here. The relative humidity in the boundary layer was set to 70 percent.

The variation of the AMF for different aerosol types is from 6 to 60 percent in the UV increasing with decreasing visibility. Actually, for high albedos the difference can reach up to 150 percent which should be taken into account for polluted regions in high latitudes during wintertime. Due to the wavelength dependency of the aerosol extinction, the deviation is a bit smaller in the visible. However, sensitivity studies carried out in this study show that for an urban aerosol with two kilometres visibility, the sensitivity of GOME and SCIAMACHY to HCHO in the lowest kilometres is close to zero.

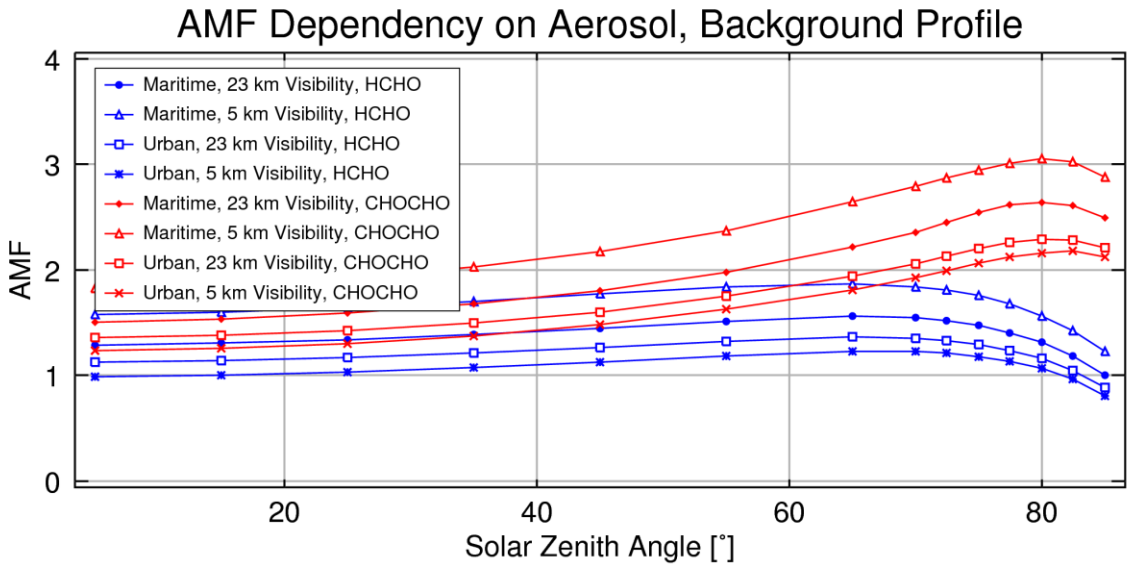

Figure 5-23: AMF in the visible (446 nm, CHOCHO) and the UV (336 nm, HCHO) for different aerosol types and visibilities (aerosol extinction). The visibility is always related to the extinction at 550 nm.

5.2.2.5 Clouds

The effect of clouds on the HCHO retrieval is similar to that of aerosols, only stronger: clouds effectively shield the atmosphere below from view and enhance the sensitivity to any absorption above them, in particular close to the cloud top which is illustrated in Figure 5-24 for a reflective cloud. Further information on the influence of clouds on satellite or airborne observations can be found e.g. in Wang et al. [2005]. Figure 5-25 which has been adapted from this study illustrates the different sensitivities for nadir and zenith-sky airborne observations in case of cloudy and non-cloudy conditions. It is notable that for both viewing geometries the block air mass factors are close to zero below and in the lower part of the cloud, while they are strongly enhanced above and in the upper part of the cloud.

Two different approaches can be used to account for the impact of clouds: either a simple cloud screening algorithm can be used to select only data below a certain cloud cover threshold or the impact of clouds can be modelled in detail based on measurements of cloud fraction and cloud top height and assumptions on the amount of HCHO below and within the cloud. Here, a simple threshold technique was used based on the FRESCO cloud cover product [Koelemeijer et al., 2001]. A rather large maximum cloud cover of 20 percent has been chosen to avoid large data gaps in the Northern Hemisphere in winter and spring. The remaining impact on the retrieved vertical column has been estimated according to Boersma et al. [2004] to less than 30 percent for most scenarios.

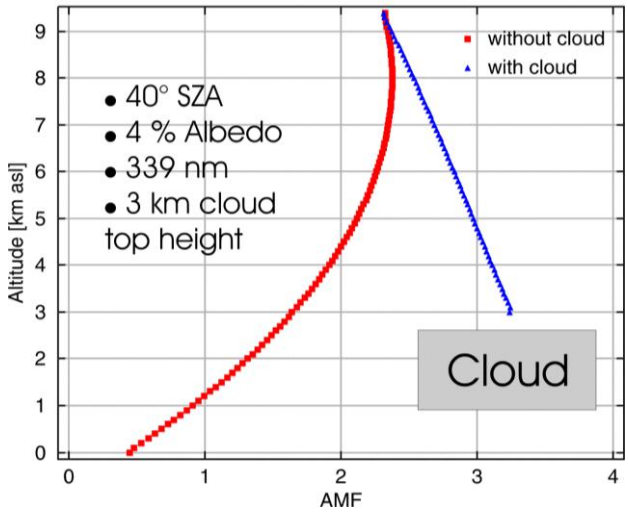

Figure 5-24: The weighting function or block air mass factor for HCHO with and without a reflective cloud. The sensitivity to HCHO above clouds is strongly enhanced, while there is no potential to detect trace gas amounts below or in this cloud.

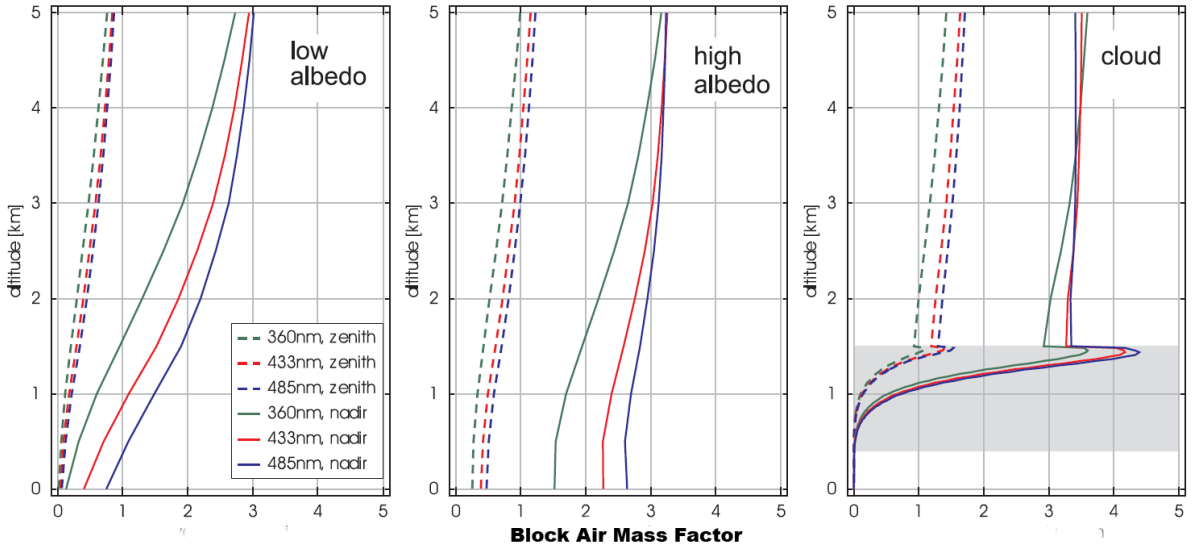

Figure 5-25: Block air mass factors for clear sky, low albedo (0.05, left), clear sky and high albedo (0.8, middle) and with a cloud (right). The shaded area indicates the position of the cloud between 0.4 and 1.5 km altitude having an optical depth of 25. Solid lines are for the nadir viewing direction, the broken lines for zenith observation. All curves are for aircraft measurements at a flight altitude of 11 km (adapted from [Wang et al., 2005]). According to the figure, a small signal should be observed in the zenith direction if there is a trace gas above the cloud or in its upper part, but not if it is within or below the cloud. As the nadir weighting function decreases much slower within the cloud, the ratio between the measurements in nadir and zenith direction can be used to estimate if the trace gas is above, below or within the cloud.

5.3 Profile retrieval from MAX-DOAS observations

As a major outcome of this work, a new algorithm for the analysis of ground-based MAX-DOAS measurements was developed: BREAM – **Bre**mian **A**dvanced **M**AX-DOAS Retrieval Algorithm. The aim of this algorithm is to derive vertical profiles as well as the tropospheric column of selected trace gases from the off-axis measurements. The following section 5.3.1 describes the mode of operation of BREAM. After that a characterisation is presented (section 5.3.2) which is followed by a discussion of the contribution of the different error sources to the overall error (section 5.3.3). In section 5.3.4, some validation results are shown exemplarily and this chapter ends with a summary (Section 5.3.5).

5.3.1 Structure of BREAM

BREAM comprises three steps to calculate the tropospheric vertical profile for the trace gas of interest, each one described in detail below. An illustrated overview of these three steps is given in Figure 5-26.

As direct input for the BREAM algorithm, the differential slant columns of the selected absorber and also of the oxygen dimer O_4 are retrieved applying the DOAS method to the measured spectra (see sections 3.2 and 5.1.19). Examples of one day for slant columns including all viewing directions of HCHO and O_4 are shown in the upper panel of Figure 5-27.

The **first step** of the retrieval is motivated by recent studies (e.g. [Wagner et al., 2004; Wittrock et al., 2004]) and was already indicated in section 5.2.1.1: The measured slant column of the oxygen dimer O_4 (O_2-O_2) can be used to derive aerosol information, i.e. the extinction profile and to some extent also the aerosol type in the atmosphere. This is possible because the O_4 profile can be exactly calculated from the temperature and pressure profiles. The knowledge of the aerosol properties is essential to retrieve the correct amount of other absorbers (e.g. HCHO). As shown before, already a relatively small error in the aerosol extinction, can lead to large errors in the calculated vertical column or the trace gas amount in a given layer ([Oetjen, 2002; Heckel et al., 2005] and section 5.2.1.1.4).

The BREAM algorithm uses the radiative transfer model SCIATRAN ([Rozanov et al., 2000; Rozanov et al., 2001; Rozanov et al., 2002]) described in section 4.1 to calculate O_4 slant columns based on meteorological data like albedo, pressure and temperature and also applying an *a priori* aerosol extinction profile. Afterwards, in an iterative process, this extinction profile in its total quantity as well as in its structure - i.e. the height of the boundary layer - is scaled until measured and modelled differential slant columns of O_4 are in agreement. The quality of the agreement is evaluated by applying two parameters: The correlation between the measurement and the modelled columns (which is mainly influenced by the height of the boundary layer) and the mean deviation of those (mainly modulated by the extinction). In general, for cloud-free scenarios a correlation better than 0.9 and a deviation smaller than 10 percent between model and measurement can be obtained for all viewing directions. The error of the retrieved total aerosol optical depth (AOD, the integrated extinction profile) has been estimated to be less than 0.05 (see section 5.3.4.1). The middle panel of Figure 5-27 shows the AOD retrieved from the given O_4 differential slant columns.

The **second step** comprises the calculation of so-called block air mass factors (see section 4.3) with respect to the chosen absorber using the afore obtained aerosol information. Again SCIATRAN in its full-spherical mode is applied. Block air mass factors are air mass factors for individual layer heights of the absorber. The overall air mass factor is simply the average of the block air mass factors weighted by the distribution of the trace gas. The

striking advantage of this concept is, that it allows describing the relation between the measurement and the absorber's profile in the atmosphere as a linear system:

$$\mathbf{y} = \mathbf{K} \bullet \mathbf{x} \tag{5.4}$$

where

$$\mathbf{K} = \frac{\partial \mathbf{y}}{\partial \mathbf{x}} \tag{5.5}$$

with **y** as the measurement vector, i.e. the set of differential slant columns under different elevation angles used for the profile retrieval, **x** the desired profile and **K** as the weighting function matrix depending on the block air mass factors.

As in many inversion problems, there is no unique solution to the inversion of equation (5.4) , because the problem is underdetermined or ill-posed. To solve this linear system the well-known and in atmospheric chemistry long-established method of Optimal Estimation by Rodgers [Rodgers, 1976; Rodgers, 1990] has been utilised in BREAM in the **third step** of the algorithm (see Figure 5-26). With this, the profile **x** is determined by adding *a priori* information:

$$\mathbf{x} = \mathbf{x_a} + (\mathbf{K^T S_\varepsilon}^{-1}\mathbf{K} + \mathbf{S_a}^{-1})^{-1}\mathbf{K^T S_\varepsilon}(\mathbf{y} - \mathbf{K x_a}) \tag{5.6}$$

where $\mathbf{x_a}$ is the *a priori* profile, and $\mathbf{S_\varepsilon}$ and $\mathbf{S_a}$ the error covariance matrices for the *a priori* and the measurements (the differential slant columns $\mathbf{y}=(y_1, ..., y_n)$ of the different viewing geometries), respectively. **K** is related to the block air mass factors by:

$$K_{ij} = \frac{DBAMF_{ij} \cdot p_j \cdot R \cdot N_A}{T_j} \cdot \Delta h \tag{5.7}$$

where p_j and T_j are the pressure and temperature in the layer j, respectively, R the molar or universal gas constant, and N_A the Avogadro number. $DBAMF_{ij}$ is the differential block air mass factor relative to the reference measurement in layer j and corresponding to the i-th measurement y_i. Δh is the thickness of the layer j.

The *a priori* profile $\mathbf{x_a}$ and the covariance error matrices for *a priori* $\mathbf{S_a}$ and measurements $\mathbf{S_\varepsilon}$ are crucial parameters in the retrieval algorithm. Since the retrieval problem is underdetermined, one very simple *a priori* profile for all three trace gases (HCHO, CHOCHO and NO_2) is used according to findings given in 5.2.2.1 to avoid solutions which are mathematically true, but physically meaningless: The profile is given in volume mixing ratio with decreasing values from 0.1 ppb_V in the surface level to 0.01 ppb_V in the top level (between 5 and 10 km depending on the measurement site). In case of the site Mérida (see section 2.3.2.3) a constant *a priori* profile is chosen due to the very high altitude.

The error covariance matrices are set as follows:

- The diagonal values of $\mathbf{S_\varepsilon}$ are allocated with the statistical errors from the trace gas DOAS retrieval. The other elements are set to zero.
- The diagonal values of $\mathbf{S_a}$ have been empirically determined to be 0.2 for HCHO and NO_2 while it is 0.1 for CHOCHO. According to Schofield et al. [2004] and Hendrick et al. [2004] this matrix can act as a tuning parameter for the retrieval. Increasing the values in the diagonal boosts the independency from the initial

profile and thus the information content of the retrieval (see section 5.3.2). However, depending on the DOAS retrieval errors sometimes unwanted oscillations in the retrieval occur. Extra-diagonal terms in $\mathbf{S_a}$ account for correlations between the trace gas content in adjacent layers and further stabilise the algorithm. Based on Barret et al. [2003] the terms were added as Gaussian functions:

$$S_{aij} = \sqrt{S_{aii} S_{ajj} \exp(-\ln(2)((z_i - z_j)/\gamma)^2)} \tag{5.8}$$

where z_i and z_j are the altitudes of i-th and j-th level, respectively. γ is the half width at half maximum of the Gaussian function. The value was determined empirically to be 25 m for all trace species.

The output of the retrieval is the profile of the selected absorber. A typical example for the evolution of the HCHO profile during the course of a day is given in Figure 5-27 in the lower panel: Formaldehyde is located mainly in the lower layers, while the diurnal variation shows maximum values in the afternoon.

The method of the Optimal Estimation can only be applied for an optically thin atmosphere: The extinction of the light is mainly caused by scattering in each layer and consequently the radiative transfer is independent of the concentration of the absorber (see section 4.3). This constraint is fulfilled for virtually all absorbers that can be retrieved via the DOAS method: NO_2, all halogen oxides, formaldehyde and glyoxal, but fails e.g. for ozone in the ultraviolet spectral range or for line absorbers such as H_2O.

Similar approaches have been applied to zenith-sky measurements of mainly NO_2 for several years [Preston et al., 1997; Hendrick et al., 2004; Schofield et al., 2004] utilising measurements for a large set of SZAs. Bruns [2004] has introduced an analogous method to retrieve NO_2 profiles from airborne multi-axis DOAS (AMAXDOAS) data. However, the algorithm BREAM comprises several modifications and conceptual differences:

1. Using O_4 measurements to retrieve information on the aerosol content in the troposphere.
2. Using the same height grid (typically 50 m) for all retrieval steps to avoid any errors due to e.g. interpolation.
3. Using differential block air mass factors which avoid any assumptions on the slant column in the reference spectrum. However, one supposition is here that the profile of the trace gas of interest does not change for the full set of measurements used for the profile retrieval.
4. Adding extra-diagonal terms to S_a to account for correlations between the trace gas amounts in adjacent layers.
5. Calculating the differential block air mass factors with SCIATRAN for the exact viewing geometry of the measurement: No interpolation in solar zenith angle, line of sight or relative azimuth.

The algorithm was designed to be quite flexible in terms of the viewing geometry, i.e. BREAM is also able to analyse data from air- and spaceborne UV/vis measurements. As the full set of differential block air mass factors is calculated within one SCIATRAN run, each profile requires merely one minute computing time on a standard PC. This permits the analysis of long time-series.

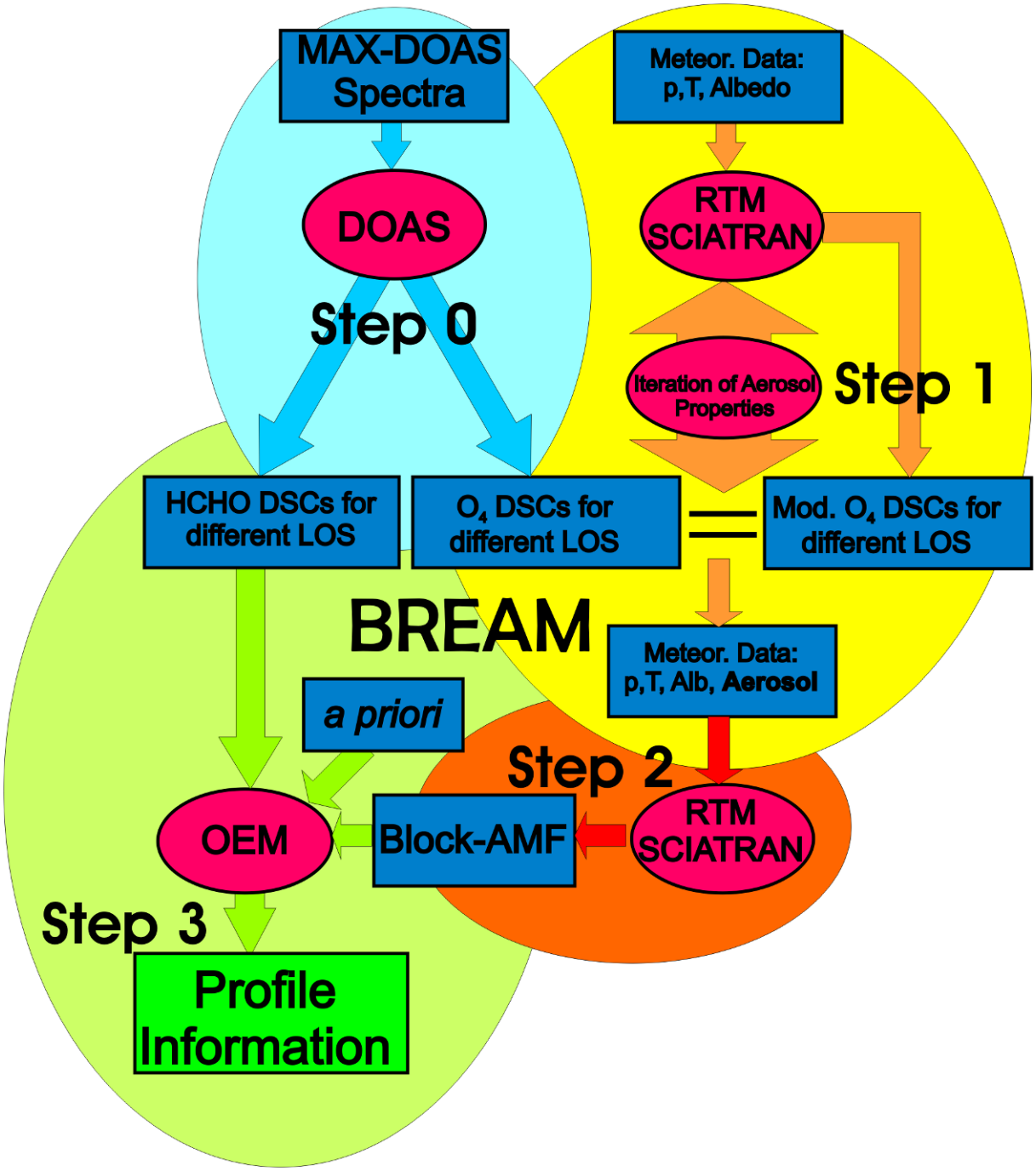

Figure 5-26: Flowchart of the different retrieval steps within BREAM (here illustrated for formaldehyde).

Various sensitivity studies about information content and stability of the profile retrieval have been performed and some of them will be shown below. In general, it is an advantage in agreement with findings from Bruns et al. [2004] to use several wavelength regions simultaneously to benefit from the different effective light paths at different wavelengths. This is possible for e.g. NO_2 but unfortunately not for HCHO or for CHOCHO (see cross-sections in Figure 5-1 and Figure 5-2) and will not be demonstrated here.

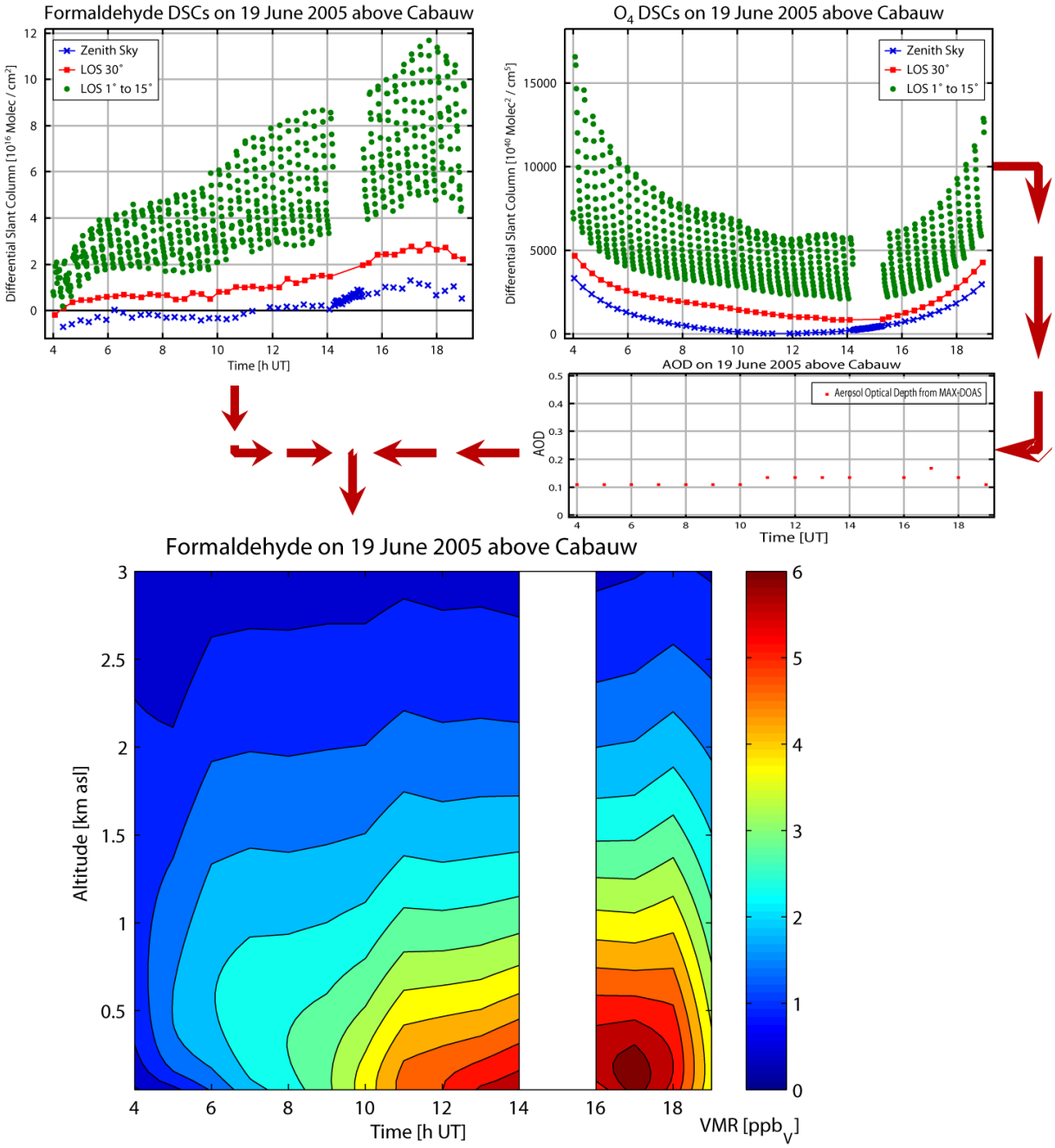

Figure 5-27: Example of input data and results for BREAM. The profile information was retrieved in temporal steps of one hour comprising in this case about three full scans of the viewing angle sequence.

5.3.2 Characterisation of the retrieval

In this chapter, the information content of the profile retrieval BREAM will be investigated:

The quality of the retrieval can be described with the averaging kernel matrix **A**. It is derived according to [Rodgers, 1990; Rodgers, 1998; Rodgers, 2000] by:

$$\mathbf{A} = \frac{\partial \mathbf{x}}{\partial \mathbf{x}_{\mathbf{true}}} = (\mathbf{K}^{\mathbf{T}}\mathbf{S}_{\boldsymbol{\varepsilon}}{}^{-1}\mathbf{K} + \mathbf{S}_{\mathbf{a}}{}^{-1})^{-1}\mathbf{K}^{\mathbf{T}}\mathbf{S}_{\boldsymbol{\varepsilon}}\mathbf{K} \tag{5.9}$$

where $\mathbf{x}_{\mathbf{true}}$ is the true atmospheric profile. Therefore the averaging kernels, the rows of the **A** matrix, give the relationship between the retrieved profile **x** and the true atmospheric profile $\mathbf{x}_{\mathbf{true}}$:

$$\mathbf{x} = \mathbf{x_a} + \mathbf{A}(\mathbf{x_{true}} - \mathbf{x_a}) + \text{ Error terms} \tag{5.10}$$

In an ideal case, **A** is equal to the identity matrix and the retrieved profile **x** tends towards the true profile $\mathbf{x}_{true}$. Each row of the matrix **A** represents the averaging kernel of one layer of the height grid. The elements within this row define the relative weighting of the true mixing ratio at each level compared to the retrieved mixing ratio. Consequently, the rows of **A** are peaked functions and the retrieved profile is only a smoothed perception of the true profile. Essentially, one way to calculate the vertical resolution in the layer *j* of the retrieval is to take the full width half maximum (FWHM) of the main peak in the row *j* of the averaging kernel matrix **A**.

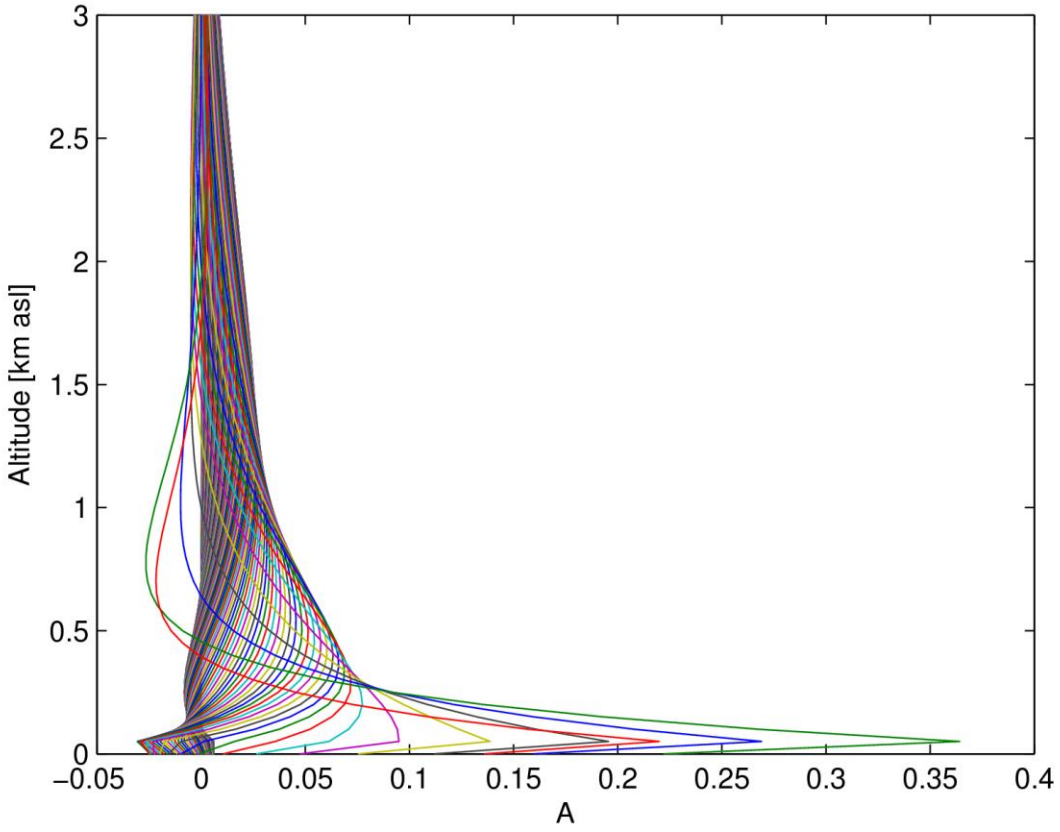

Figure 5-28: Averaging kernel matrix **A** for MAX-DOAS observations in Cabauw on 19 June 2005 using measurements from 1° to 15° in 1° steps and from 30° elevation angle having a solar zenith angle of about 35°. This plot illustrates the high sensitivity to the lowermost layers while for altitudes more than one kilometre there is only very little height information. Here, the trace T_A of **A** is about 2.8 (see text below).

Figure 5-28 shows exemplarily the averaging kernel matrix for one set of measurements of formaldehyde in Cabauw (see section 2.3.2.5.4) on 19 June 2005. It illustrates the typical behaviour of the matrix for ground-based MAX-DOAS observations. The FWHM of the averaging kernels is rapidly increasing with altitude from about 150 m in the lowest part of the troposphere to about 2 km above 1.5 km altitude. Thus, there is only limited profile information on the trace gases in the free troposphere at least for measurement sites near to sea level. Consequently, possible amounts of the trace gas in higher layers due to convection will be retrieved as an offset in the volume mixing ratio in altitudes above the boundary layer.

The trace of the matrix **A** (T_A) determines the number of pieces of independent information with respect to the height layers, i.e. the degrees of freedom of this measurement. A typical scanning time for the ground-based

MAX-DOAS observations within BREDOM (around 20 minutes) together with a moderate aerosol content yields a number for T_A of about two to three. The whole range includes results from about 1.5 for low visibility, i.e. high aerosol up to about five when also large solar zenith angles (SZA > 75°) with very good visibility are considered. The latter one is caused by the rapid changes in the effective light paths for different lines of sight at high solar zenith angles. As pointed out in the sections 5.2.1.1.4 and 5.2.2.4, aerosols reduce the sensitivity in particular in the lowest layers. Thus, the 'degrees of freedom for signal' [Rodgers, 2000] are also scaled down.

Data subsets with different combinations of viewing angles of 19 June 2005 in Cabauw have been investigated to illustrate the effect of the number of lines of sight on the information content within the retrieval algorithm. It turns out that the usage of 1° steps in elevation angle (in total 16 measurement points: 1° to 15° and 30°) yields a gain of about 0.8 to the information content compared to scans comprising four off-axis angles. This has been confirmed by using data sets from other sites. Contrariwise, the effect on the tropospheric column is small: The difference is less than 3 percent for the aforementioned measurement cycles.

5.3.3 Error analysis

The total error of the retrieved profile has three components:

1. The error due to the measurement noise introduced by the covariance matrix $\mathbf{S}_\varepsilon$.
2. The error due to smoothing of the true profile. This is related to the averaging kernel matrix **A**.
3. The error due to systematic errors in the forward model.

The first part is the most intuitive one. The measurement error is defined as:

$$\mathbf{S_m} = \mathbf{G}\mathbf{S_\varepsilon}\mathbf{G}^\mathbf{T} \tag{5.11}$$

where **G** is the so-called contribution function matrix, which expresses the sensitivity of the retrieved profile to changes in the measured trace gas differential slant columns and is defined as:

$$\mathbf{G} = \frac{\partial \mathbf{x}}{\partial \mathbf{y}} = (\mathbf{K}^\mathbf{T}\mathbf{S_\varepsilon}^{-1}\mathbf{K} + \mathbf{S_a}^{-1})^{-1}\mathbf{K}^\mathbf{T}\mathbf{S_\varepsilon}^{-1} \tag{5.12}$$

The smoothing error $\mathbf{S_s}$ is given according to [Rodgers, 2000] by:

$$\mathbf{S_S} = (\mathbf{A}-\mathbf{I})\mathbf{S}_{\hat{\mathbf{x}}}(\mathbf{A}-\mathbf{I})^\mathbf{T} \tag{5.13}$$

where **I** is the identity matrix. To estimate the actual smoothing error, knowledge of the true state is needed, which is of course not available. Instead of that, the covariance of the ensemble of states about the mean state is introduced: $\mathbf{S}_{\hat{\mathbf{x}}}$. Thus, to estimate the smoothing error, the variability of the climatological profiles must be known. Since there is not a climatology of highly resolved profiles for HCHO and a fortiori not for CHOCHO available, a simple approach is taken here: Based on profile observations of [Junkermann, 2003] the variance has been estimated to 30 percent of the scaled initial profile for all altitudes.

The last error term, the forward model error $\mathbf{S_f}$ is the propagation of errors due to inadequate modelling into the retrieval. Possible error sources are e.g.: Aerosol loading, surface albedo, pointing errors.

$\mathbf{S_f}$ is defined by:

$$\mathbf{S_f} = \mathbf{G}\mathbf{K_o}\mathbf{S_o}\mathbf{K_o}^\mathbf{T}\mathbf{G}^\mathbf{T} \tag{5.14}$$

where **G** is again the contribution function matrix, $\mathbf{K_o}$ is the sensitivity to variations of the model parameter *o*, and $\mathbf{S_o}$ is the covariance matrix of *o*. Since it is in most cases difficult to give a reasonable assumption of $\mathbf{S_o}$, sensitivity studies for the most important parameters were carried out to calculate the forward model error $\mathbf{S_f}$.

The following Figure 5-29 illustrates the influence of some important parameters on the retrieved profile. The calculations in this case have been carried out using MAX-DOAS observations of formaldehyde in Cabauw on 19 June 2005. However, the results presented here are believed to be representative for other sites and/or other trace gases, too. In addition, the effects of temperature and pressure were investigated but found to play a minor role in the profile retrieval (less than 2 percent for all altitudes). Thus, they are not shown in the graph.

The total forward model error can be estimated from the graph to less than 15 percent for a single layer, assuming the worst case: All errors change the profile in the same direction. For the tropospheric vertical column the uncertainty has been estimated to be less than 8 percent, reflecting the fact that some parameter errors have different effects at different altitudes (e.g. aerosol). It is notable, that the error with respect to the albedo might increase strongly for varying surface reflectance near to the measurement site, e.g. a mixture of snow and open water which can be regularly observed in Ny-Ålesund in spring and fall. Therefore, it is preferable to have all MAX-DOAS sites equipped with a web camera in order to obtain a good estimate of the albedo.

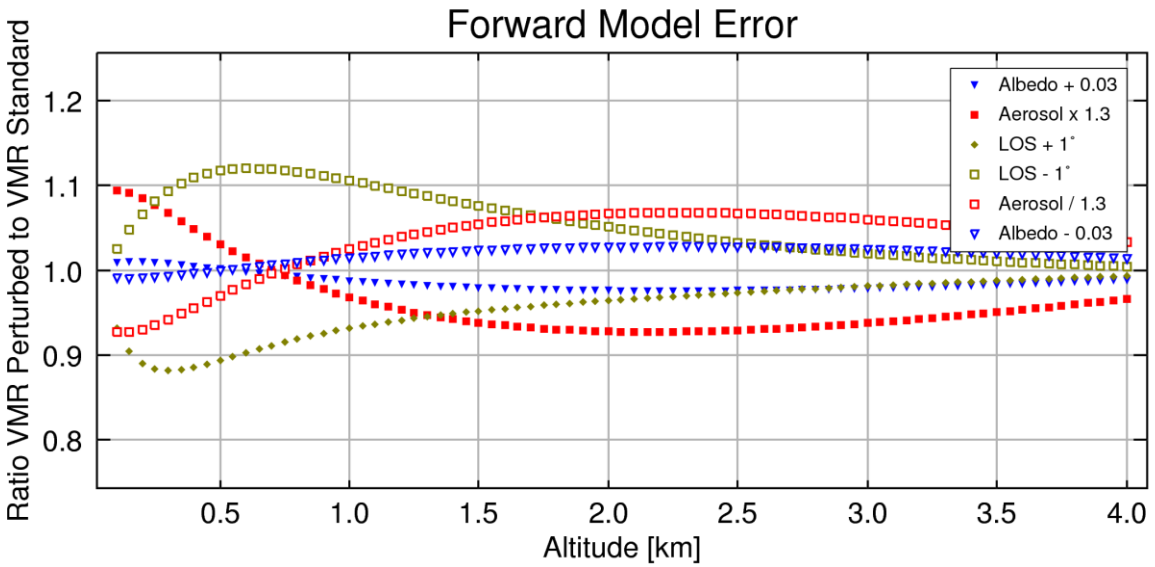

Figure 5-29: Ratio of the profile retrieved with a perturbed parameter to the profile retrieved with basic settings. These calculations have been carried out using MAX-DOAS observations of HCHO above Cabauw on 19 June 2005 during noon (see also Figure 5-28).

The following Figure 5-30 illustrates the error budget for a profile retrieved with the same differential slant columns utilised in Figure 5-28. From that, it becomes clear that the smoothing error is the main source of uncertainty for all height levels. For altitudes higher than 3 km the total error becomes larger than the expected natural variability.

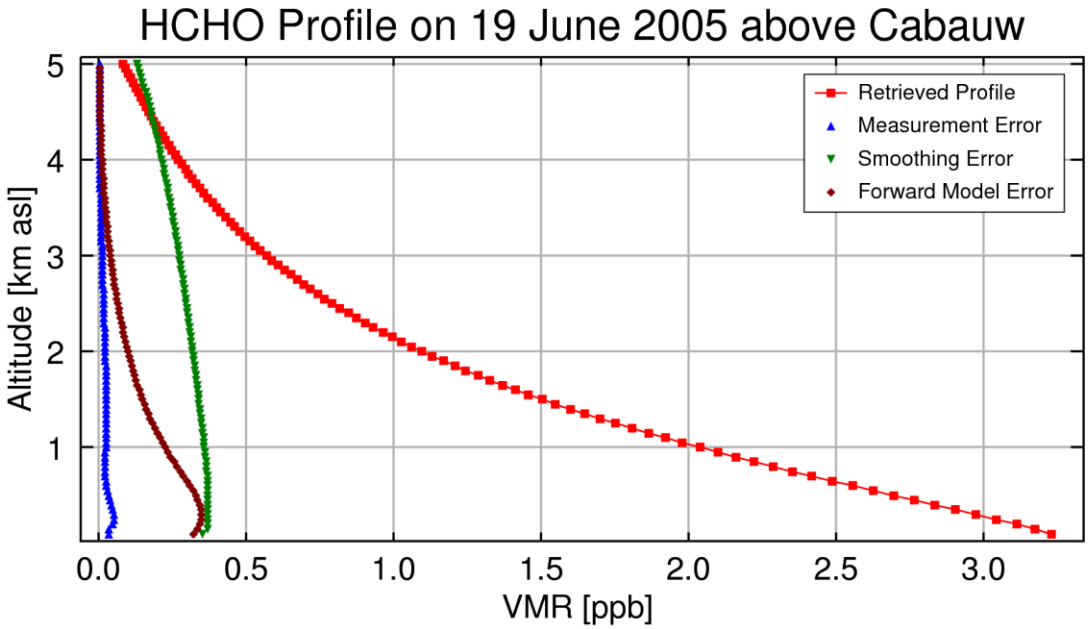

Figure 5-30: Retrieved profile for HCHO observation on 19 June 2005. In addition, the absolute errors for the retrieval are shown.

5.3.4 Validation of BREAM

In order to investigate the quality of the retrieval algorithm BREAM, different complementary data sets have been utilised here to validate the calculated aerosol optical depths, trace gas mixing ratios at ground, vertical columns and the profiles.

5.3.4.1 Validation of aerosol measurements

Figure 5-31 illustrates the quality of the retrieved aerosol data. A comparison of the aerosol optical density measured by three different instruments during the first FORMAT campaign in 2002, is shown: Measurements with a sun photometer from the nearby site ISPRA obtained from the AERONET as well as with a MICROTOPS-instrument [Junkermann, 2003] together with the aerosol optical density retrieved from the O_4 measurements with a MAX-DOAS instrument. The general agreement between the three instruments is excellent. The deviation between MAX-DOAS and the sun photometer on 31 July 2002 might be explained with the distance of about 50 km between the measurement sites and not very favourable weather conditions on that day. A similar comparison has been carried out with data from Ny-Ålesund where also good agreement was found.

From these validation studies the conclusion is drawn that the assumption of 30 percent uncertainty for the aerosol extinction (see section 5.3.3) is reasonable and should reflect the maximum error introduced by this parameter into the retrieval.

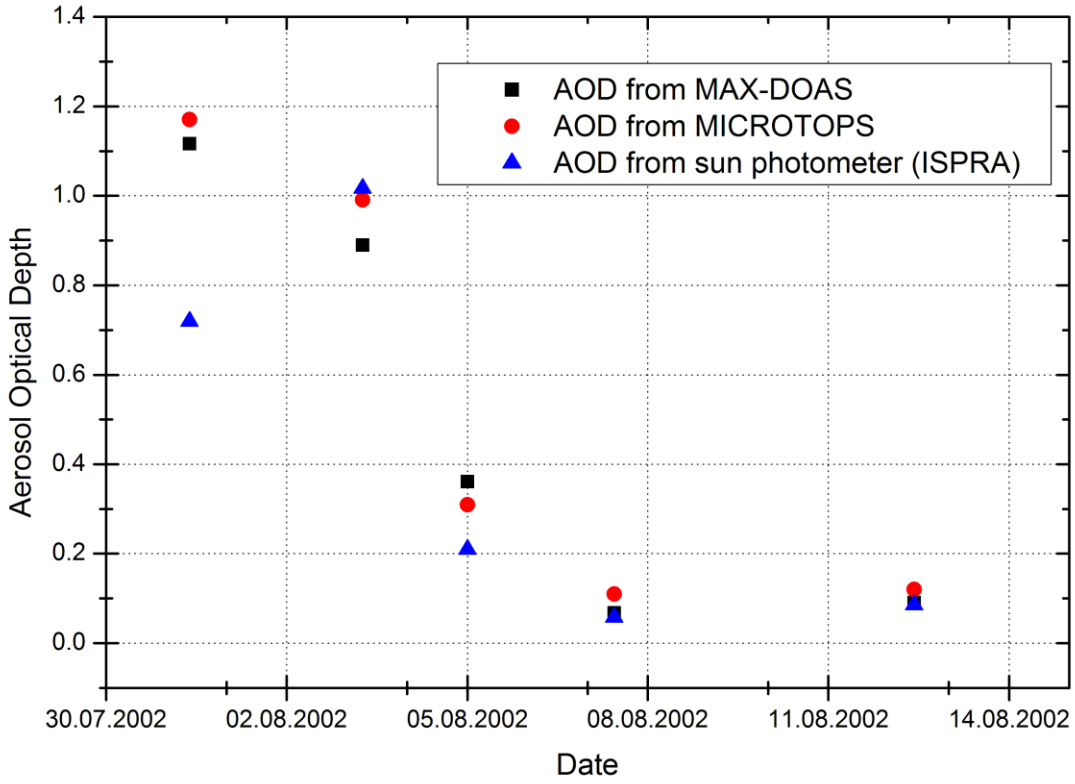

Figure 5-31 Comparison of different aerosol measurements at Alzate, Italy. The MAX-DOAS results have been retrieved using BREAM.

5.3.4.2 Validation of trace gas mixing ratios near to the ground

The measurement campaigns in Alzate (see section 2.3.2.5.3) and Cabauw (see section 2.3.2.5.4) have provided the opportunity to compare the results of BREAM with other instruments. This was possible in Alzate for NO_2 and HCHO with *in situ* [Junkermann, 2003; Ordonez, 2003] and Long-Path DOAS [Hak, 2005] observations while in Cabauw only NO_2 was monitored with an *in situ* instrument [Brinksma, 2005] near to the ground. In the following only those MAX-DOAS retrieval results will be shown where the first retrieval step (see section 5.3.1) yields a good correlation (> 0.9) between observed and modelled O_4 which signified good weather conditions without clouds. The temporal resolution was fixed to one hour. The mixing ratio of the three lowermost layers (0 – 125 m) have been averaged and then compared to results from the other measurement techniques.

Figure 5-32 shows the various measurements of the HCHO mixing ratio close to the ground in Alzate in 2002 and 2003. In general, a good agreement was found. The day-to-day as well as the diurnal variation is captured by all instruments in a similar way. The MAX-DOAS measurements yield the largest absolute values, while from the Long-Path observations somewhat higher amounts than from the *in situ* instrument which applies the fluorimetric Hantzsch reaction technique were derived. This might be explained with a negative gradient towards the surface in the lowermost part of the boundary layer [Junkermann, 2003]. Another possible explanation is a local source in the viewing direction of the MAX-DOAS instrument: A small forest was located near to the measurement site in the same direction as the off-axis port of the instrument. However, one should take into account, that

even between *in situ* measurements at one site only a reasonable agreement was found in several studies. E.g. [Hak et al., 2005] have reported 11 percent deviation between five different Hantzsch instruments, while the difference between Hantzsch and optical methods was found to be 15 percent. This intercomparison has been carried out during the first FORMAT campaign at the site Bresso airport (see Figure 2-10).

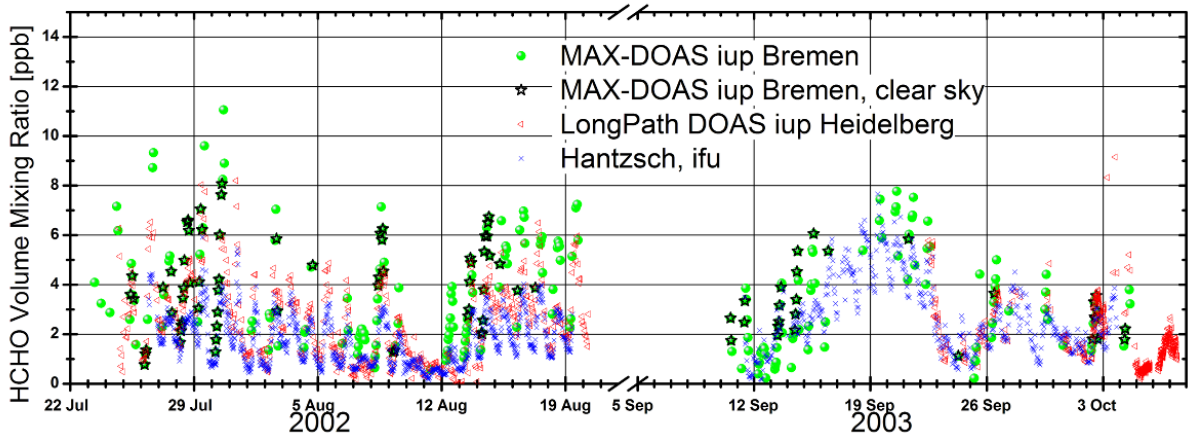

Figure 5-32: HCHO mixing ratios obtained during the FORMAT campaigns in 2002 and 2003 from a Hantzsch *in situ*, a Long-Path DOAS, and a MAX-DOAS instrument. On clear days a correlation better than 0.85 was found, with MAX-DOAS having about 8 and 15 percent higher values on average than the Long-Path and the Hantzsch instrument, respectively.

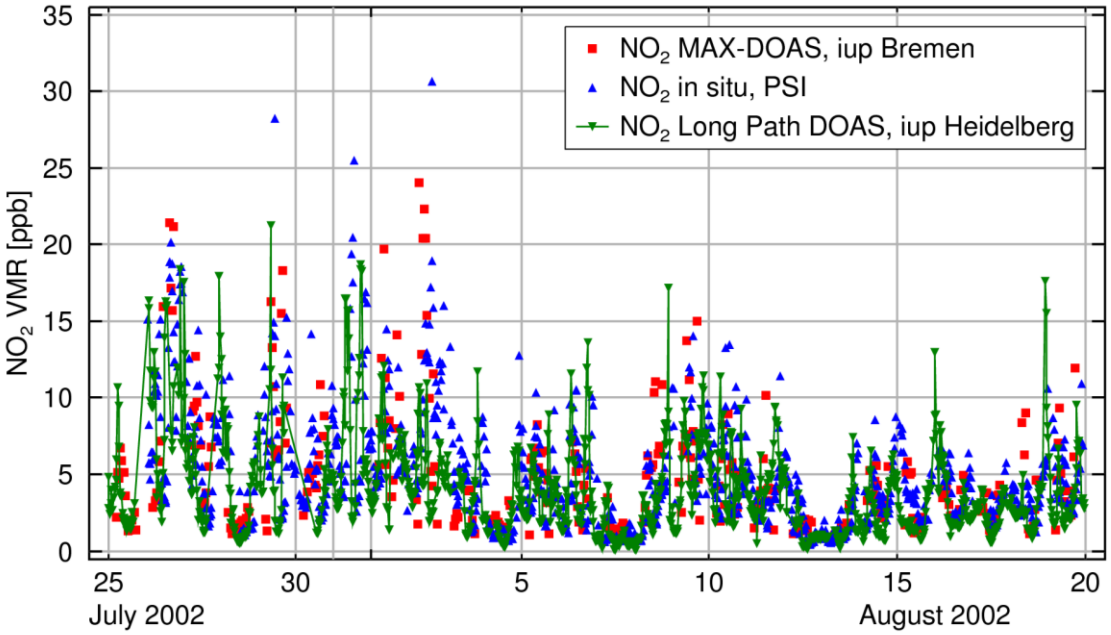

Figure 5-33: NO_2 mixing ratios obtained during the FORMAT campaign in 2002 from an *in situ*, a Long-Path DOAS, and a MAX-DOAS instrument.

Figure 5-33 shows a similar comparison for NO_2. Here again the day-to-day variation agrees reasonably for all instruments. But in contrast to HCHO the MAX-DOAS yields in average lower values than the other techniques possibly caused by the strong positive gradient of NO_2 towards the surface. In general, compared to formaldehyde, nitrogen dioxide shows much higher short-time variability due to local sources (e.g. traffic near to the

measurement site). Thus, one cannot expect a very good agreement between the different measurement techniques used here.

As part of the DANDELIONS campaign in Cabauw from May to July 2005 *in situ* measurements of NO_2 were carried out. Figure 5-34 shows the results of both, *in situ* and the Bremen MAX-DOAS instrument during that campaign. The findings are quite similar to those of the FORMAT campaign. The general agreement is quite reasonable, but some of the short-time variation cannot be captured by the MAX-DOAS measurements.

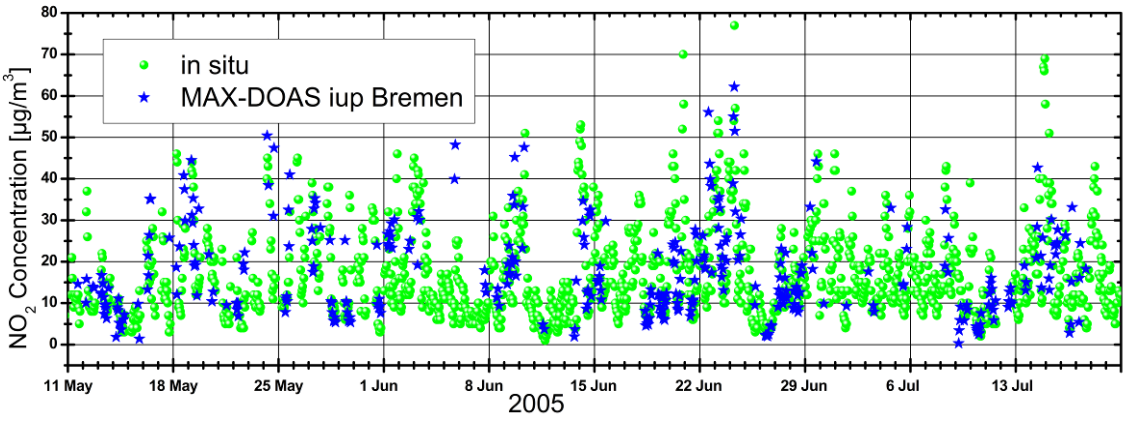

Figure 5-34: NO_2 concentrations near to the surface as observed from *in situ* and from MAX-DOAS.

5.3.4.3 Validation of tropospheric columns

A mobile FTIR system denoted SOF (Solar Occultation Flux) was applied by Chalmers University, Gothenburg measuring total vertical columns of HCHO during the FORMAT campaigns. On two days the system carried out measurements near to Alzate which provides the possibility of the direct comparison to the MAX-DOAS data. The vertical columns of the MAX-DOAS data set have been derived by integrating the retrieved profiles. Again the correlation between both techniques is excellent.

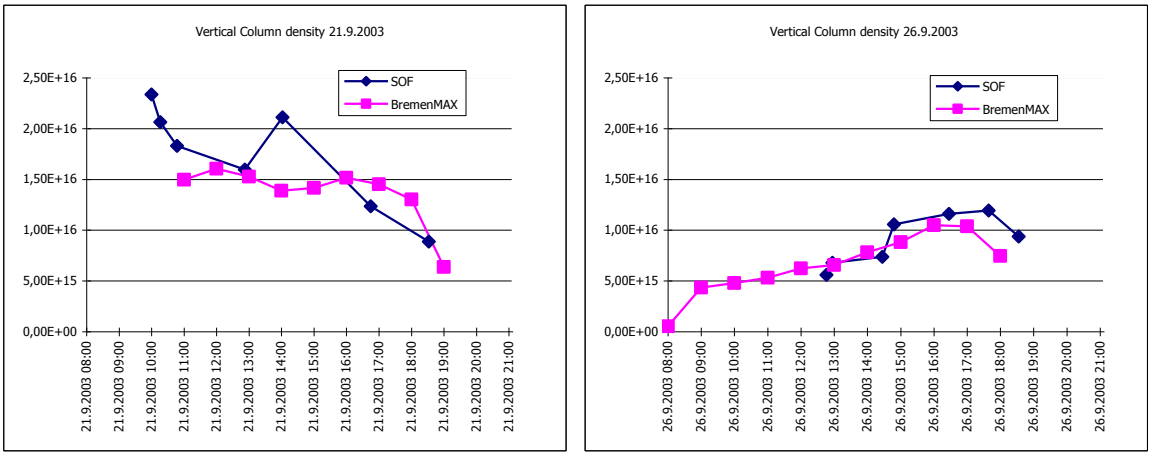

Figure 5-35: Vertical columns of formaldehyde derived from SOF and MAX-DOAS observations. The spatial distance was up to 40 km. These graphs have been adapted from the final FORMAT report.

5.3.4.4 Validation of profiles

During the FORMAT campaigns several airborne measurements of HCHO were performed, some of them near to the measurement site in Alzate. Here two profiles measured with the Hantzsch technique aboard a small microlight aircraft were used to validate the profile retrieval (see Figure 5-36).

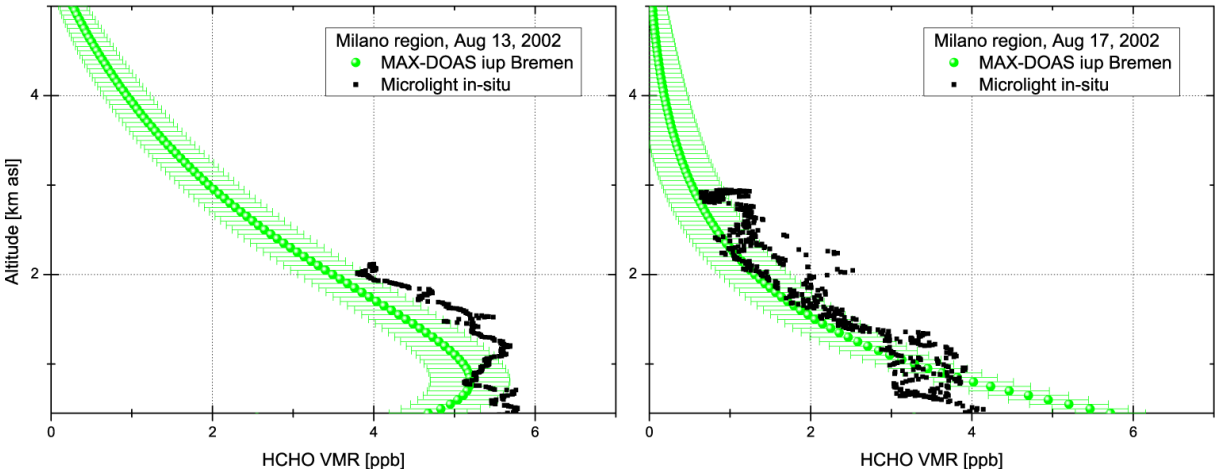

Figure 5-36: Formaldehyde profiles derived with BREAM and obtained from an *in situ* Hantzsch instrument aboard an microlight plane [Junkermann, 2003]. Only MAX-DOAS measurements within a temporal offset of 30 minutes to the airborne measurements were taken into account. The spatial distance was about 20 km. The error bars denote the smoothing and the measurement error in this case.

In general, the MAX-DOAS profiles match the *in situ* profiles quite well. This includes the overall shape and the magnitude of the formaldehyde mixing ratios. The agreement is somewhat poorer in the lowest layers but due to the spatial distance of the measurements a perfect correlation is not expected.

5.3.5 BREAM summary

Section 5.3 has shown that one of the major aims of this study, the development of a profile retrieval algorithm, has been reached with success:

- The utilisation of O_4 observations significantly reduces the uncertainty of the profile retrieval due to the aerosol settings.
- The total error of BREAM has been quantified and was found to be less than 20 percent for altitudes lower than 1.5 km
- It was shown that depending on the focus of the measurements the step size of the elevation angles of the MAX-DOAS observation should be set to 1° between 1° and 15° for profile retrievals, while for the analysis of tropospheric columns in total 4 steps between 2° and 30° seem to be appropriate.
- Comparisons with other measurement techniques have shown a very good agreement with respect to the ground values, the vertical column, and the profile shape.

In summary, it can be said that profiles from MAX-DOAS measurements are suitable to study tropospheric pollutants. Unlike active systems (e.g. Long-Path DOAS), an automated operation is possible. At this point, the only imposed constraint to the retrieval is the necessity of more or less cloud-free situations.

The following Table 11 gives an overview on the standard settings for BREAM as used in this study.

Table 11: Standard settings and typical properties of BREAM in this study. The height of the boundary layer gives the limits in altitude to which the aerosol extinction profile is scaled.

	HCHO	*CHOCHO*
Height grid	0 – 5 km agl, 50 m resolution	0 – 5 km agl, 50 m resolution
Height of boundary layer	0.8 to 2 km	0.8 to 2 km
a priori	0.1 at ground, 0.01 at top	0.1 at ground, 0.01 at top
***a priori* variance**	0.2	0.1
HWHM γ	25 m	25 m
Temporal resolution	1 hour	1 hour
Information content scan	3	2.5
Information content 4 viewing angles	2.2	1.8
Error vertical column	8 %	10 %
Error VMR at ground level	15 %	15 %

5.4 Implementation of AMF look-up tables for satellite observations

As shown in section 5.2.2, the AMF for satellite observations depends strongly on several meteorological boundary conditions. Compared to the standard AMF used in previous studies [Wittrock et al., 2000], deviations by a factor of up to four are possible. This is particularly true for the source regions as they not only have the largest values close to the surface but in addition, are often correlated with regions of enhanced aerosol burden. In order to obtain a realistic global picture of HCHO and CHOCHO, it is therefore necessary to account for all the parameters mentioned above in the radiative transfer calculations. The most practical way to do this is to create pre-calculated tables of AMF for a set of SZAs which depend on time and location and are interpolated to the conditions of an individual measurement. In order to be able to investigate the satellite measurements even on a regional scale, the spatial resolution for the AMF tables was selected to 1° x 1° in latitude and longitude.

The use of tabulated AMF is not a new approach. It has already been successfully applied to NO_2 by Martin et al. [2003], Eskes and Boersma [2003], and Nüß [2005] and also for HCHO by Palmer et al. [2001]. However, with the exception of Nüß [2005], all previous studies have used a modelled or no aerosol scenario, which can lead to significant inaccuracies. On the other hand, in most recent studies the vertical distribution of the trace gas of interest was taken from a 3D-CTM (3-dimensional chemistry and transport model) which then was also compared to the GOME results. Although the algorithm developed here can also be applied in this way, a different approach has been realised here for several reasons:

1. Vertical distributions of HCHO from the LMDz/INCA-Model ([Hauglustaine et al., 2004], see section 6.4) were not available until very recently, and could therefore not be used in the data evaluation. For future stud-

ies, this can be easily implemented in the algorithm. For glyoxal, there are so far only preliminary results from 3D-CTMs (see chapter 0).

2. Previous studies comparing measurements and model results for the vertical distribution show only vague agreement with large deviations for individual comparisons (e.g. [Frost et al., 2002; Kormann et al., 2003]).
3. The spatial resolution of current models is low (typically 2.5° to 3° both, in longitude and latitude). Therefore, point sources such as cities like Milan or Hong Kong cannot be represented properly by the models (see e.g. Figure 6-14).
4. In contrast to the situation for NO_2, atmospheric measurements of HCHO show very similar vertical distributions over a wide range of boundary conditions. The largest values are observed close to the surface in a well-mixed boundary layer [Junkermann, 2003]. Above this layer, concentrations typically decrease towards the tropopause. Only under special dynamical conditions such as outflow from the Indian monsoon different profiles have been observed [Kormann et al., 2003].

Thus, this study uses only three standard profiles based on observations reported in literature, which are assigned to the individual pixels and times based on external information described below. The profiles are shown in Figure 5-19 and a brief description is given here:

1. The standard profile with 450 ppt_V in the boundary layer and a linear decrease to 50 ppt_V at 10 km (e.g. [Heikes et al., 2001; Frost et al., 2002])
2. The urban profile with 1.5 ppb_V in the boundary layer and decreasing amounts to 100 ppt_V at 10 km (e.g. [Kormann et al., 2003; Heckel et al., 2005].
3. The biogenic profile with a peak of 3 ppb_V at the surface, decreasing to 2 ppb_V to the top of the boundary layer, than further sloping to 150 ppt_V at 10 km (e.g. [Kesselmeier et al., 2000]). This profile was also used in case of biomass burning since it is known, that formaldehyde and other oxygenated volatile organic compounds comprise one-half of the initial organic emissions from fires in temperate and boreal ecosystems (e.g. [Goode et al., 1999; Yokelson et al., 1999; Goode et al., 2000; Yokelson et al., 2003]). Thus, high values near to the surface are very likely.

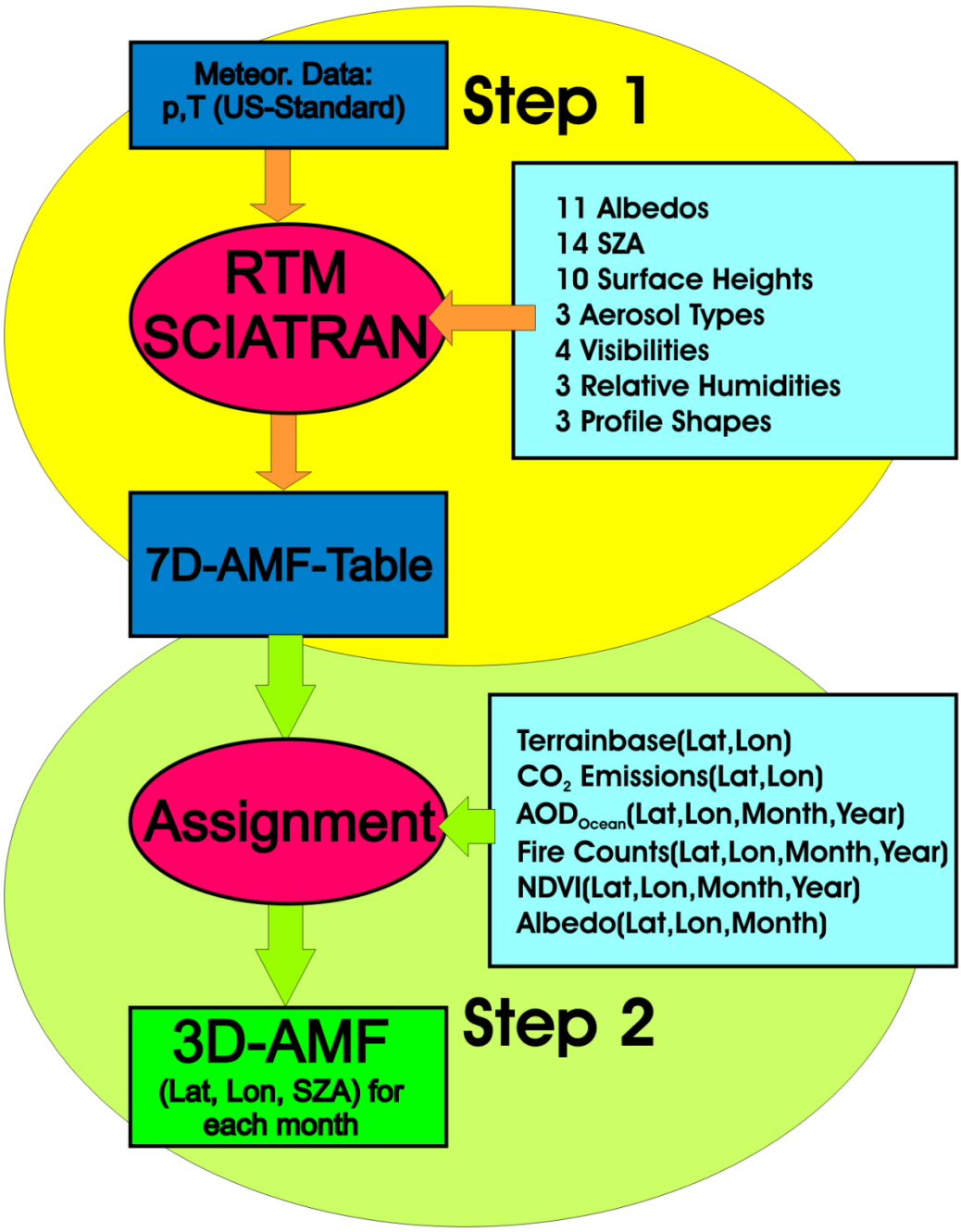

Figure 5-37: Flowchart for the preparation of the AMF look-up tables. Different relative humidities were not applied in step 2 in this study. However, the extension of step 2 to further external information is easy and foreseen for the future.

In general, the algorithm is designed to be flexible with respect to the inputs used and comprises two steps (see Figure 5-37). Most time-consuming is the **first step**, which is the computation of air mass factors with the radiative transfer model SCIATRAN (see section 4.1) based on the selected boundary conditions for albedo, SZA, surface height, aerosol properties and profile shape of the absorber. These are listed in Table 12.

In the **second step**, the different scenarios are assigned to a geographical location/time using external information (see both, Table 11 and Table 12). Particularly, the data sources discussed in chapter 2.4 are used: ATSR for biomass burning counts and AVHRR for the normalised differential vegetation index (NDVI) and the aerosol optical depth (AOD) above oceans. Further data sets comprise EDGAR CO_2 emissions and albedo databases.

As pointed out in section 5.2.2.3 the albedo is the single most important parameter in radiative transfer for satellite observations. Thus, the use of an albedo climatology will significantly improve the accuracy of the HCHO and CHOCHO columns on average. Here two different albedo databases were applied: [Tanskanen, et al., 2003] in the UV for the interpretation of HCHO, while [Koelemeijer, et al., 2003] is applied in the visible wavelenth region for the analysis of CHOCHO. One reason for the implementation of the [Tanskanen, et al., 2003] database is, that it provides daily global maps for the surface albedo which in principle reduce the uncertainty due to this parameter. However, in order to have a consistent view on both trace gases in this study, all results presented in chapter 6 were analysed with monthly averages of the albedo. One should note that for individual measurements quite large errors can be introduced if the actual surface albedo differs from the one in the climatology as a result of snow coverage, land use change or variations in albedo below the resolution of the data base (1° x 1°). This is in particular true since the data bases do not include year-to-year variation.

The other important parameter in the retrieval is the aerosol content in the atmosphere (see section 5.2.2.4). Unfortunately, there is very little information available on the global distribution of aerosols, and the large variability in space and time makes this input particularly difficult to assess. Measurements available show large deviations – e.g. [Myhre et al., 2005] have reported differences up to a factor of three for the retrieved aerosol optical depth of various satellite instruments even above oceans. In [Kinne et al., 2003] a global comparison among models, satellite data, and ground data was carried out. They found largest differences near to expected source regions in case of biomass burning (black carbon) and dust.

For the HCHO and CHOCHO data presented here a simple approach was selected to calculate the AMF based on the aerosol parameterisation of the LOWTRAN model [Shettle and Fenn, 1976] (see section 5.2.1.1.4). Three types of aerosols were distinguished: a maritime aerosol over the oceans, an urban aerosol over industrialised regions and areas with biomass burning and a rural aerosol elsewhere (currently, 70% relative humidity has been assumed for all cases). Complementary data have been used to distinguish between these aerosol types and in addition, four different visibilities: 5, 10, 23 and 50 km.

Table 13 gives an overview how the data sets were applied to assign the pre-calculated AMF. The lowest visibility (5 km) was selected for highly polluted regions (e.g. Northeastern China) taking into account the EDGAR emission data base [Olivier and Berdowski, 2001] for CO_2, and for areas with intense biomass burning (e.g. Indonesia in September 1997) according to the ATSR data. A somewhat higher visibility (10 km) was assigned to areas having moderate values for CO_2 and fire counts while a small CO_2-treshold was used to identify regions with a visibility of 23 km. Data from the Global Aerosol Climatology Project (GACP) [Geogdzhayev et al., 2002; Mishchenko et al., 2002] were utilised to estimate the visibility above oceans taking into account the *Koschmieder* equation (5.3).

Figure 5-38 shows the visibility as obtained for September 2000. In general, the pattern is very similar to MODIS satellite observations of the aerosol optical depth (fine-coarse-mode) recently published [Tie et al., 2005]. However, there are discrepancies particularly in tropical regions without biomass burning, where MODIS data show higher values of the AOD than assumed here. This point has to be investigated in more detail in future studies.

Table 12: Overview on parameters used to calculate the three-dimensional fields of air mass factors for the satellite observations.

Parameter	*Source for assignment to the global field*	*Values for Radiative Transfer Model*	*Interpolation*
Albedo	[Tanskanen et al., 2003] in UV (HCHO), [Koelemeijer et al., 2003] in visible (CHOCHO)	0.02, 0.04, 0.06, 0.08, 0.10, 0.15, 0.20, 0.40, 0.60, 0.80, 1.00	Nearest neighbour
SZA	Measurement	5,15, 25, 35, 45, 55, 65, 70, 72.5, 75, 77.5, 80, 82.5, 85°	Linear
Surface Height	TerrainBase Global DTM Version 1.0 [Row et al., 1994]	0 - 2400m, 400 m layers, 3.6 km, 4.8 km, 6 km	Nearest neighbour
Aerosol	EDGAR CO_2 [Olivier and Berdowski, 2001], Global Aerosol Climatology Project (GACP) [Geogdzhayev et al., 2002; Mishchenko et al., 2002], ATSR Fire Counts see section 2.4.1, Terrain Base	LOWTRAN: urban, rural, maritime Visibility: 5, 10, 23, 50 km	Nearest neighbour
Vertical Profile Shape	ATSR Fire Counts, AVHRR and MODIS NDVI, see section 2.4.2	Background, biogenic, urban	Nearest neighbour
Latitude / Longitude	Measurement	1° x 1°	Linear
Time	Measurement	Year and month	Nearest neighbour

Table 13: Thresholds for the assignment of pre-calculated AMF.

Parameter	*Value*	*Threshold*	*Source*
Aerosol type	Maritime	Altitude < 0 m asl	TerrainBase
	Urban	CO_2 > 1 Tg CO_2/year	EDGAR emission data base
		or fire counts per month > 5	ATSR
	Rural	elsewhere	
Visibility	5 km	Fire counts per month > 100	ATSR
		or CO_2 > 30 Tg CO_2/year	
	10 km	Fire counts per month > 5	ATSR
		or AOD_{Ocean} > 0.55	GACP
		or CO_2 > 9 Tg CO_2/year	EDGAR emission data base
	23 km	0.15 < AOD_{Ocean} < 0.55	GACP
		or CO_2 > 1 Tg CO_2/year	EDGAR emission data base
	50 km	elsewhere	
Profile Shape	Biogenic & burning	NDVI > 0.6	AVHRR
		or fire counts per month > 5	ATSR
	Urban	CO_2 > 1 Tg CO_2/year	EDGAR emission database
	Background	elsewhere	

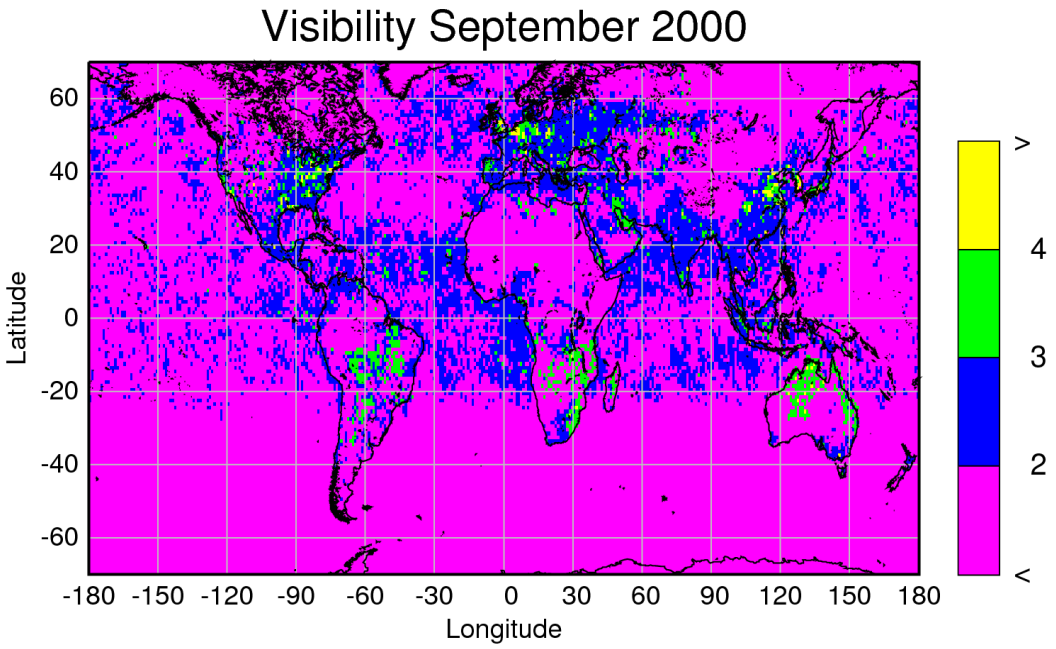

Figure 5-38: Visibility used for the AMF table in September 2000. Purple (1): 50 km; blue (2): 23 km; green (3): 10 km; yellow (4): 5 km.

Adaptation of other data sources such as new emission inventories (e.g. from the Model of Emissions of Gases and Aerosols from Nature (MEGAN) [Guenther et al., 2005], the successor of the emission database for non-methane hydrocarbons from [Guenther et al., 1995]) or model output (see section 6.4) is simple and foreseen for future studies.

In order to illustrate the effect of the three-dimensional AMF on the results, exemplarily the results obtained for GOME measurements of HCHO in September 1997 are shown here in Figure 5-39 and Figure 5-40. The largest changes occur above polluted areas with low visibility e.g. biomass burning regions in Indonesia and Australia and industrialised areas in North America: Here the standard AMF [Wittrock et al., 2000] leads to an underestimation of the HCHO amounts of up to 80 percent. On the other hand, the total column above areas with high albedo and/or high surface level is overestimated by up to 60 percent. These differences depend on season and larger values are expected for polluted scenarios in wintertime having a high surface albedo.

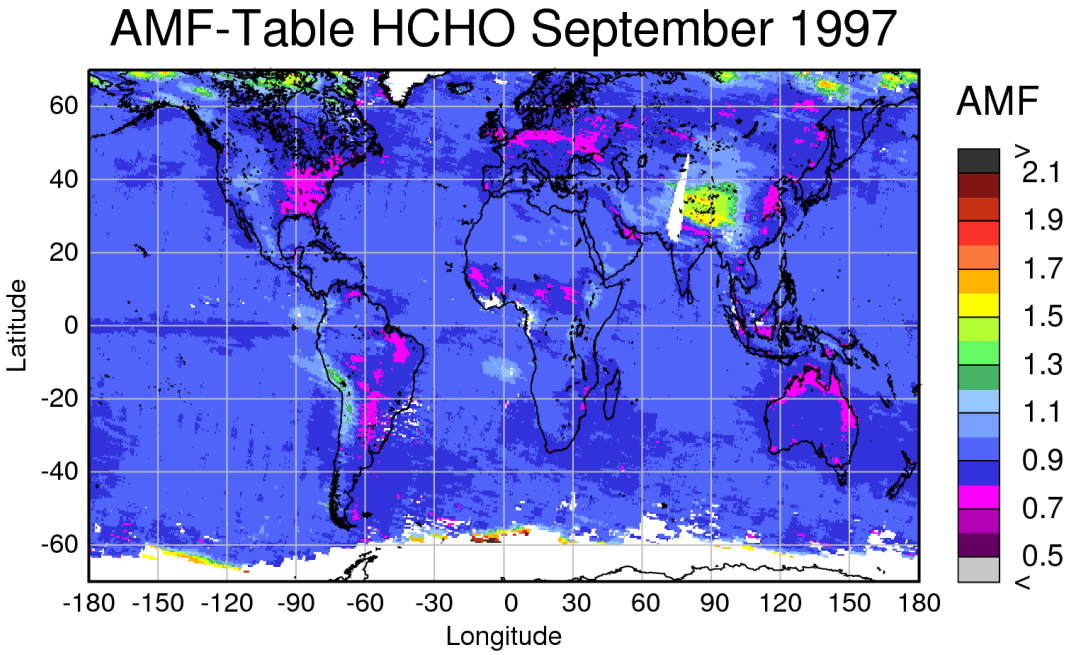

Figure 5-39: 2D-Plot of the air mass factors for the GOME measurements of HCHO in September 1997.

In summary, the adaptation of more-dimensional fields of AMF to the satellite retrieval of tropospheric trace gases is crucial to receive realistic results. In contrast to other studies, which have implemented modelled trace gas profiles into the calculation of the AMF, the main focus is to have a flexible interface to use external information to create realistic distributions of albedo and aerosol conditions. The other advantage of this approach is to reduce the impact from model assumptions as measurements are used.

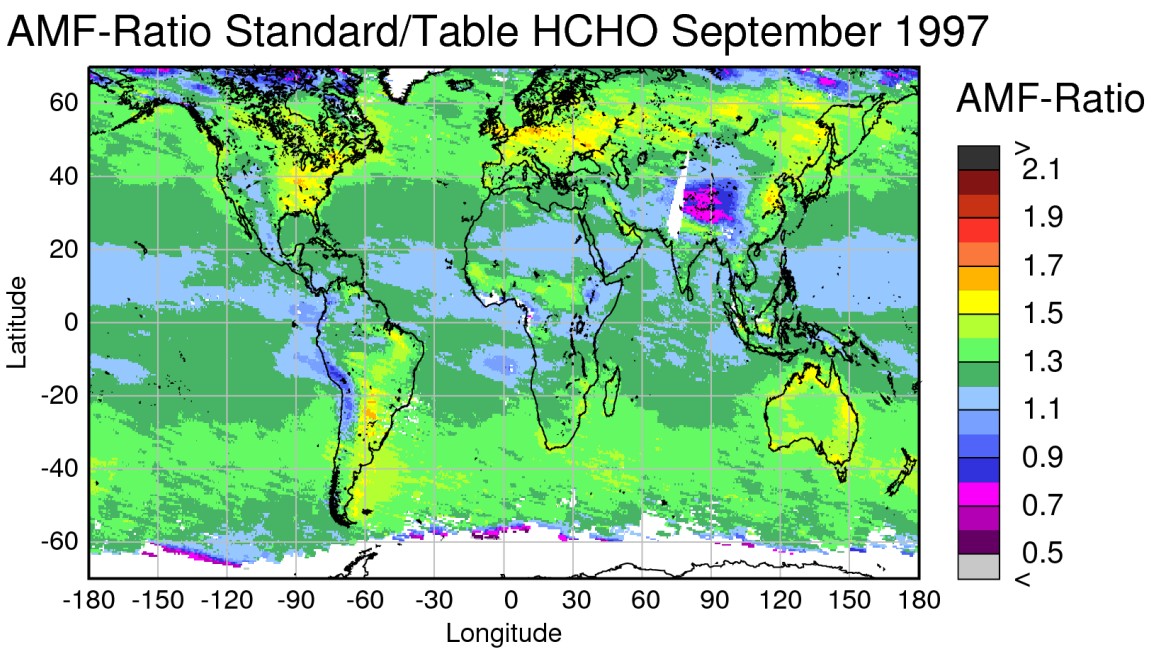

Figure 5-40: Graph of the air mass factor ratio between the standard AMF which has been applied in [Wittrock et al., 2000] and the new AMF tables exemplarily for GOME measurements of HCHO in September 1997. The values range from 0.4 to 1.8.

5.5 Error analysis

The total error of the DOAS measurements of HCHO and CHOCHO comprises a number of different error sources, both, random and systematic, correlated and not correlated, and most of them described in detail in previous sections. However, the aim of this section is to give a compact overview on the different errors for the observation platforms utilised here. Thus, in the following the different error sources will be briefly characterised and finally quantified in Table 14. Some of the statements given here are based on the work by [Boersma et al., 2004].

5.5.1 Random measurement error

This error is determined by the total signal intensity and the absorption strength. In the limiting case of shot noise, the random error is the smallest possible error that can be achieved with this measurement. As the error is random, averaging in space and time reduces the uncertainty following Poisson statistics (square root of the number of measurements).

5.5.2 Air mass factor errors

The air mass factor error is the contribution from the uncertainty in the light path which is dominated by the uncertainty in the input parameters, but not the calculation of the light path itself. The most important factors are surface albedo, cloud cover, aerosol loading and profile and the vertical profile of the absorber itself (see section 5.2). Most of the air mass factor uncertainties are systematic and therefore not necessarily reduced by averaging. However, some components such as cloud cover do have a substantial random component which is less important when looking at monthly or annual averages. This applies for the satellite observations presented here.

5.5.3 Offset errors

For weak absorbers, the DOAS retrieval often suffers from uncertainties in the absolute values. Even small effects such as the angle dependent reflectivity of the diffuser plate in the GOME instrument (section 5.1.6) or changing etalons on the detectors after cooler switches (section 5.1.7) can introduce large offsets in the results. This error component is difficult to quantify and varies over time. One approach to reduce the impact of these factors is to normalise the columns over an area with known atmospheric amounts of the absorber, if needed also as a function of latitude. This significantly homogenises the data set and is routinely done for NO_2 [Richter and Burrows, 2002], BrO [Richter et al., 2002], and HCHO [Wittrock et al., 2000; Palmer et al., 2003] GOME data analysis. The disadvantage of this method is that the absolute reference point is lost and a free parameter is introduced, thus reducing the informational content of the measurements. Also, it is often difficult to find the information necessary to actually apply the normalisation as little is known on the global distribution of HCHO and in particular CHOCHO. For the GOME HCHO and the SCIAMACHY CHOCHO time series, a region over the eastern Pacific (10°S to 10°N, 180°W to 140°W) was chosen, where only background concentrations can be assumed for both, formaldehyde and glyoxal. In the case of formaldehyde, the background value was set to $3x10^{15}$ molec/cm^2 for the slant column according to measurements from [Heikes et al., 2001], that for glyoxal was chosen to be $1x10^{14}$ molec/cm^2. For the SCIAMACHY formaldehyde retrieval, the reference region was extended to the full latitude range due to the possible interference with BrO and ozone in the, compared to GOME, smaller formaldehyde fitting window (see section 5.5.4).

5.5.4 Correlation errors

The most problematic error sources in the DOAS retrieval are correlations between the absorption spectrum of the species of interest and other effects such as calibration functions, interfering cross-sections, absorbers not accounted for or surface reflectance structures. Depending on the physical variability of the interfering effects, artefacts can be introduced in the retrieval of weak absorbers, leading to offsets and also factors which vary in space and time. Prominent examples are the impact of absorption by liquid water (section 5.1.17) and of vibrational Raman scattering in sea water that leads to spectral features in the earth shine radiances. These feature can interfere with those of weak absorbers (e.g. [Vountas et al., 2003] and section 5.1.3).

As pointed out in the last section, the small fitting window for the SCIAMACHY HCHO suffers interference with ozone and BrO. This leads to decreasing formaldehyde columns for increasing SZAs beyond a threshold of about 65° depending on ozone and/or BrO amounts. Therefore, global fields of SCIAMACHY formaldehyde have been derived with the following limitations: Only measurements for SZA less than 60° were investigated which limits the spatial coverage to latitudes of 30° in the winter hemisphere. In addition, the region chosen as reference was extended to the full latitude range instead of using a small area near to the equator as for GOME HCHO.

5.5.5 Other systematic errors

The temperature dependence of the absorption cross-section and inaccuracies of its absolute value are additional systematic errors in the data evaluation which have to be taken into account. However, as can be seen from Table 14 they are of minor importance. The error due to the temperature dependence of the HCHO cross-section [Meller and Moortgat, 2000] has been estimated to be three percent. Temperature dependent cross-sections of glyoxal are not available. Thus, a similar dependence was assumed here. The error of the absolute cross-sections has been assessed to 5 percent by the authors [Meller and Moortgat, 2000; Volkamer et al., 2005].

Table 14: Overview on errors in the HCHO and CHOCHO retrieval (typical values for SZA smaller than 70° or 60° for SCIAMACHY). The values in the last two rows are given for characteristic applications of the trace gas observations: one hour averages for MAX-DOAS observations / monthly average for satellite observations. This reflects also the results presented in chapter 6.

	BREDOM		***SCIAMACHY***		***GOME***
	HCHO	*CHOCHO*	*HCHO*	*CHOCHO*	*HCHO*
Absorption cross-section	5 %	5 %	5 %	5 %	5 %
Temperature	3 %	3 %	3 %	3 %	3 %
Spectral calibration	2 %	2 %	5 %	2 %	2 %
Reference column [molec/cm^2]			$2\cdot10^{15}$	$2\cdot10^{14}$	$2\cdot10^{15}$
Aerosol	5 %	5 %	15 %	15 %	15 %
Clouds	5 %	5 %	30 %	30 %	30 %
Albedo	2 %	2 %	10 %	10 %	10 %
LOS BREDOM/ Profile shape satellite	5 %	5 %	10 %	10 %	10 %
Fitting error for single spectrum (SC) [molec/cm^2]	$3\cdot10^{15}$	$5\cdot10^{14}$	$1.0\cdot10^{16}$	$5\cdot10^{14}$	$6\cdot10^{15}$
1 hour BREDOM/ 1 month satellite (SC) [molec/cm^2]	$1.5\cdot10^{15}$	$2.5\cdot10^{14}$	$4\cdot10^{15}$	$2\cdot10^{14}$	$2\cdot10^{15}$
Overall error of the analysis for the VC [molec/cm^2]	$1\cdot10^{15}$	$1.5\cdot10^{14}$	$7\cdot10^{15}$	$4\cdot10^{14}$	$3\cdot10^{15}$

6 Results

This chapter gives an overview on the results on formaldehyde and glyoxal. In the first section 6.1, selected data sets from the ground-based instruments are presented together with a first validation study for the satellite measurements. A more detailed view on the results from the BREDOM sites and their possibilities to validate spaceborne observations will be given by Fietkau [2006] and Medeke [2006]. The second part 6.2 is on the global picture obtained from the satellite instruments and the next one (section 6.3) compares results from this study to other work published so far. The last part 6.4 is a detailed comparison of GOME HCHO with model data.

6.1 MAX-DOAS observations of formaldehyde and glyoxal

In section 5.3, it was shown that the MAX-DOAS observations can be used to derive trace gas profiles. The BREAM algorithm has been applied to various data sets obtained from the permanent BREDOM and the campaign sites. Results will be presented in the following sections.

6.1.1 Selected MAX-DOAS results

6.1.1.1 Cabauw

Here, ground-based MAX-DOAS measurements are presented from a campaign in Cabauw in summer 2005 (see section 2.3.2.5.4). The spectra have been analysed for formaldehyde and glyoxal. The quality of the fit has already been illustrated in Figure 5-8. These measurements depict the first ever detection of glyoxal with the MAX-DOAS technique.

Using the profile retrieval algorithm BREAM, time series of tropospheric columns have been generated for the two species for the whole measurement campaign (see Figure 6-1 and Figure 6-2). Over this time period, the average tropospheric column of Glyoxal was about 4.2 x 10^{14} molec/cm^2. The tropospheric columns of formaldehyde are more variable than the ones for glyoxal probably due to the impact of direct emissions from anthropogenic sources in the heavily polluted area. On average, a tropospheric column of 5.7 x 10^{15} molec/cm^2 is retrieved. However, similarities can be observed: Enhanced formaldehyde is always associated with an increase in glyoxal, e.g. 25/26 May or around 20 June, although this increase is not as pronounced as for HCHO.

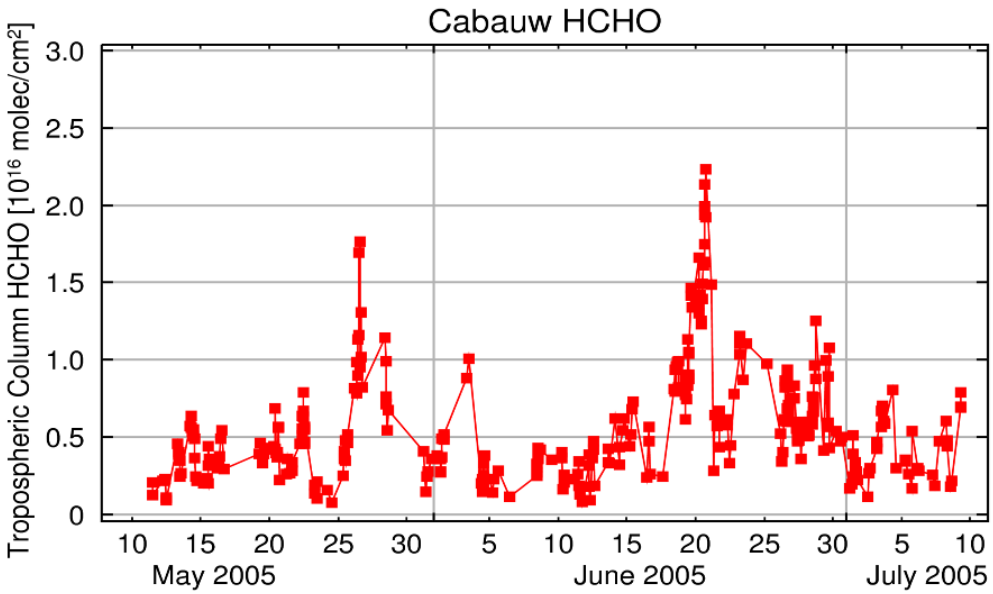

Figure 6-1: Vertical columns of formaldehyde during the DANDELIONS campaign.

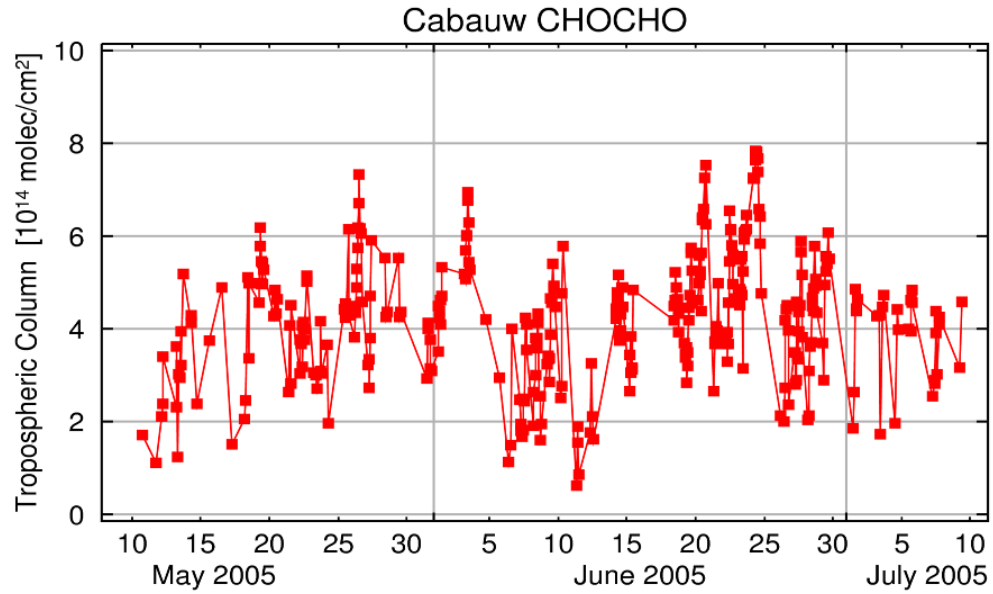

Figure 6-2: Vertical columns of glyoxal during the DANDELIONS campaign.

For 18 June, the slant columns of O_4, nitrogen dioxide, glyoxal and formaldehyde are shown for three consecutive days in Figure 6-3. The slant columns of O_4 reveal most of the time good weather conditions. Especially, on 19 June the effect of the changing relative azimuth angle between the telescope and the sun can be observed quite nicely in the off-axis slant columns (see also section 5.2.1.1.2) which indicates very good visibility. The variation of tropospheric NO_2 over these three days is completely different from both formaldehyde and glyoxal whereas the latter two species exhibit an analogous increase during this time period. This can again be interpreted as signature of the differences in sources and atmospheric life-time: NO_2 is mainly produced from NO_x emitted by combustion processes, in particular from traffic and power generation. Road traffic on nearby streets can

have a large impact on NO_2 measurements, as can transport of air masses from industrial regions such as nearby Utrecht, Rotterdam and The Hague. It is evident from GOME and SCIAMACHY measurements (e.g. [Stohl et al., 2003; Huntrieser et al., 2005]), as well as from airborne campaigns that NO_2 can be transported from the source regions over regional and even continental distances, whereas both HCHO and CHOCHO have relatively short life times. One would therefore expect that NO_2 levels are more affected by transport patterns whereas HCHO and CHOCHO depend more on local photochemistry.

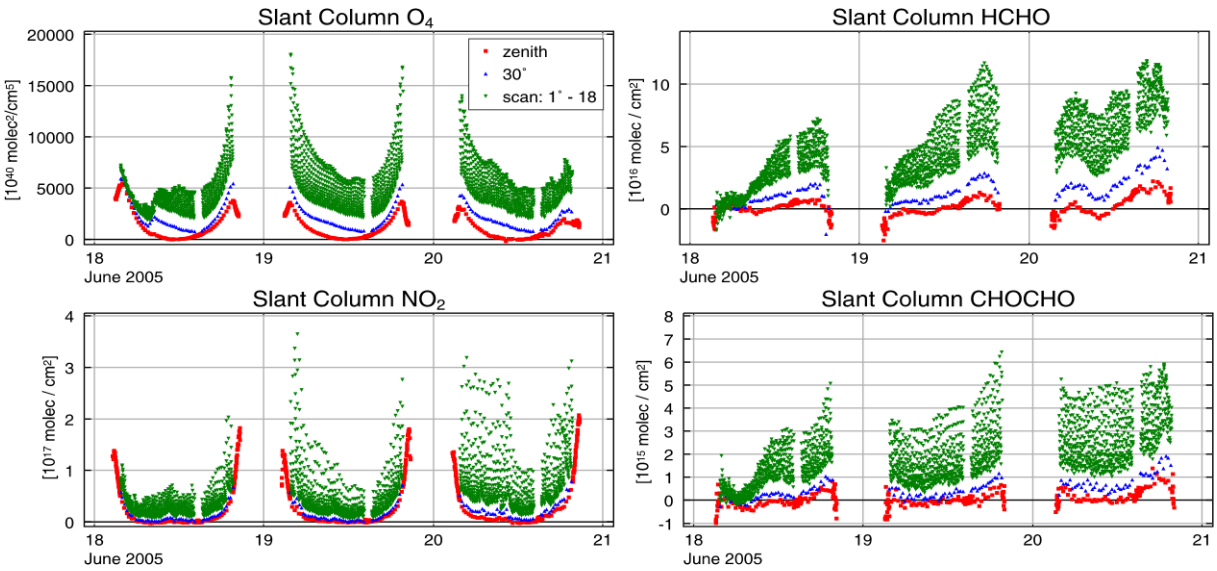

Figure 6-3: Differential slant columns for O_4, NO_2, HCHO, and CHOCHO from 18 to 20 June 2005 above Cabauw.

The evolution of the HCHO and CHOCHO profiles in Cabauw during the three days is illustrated in Figure 6-4. Glyoxal volume mixing ratios of up to 0.14 ppb_V and formaldehyde volume mixing ratios of up to 3.8 ppb_V are found. The maximum VMRs are present in the afternoon and close to the ground for both species. The similarities for both species indicate that the sources of glyoxal and formaldehyde are quite alike. NO_2 in contrast has two maxima, one in the morning and one in the evening, probably as result of road traffic during the rush hours. Compared to the hydrocarbons, the surface maximum is even more pronounced, again in agreement with sources close to the ground.

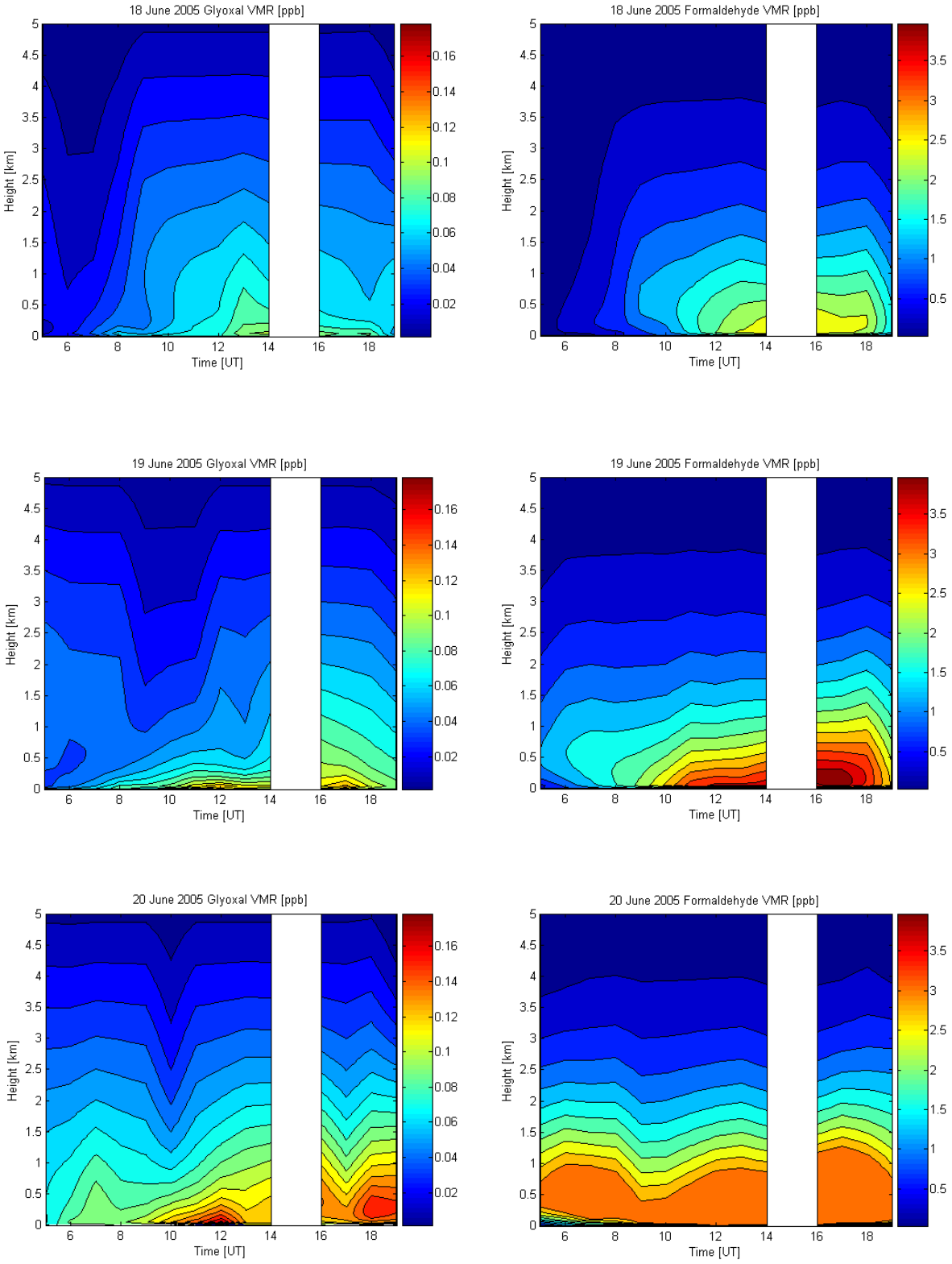

Figure 6-4: Profiles of CHOCHO and HCHO above Cabauw from 18 to 20 June 2005. The mixing ratios were retrieved with BREAM utilising the differential slant columns shown in Figure 6-3.

6.1.1.2 Arctic Sites

Measurements from both Arctic sites, Summit (section 2.3.2.5.1) and Ny-Ålesund (section 2.3.2.1) have been investigated for formaldehyde. While in Summit no clear evidence for HCHO was found, the Ny-Ålesund data exhibit quite regularly significant amounts of HCHO from March to September each year. One example for the usually quite smooth diurnal variation of the formaldehyde profile is given in the next Figure 6-5. In general, formaldehyde amounts of more than 600 ppt_V close to the ground were found with the maximum values in May and June of each year. This is in reasonable agreement both in seasonal variation and in magnitude to FTIR measurements from Notholt et al. [1997] and Albrecht et al. [2002] and to findings from Riedel et al. [1999] for Antarctica. However, the FTIR measurements usually show larger vertical columns of about 7.0×10^{15} molec/cm^2 than the MAX-DOAS measurements: Maximum columns of about 4.5×10^{15} molec/cm^2 have been derived with BREAM. Jacobi et al. [2002] have reported up to 150 ppt_V formaldehyde for the Summit site. This is close or below the detection limit of the MAX-DOAS instrument.

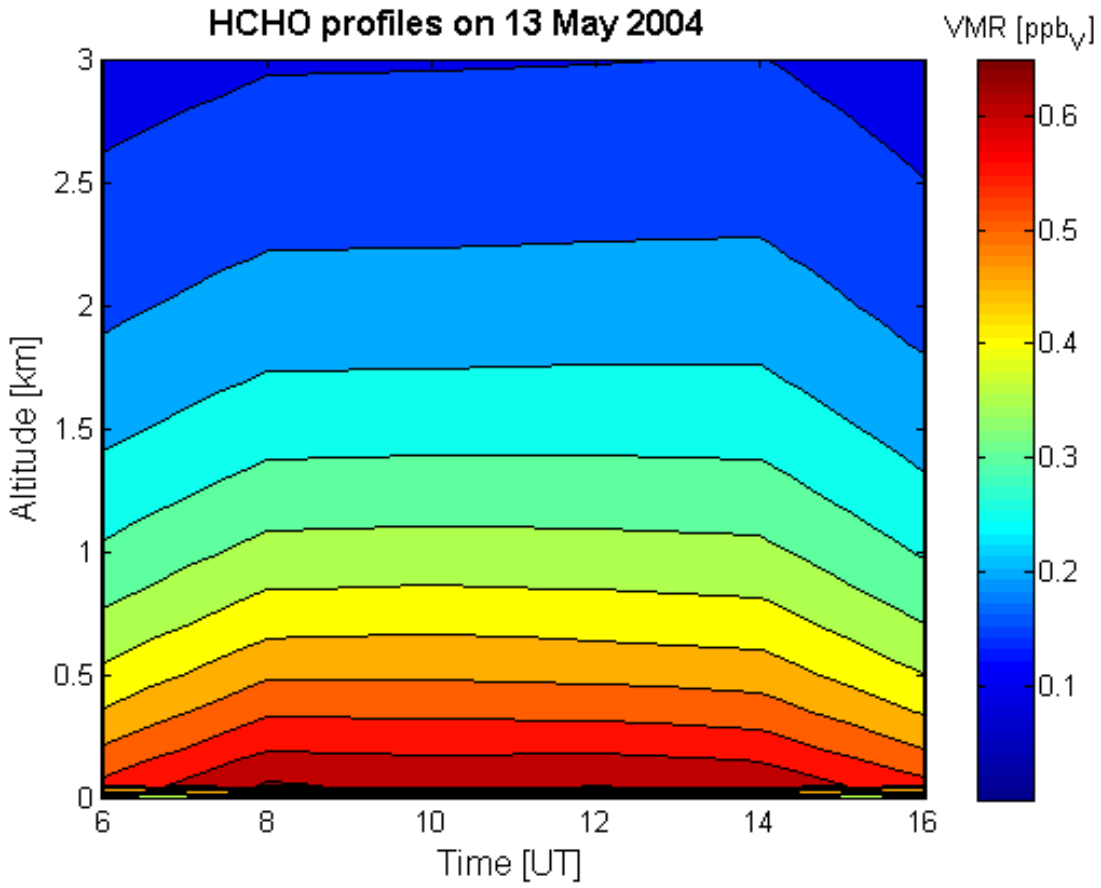

Figure 6-5: HCHO profiles above Ny-Ålesund on 13 May 2004 calculated with BREAM. The maximum amount is usually observed around noon: Here the VMR is 650 ppt_V, the vertical column about 2.9×10^{15} molec/cm^2.

6.1.1.3 Mountain Sites

MAX-DOAS measurements from Mérida (section 2.3.2.3) and Zugspitze (section 2.3.2.5.2) were analysed for formaldehyde and significant amounts have been found regularly. In Mérida, a clear seasonal cycle was observed with largest amounts of HCHO from January to particularly March. This is known as the main biomass burning

season in the nearby Llanos. During that period, VMR of up to 1 ppb_V close to the altitude level of the instrument was observed, while it was half of the amount in maximum during the rest of the year.

Although the Zugspitze site is about two kilometres lower than the Pico Espejo station, with 300 ppt_V (in March) to 800 ppt_V (in June) somewhat smaller amounts of formaldehyde were retrieved. This is presumably due to missing or at least minor biogenic and biomass burning sources. Both data sets will be presented in detail by Medeke [2006] applying trajectory analysis to identify both, main precursors and their source regions.

The following Figure 6-6 shows exemplarily formaldehyde volume mixing ratios close to the measurement site in Mérida in conjunction with the monthly mean fire counts above the Llanos in Venezuela. Due to the prevailing wind direction (East) air masses from the biomass burning regions could be detected from the MAX-DOAS instrument on top of the Pico Espejo.

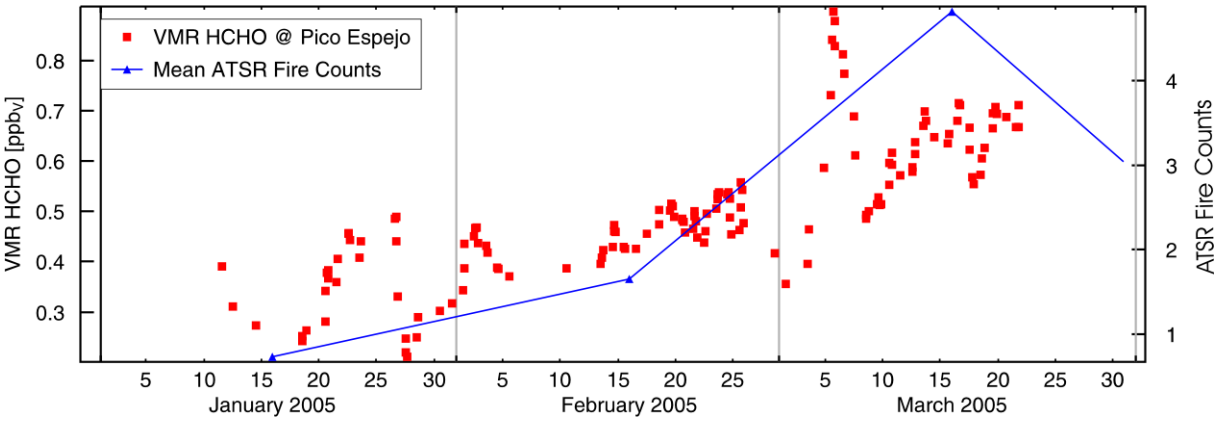

Figure 6-6: VMR of HCHO at 4.8 km asl with mean ATSR fire counts above Llanos in Venezuela.

6.1.1.4 Nairobi

MAX-DOAS data from the African site Nairobi (section 2.3.2.4) have been investigated for both, formaldehyde and glyoxal. Due to several instrumental problems, the data set has many gaps. Thus, in particular for CHOCHO only a limited data set is available up to now. However, on several days in particular during the dry season in the beginning of 2004 both trace gases could be clearly identified. One example is given in Figure 6-7.

The CHOCHO values in that graph are scaled with a factor of 10. In general, the variation is quite similar for both trace gases in analogy to the observations in Cabauw (section 6.1.1.1). But HCHO shows peaks in early morning and late afternoon. As pointed out by Fietkau [2006], this is frequently correlated with the traffic volume in downtown Nairobi. Thus, these peaks are presumably caused by direct emissions of cars.

In contrast to previous expectations, the measurement site is not suitable for investigating biomass burning events. Due to the prevailing easterly winds, air masses from biomass burning regions have not been observed until now. Otherwise, this site provides the opportunity to study the photochemistry in a highly polluted urban region near to the equator.

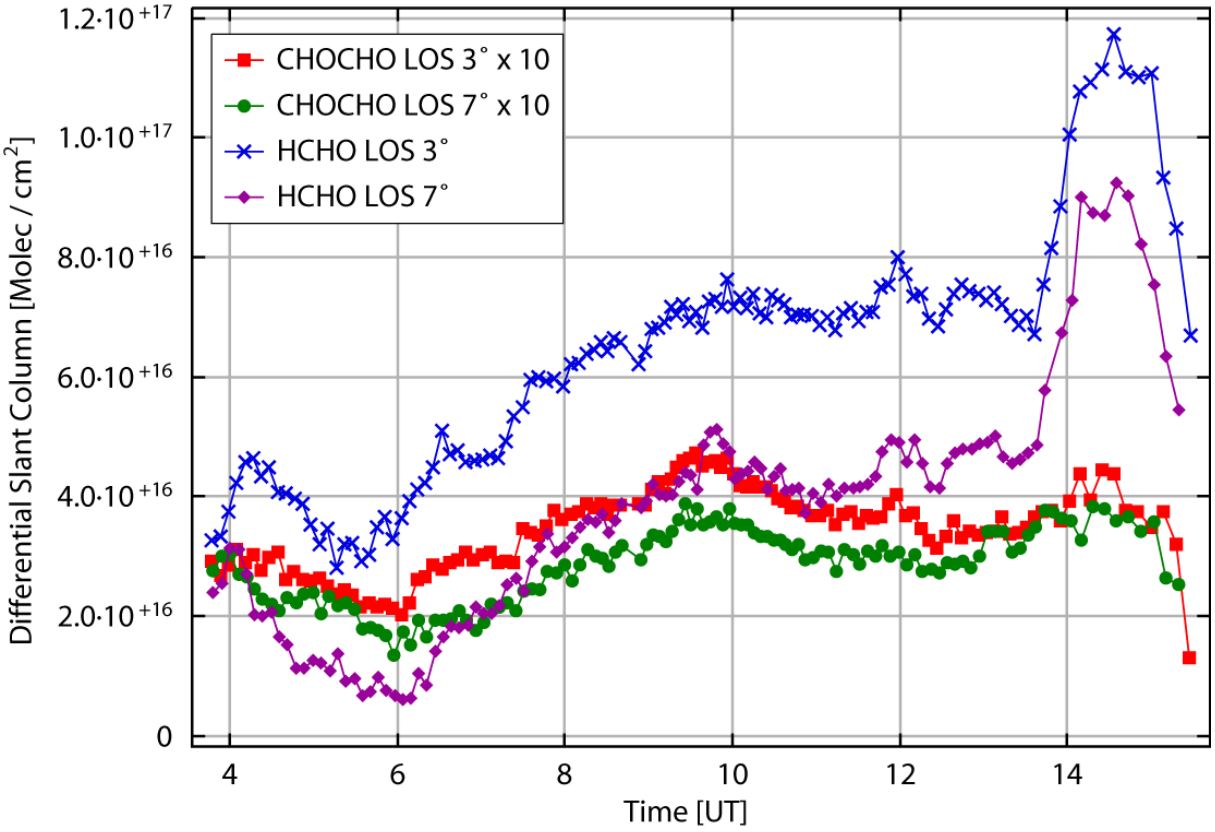

Figure 6-7: Diurnal variation of formaldehyde and glyoxal above Nairobi on a clear day on 31 March 2004.

6.1.2 Validation of satellite observations

One of the aims of this study is to provide techniques and data sets to validate scientific data products like HCHO and CHOCHO from satellite observations. In section 5.3.4, the ability of BREAM to retrieve VMRs, profiles and tropospheric columns was demonstrated. For satellite validations mainly the tropospheric column is of interest and here, a first attempt has been made to apply the ground-based measurements to validate tropospheric formaldehyde and glyoxal columns. One important reason for validation is the problem of degradation: The characteristics of the satellite instrument change with time in space. Thus, an absolute value at least for the minor trace gases is not available. Consequently, regular comparisons with data from ground-based stations are necessary.

Tropospheric columns of nitrogen dioxide are easier to detect than formaldehyde or glyoxal due to the greater abundance. Therefore exemplarily, results will be shown for NO_2 first to prove the high accuracy of the algorithm. Here again, results from the measurement campaign in Cabauw will be presented. The upper and lower panels in Figure 6-8 show ground-based NO_2 measurements compared to satellite data and to *in situ* measurements, respectively. For the satellite data, pixels with less than 30 percent cloud cover and values within a 50 km radius around Cabauw have been applied leaving only 20 data points for the whole time series. A correlation of 0.72 between ground-based and satellite-based results is found. The satellite rather depicts the lower range of the ground-based results. The MAX-DOAS concentrations of NO_2 are averaged over the lowest layers of 50 m thickness from the profile derived with BREAM. Here, days with clouds are included. The excellent agreement of the tropospheric columns and of the NO_2 concentrations is demonstrating the ability of the MAX-DOAS to act as a link between *in situ* and satellite observations.

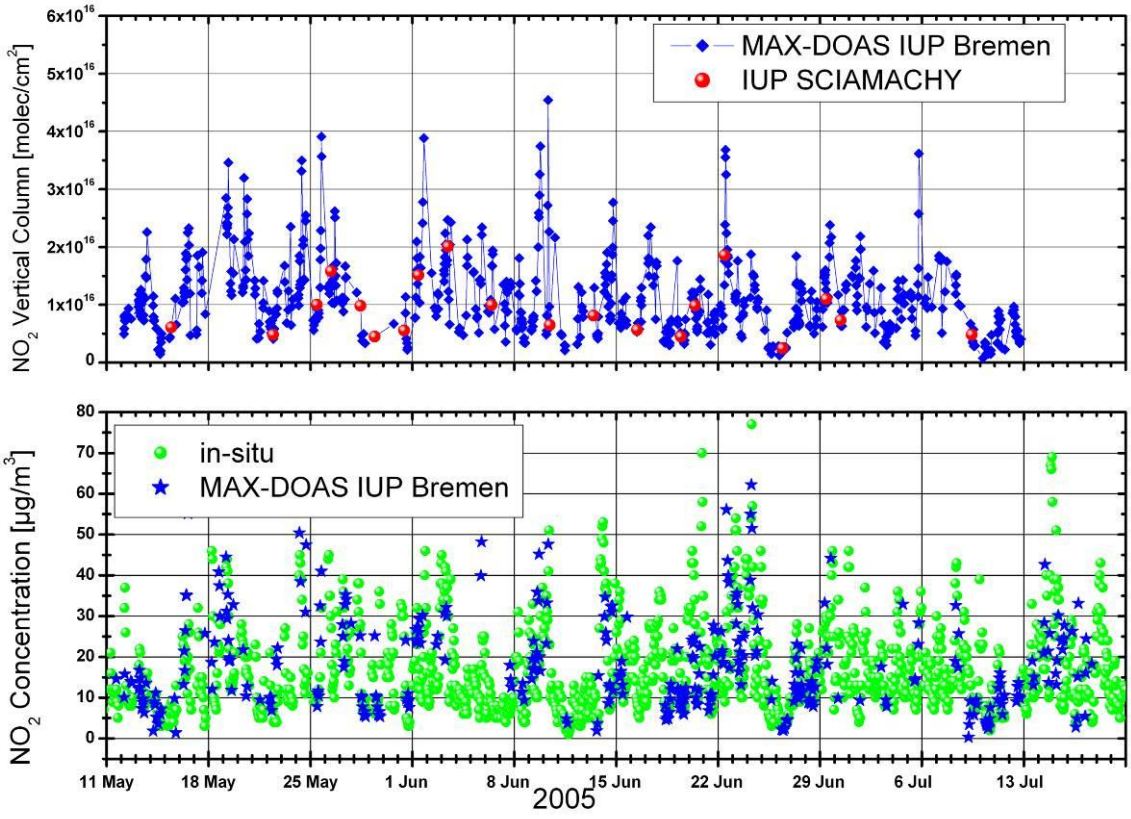

Figure 6-8: Upper panel: Comparison between SCIAMACHY NO_2 and the VC retrieved with BREAM from MAX-DOAS observations above Cabauw. Lower panel: Comparison between *in situ*-measurements and the concentration close to the surface retrieved with BREAM at the same site.

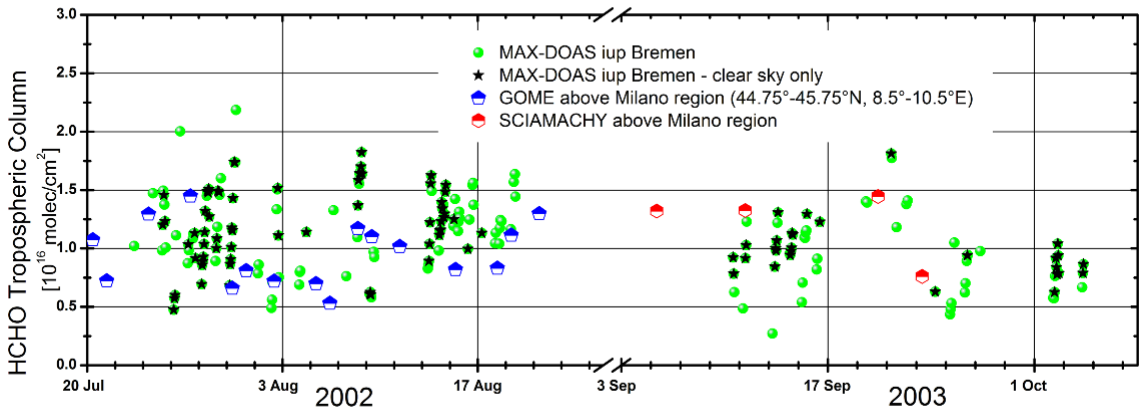

Figure 6-9: Vertical columns of formaldehyde above Alzate in 2002 and 2003. The MAX-DOAS results have been derived with the BREAM algorithm described in 5.3. For the satellite observations only pixels were selected within 100 km distance to the ground measurement site.

Measurements for the two FORMAT-campaigns at Alzate in 2002 and 2003 are presented in Figure 6-9. For the year 2002, GOME formaldehyde columns and for 2003, SCIAMACHY columns are included. The overall agreement is good despite the sparse data points especially for SCIAMACHY in 2003.

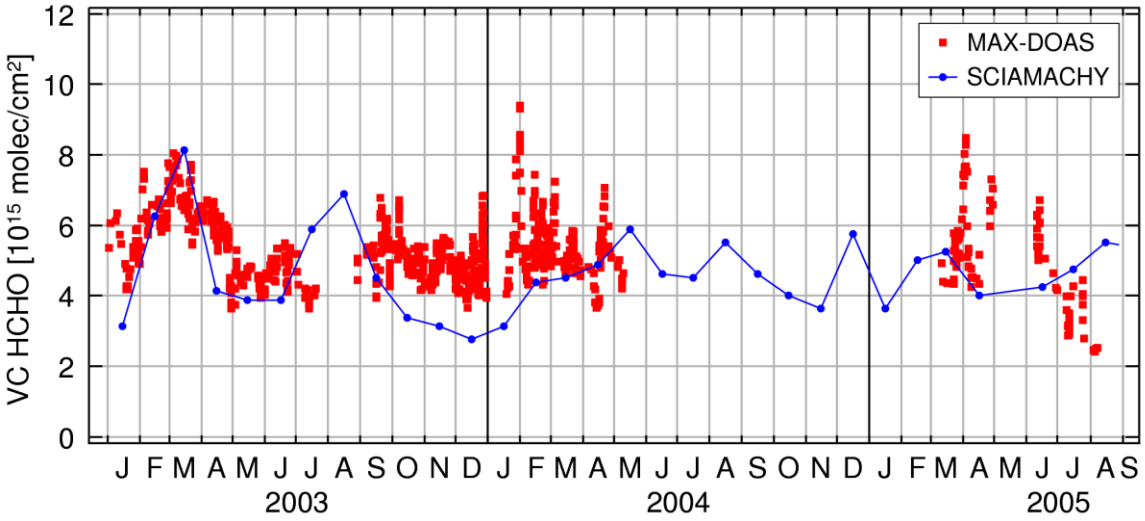

Figure 6-10: Vertical columns of formaldehyde above Nairobi from 2003 to 2005. The MAX-DOAS results have been derived with the BREAM algorithm. For SCIAMACHY, monthly means have been calculated using only ground pixels within 100 km distance to the ground measurement site.

Due to instrumental problems, there are data gaps in the ground-based time series over Nairobi (see Figure 6-10). However, particularly in the beginning of 2003, the seasonal variation of the SCIAMACHY columns agrees well with the ground-based data for formaldehyde. Also for the rest of the time period of almost three years, the overall magnitude of the columns shows quite good consistency.

In Figure 6-11, the tropospheric columns of formaldehyde as well as glyoxal which have been already shown in the previous section 6.1.1.1 are compared to the monthly mean of SCIAMACHY at Cabauw. Again the overall magnitude shows reasonable agreement for both trace gases, which gives confidence in particular into the first ever retrieval of glyoxal on a global scale.

In general, tropospheric columns of formaldehyde are twice as high in Alzate as at the two other sites: Cabauw and Nairobi. The following section 6.2 will give an overview of the global pattern for formaldehyde.

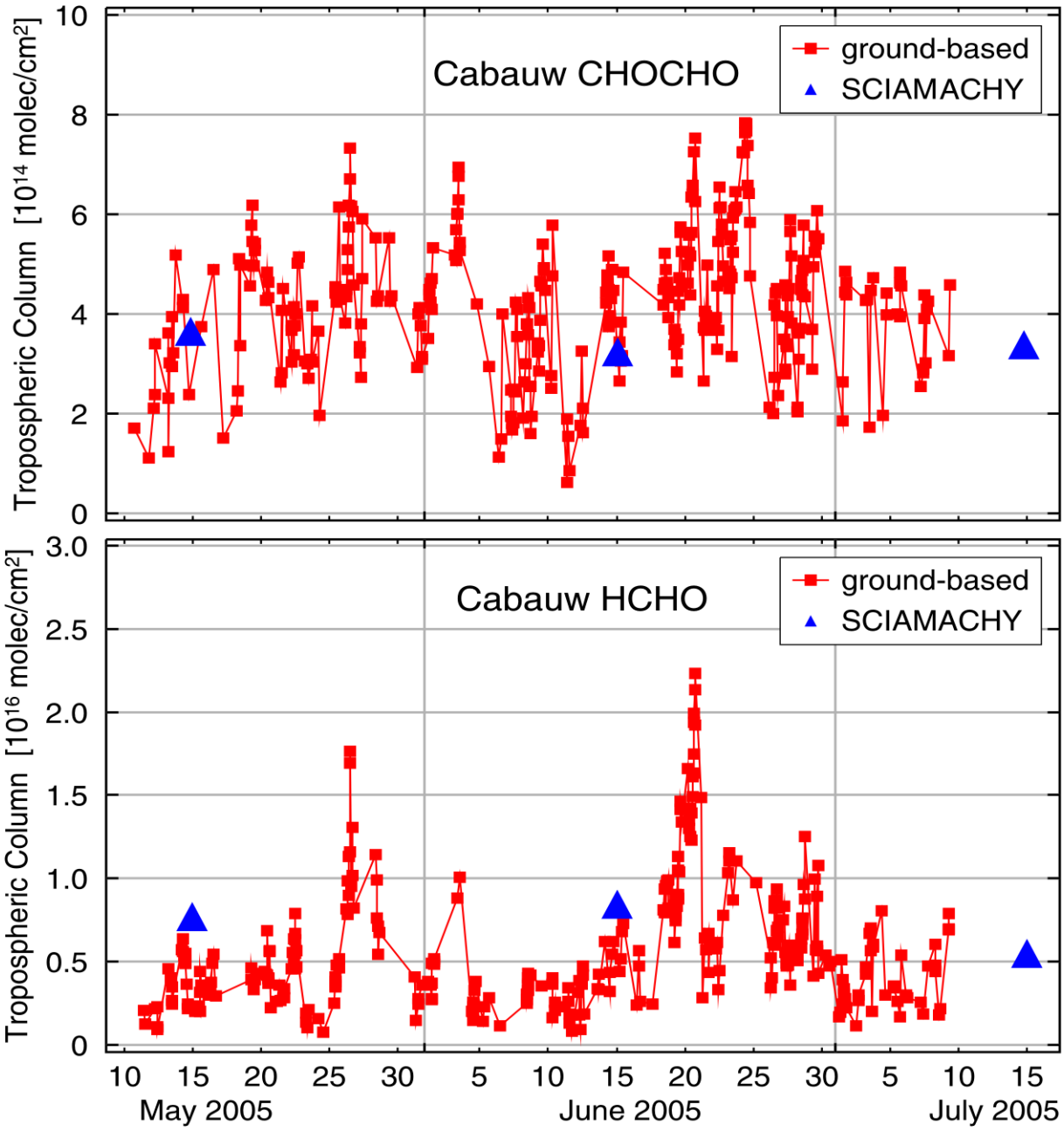

Figure 6-11: Validation of HCHO and CHOCHO above Cabauw. Again, for SCIAMACHY monthly means were calculated.

6.2 HCHO and CHOCHO – The global view

6.2.1 GOME HCHO

To investigate the global behaviour of the HCHO, vertical column densities have been calculated using the AMF look-up tables described in section 5.4. To account for the degradation of the GOME instrument which results in offsets of the retrieved HCHO slant columns, monthly averages have been normalised to a reference region in the Pacific (see also section 5.5.3). For this, it is assumed that the formaldehyde column in that region has only small seasonal and year-to-year variation. The following Figure 6-12 shows the global view of the mean vertical columns derived from GOME monthly averages from April 1996 to March 2003 comprising seven full years of GOME data. As the east and centre pixel exhibit offsets compared to the centre and west ones for the later years – which is again a consequence of increasing degradation of the scan mirror – only the latter are included in the composite pictures shown here.

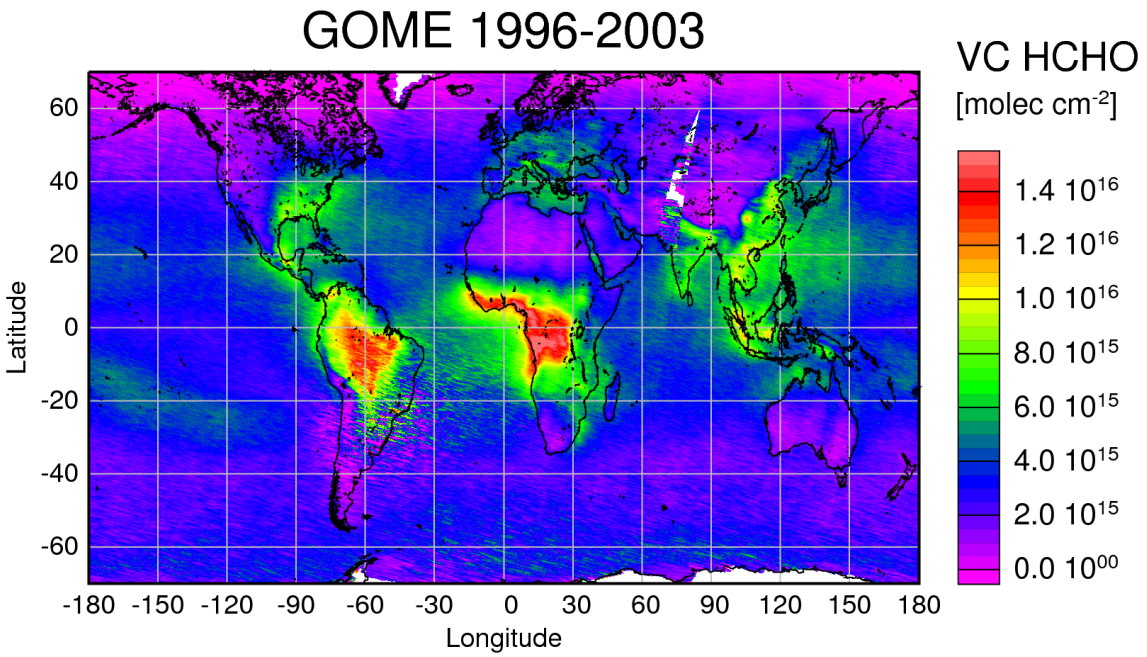

Figure 6-12: Mean GOME HCHO columns from April 1996 to March 2003. Only centre and west pixels having a cloud fraction less than approximately 20 percent are included. The data are gridded to 0.5° x 0.5°.

Large areas with high amounts of formaldehyde can be found over South America, Africa and Indonesia. Over these regions, the mean columns reach values of more than 1.5×10^{16} molec/cm^2. But also Europe, Asia and eastern North America exhibit significantly elevated columns of formaldehyde.

In the following, Figure 6-13 to Figure 6-19 offer a closer look: For six regions on the globe, formaldehyde together with the seven-year mean of nitrogen dioxide from GOME [Richter et al., 2005] as indicator for anthropogenic sources is presented. The mean fire counts from the ATSR (see section 2.4.1) and the normalised differential vegetation index (NDVI) from the AVHRR (see section 2.4.2) will be applied to attribute biomass burning and biogenic sources, respectively.

In Africa (see Figure 6-13), highest vertical columns of formaldehyde are associated with the rain forest whereas moderate values seem to be mainly influenced by biomass burning. Also, some elevated levels of formaldehyde above the oceans can be observed, particularly towards the west from the Congo region following the prevailing

wind direction in that region (see section 1.2). There is no indication for anthropogenic sources of formaldehyde when comparing the formaldehyde pattern with the NO_2 graph which only displays increased NO_2 around the urban region of Pretoria.

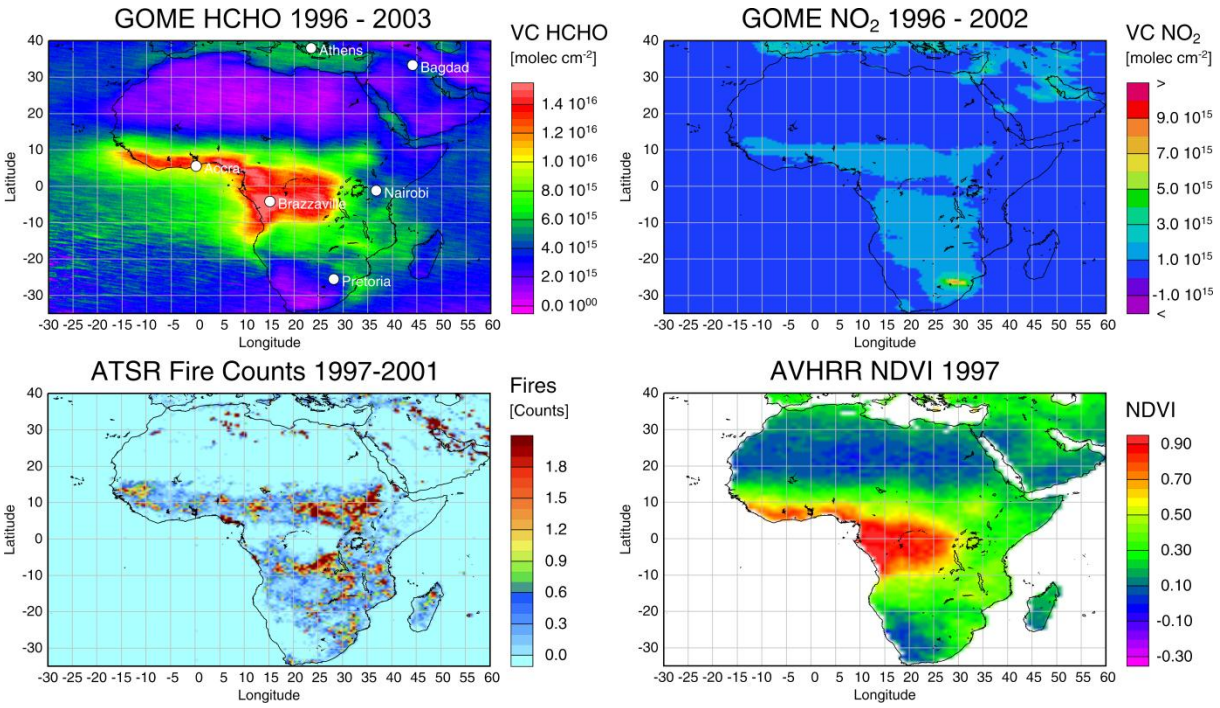

Figure 6-13: Mean values above Africa. The highest amounts of HCHO show up near to Brazzaville in the rain forests of Congo while the Sahara area and other desert regions exhibit very low values, even lower than those above the oceans. Downwind of the main source regions near to the equator, fairly high amounts of formaldehyde can be found. A detailed study on HCHO and other trace gas columns above Africa for September 1997 has been carried out by [Meyer-Arnek et al., 2005] applying trajectory analysis to identify different source regions for HCHO precursors.

In the mean GOME NO_2, the larger cities in Asia can be easily discerned (see Figure 6-14): Xianggang (formerly known as Hong Kong), Shanghai, Peking, Seoul, Osaka, and Tokyo. The pattern for formaldehyde cannot be allocated so clearly: While on the one hand hot spots can be assigned to areas with known strong pollution like Chengdu or Xianggang (see also Figure 6-15) on the other hand these regions are also very biologically active according to the NDVI. A precise classification towards biogenic or anthropogenic sources seems to be difficult for Asia without regional modelling. In addition, quite large amounts of formaldehyde are retrieved over the South China Sea.

As biomass burning does not occur often in Europe with the exception of some forest fires in summer (see Figure 6-16), the rather weak formaldehyde signal can be assigned to heavily polluted regions as for example the Po Valley or the Netherlands / north western Germany. In agreement with results from airborne measurements during the MINOS campaign [Kormann et al., 2003; Ladstätter-Weißenmayer et al., 2003] which took place at the Mediterranean in August 2001 increased formaldehyde is also observed over the Mediterranean Sea.

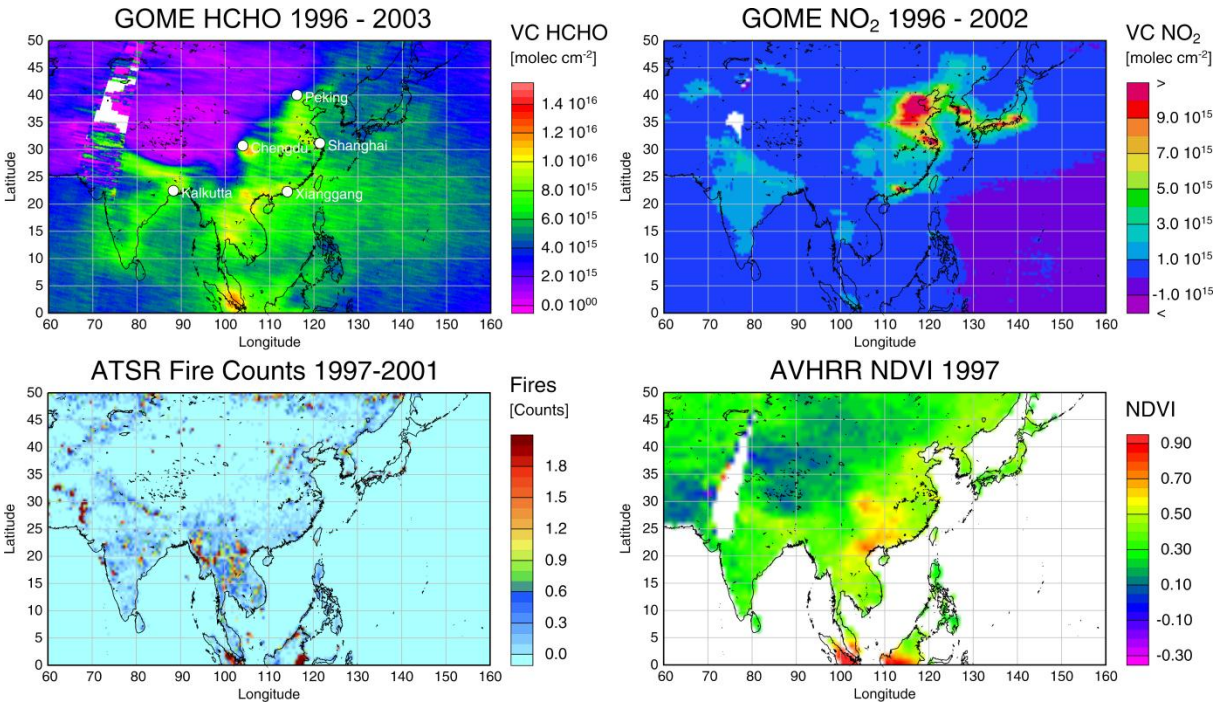

Figure 6-14: The mean values above Asia show quite interesting features. Vertical columns of HCHO above the rain forests, e.g. in Thailand and Malaysia are significantly smaller than over their counterparts in Africa. On the other hand in China, several regions show up with high values, which are known to feature extensive air pollution. China is shown in more detail in Figure 6-15.

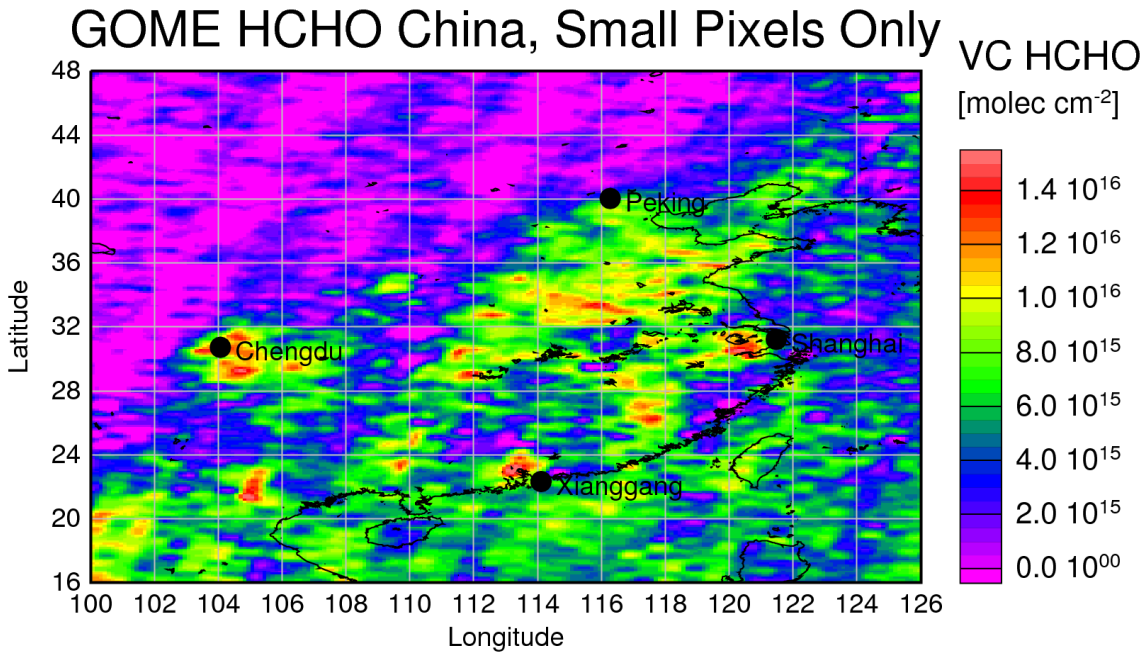

Figure 6-15: Formaldehyde above China from GOME narrow swath mode mesurements only which are performed usually every tenth day during nominal operation. This mode exhibits a much better spatial resolution (80x40 km^2). Small regions of elevated formaldehyde can be associated directly to possible sources, e.g. very polluted areas as the region of Xianggang (formerly known as Hong Kong) or the Red Basin near to Chengdu. The latter holds about 110,000,000 inhabitants and is girded by high mountain ranges. The disadvantage of the narrow swath mode is the poor global coverage: Each pixel in Figure 6-15 holds about 10 to 20 overpasses for the full time period from 1996 to 2003. A detailed study using the narrow swath mode has been carried out for NO_2 [Beirle et al., 2004].

Figure 6-17 shows the results for Indonesia and Australia. Although only a slight increase of NO_2 is observed over the urban regions of Bangkok, Singapore and Jakarta, a strong signal of formaldehyde can be assigned to these regions. But these are also areas with very strong biomass burning and a high NDVI. Again, in analogy to the interpretation of Figure 6-14, it is difficult to separate between anthropogenic and biogenic emissions over Indonesia. On the other hand, the rain forests in Borneo and New Guinea can be easily identified in the formaldehyde graph. In Australia over Brisbane, Sidney and Melbourne, emissions of NO_2 can be compared to columns over urban regions in Indonesia. Only along the north coast of Australia, formaldehyde from biomass burning activity and biogenic emissions can be observed which is surprising: One of the dominant tree species on the Australian continent is eucalyptus, a member of the myrtaceae family. These trees are known to be very efficient isoprene emitters [Kesselmeier and Staudt, 1999].

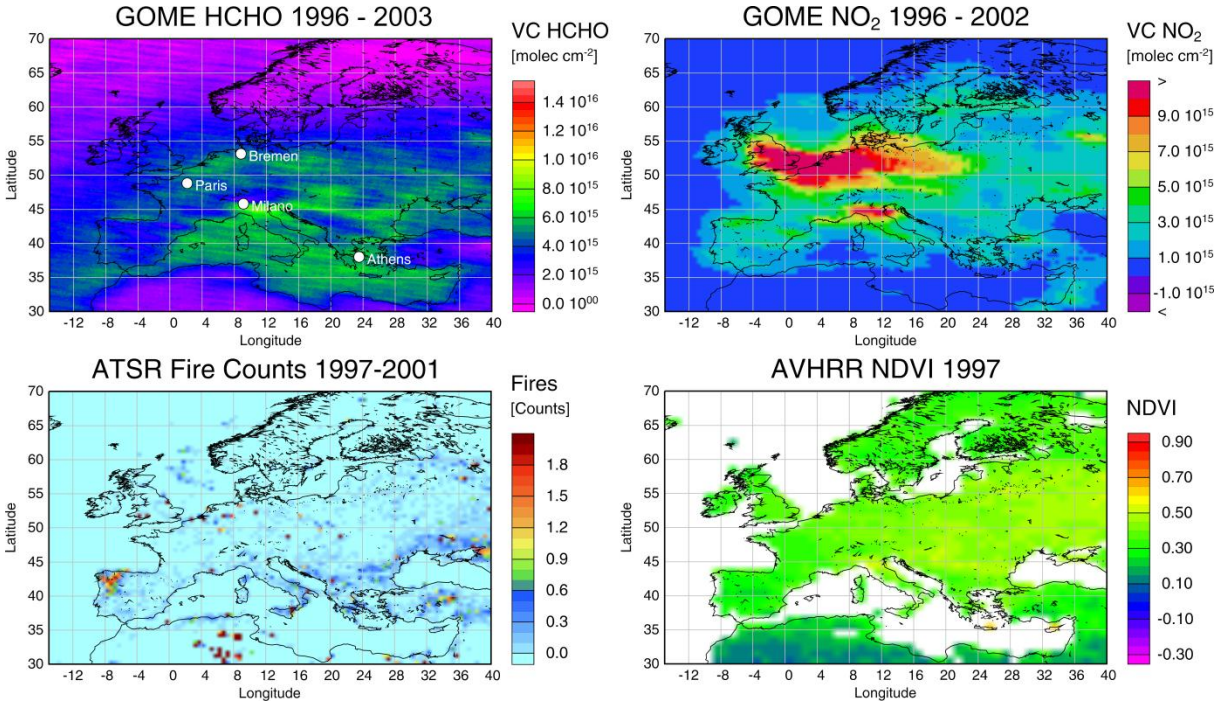

Figure 6-16: Mean values above Europe. In general, the HCHO amounts above Europe are close to the detection limit of the measurements. However, the multiannual mean shows some regions with enhanced values of formaldehyde: Belgium, The Netherlands, the Po valley near to Milan and some other small areas mostly in the eastern part of Europe. While the latter is probably related to isoprene emission from forests, the other areas feature strong anthropogenic sources, which contribute to the total formaldehyde signal.

High values of formaldehyde occur above the southeast of North America near to the Gulf of Mexico (see Figure 6-18). These observations agree well with recent studies by e.g. [Abbot et al., 2003] and are believed to reflect the high isoprene emissions in the growing season. One of the main species in that region is the oak tree. These trees have been investigated in several studies and are known as efficient emitters of both, isoprenes and monoterpenes (e.g. [Wiedinmyer et al., 2005] and references therein). A small region with high amounts of HCHO is the rain forest southeast of Mexico City which is also a hot spot for biomass burning.

Figure 6-19 displays mainly the biogenic formaldehyde signal from isoprene and other biogenic VOCs over rain forests. The biomass burning regions on that continent exhibit medium amounts of HCHO e.g. in the Llanos, which is located east and southeast of Mérida (see sections 2.3.2.3 and 6.1.1.3).

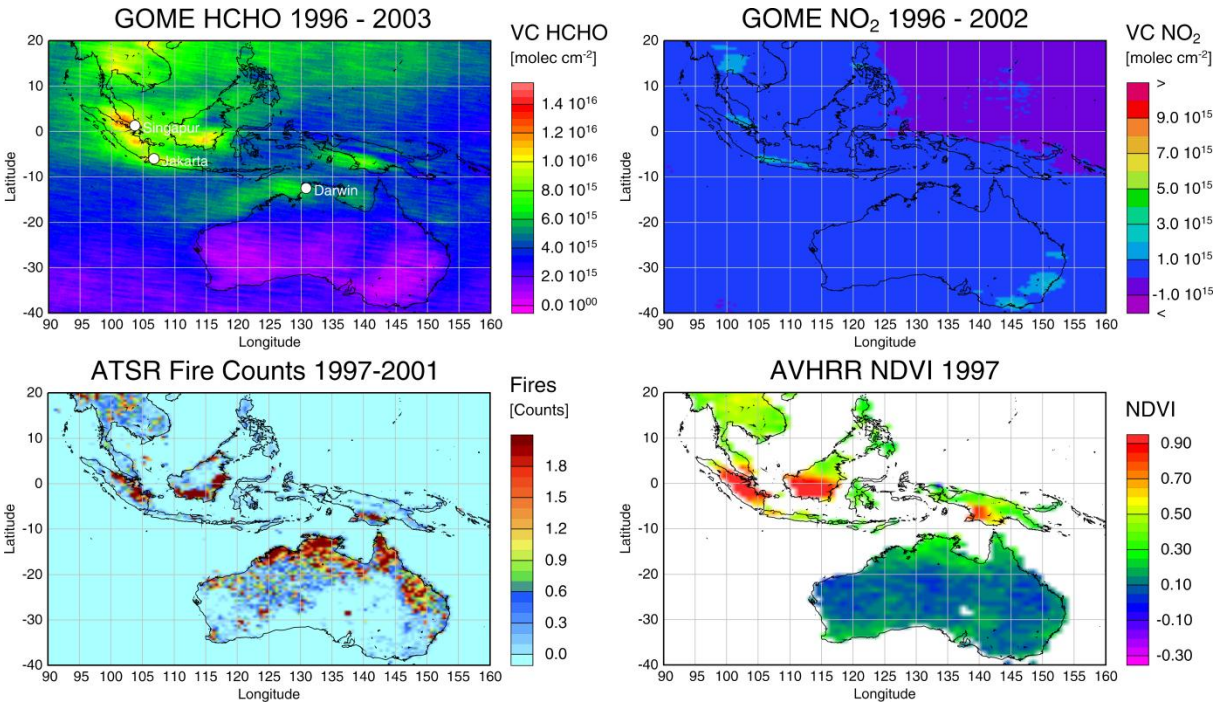

Figure 6-17: Mean values above Australia and Indonesia. Largest amounts of formaldehyde are found above Indonesia. It is remarkable that rain forests above Papua New Guinea and Kalimantan show less amounts of HCHO than there counterparts on Sumatera.

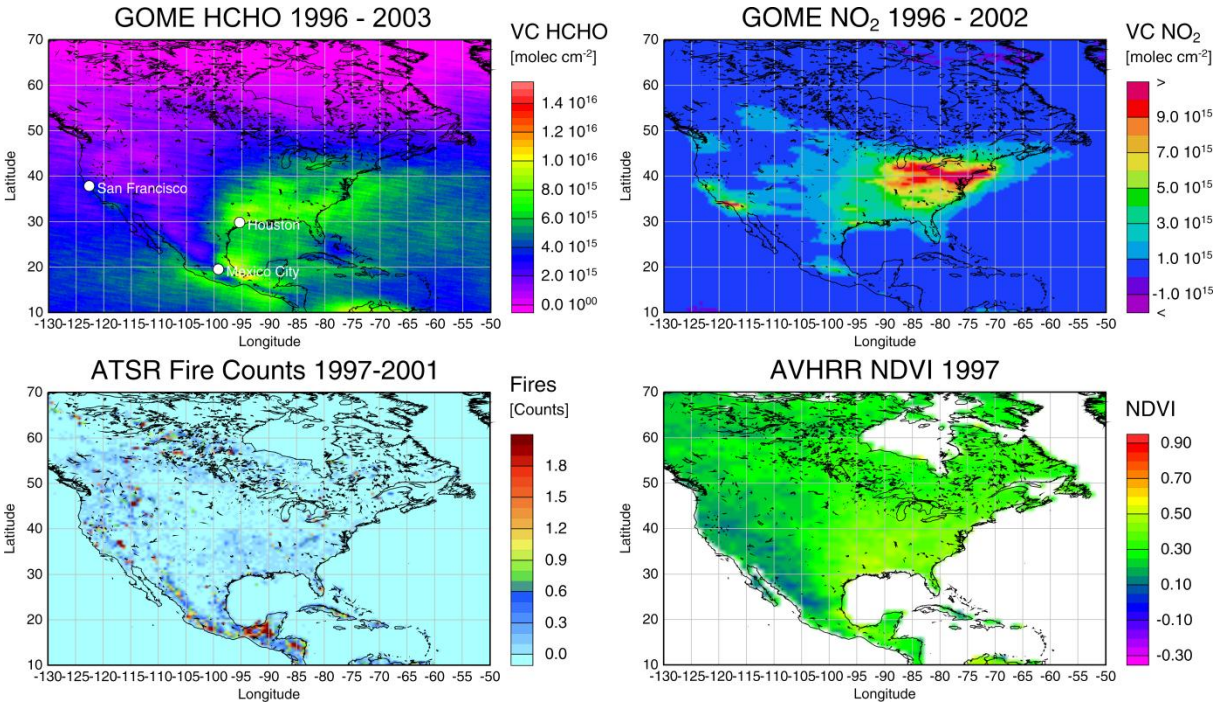

Figure 6-18: Mean values above North America. High values occur above the southeast near to the Gulf of Mexico. This pattern is in good agreement to recent studies e.g. from [Abbot et al., 2003] and is believed to reflect the high isoprene emissions in the growing season of that region. The values above Canada and the West of North America are in general low and close to or below the detection limit. Smaller regions with significant amounts of HCHO are the rain forests in the southeast of Mexico City.

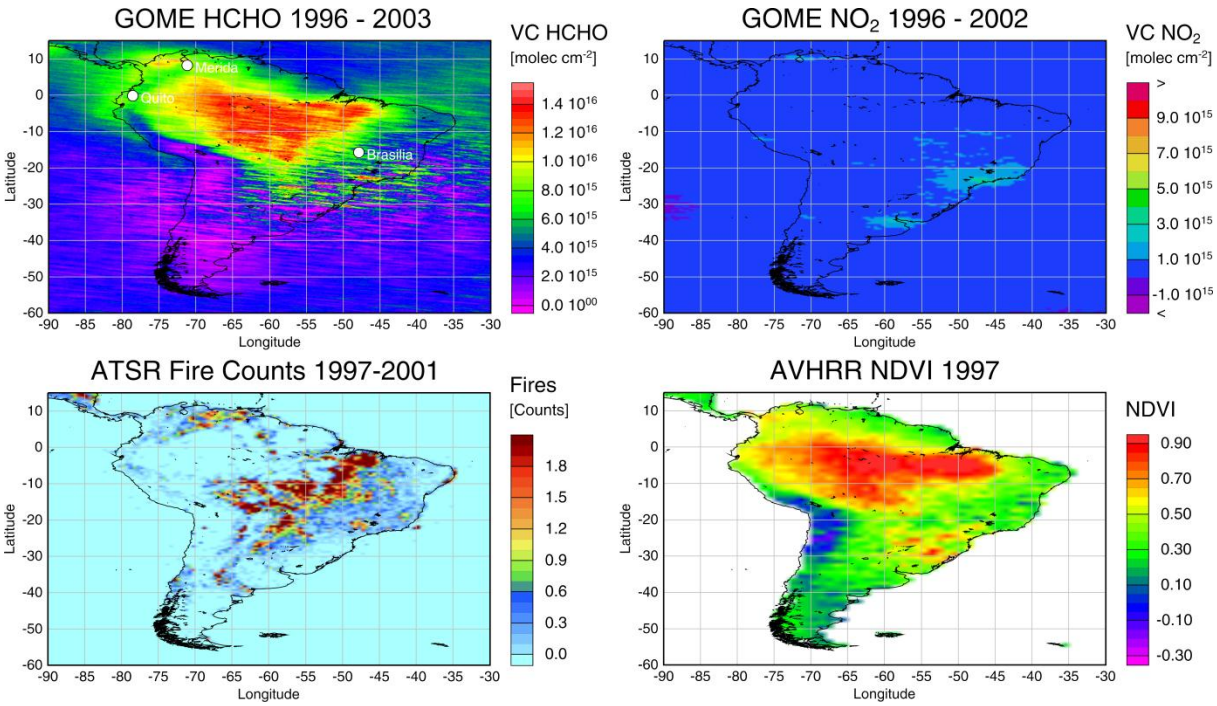

Figure 6-19: Mean values above South America. The large scatter in East Brazil and above Argentina is due to the Southern Atlantic Anomaly (SAA, see section 5.1.18). Largest amounts of HCHO are found above the tropical rain forests in Brazil. Other interesting features are the bulk of formaldehyde west of Mérida and high values between the Galapagos Islands and the coast of Colombia and Ecuador, respectively.

In summary, it can be concluded that biogenic emissions from forests are the dominant sources for formaldehyde on a global scale. Formaldehyde produced from anthropogenic sources is only of minor importance but nevertheless, can be identified from the multiannual averages which is in contrast to findings from e.g. [Palmer et al., 2003]. Therein, the authors state that the GOME footprint is too coarse to resolve anthropogenic emissions. Although biomass burning seems to contribute quite significantly in some regions, the strongly elevated formaldehyde is mainly attributed to the large rain forests along the equator. On the other hand, forests in Canada / Alaska or Siberia which are mainly needleleaf forests (see Figure 6-20) are not a significant source of formaldehyde precursors. Figure 6-21 assigns the mean GOME HCHO columns to the global land cover: The largest contributions originate from the evergreen broadleaf forests (i.e. the rain forests) as expected, but even woodland, wooden grassland, deciduous broadleaf forest and cropland show up with elevated levels of formaldehyde well above the background amounts.

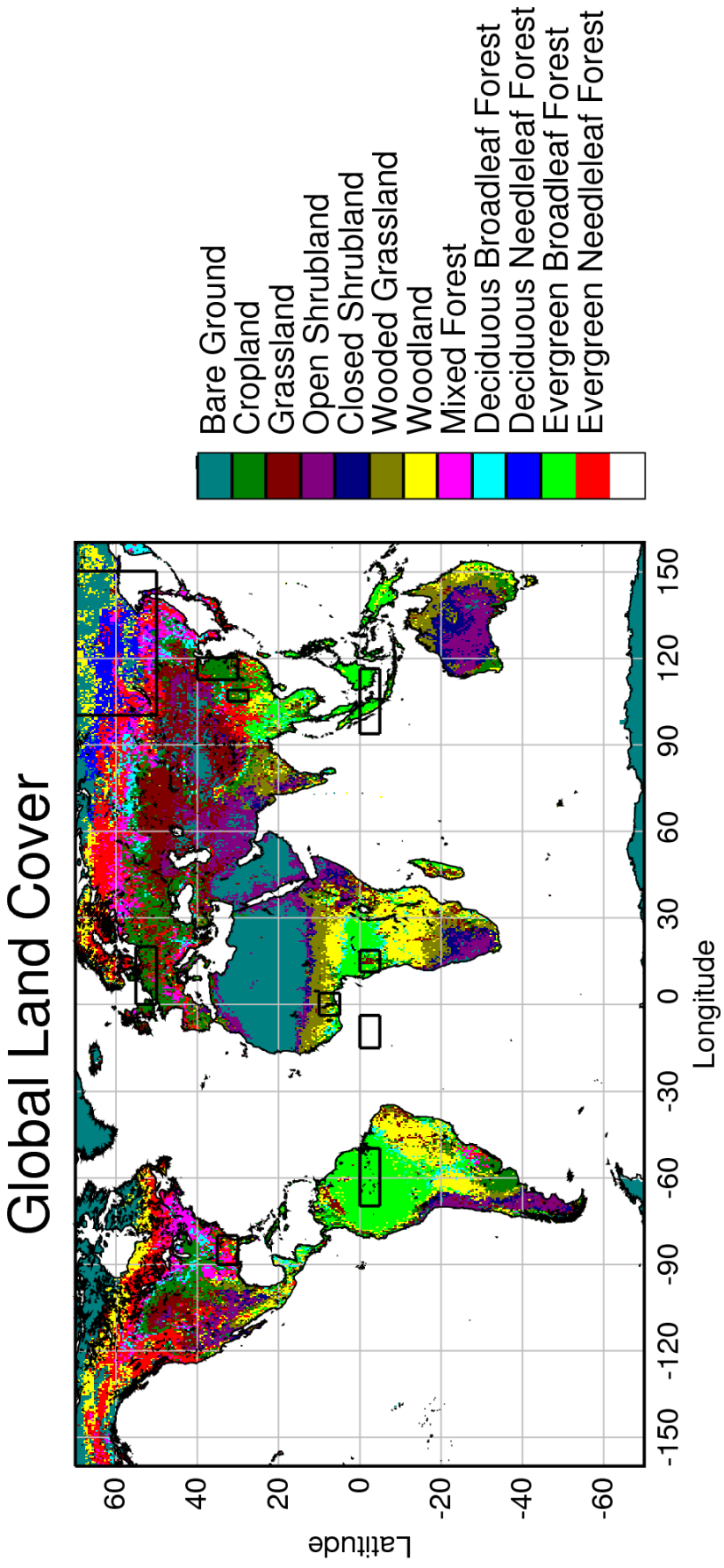

Figure 6-20: Illustration of the global land cover, see also Figure 6-21. Black rectangles indicate regions selected for the model comparison in section 6.4.3.

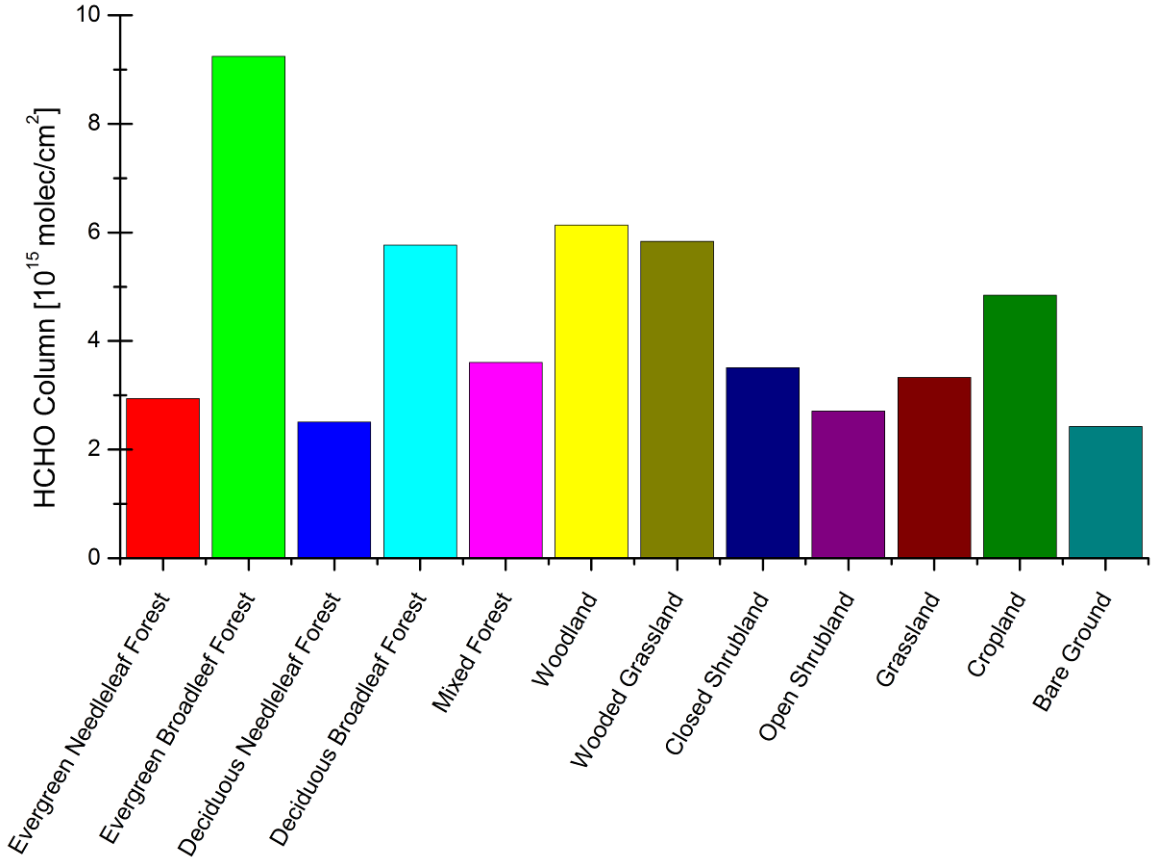

Figure 6-21: Mean formaldehyde columns for different land cover types according to the classification by the Global Land Cover Facility (GLCF), University of Maryland Institute for Advanced Computer Studies [Defries and Townshend, 1999; Hansen et al., 2000]. For this plot, the GLCF data product at 8 km resolution has been regridded to 0.5°x0.5° and then used to assign the GOME HCHO columns.

Surprisingly, quite large amounts of formaldehyde were detected over the oceans and other large bodies of water like the Mediterranean Sea, the Gulf of Mexico and west of Columbia and Ecuador. Besides problems of the retrieval over water cannot be excluded completely, also transport and local sources could be responsible for the enhanced formaldehyde. The lifetime of formaldehyde and also that of the main biogenic precursors, isoprene and monoterpenes is estimated to be a few hours (e.g. [Kesselmeier and Staudt, 1999; Meyer-Arnek et al., 2005]) which rules out long range transport and rather indicates the possibility of e.g. *in situ* production from long-lived hydrocarbon compounds in biomass burning plumes and/or airmasses with biogenic origin (e.g. MBO [Guenther et al., 1995], ethene, propene, methanol [Heikes et al., 2002], some of them observed in significant levels above the oceans [Singh et al., 2004]). Marine fluxes of biogenic VOCs (e.g. isoprene), with seaweed and phytoplankton as known sources (e.g. [Shaw et al., 2003]) are another possible explanation of elevated levels of formaldehyde above remote ocean sites. Even though the total fluxes of isoprene were estimated to be two to three orders of magnitude smaller for the oceans than that of terrestrial origins (e.g. [Palmer and Shaw, 2005] and references therein), the abundance of small amounts in marine air may significantly elevate formaldehyde above that level generated by methane oxidation only [Lewis et al., 2001].

Extremely low formaldehyde is observed over deserts and other arid regions implying either measurement artefacts due to the high albedo which is not very likely or a chemical explanation: Due to the very low relative humidity over these regions, there is a lack of OH, consequently preventing production of formaldehyde.

6.2.2 SCIAMACHY HCHO and CHOCHO

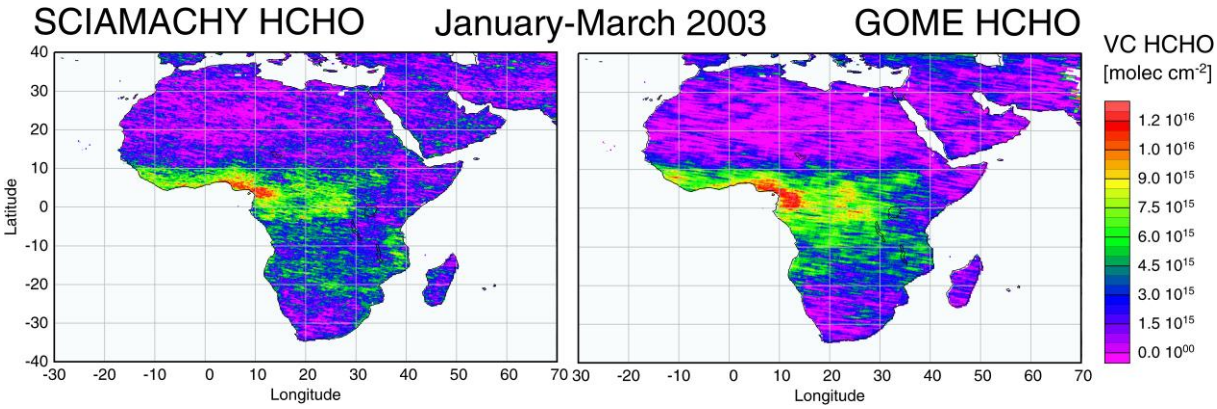

Figure 6-22: Comparison of GOME and SCIAMACHY results for January to March 2003. The GOME data have been selected to match SCIAMACHY nadir measurements.

In order to test the quality of the SCIAMACHY formaldehyde retrieval, several comparisons with GOME data have been carried out. Unfortunately, the overlap between GOME and SCIAMACHY global observations is limited to a few months. This prevents possible studies on different seasonal behaviour of the two instruments. In addition, poorer spatial coverage and a smaller SNR of SCIAMACHY make validation of single orbits difficult. Thus, Figure 6-22 shows a comparison of both instruments for formaldehyde above Africa only from January to March 2003. This region was selected because it exhibits significant amounts of HCHO during that season. The GOME data shown here are chosen to match the SCIAMACHY nadir observations. In general, the agreement is reasonable having a correlation of 0.73 and somewhat smaller column values in source regions (up to about $1x10^{15}$ molec/cm^2) for SCIAMACHY. Although this might be in part explained by the diurnal cycle of formaldehyde, an artefact due to the shifted fitting window is likely.

The yearly mean shown in Figure 6-23 reflects a similar global distribution of HCHO as that obtained from the GOME measurements which gives confidence into the retrieval algorithm. Actually, the SCIAMACHY pattern benefits from the better spatial resolution and small source regions are more accentuated. This is the case e.g. in Asia near to the Himalayas, in China for strongly polluted areas and in particular in South America for the Andes.

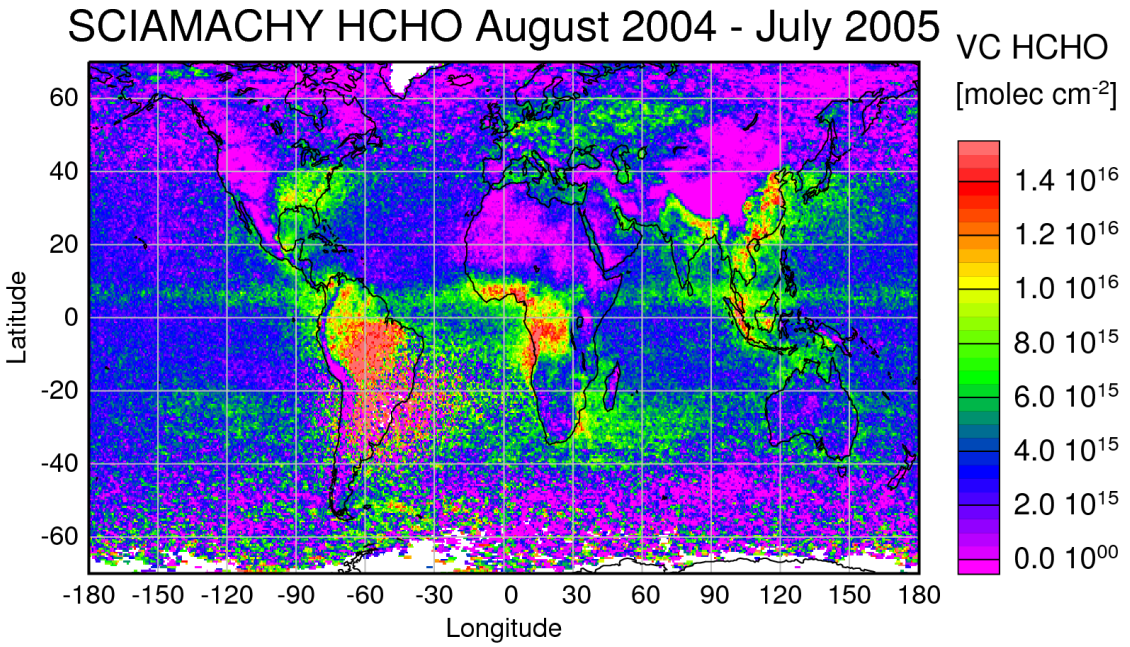

Figure 6-23: Yearly mean of HCHO derived from SCIAMACHY observations from August 2004 to July 2005. Small source regions are more accentuated than in GOME due to the better spatial resolution of the instrument. Again, desert areas as well as mountain sites exhibit the lowest amounts of HCHO. The small stripe a few degrees north of the equator is probably an artefact due to the reference sector method applied to the SCIAMACHY measurements of formaldehyde (section 5.5.3).

Very similar to GOME, several water bodies show up with increased amounts of formaldehyde: the Mediterranean Sea, the Arabic Sea, the Pacific west of Colombia, the Atlantic west of Congo. High values showing up in the southern hemisphere near to 60°S are presumably an artefact due the poorer SNR in the SCIAMACHY measurements and/or an interference to ozone and BrO which are the dominant absorbers in the fitting window (section 5.1.2).

Figure 6-24 presents the first global picture of glyoxal. Even though other groups have found evidence for CHOCHO in some regions (e.g. close to biomass burning areas in South Africa, [Kurosu, 2005]) from spaceborne OMI measurements, this is the first study showing significant levels of glyoxal in various regions on the globe.

The three main regions with enhanced glyoxal and amounts larger than $1x10^{15}$ molec/cm^2 are in South America, Africa and Asia. At first sight, this pattern is quite similar to the global picture of formaldehyde. However, a closer look reveals some differences: Increased amounts of glyoxal are rather limited to the source regions reflecting the short lifetime of glyoxal. In South America, high column values can be found at the Amazon Basin which forms the world's largest tropical rain forest. Otherwise, the topography is reflected in the picture: At the Andes itself and to the west but also the massif in eastern Venezuela show up with only background glyoxal as expected. Also in Africa, enhanced glyoxal can be found at regions with tropical rain forests and biomass burning.

In Asia, glyoxal is mainly found at Cambodia, Thailand, Sumatra, Borneo and particularly Nepal/ northern India. Here, the southern mountainside of the Himalayas is covered with rhododendron species. These plants belong to

the family of the ericaceae and some of them produce a toxin (Grayanotoxin, [Zhang et al., 2005]) that belongs to the diterpenes which are possible precursors of CHOCHO .

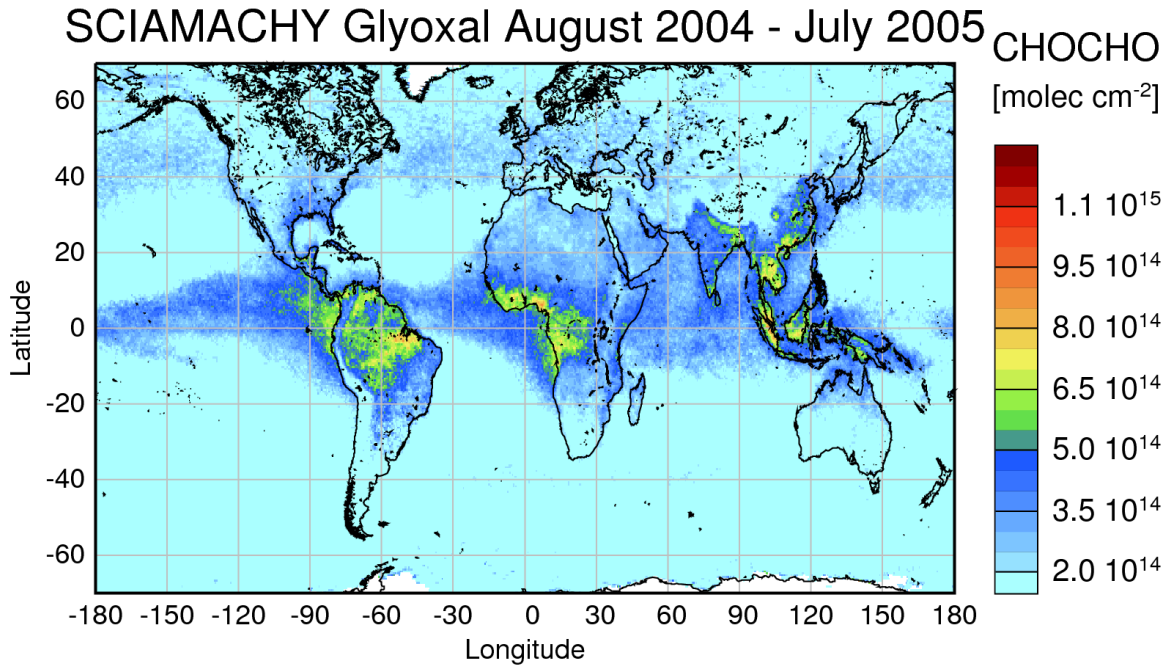

Figure 6-24: Yearly mean for CHOCHO derived from SCIAMACHY observations from August 2004 to July 2005. The pattern is quite similar to that of formaldehyde which supports prospects on similarities of precursors for both trace gases.

Column amounts over water are influenced by liquid water absorption (see also section 5.1.17). This can lead to negative values above clear water regions. However, as can be seen in Figure 6-24, several regions above water bodies exhibit significant elevated levels of glyoxal. This includes regions which are known as biologically very active: E.g. near to the equator, in front of the Arabian Peninsula and close to the coast of China. In analogy to formaldehyde, the Pacific between the Galapagos Islands and the coast of Colombia yield high amounts of glyoxal of up to $8x10^{14}$ molec/cm^2. Since it is very unlikely that the retrieval for both, HCHO and CHOCHO fails in the same region, these observations are probably due to a large source of biogenic VOC here. Recently, Warneck [2005] has pointed out in a box model study that glyoxal is a prominent oxidation product from ethene, acetylene, propane, propene and acetic acid in the marine troposphere.

Figure 6-25 illustrates the distribution of formaldehyde and glyoxal during a biomass burning event in Alaska in June 2004. Significant amounts of both trace gases were found and correlate well with fire counts observed by the AATSR instrument. In analogy to what has been stated above, glyoxal seems to be more limited to the source regions than formaldehyde. The total amount of CHOCHO is about 5 to 7 percent of that of HCHO.

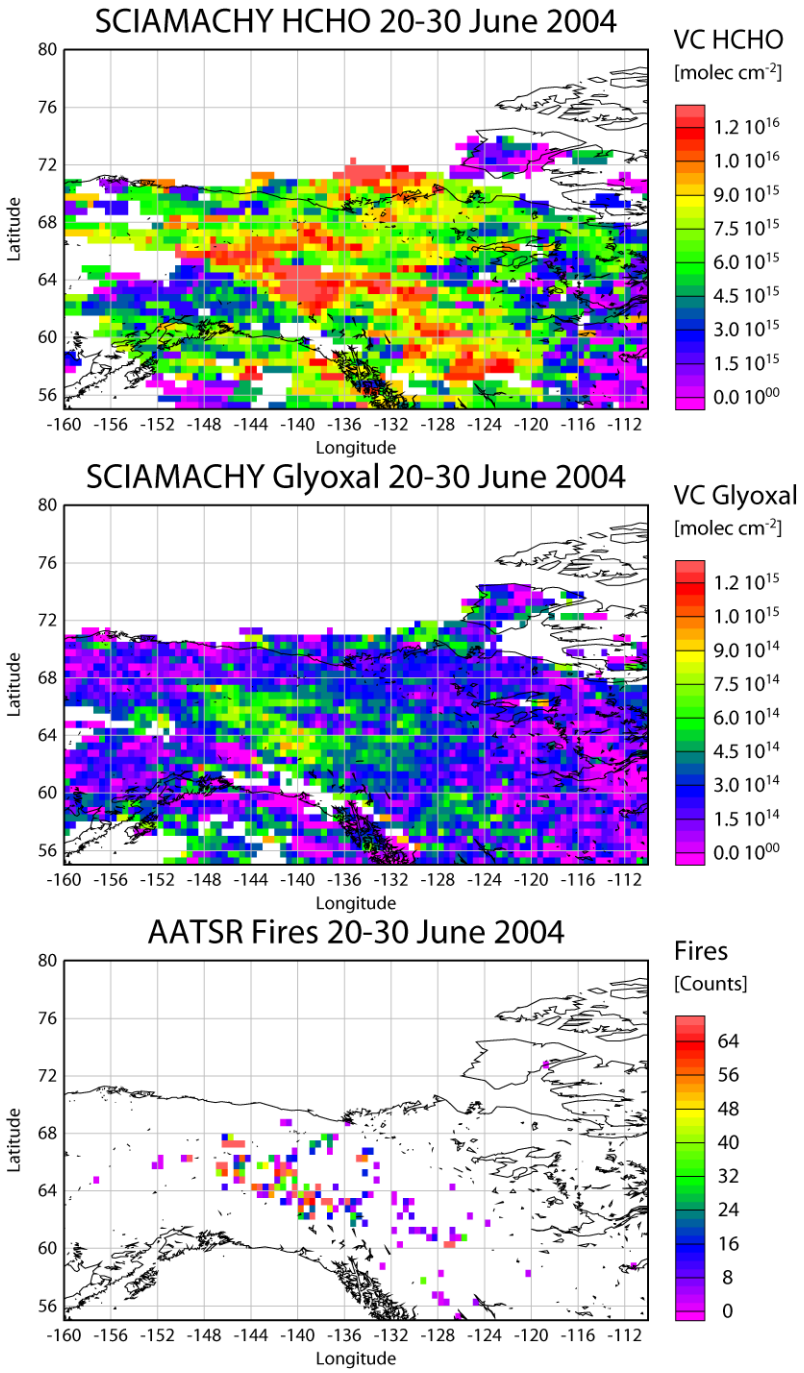

Figure 6-25: Observation of formaldehyde and glyoxal during massive biomass burning in Alaska in June 2004.

In summary, glyoxal exhibits a very similar pattern as formaldehyde on the global scale. This gives confidence into the retrieval algorithm developed here since the fate of both trace gases in terms of sources and sinks in the atmosphere is quite similar (section 1.6.2). The ratio between both glyoxal and formaldehyde was found to be about one to twenty for source regions like tropical rain forests which is in the same range as that found from MAX-DOAS observations (section 6.1.1.1). Again, that is in this stage of investigation a brilliant result which supports expectations by e.g. Volkamer et al. [2005].

6.3 Comparison with recent studies

Formaldehyde has been measured in the atmosphere for several decades. The following Table 15 gives an overview on selected studies mainly on HCHO observation in mid- and low latitudes. The emphasis was placed on measurments with a large spatial coverage. Some of them have been used to prove the findings from this study, where the focus is on the GOME time series from 1996 to 2001 and on observations above water bodies.

6.3.1 Tropospheric distribution of formaldehyde during TROPOZ II

A very comprehensive study on the distribution of formaldehyde in the troposphere was carried out by Arlander et al. [1995]. They have reported on airborne *in situ* measurements of formaldehyde as part of the TROPOZ II campaign in January 1991. The data set includes 30 profiles between 70°N and 60°S covering the coasts of western Europe, East Africa, South America and eastern North America. Formaldehyde was measured from ground to 10 km altitude and a vertical decrease was found in all cases. This is in good agreement with finding from this study (section 6.1.1). Here, we have calculated the vertical columns by integrating the airborne profiles of some of the flight tracks and then compared them to the mean GOME observations of every January from the full time series, i.e. 1996 to 2003. This seems to be appropriate since the year-to-year variation of the global formaldehyde is small (see section 6.4.3).

For measurements near to the coast of Colombia which is one of the water bodies with elevated levels of formaldehyde, a vertical column of $8x10^{15}$ molec/cm^2 was derived from the *in situ* measurements. This result matches quite well the observations of GOME in the range of 7.5 to $9x10^{15}$ molec/cm^2 (see Figure 6-19). While above the South Atlantic close to Argentina, VCs in the order of $4x10^{15}$ molec/cm^2 were obtained from GOME, the airborne measurements show up with $4.5x10^{15}$ molec/cm^2. Very high values of formaldehyde in the boundary layer (up to 2.5 ppb_V) were found on flights near to Abidjan in West Africa probably due to biomass burning and biogenic emissions. The VCs were estimated to be in the range of 1.0 to $1.9x10^{16}$ molec/cm^2 which is again in good agreement to typical values of 1.3 $x10^{16}$ molec/cm^2 obtained from GOME. These results again put trust into the retrieval of GOME formaldehyde since even HCHO amounts near to the background and above oceans were found in the same range as from these independent measurements.

Table 15: Observations of Formaldehyde in the atmosphere with the main focus on mid- and low latitudes.

Authors	*Time*	*Location*	*Instrument*	*Platform*	*Major findings*
[Arlander et al., 1995]	Jan 1991	70°N – 60°S	*in situ*	airborne	Several ppb_V in boundary layer close to source regions, always decreasing profile shape with 50 to 100 ppt_V in 8 to 10 km altitude
[Notholt et al., 2000], partly unpublished	1996 – 2003	Atlantic 60°N – 60°S	FTIR	ship	Vertical columns between $3x10^{15}$ and $2x10^{16}$ molec/cm^2, maximum near to ITCZ, good agreement to [Weller et al., 2000]
[Weller et al., 2000]	Oct. – Nov. 1996	Atlantic 50°N – 40°S	*in situ*	ship	200 – 1100 ppt_V, maximum near to ITCZ, up to factor 3 compared to model including CO and CH_4 photooxidation
[Martin et al., 2004]	1999 – 2000	Texas	i*n situ* / GOME (UV/vis)	ground-based/ satellite	Vertical columns 1–$3x10^{16}$ molec/cm^2, 60 percent of HCHO and 75 percent of NO_2 in boundary layer (1-2 km), consistent to *in situ*
[Palmer et al., 2003] **[Abbot et al., 2003]**	July 1996 Summer 1996 - 2001	North America	GOME (UV/vis)	satellite	Correlation GOME/model 0.83, emissions improved with GOME HCHO, then correlation 0.84; lowest values in summer 1997
TEMIS website (KNMI, IASB/BIRA)	Jan 1997 – Dec 2001	global	GOME (UV/vis)	satellite	up to now, no publications on this time series, see section 6.3.3
[Marbach et al., 2005]	1997	global	GOME (UV/vis)	satellite	slant columns only, good correlation between biomass burning and elevated HCHO columns
[Singh et al., 2004]	Feb – Apr 2001	Pacific Ocean	*in situ*	airborne	Profiles: 500 ppt_V in remote MBL, 50 to 150 ppt_V in upper troposphere
[Wagner et al., 2001]	Feb – Mar 1999	Indian Ocean (INDOEX)	*in situ*	ship	Different air masses with 200 to 500 ppt_V in MBL, enhanced values in the outflow of the Indian subcontinent

6.3.2 *Polarstern* cruise 1996

Here, GOME measurements of formaldehyde are compared to results from *in situ* [Weller et al., 2000] and FTIR [Notholt et al., 2000] measurements carried out onboard the German research vessel *Polarstern*. The Atlantic traverse ANT XIV/1 started in Bremerhaven, Germany (54°N) on 5 October 1996 and ended in Punta Quilla, Argentina (50°S) on 10 November 1996. The itinerary of the cruise and the corresponding GOME formaldehyde columns for the whole region are shown in Figure 6-26.

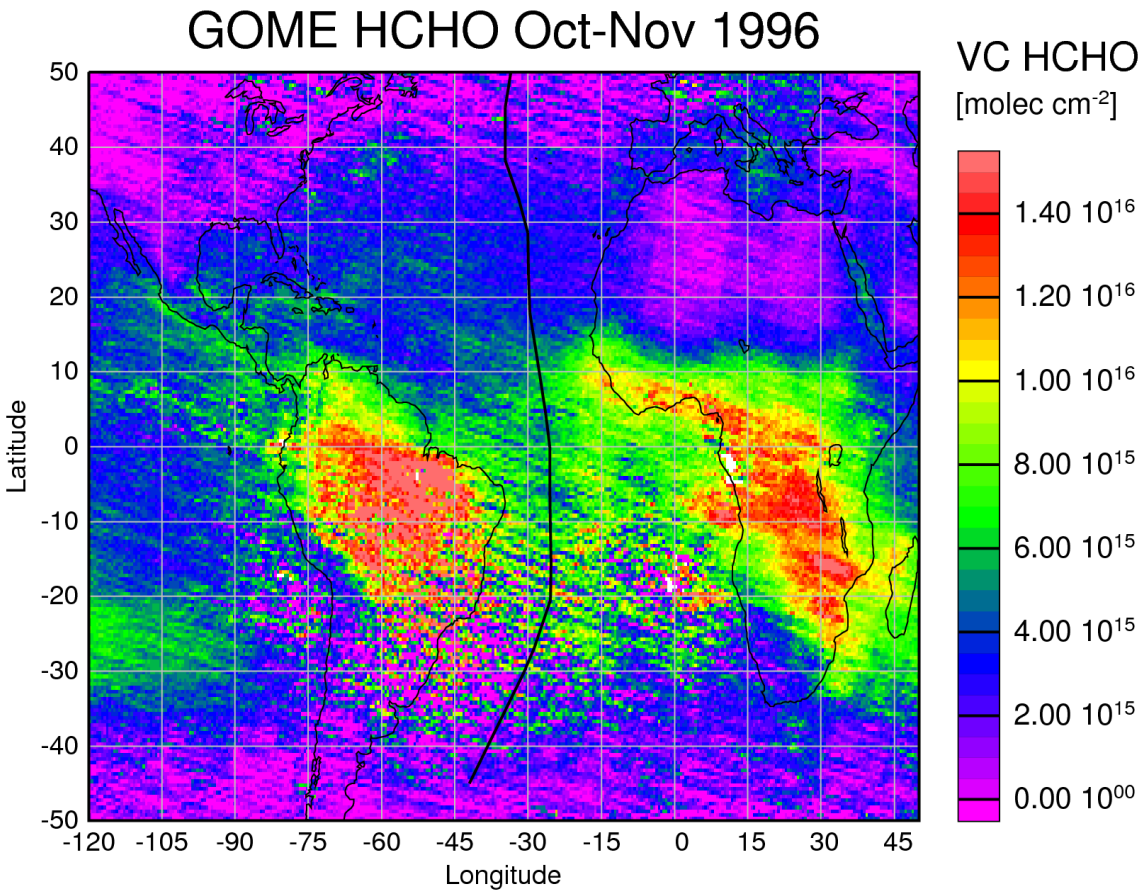

Figure 6-26: Itinerary of the *Polarstern* expedition ANT XIV/1. As background the mean GOME measurements of formaldehyde for October to November 1996 are shown.

The GOME measurements shown in Figure 6-27 were selected for the corresponding values from the FTIR measurements. The *in situ* measurements were converted to vertical columns applying the background profile shape of formaldehyde introduced in 5.2.2.1. In general, the GOME measurements show a reasonable agreement to the vertical columns derived from the *in situ* experiment but there is a large difference up to a factor of three to the columns obtained from the FTIR. Although the reason for that is not clear now, one explanation might be a problem with the absolute values of the formaldehyde cross-section in the infrared. This would also account for the differences found in Ny-Ålesund as described in section 6.1.1.2 .

As further information the HCHO columns obtained from the LMDz-INCA model (see section 6.4) for that region were added to Figure 6-27. There is an excellent agreement for latitudes 10°N to 50°N and those south of 30°S. However, the model underestimates amounts of formaldehyde near to the equator region by a factor of two. This is in agreement with findings from Weller et al. [2000]. They have investigated the measurements of

formaldehyde using a photochemical box model and claimed that the HCHO mixing ratios observed were significantly higher than predicted by the current photochemical theory based on the photooxidation of CH_4 and CO.

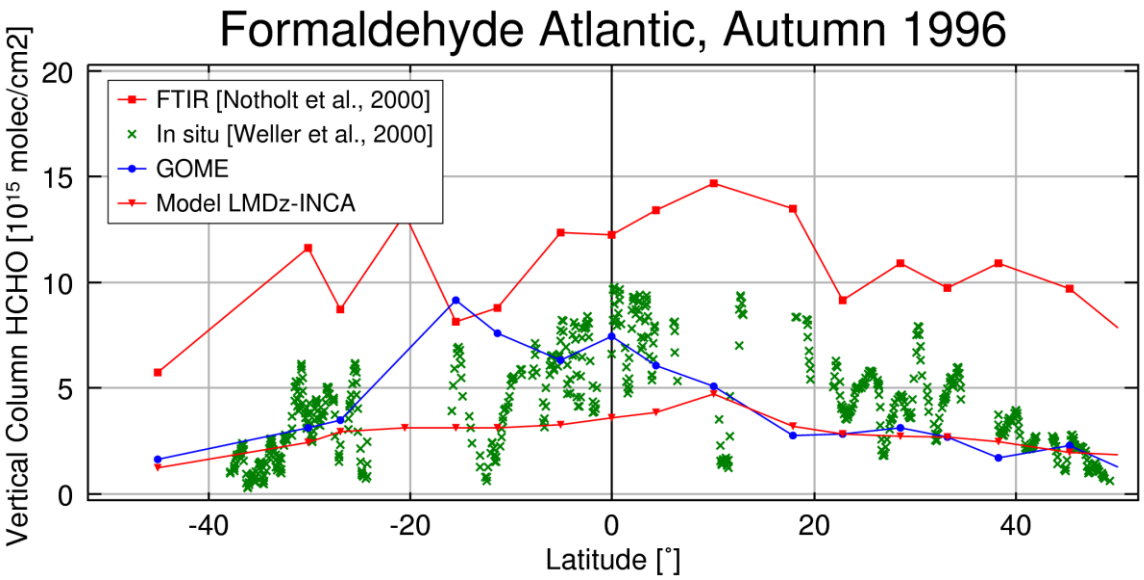

Figure 6-27: Comparison between *in situ*, FTIR, and GOME observations together with model predictions of formaldehyde for the transect illustrated in Figure 6-26.

6.3.3 Other satellite retrievals

Here other retrievals of GOME HCHO are described briefly and major findings compared to those from this study. For SCIAMACHY further data sets are not available.

The focus of the HCHO evaluation of the Harvard group is the interpretation of data above North America. Several studies were carried out [Chance et al., 2000; Palmer et al., 2001; Abbot et al., 2003; Palmer et al., 2003; Wiedinmyer et al., 2005], most of them already mentioned before. The authors use a slightly different approach to calculate the slant columns from the GOME spectra: GOME radiances are fitted directly without smoothing or filtering. The uncertainty was found to be about $4x10^{15}$ molec/cm^2 which is in the same range as estimated here ($3x10^{15}$ molec/cm^2). In general, data for cloud fractions less than 40 percent were given. The slant columns are converted to vertical columns using so-called shape factors, i.e. block air mass factors, derived with profile output from the GEOS-CHEM chemical transport model. The most comprehensive data set from this group was published by Abbot et al. [2003] where the seasonal and interannual variability of formaldehyde above North America was investigated (only for months March to October). The authors found summer maxima lowest in 1997 which is in good agreement to observations presented here (see Figure 6-36, upper panel). They account at least part of the year-to-year variations in the formaldehyde to anomalies in mean surface air temperature reflecting the temperature dependence of isoprene emissions [Guenther et al., 1995]. The largest values, they report ($3.2x10^{16}$ molec/cm^2), are about 20 percent higher than those found here. Even though the authors show enhanced levels of HCHO larger than $1x10^{16}$ molec/cm^2 above the oceans in their figures no further interpretation was given on this.

Marbach et al. [2005] have investigated in detail the ENSO year 1997 on a global scale. They derived HCHO and NO_2 from GOME spectra applying an analogue approach than that one presented here. However, in case of HCHO only slant columns were given preventing any interpretation of the data set at higher latitudes. The over-

all pattern of the HCHO observations with largest values above South America, Africa and Indonesia is quite similar to that found here. The authors report on good correlation between biomass burning and formaldehyde for all regions mentioned above and conclude that biomass burning is a major source of HCHO. This is in contrast to the findings presented here, where biogenic emissions of VOCs are found as the dominant source of HCHO on a global scale.

As part of the TEMIS project, GOME formaldehyde data from 1997 to 2001 were made available to the public. Slant columns of HCHO were retrieved from GOME spectra using the WinDOAS software [Vandaele et al., 2005]. The wavelength region of 337.5 to 359 nm used for the DOAS retrieval is very similar to that chosen here. The results are scaled to the monthly mean values in the 180°W to 150°W reference sector. In a second step the FRESCO algorithm [Koelemeijer et al., 2001] was applied to GOME data to derive cloud fraction and cloud top pressure. The outcome of that step is then used for calculations of the air mass factors to convert the HCHO slant columns to vertical columns. The formaldehyde profile shape necessary for the radiative transfer modelling is given by the chemistry transport model TM4. The following Figure 6-28 and Figure 6-29 shows the TEMIS results and the GOME columns obtained in this study, respectively, exemplarily for September 1997.

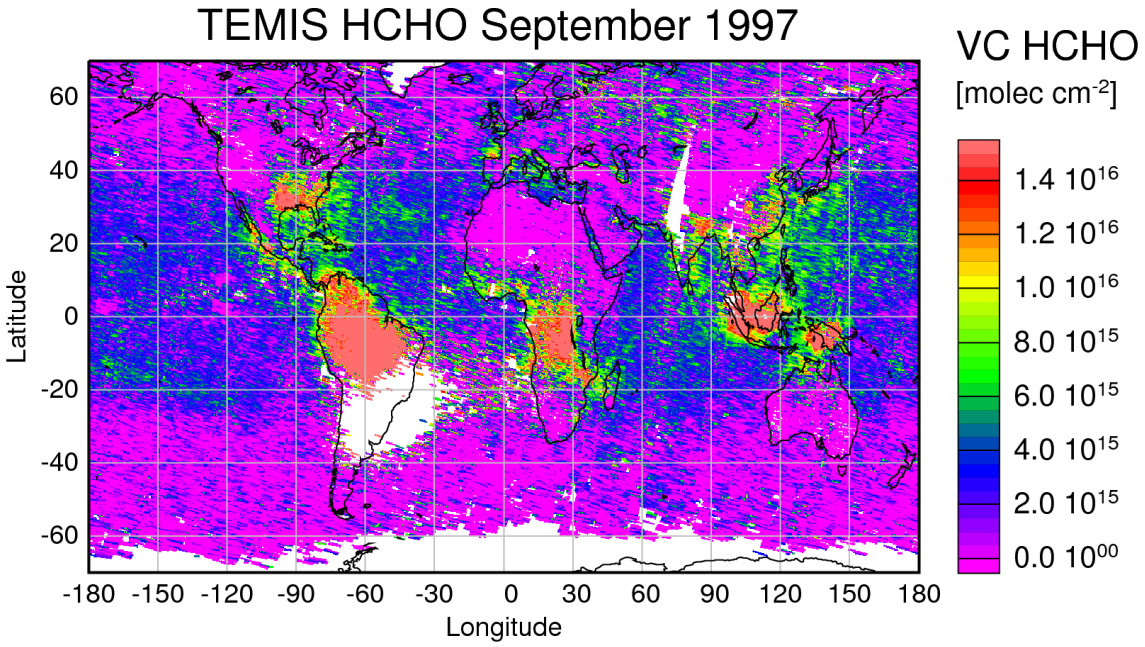

Figure 6-28: GOME HCHO for September 1997 from the TEMIS project. The data are gridded to 0.25° x 0.25°.

The overall agreement between both data sets is excellent. The correlation for September 1997 is 0.78 on the grid of 0.25° x 0.25° with a slope of 0.97 and a small offset of 5×10^{14} molec/cm^2 towards the Bremen data set which might reflect the different assumptions for the reference region.

However, some differences should be pointed out:

1. In general, the TEMIS data product exhibits somewhat smaller values above water and deserts.
2. The scatter above high latitudes is a little bit higher for the TEMIS HCHO.
3. Values above regions with low visibility or high cloud coverage (e.g. Indonesia) are in general larger for TEMIS which might be due to model predictions for the formaldehyde profile in those cases: Although the

GOME instrument observes very small amounts of HCHO because the signal is shielded by clouds and/or smoke, the model predicts high amounts of formaldehyde in the lowest part of the atmosphere. Then the TEMIS algorithm scales the small signal towards the model value: A self-fulfilling prophecy.

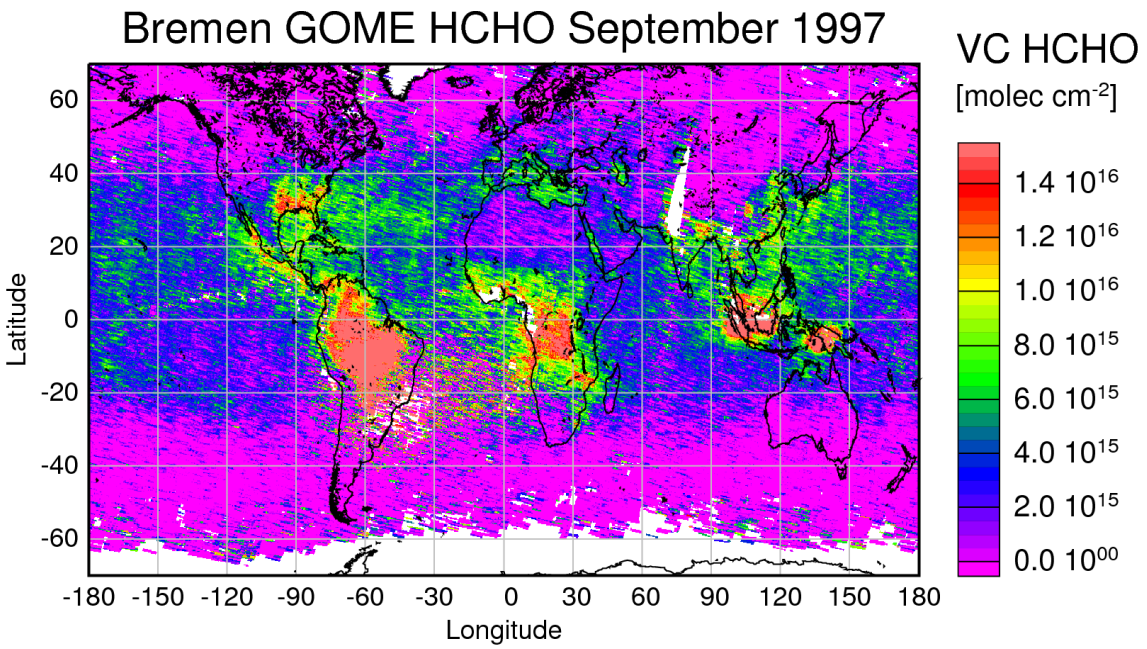

Figure 6-29: GOME formaldehyde data for September 1997 applying the algorithm developed in this study. The grid is the same as in Figure 6-28.

In summary, the agreement with other studies was found to be quite reasonable in section 6.3. In particular, it was shown that high amounts of formaldehyde above water bodies were also observed by *in situ* measurements.

6.4 Comparison of GOME HCHO with model results

Here, a systematic comparison of HCHO columns obtained from the GOME instrument using the algorithms described in chapter 5 with a state-of-the-art model is presented. This comparison comprises the years 1997 to 2001 and is the first study, where long-term global observations of HCHO are compared to model output. All GOME data presented here were gridded on the spatial resolution of the model (3.75° x 2.5°). Further adaptations were not applied (e.g. using model data for a reference sector).

6.4.1 Model LMDz-INCA

The LMDz (Laboratoire de Meteorologie Dynamique, zoom) is a grid point General Circulation Model (GCM) developed initially for climate studies by Sadourny and Laval [1984]. In LMDz the finite volume transport scheme of Leer [1977] is used to calculate large-scale advection of tracers. The parameterisation of deep convection is based on the scheme of Tiedke [1989] and a local second-order closure formalism is used to describe turbulent mixing in the planetary boundary layer (PBL). LMDz (in its version 3.3) has a horizontal resolution of 3.75° in longitude and 2.5° in latitude and uses 19 vertical sigma-p levels extending from the surface to 3 hPa. The Interactive Chemistry and Aerosols (INCA) model has been integrated into LMDz. INCA simulates tropospheric chemistry, emissions and deposition of primary tropospheric trace species including non-methane hydro-

carbons. The INCA chemical scheme includes 85 chemical species and 303 chemical reactions. A detailed description and evaluation of LMDz-INCA can be found in Hauglustaine et al. [2004], Folberth et al. [2005] and Lathiere et al. [2005].

This five-year simulation was performed by Sophie Szopa, using the nudged version for meteorology (i.e. meteorological fields are relaxed toward the ERA40 reanalysis). Regarding emissions, anthropogenic emissions are from the EDGAR V2.0 inventory [Olivier et al., 1994], biomass burning emissions are those of [van der Werf et al., 2003; van der Werf et al., 2004], biogenic emissions are from GEIA [Guenther et al., 1995] and aircraft emissions are provided by the NASA. Two different runs were carried out: one with a static scenario for biomass burning (run 33), the other one considering the interannual variability of biomass burning (run 34). The model output is analysed at 10:30 local time, close to the overpass time of the satellite. Here, no collocation with the measurements was carried out which might lead to biases due to the incomplete spatial coverage of the instrument. However, this should affect only a few months of this multiannual comparison.

6.4.2 Model and GOME formaldehyde on a global scale

Figure 6-30 shows the mean formaldehyde columns from GOME but with a resolution adapted from the model. The corresponding model results for the same time period from 1997 to 2001 are illustrated in Figure 6-31. Figure 6-33 to Figure 6-35 show the monthly means for both, model and GOME observations. For these graphs the single months from 1997 to 2001 have been averaged.

Obviously, the coarse grid of the model introduces some errors at mountain ranges: Although the outline of the Himalayas seems to be captured well, there are problems in the Andes which have only a very small extent in longitudinal direction.

In general, over land, the model retrieves larger columns of formaldehyde than those observed by GOME, particularly above South America. However, the pattern of the main source regions of formaldehyde in the tropics as well as the general latitudinal distribution and the seasonal trend with higher values in each hemisphere in summer are in good agreement.

In contrast, the formaldehyde over the oceans evident in the measurements is not reproduced by the model. The scatter plot of Figure 6-32 illustrates the correlation between the measurement and the model: While the correlation coefficient for measurement and model is high (overall 0.81) and also for land and ocean separately (0.89 and 0.83, respectively), the model systematically overestimates the formaldehyde over land and underestimates HCHO over most parts of the oceans. The correlation coefficients for single months are somewhat lower but nevertheless with values between 0.63 (in January and June) and 0.78 (in March) quite reasonable. The poorer agreement in January and June is at least partly due to albedo effects in the GOME observations: High latitudes in winter exhibit in some regions high amounts of HCHO caused by too low albedo values utilised in the air mass factor calculation (see section 5.4) which leads to an overestimation of the HCHO column.

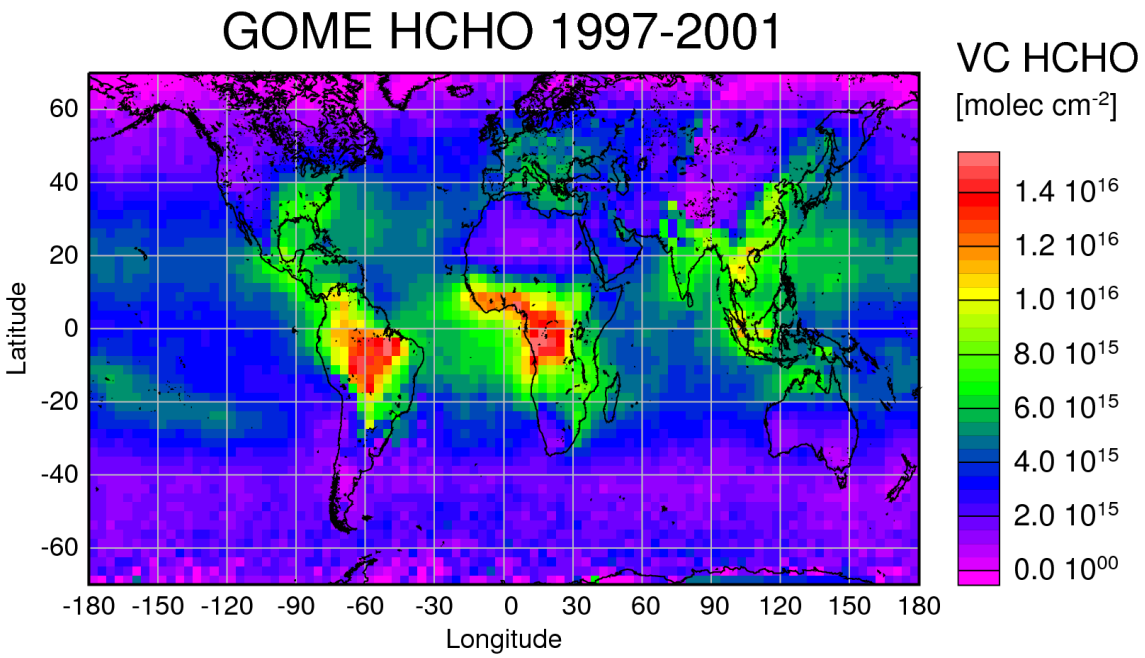

Figure 6-30: Mean values from GOME on model resolution (2.5° x 3.75°) derived from monthly means from January 1997 to December 2001.

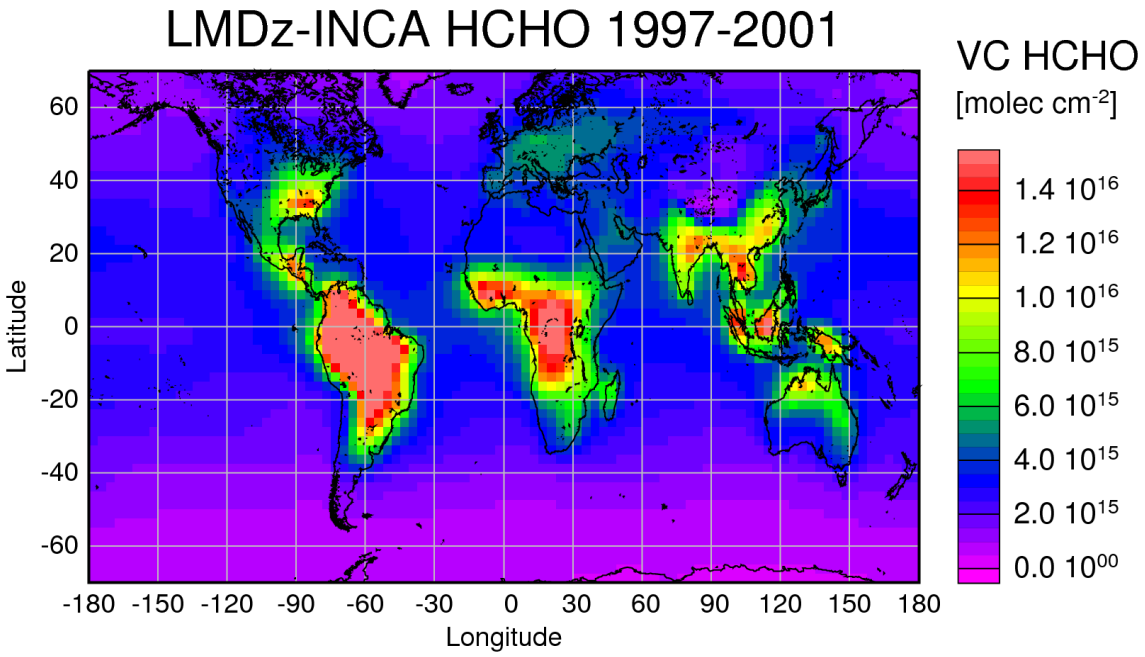

Figure 6-31: Mean values from model – here, the run taking into account the annual variability of biomass burning was utilised (run 34).

As mentioned before, transport of isoprene and formaldehyde seems to be an unlikely explanation of the high columns observed over some oceanic regions due to their short lifetime of up to a few hours only. Transport over distances of about 50 to 150 km is feasible, but not long-range transport as would be necessary to explain the high values e.g. west of Africa. Two other explanations are possible: As already mentioned in section 6.2.1, *in situ* production of HCHO from other more long-lived precursors or an oceanic source.

In particular, biomass burning plumes are known to contain high concentrations of other hydrocarbons [Price et al., 2004; Holzinger et al., 2005], and little is known on the atmospheric chemistry and fate of these substances, which are not included in the INCA model run. Similarly, biogenic emissions from forests are not limited to isoprenes and monoterpenes, and potentially other molecules which are correlated to isoprene emissions could act as HCHO precursors. In addition, recycling mechanisms within an aging plume are conceivable, but at this point mere speculation.

As oceanic source, biogenic emissions are again a possibility, and algae are known to be a source of carbohydrates (section 6.2.1).

A very prominent difference between model and measurements are the lower HCHO columns measured over Australia and the southern part of South America. While the overall hemispherical gradient agrees between measurement and model, there is very little evidence for HCHO over Australia in the measurements in particular in the southern hemispheric winter with the exception of the far north, an area of intense burning activity. This is particularly surprising as eucalyptus is known to be an efficient isoprene emitter as discussed above.

In order to identify more distinctively the deviations between model and GOME observations several regions on the globe were picked to create time series of formaldehyde from 1997 to 2001 for both, GOME and model. This comparison is presented in section 6.4.3.

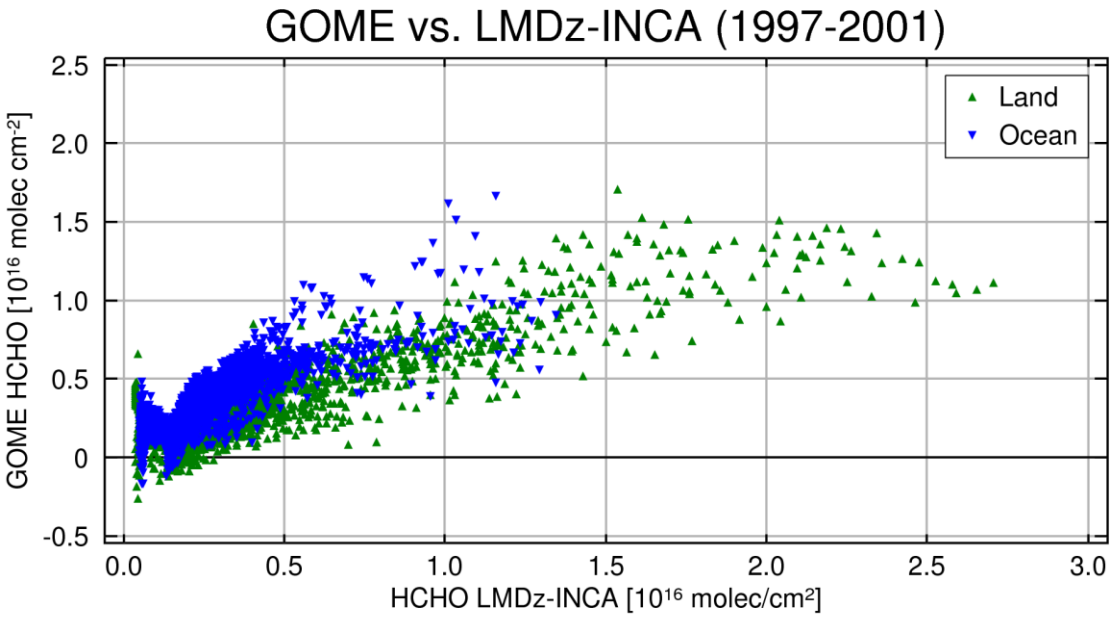

Figure 6-32: This scatter plot shows the correlation between GOME observation shown in Figure 6-30 and the Model results given in Figure 6-31. The correlation coefficient is 0.81 overall, while it is for the continents 0.89 and the oceans 0.83, respectively. The slope is 0.64 for the continents and 1.05 for the ocean.

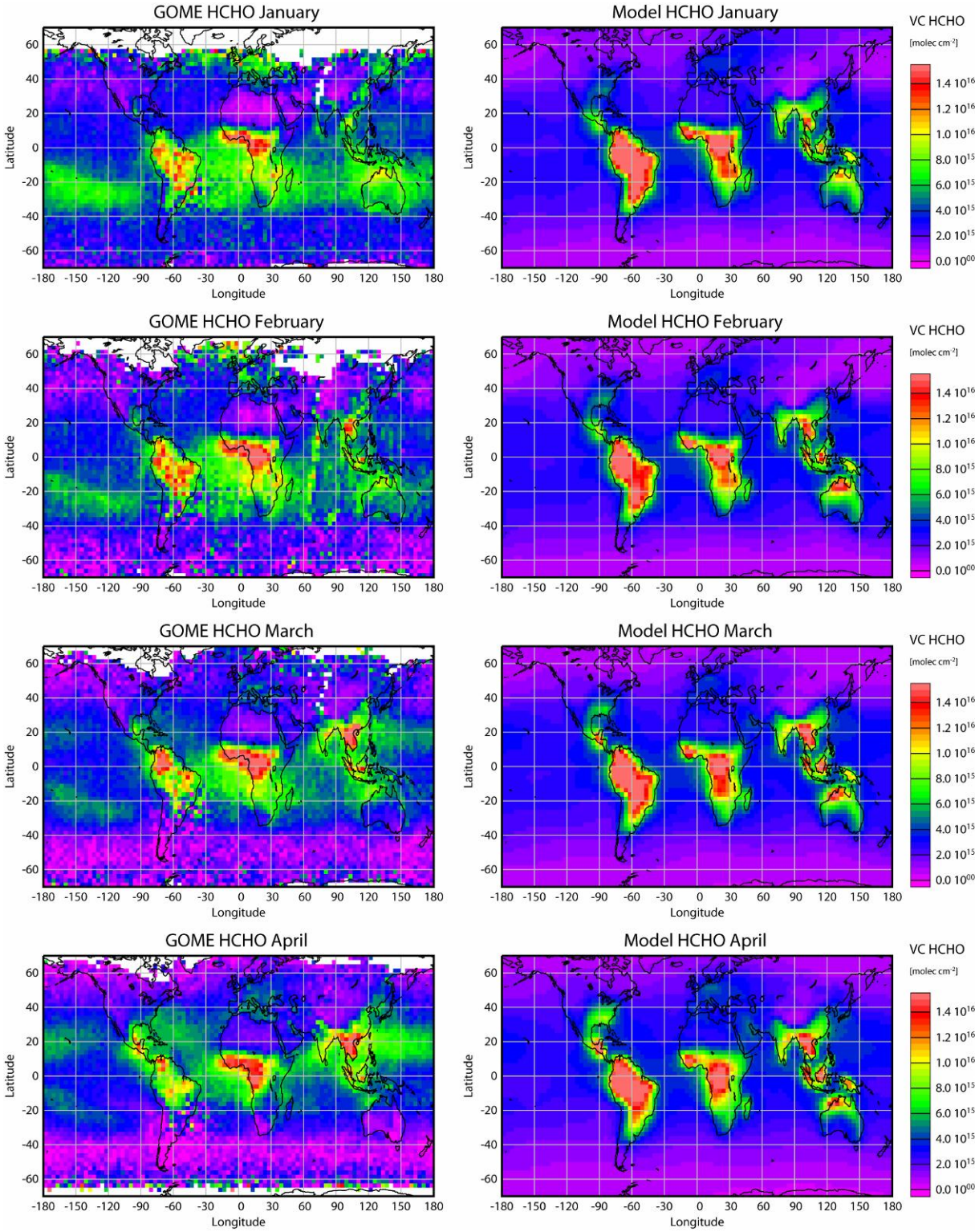

Figure 6-33: GOME and model (run 34) monthly means from January to April. Particularly in January and February, the GOME observations yield high amounts of HCHO in northern high latitudes which is most probably according to albedo effects in the AMF calculation and therefore not real.

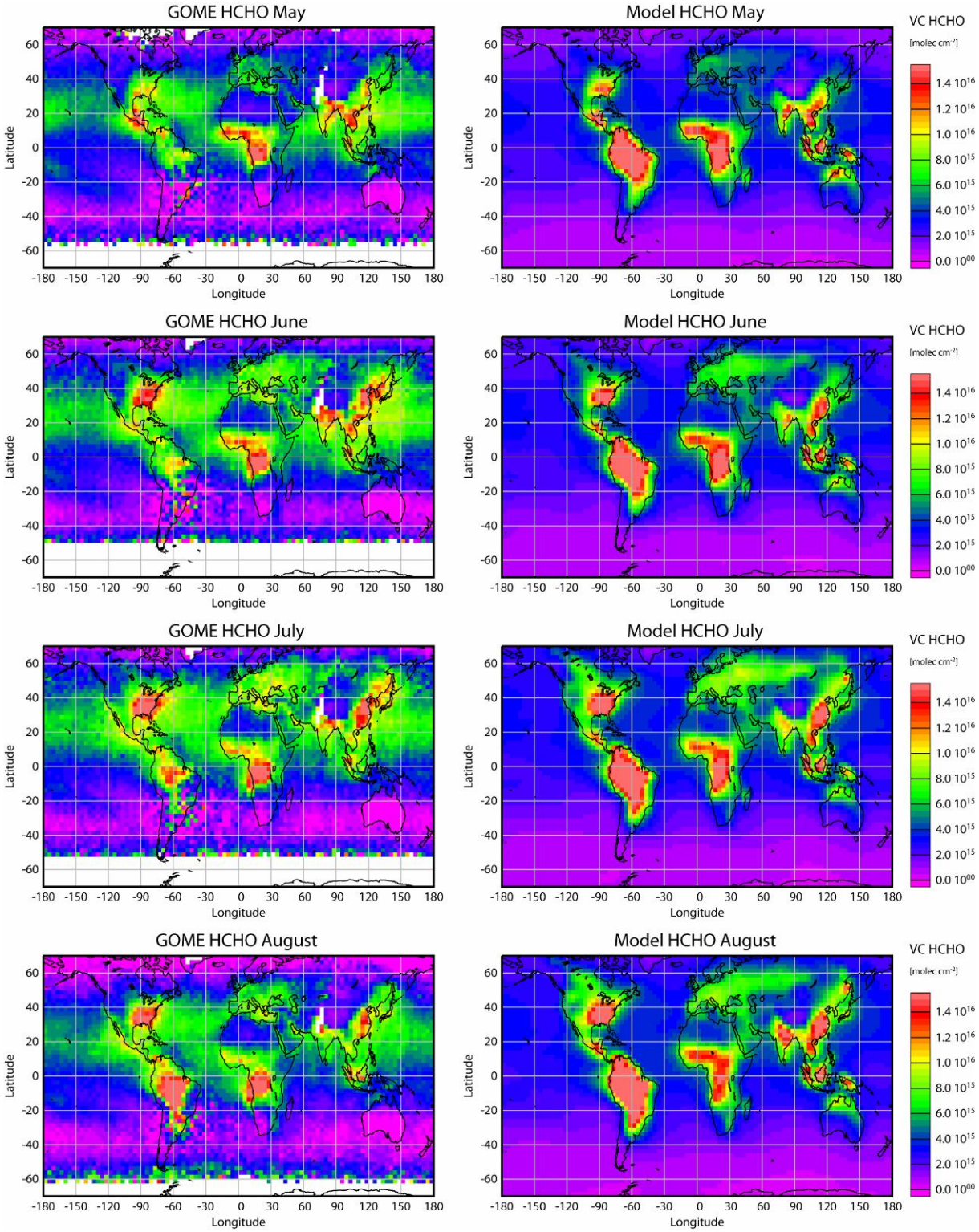

Figure 6-34: GOME and model (run 34) monthly means from May to August. The agreement above the continents is excellent, both in pattern and in magnitude, with the exception of South America and North Australia. Particularly in May and June, the model overestimates the HCHO column by a factor of two. Similarly to the winter months in the northern hemisphere, GOME observations show unrealistic amounts of HCHO in southern high latitudes.

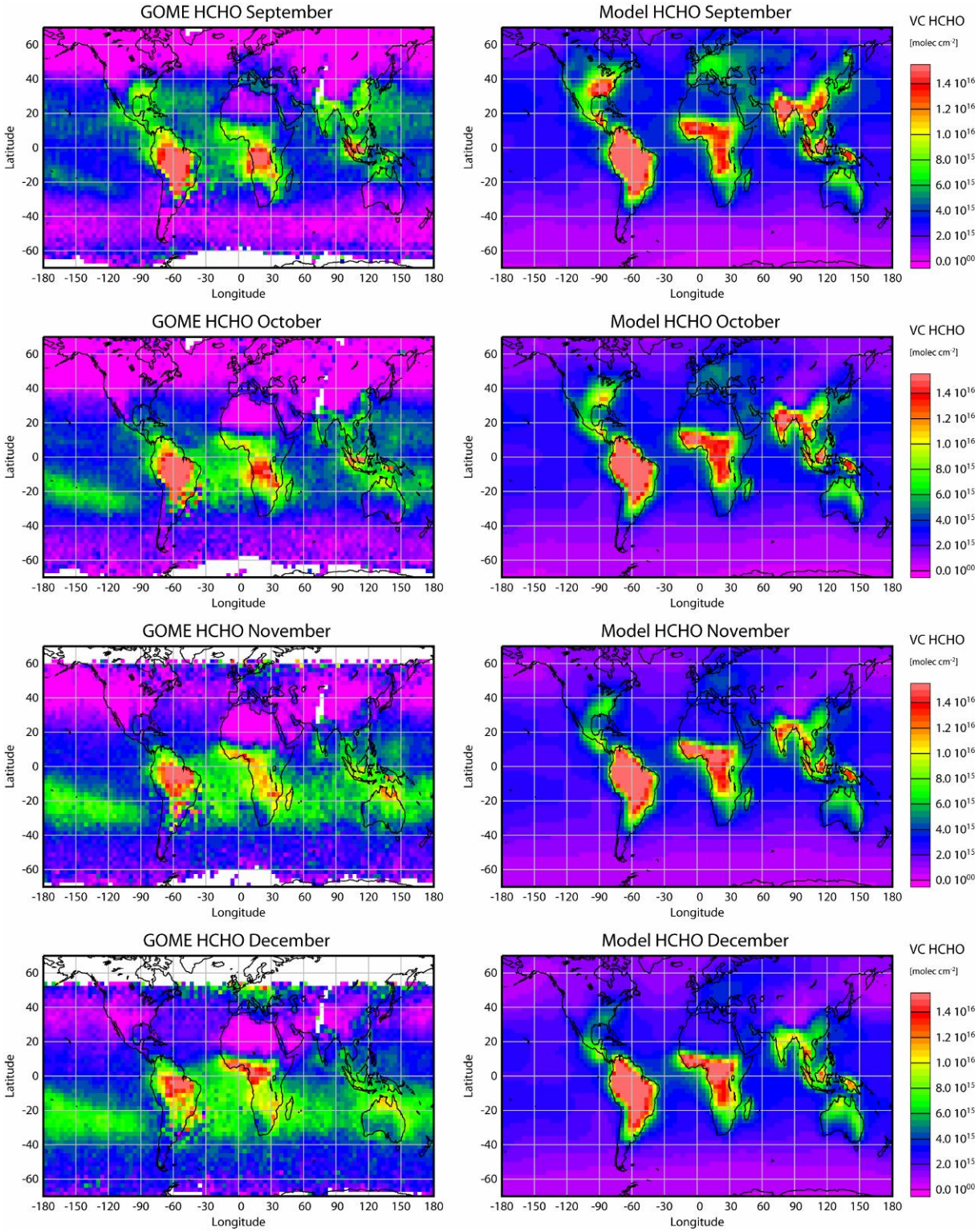

Figure 6-35: GOME and model (run 34) monthly means from September to December. Again, the agreement above continents is very good. Even though the model is not able to reproduce the formaldehyde above water, some spatial structures are found in both, model and GOME: E.g. lower values of HCHO in the Pacific near to Chile.

6.4.3 Model and GOME formaldehyde for selected regions

For eleven selected regions marked in Figure 6-20, the seasonal cycle of GOME formaldehyde is compared to model data over a time period of five years. Here, the monthly mean data is shown. The regions were selected in order to obtain a representative set with different scenarios like biogenic emissions, biomass burning and anthropogenic emissions.

The oak forests in the so-called Ozarks of south eastern North America are efficient emitters of isoprene [Wiedinmyer et al., 2001; Wiedinmyer et al., 2005]. Depending on light intensity as well as growing season (May to August) formaldehyde production is expected to be largest in summer, which is reflected by measurement and model (see Figure 6-36, upper panel). The seasonal cycle correlates by 0.95 indicating a good representation of the biogenic sources and their seasonality in the model. This is not surprising as these areas are amongst the most intensely studied and best characterised, and have in fact already been compared to measurements in previous studies (e.g. [Chance et al., 2000; Abbot et al., 2003; Palmer et al., 2003] and section 6.3.3). However, the wintertime background levels of 0.5 x 10^{16} molec/cm^2 are not confirmed by the measurements indicating a too large source of isoprenes in winter. On the other hand, as these values are rather low, measurement errors cannot be neglected and the lack of a signal could at least in parts be related to the detection limit of the GOME data.

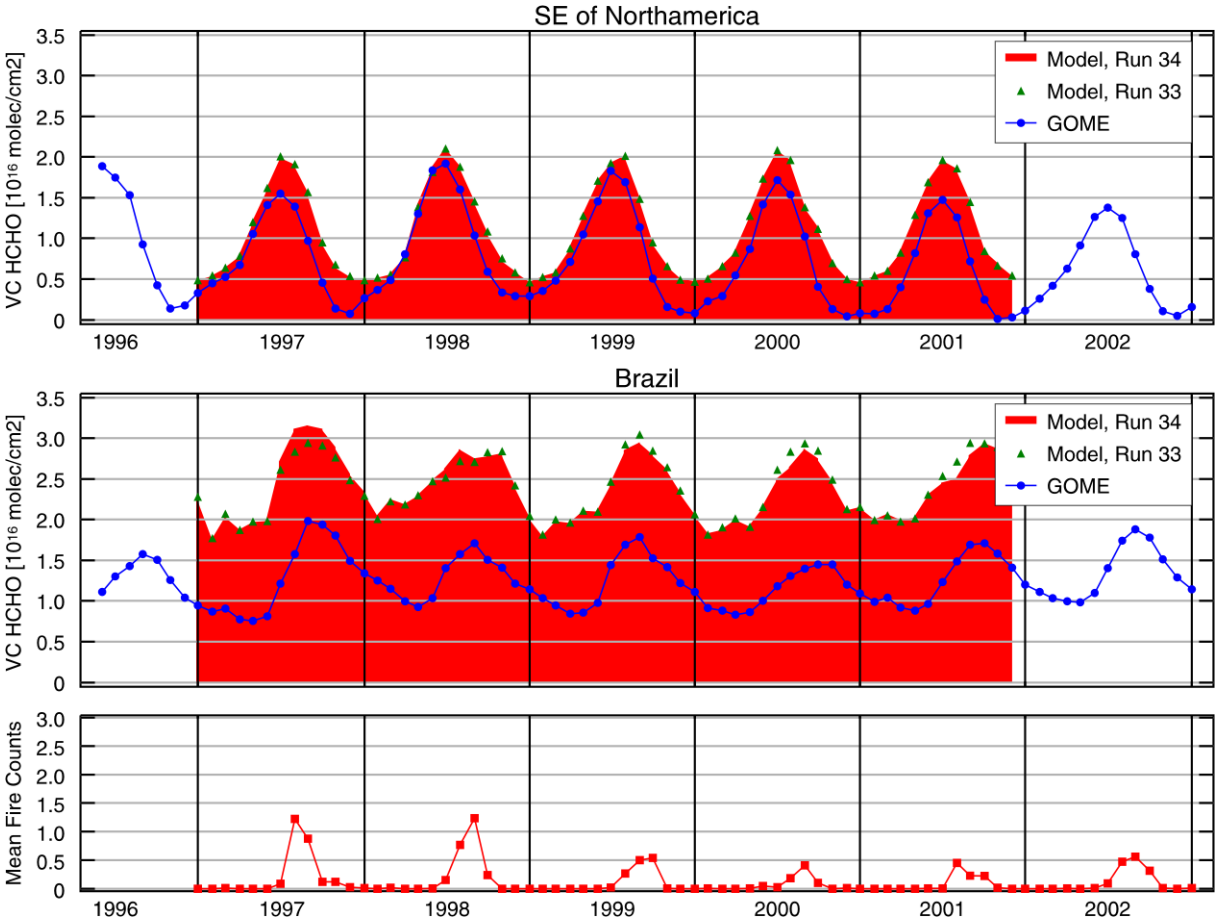

Figure 6-36: Comparison between GOME observations and model for regions in America.

In Brazil (see Figure 6-36, lower panel) the amplitude and also the time of maximum formaldehyde of the seasonal variation is reproduced nicely by the model. The correlation for the model run 34 to the measurement is

0.91. Maximum formaldehyde correlates with the burning season in this region in summer. However, over the time period of five years the average model column is almost a factor of two larger. The year-round background values of about 0.8 x 10^{16} molec/cm^2 are caused by biogenic emissions which seem to be significantly overestimated in the model. For the measurements, cloud contamination over the rain forest could be a reason for a systematic underestimation, but a study on the dependence of HCHO columns on cloud fraction does not give any indication for such an effect. This point will have to be revisited once satellite measurements with higher spatial resolution and thus less cloud problems become available, e.g. OMI.

Figure 6-37 illustrates the situation in Africa: Due to the ITCZ, the dry season and consequently the burning season are shifted in time in the two selected regions of Ghana and Congo. The measurements of formaldehyde display a seasonal cycle with a maximum at the time of biomass burning. Although the amplitude of model and measurement of this seasonal cycle as well as the average column agree well (see also Table 16), the phase of the measurements is completely missed and rather exhibits a double maximum indicating problems in the parameterisation of the biomass burning events in the model for both regions and a clear overestimation of the biogenic contributions. Again, contamination by clouds and biomass burning aerosols could be a problem for the satellite measurements, but the overall consistency of the measurements is more indicative of a model deficiency.

In addition to the continental regions, also an area over the Atlantic close to Africa was selected: Here, the model only shows the background formaldehyde produced by methane oxidation whereas GOME sees on average a 60 percent higher column (see Figure 6-37, lower panel) readdressing the discussion in the previous section 6.2 about *in situ* formation of formaldehyde. It is notable, that the small seasonal variation above the ocean does not correlate with biomass burning above the Congo region. This might be a hint that rather biogenic emissions than plumes of biomass burning cause the elevated levels of HCHO above water.

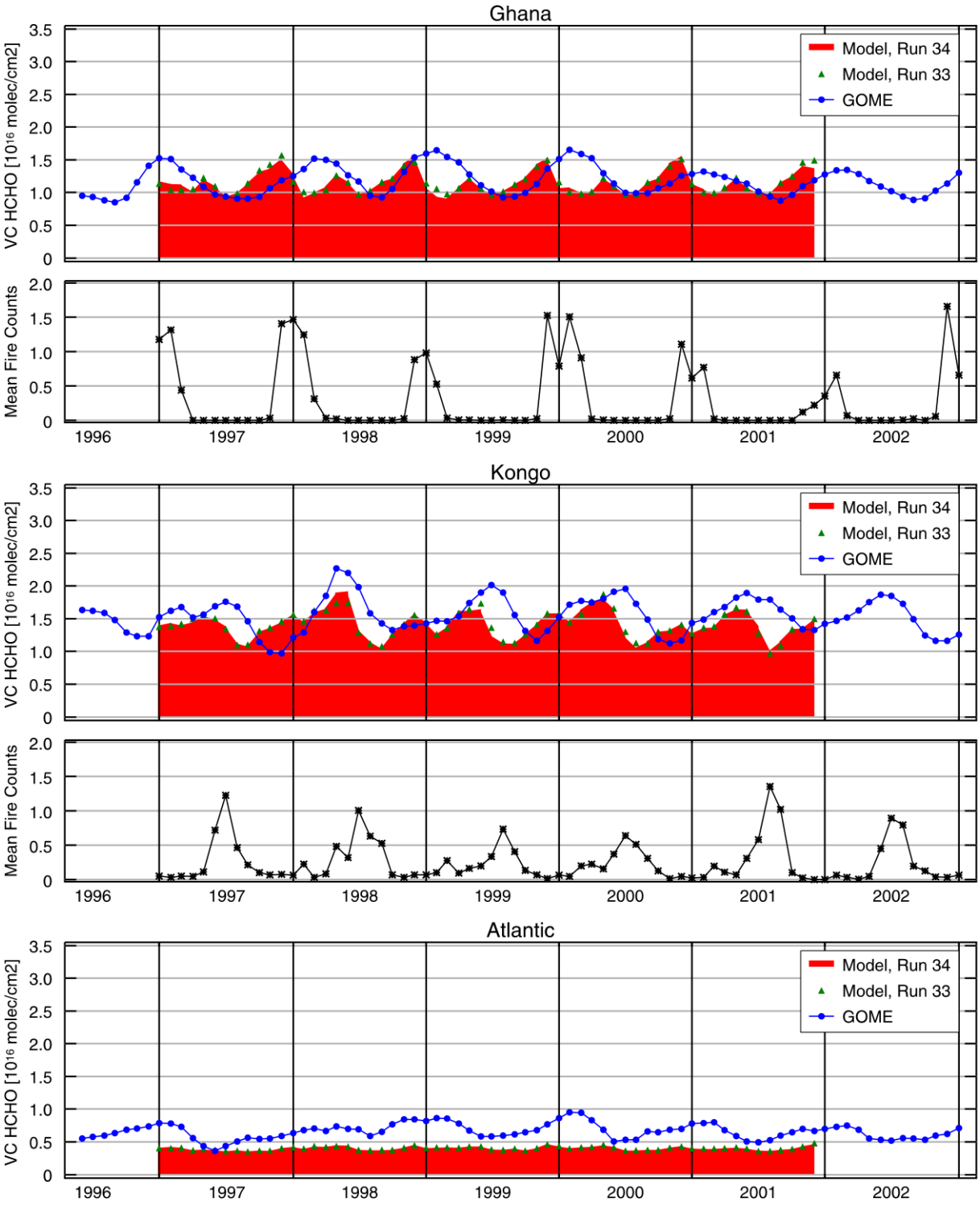

Figure 6-37: Comparison between GOME observations and model for regions in Africa.

In Siberia (see Figure 6-38, upper panel), formaldehyde columns are very low and close to the detection limit. Although a correlation with the fire counts can be observed, in particular in 1998, the measurements also show enhanced formaldehyde at winter time which is likely caused by albedo artefacts.

Indonesia is a region that is influenced by ENSO effects resulting in drier conditions and subsequently, increased forest fires there. In the years 1997 and 2002 El Niño events lasted for several months (see Figure 6-38, lower panel) causing high formaldehyde columns. Ergo, only the model run 34 which assimilates an emission invento-

ry based on satellite fire counts is able to reproduce the enhanced formaldehyde in 1997. For both regions, the overall magnitude of HCHO is captured quite well.

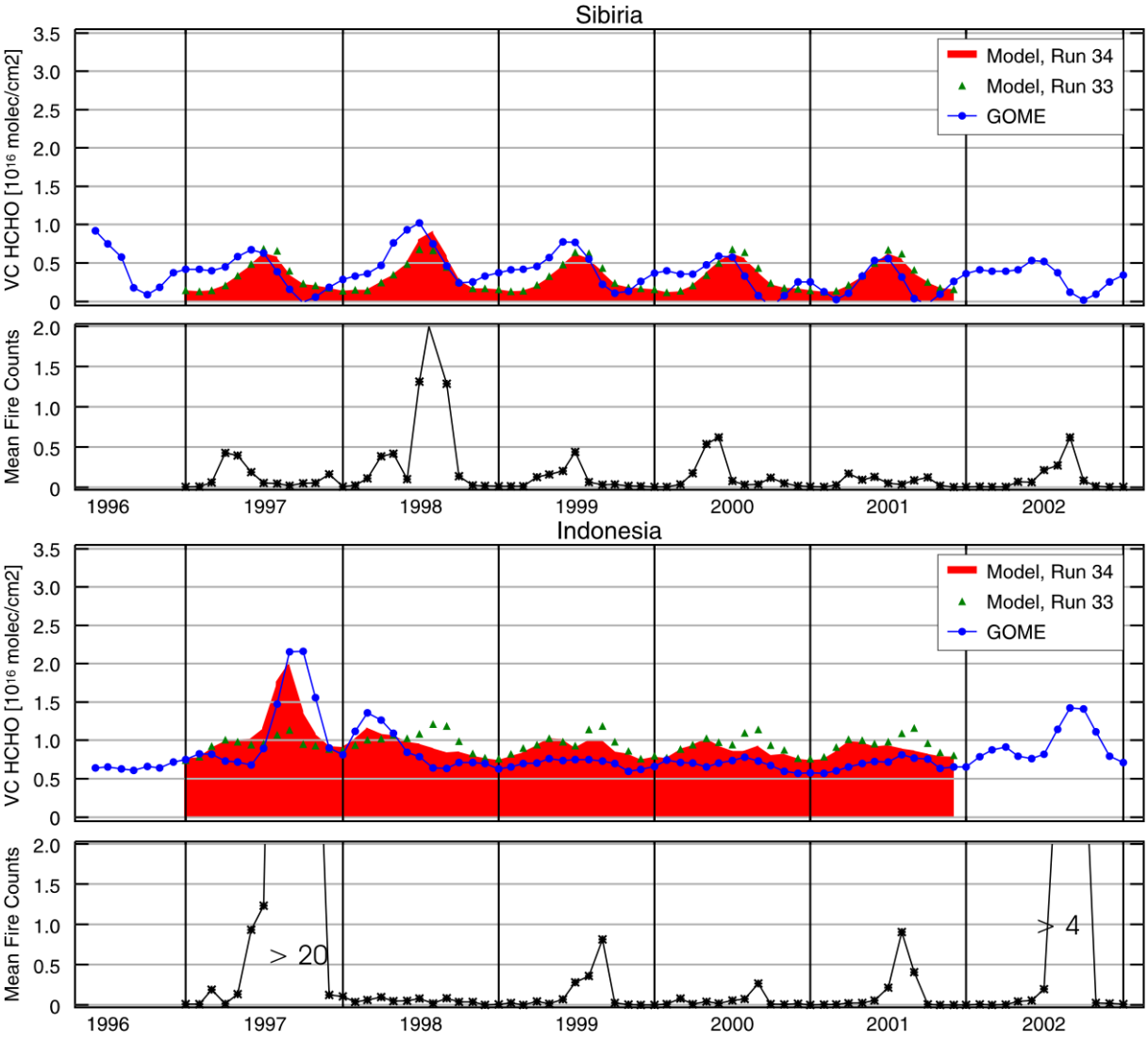

Figure 6-38: Comparison between GOME observations and model for regions with biomass burning in Asia.

In Figure 6-39 formaldehyde time series over polluted regions are presented: In general, HCHO is again captured quite similar from model and GOME. All four areas are located in the northern hemisphere resulting in peak formaldehyde in summer due to the photochemistry (see section 1.6). The two locations in China exhibit a strong seasonal cycle. For the other two areas this seasonal cycle is partly masked by the albedo effect: As in Siberia, for mid-Europe and also partly in Milan as well as the Red Basin, the seasonal variation with a second peak in wintertime might be caused by snow-covered ground and a consequently not correct AMF. In order to separate anthropogenic and biogenic contributions in the HCHO column above these regions additional model runs are necessary which should be available at the end of the RETRO project (mid of 2006).

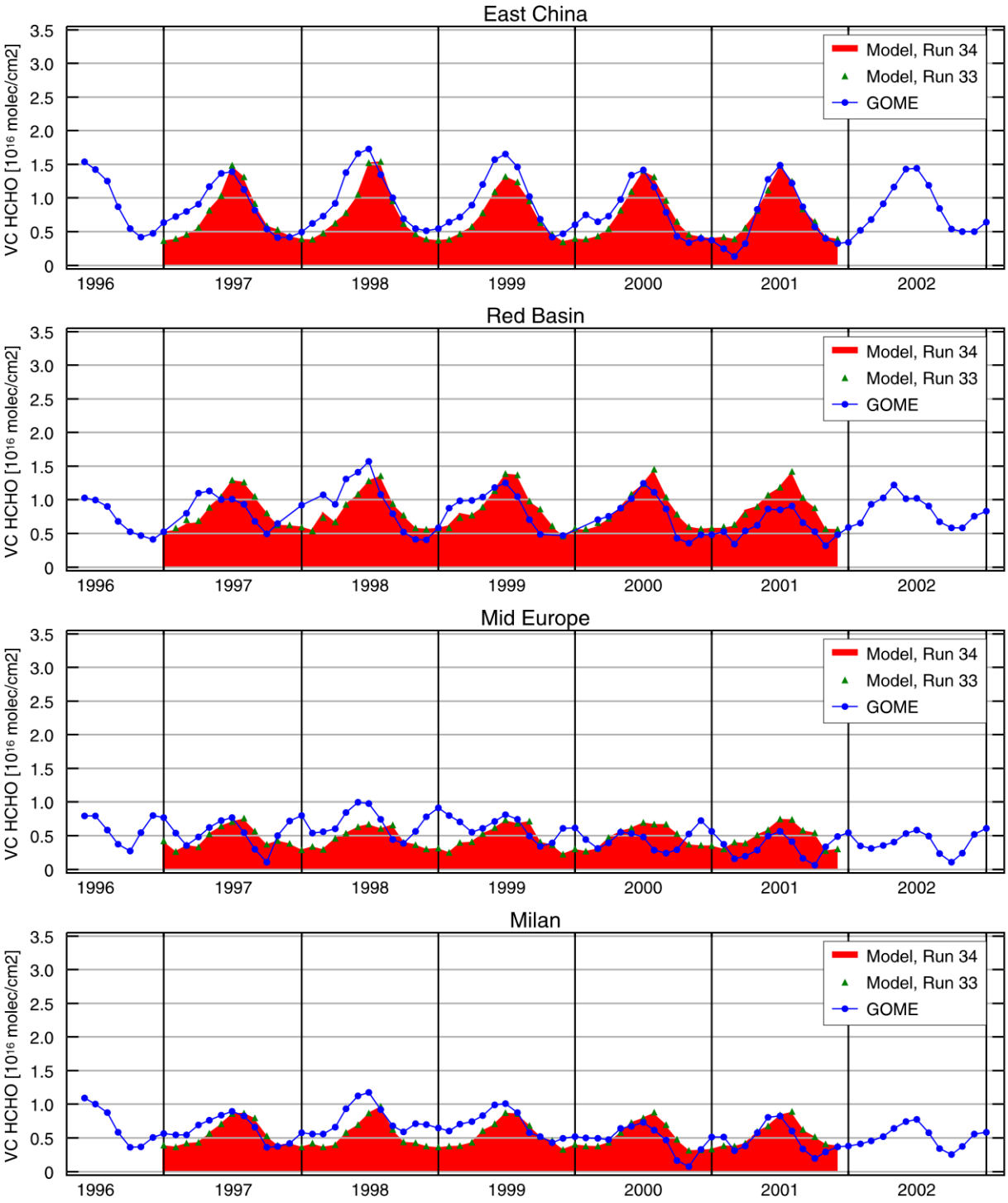

Figure 6-39: Comparison between GOME observations and model for regions with high anthropogenic air pollution.

Table 16 presents an overview of the mean HCHO columns from model and measurement together with the correlation coefficient.

In summary, highest background signals of formaldehyde can be found in regions with rain forests: Brazil, Ghana, Congo and Indonesia. Low formaldehyde is detected over Europe, Siberia and the oceans. The most pronounced seasonal variations seem to be connected to regions with a distinct growing season in summer as in south eastern North America and eastern China. There is, for all regions investigated here, no clear trend in the data even in those areas (East China) where this was clearly identified for NO_2 [Richter et al., 2005]. Regions

with biogenic emissions reveal an earlier onset of enhanced formaldehyde in the measurements compared to the model in the growing season. Reasons for this could be either an earlier start in the year of biogenic isoprene emissions as expected or simply a too late onset of photochemical production of formaldehyde in the model.

The largest differences in absolute values between model and observations were found for the rain forests of South America which might be due to an overestimation of isoprene emissions in current databases for that region. However, as mentioned above this result has to be confirmed with other techniques.

In order to resolve the discrepancies between model runs and GOME observations, case studies are necessary where single parameters like emission inventories of isoprenes and other biogenic VOCs or different data bases for the biomass burning events are investigated in more detail. This will be carried out in the near future within the European RETRO project.

Table 16: Properties for „Regions of Interest" in the GOME-model comparison (see also Figure 6-20).

	Mean model HCHO column (run 34) [10^{16} molec/cm^2]	*Mean meas. HCHO column [10^{16} molec/cm^2]*	*Correlation coefficient for run 33*	*Correlation coefficient for run 34*
SE of North America 30°N-35°N,90°W-80°W	1.08	0.74	0.95	0.95
Brazil 5°S-0°S,70°W-50°W	2.38	1.23	0.88	0.91
Ghana 5°N-10°N,3.75°W-3.75°E	1.15	1.21	-0.02	-0.02
Congo 5°S-0°S,11°E-19°E	1.40	1.57	0.25	0.30
Atlantic 5°S-0°S,15°W-3.75°W	0.40	0.67	0.55	0.55
Siberia 50°N-70°N,100°E-150°E	0.31	0.37	0.62	0.62
Indonesia 5°S-0°S,94°E-116°E	0.94	0.82	0.26	0.83
East China 30°N-40°N,112.5°E-120°E	0.74	0.85	0.86	0.86
Red Basin 27.5°N-30°N,105°E-109°E	0.85	0.80	0.59	0.58
Mid Europe 50°N-55°N,0°E-20°E	0.48	0.53	0.08	0.08
Milan 42.5°N-45°N,7.5°E-11°E	0.55	0.61	0.62	0.62

7 Conclusions and Outlook

This thesis focuses on global measurements of two chemical reactive hydrocarbons, formaldehyde (HCHO) and glyoxal (CHOCHO) with optical absorption spectroscopy from space and from the ground. These measurements substantially add to our current knowledge on the global emissions of non-methane hydrocarbons (NMHC). NMHC are present at relatively low quantities in our atmosphere. Nevertheless, they play a key role in atmospheric photochemistry. For example, the oxidation of NMHC is significant for the formation of ozone in the troposphere. In spite of their importance, their global source and sinks budgets are still not well understood.

The main progress and results obtained in this thesis can be summarised as follows:

Global measurements of formaldehyde. Over seven years of global measurements from the GOME (Global Ozone Monitoring Experiment) satellite instrument were analysed for tropospheric HCHO columns using the Differential Optical Absorption Spectroscopy (DOAS) method. By applying appropriate adaptations to the retrieval, HCHO columns were also derived for the first time from measurements of the SCIAMACHY (Scanning Imaging Absorption Spectrometer for Atmospheric Cartography) instrument, extending the data set to more than a decade. Extensive radiative transfer studies combined with ancillary data from different sources were used to construct a set of tabulated air mass factors with high spatial resolution (1° x 1°) and little dependence on model results. This provides high accuracy for the retrieved columns and independence of model assumptions at the same time.

The global HCHO fields are found to be dominated by biogenic emissions of isoprenes and terpenes, in particular in the tropical regions. Biomass burning is also a significant contribution locally during intense burning periods, e.g. in Africa or Indonesia. Anthropogenic signals are much smaller and limited to the most polluted areas (e.g. Po Valley in Europe, China) but can clearly be discerned in the long-term averages.

Comparison of satellite HCHO measurements with model results. GOME measurements have been compared in detail with results from the LMDz-INCA model. Overall, excellent agreement was found over the continents, but significant underestimation in the model over the oceans. Here, the satellite measurements show clearly enhanced columns in some areas affected by continental outflow, indicating either a longer than modelled lifetime of HCHO or more probably in-situ production by decomposition of long-lived organic compounds. The seasonal variation of modelled HCHO columns shows excellent agreement with the measurements in some regions (North America), underestimation of the overall amplitude in South America and varying degrees of agreement over different parts of Africa and Asia, indicating model deficiencies in the parameterisation of the emission of biogenic precursors and their timing. In regions with strong biomass burning, the use of measurement-based fire distributions improves the agreement between model and observation as expected.

Global measurements of CHOCHO. Global fields of CHOCHO (glyoxal) columns have been derived from SCIAMACHY measurements. This is the first detection of CHOCHO using SCIAMACHY data, and the first global data set of CHOCHO available. The global distribution of glyoxal is found to be similar to that of HCHO and both the absolute values and the ratio to HCHO are of the expected magnitude. Over some areas of the oceans, SCIAMACHY CHOCHO columns are significantly enhanced and so far it is not clear if this is real or indicates an unresolved problem in the data analysis. With these results, global measurements of another relevant atmospheric hydrocarbon have become available for validation of model results.

Improvements of ground-based scattered light measurements. To improve the sensitivity of ground-based DOAS observations to tropospheric absorbers, the instruments of the BREDOM network were modified to take not only zenith-sky, but also horizon-viewing measurements. This technical development in combination with extensive radiative transfer studies modelling the sensitivity and its dependence on boundary conditions (viewing geometry, surface albedo, aerosol loading) greatly enhanced the usefulness of this type of measurements. This part of the thesis was a collaborative effort with two other PhD students (S. Fietkau and T. Medeke).

Development of a profile retrieval algorithm for ground-based MAX-DOAS measurements. Based on the sensitivity studies described above, an automated optimal estimation based profile retrieval algorithm (BREAM) was developed for MAX-DOAS measurements. The method first determines appropriate aerosol settings using measurements of the O_4 columns and then inverts the profile of the absorber of interest, e.g. NO_2, HCHO, or CHOCHO. Depending on measurement conditions, between 2 and 4 pieces of information can be retrieved, and in addition the optical aerosol depth. Results from the retrieval have been validated by comparison with independent measurements during two campaigns for NO_2, HCHO, and aerosol depth, and good agreement was found. This constitutes a major improvement for the application of passive DOAS measurements, and due to its automated operation has the potential to extend existing *in situ* and active DOAS measurements.

MAX-DOAS measurements of HCHO and CHOCHO and application to satellite validation. MAX-DOAS measurements have been analysed for HCHO and for the first time, also for CHOCHO, and the results compared to the satellite data. The diurnal variation of the two species is similar, indicating common sources. In the vicinity of anthropogenic emissions, HCHO shows larger variability, probably as a result of direct emissions which are thought to be negligible for CHOCHO. Even at the high altitude stations (Mérida and Zugspitze), HCHO could be detected, albeit at low concentrations. This and the profiles retrieved confirm other measurements that showed negative gradients of HCHO with altitude. The vertical profiles retrieved for HCHO and CHOCHO are similar, underlining again the link between these two reactive hydrocarbons.

Validation of satellite measurements of HCHO and CHOCHO is complicated by the low signals and high variability of the columns, but satisfactory agreement was found between the two data sets in several places, adding confidence to the satellite data.

In conclusion, several tools for the analysis of measurements of atmospheric trace species using absorption spectroscopy have been developed, and a large data set on HCHO and CHOCHO observations been created and analysed. Several aspects of this work should be followed on in future work:

The comparison of modelled and measured HCHO fields should be extended by systematic variation of emission parameters and their implementation in the model to identify the key uncertainties. Also, glyoxal data should be included in the comparison. Another logical step is the comparison of satellite and in particular MAX-DOAS measurements with regional models as has already been initiated with the DANDELIONS project.

A more extensive validation of the satellite measurements with ground-based data is necessary and possible and in fact will in part be presented by Sixten Fietkau and Thomas Medeke. In order to confirm (or falsify) the presence of significant amounts of HCHO and CHOCHO over the oceans, dedicated MAX-DOAS measurements from ships should be taken during a latitudinal transect.

Data from new satellite instruments providing better spatial resolution and more coverage such as OMI and GOME-2, but even more so the proposed geostationary instruments should be able to provide much more detail

on the spatial and temporal variation of both formaldehyde and glyoxal and their sources, and at the same time make validation with local measurements more practical and thereby improve absolute accuracy over what could be achieved within this thesis.

Appendix

The author has contributed to the following peer-reviewed publications:

Afe, O. T.; Richter, A.; Sierk, B.; Wittrock, F. and Burrows, J. P. (2004): *BrO emission from volcanoes: A survey using GOME and SCIAMACHY measurements*, Geophysical Research Letters 31 [24].

Beyerle, G.; Neuber, R.; Schrems, O.; Wittrock, F. and Knudsen, B. (1994): *Multiwavelength Lidar Measurements of Stratospheric Aerosols above Spitsbergen during Winter 1992 93*, Geophysical Research Letters 21 [1], pp. 57-60.

Heckel, A.; Richter, A.; Tarsu, T.; Wittrock, F.; Hak, C.; Pundt, I.; Junkermann, W. and Burrows, J. P. (2005): *MAX-DOAS measurements of formaldehyde in the Po-Valley*, Atmospheric Chemistry and Physics 5, pp. 909-918.

Hendrick, F.; Roozendael, M. Van; Kylling, A.; Petritoli, A.; Rozanov, A.; Sanghavi, S.; Schofield, R.; Friedeburg, C. von; Wagner, T.; Wittrock, F.; Fonteyn, D. and Mazière, M. De (2006): *Intercomparison exercise between different radiative transfer models used for the interpretation of ground-based zenith-sky and multi-axis DOAS observations*, Atmospheric Chemistry and Physics 6, pp. 93-108.

Ladstätter-Weißenmayer, Annette; Meyer-Arnek, Julian; Richter, Andreas; Wittrock, Folkard and Burrows, John P. (2005): *Tropospheric O_3 over Indonesia during biomass burning events measured with GOME (Global Ozone Monitoring Experiment) and compared with trajectory analysis*, Atmospheric Chemistry and Physics Discussions 5, pp. 3105-3130.

Ladstätter-Weißenmayer, A.; Heland, J.; Kormann, R.; von Kuhlmann, R.; Lawrence, M. G.; Meyer-Arnek, J.; Richter, A.; Wittrock, F.; Ziereis, H. and Burrows, J. P. (2003): *Transport and build-up of tropospheric trace gases during the MINOS campaign: comparsion of GOME, in situ aircraft measurements and MATCH-MPIC-data*, Atmospheric Chemistry and Physics 3, pp. 1887-1902.

Meyer-Arnek, J.; Ladstätter-Weißenmayer, A.; Richter, A.; Wittrock, F. and Burrows, J. P. (2005): *A study of the trace gas columns O_3, NO_2 and HCHO over Africa in September 1997*, Faraday Discussions 130, pp. 387-405.

Müller, R. W.; Bovensmann, H.; Kaiser, J. W.; Richter, A.; Rozanov, A.; Wittrock, F. and Burrows, J. P. (2002): *Consistent interpretation of ground based and GOME BrO slant column data*, Remote Sensing of Trace Constituents in the Lower Stratosphere, Troposphere and the Earth's Surface: Global Observations, Air Pollution and the Atmospheric Correction 29 [11], pp. 1655-1660.

Richter, A.; Wittrock, F.; Eisinger, M. and Burrows, J. P. (1998): *GOME observations of tropospheric BrO in northern hemispheric spring and summer 1997*, Geophysical Research Letters 25 [14], pp. 2683-2686.

Richter, A.; Wittrock, F.; Ladstätter-Weißenmayer, A. and Burrows, J. P. (2002): *GOME measurements of stratospheric and tropospheric BrO*, Remote Sensing of Trace Constituents in the Lower Stratosphere, Troposphere and the Earth's Surface: Global Observations, Air Pollution and the Atmospheric Correction 29 [11], pp. 1667-1672.

Richter, A.; Wittrock, F.; Weber, M.; Beirle, S.; Kuhl, S.; Platt, U.; Wagner, T.; Wilms-Grabe, W. and Burrows, J. P. (2005): *GOME observations of stratospheric trace gas distributions during the splitting vortex event in the antarctic winter of 2002. Part I: Measurements*, Journal of the Atmospheric Sciences 62 [3], pp. 778-785.

Sinnhuber, B. M.; Arlander, D. W.; Bovensmann, H.; Burrows, J. P.; Chipperfield, M. P.; Enell, C. F.; Friess, U.; Hendrick, F.; Johnston, P. V.; Jones, R. L.; Kreher, K.; Mohamed-Tahrin, N.; Muller, R.; Pfeilsticker, K.; Platt, U.; Pommereau, J. P.; Pundt, I.; Richter, A.; South, A. M.; Tornkvist, K. K.; Van Roozendael, M.; Wagner, T. and Wittrock, F. (2002): *Comparison of measurements and model calculations of stratospheric bromine monoxide*, Journal of Geophysical Research-Atmospheres 107 [D19].

Sinnhuber, B.M.; Rozanov, A.; Sheode, N.; Afe, O.T.; Richter, A.; Sinnhuber, M.; Wittrock, F.; Burrows, J.P.; Stiller, G.P.; von Clarmann, T. and Linden, A. (2005): Global observations of stratospheric bromine monoxide from SCIAMACHY, Geophysical Research Letters 32 [20].

Sommar, J.; Wangberg, I.; Berg, T.; Gardfeldt, K.; Munthe2, J.; Richter, A.; Urba, A.; Wittrock, F. and Schroeder, W. H. (2004): *Circumpolar transport and air-surface exchange of atmospheric mercury at Ny-Ålesund (79° N), Svalbard, spring 2002*, Atmospheric Chemistry and Physics Discussions 4, pp. 1727-1771.

Van Roozendael, M.; Wagner, T.; Richter, A.; Pundt, I.; Arlander, D. W.; Burrows, J. P.; Chipperfield, M.; Fayt, C.; Johnston, P. V.; Lambert, J. C.; Kreher, K.; Pfeilsticker, K.; Platt, U.; Pommereau, J. P.; Sinnhuber, B. M.; Tornkvist, K. K. and Wittrock, F. (2002): *Intercomparison of BrO measurements from ERS-2 GOME, ground-based and balloon platforms*, Remote Sensing of Trace Constituents in the Lower Stratosphere, Troposphere and the Earth's Surface: Global Observations, Air Pollution and the Atmospheric Correction 29 [11], pp. 1661-1666.

Vandaele, A. C.; Fayt, C.; Hendrick, F.; Hermans, C.; Humbled, F.; Van Roozendael, M.; Gil, M.; Navarro, M.; Puentedura, O.; Yela, M.; Braathen, G.; Stebel, K.; Tornkvist, K.; Johnston, P.; Kreher, K.; Goutail, F.;

Mieville, A.; Pommereau, J. P.; Khaikine, S.; Richter, A.; Oetjen, H.; Wittrock, F.; Bugarski, S.; Friess, U.; Pfeilsticker, K.; Sinreich, R.; Wagner, T.; Corlett, G. and Leigh, R. (2005): *An intercomparison campaign of ground-based UV-visible measurements of NO_2, BrO, and OClO slant columns: Methods of analysis and results for NO_2*, Journal of Geophysical Research-Atmospheres 110 [D8].

Vountas, M.; Richter, A.; Wittrock, F. and Burrows, J. P. (2003): *Inelastic scattering in ocean water and its impact on trace gas retrievals from satellite data*, Atmospheric Chemistry and Physics 3, pp. 1365-1375.

Wagner, T.; Wittrock, F.; Richter, A.; Wenig, M.; Burrows, J. P. and Platt, U. (2002): *Continuous monitoring of the high and persistent chlorine activation during the Arctic winter 1999/2000 by the GOME instrument on ERS-2*, Journal of Geophysical Research-Atmospheres 107 [D20].

Weber, M.; Dhomse, S.; Wittrock, F.; Richter, A.; Sinnhuber, B. M. and Burrows, J. P. (2003): *Dynamical control of NH and SH winter/spring total ozone from GOME observations in 1995-2002*, Geophysical Research Letters 30 [11].

Weber, M.; Eichmann, K. U.; Wittrock, F.; Bramstedt, K.; Hild, L.; Richter, A.; Burrows, J. P. and Muller, R. (2002): *The cold Arctic winter 1995/96 as observed by GOME and HALOE: Tropospheric wave activity and chemical ozone loss*, Quarterly Journal of the Royal Meteorological Society 128 [582], pp. 1293-1319.

Wittrock, F.; Eisinger, M.; Ladstätter-Weißenmayer, A.; Richter, A. and Burrows, J.P. (1996): *Ground-based UV/vis measurements of O_3, NO_2, OClO and BrO over Ny-Ålesund (79°N,12°E)*, XVIII Quadrennial Ozone Symposium, L'Aquila, Italy.

Wittrock, F.; Müller, R.; Richter, A.; Bovensmann, H. and Burrows, J. P. (2000): *Measurements of iodine monoxide (IO) above Spitsbergen*, Geophysical Research Letters 27 [10], pp. 1471-1474.

Wittrock, F.; Oetjen, H.; Richter, A.; Fietkau, S.; Medeke, T.; Rozanov, A. and Burrows, J. P. (2004): *MAX-DOAS measurements of atmospheric trace gases in Ny-Ålesund - Radiative transfer studies and their application*, Atmospheric Chemistry and Physics 4, pp. 955-966.

Wittrock, F.; Richter, A.; Oetjen, H.; Burrows, J.P.; Kanakidou, M.; Myriokefalitakis, St.; Volkamer, R.; Beirle, St.; Platt, U. and Wagner, Th. (2006): *Simultaneous Global Observations of Glyoxal and Formaldehyde from Space*, Geophysical Research Letters, 33, L16804, doi:10.1029/2006GL026310.

Danksagung / Acknowledgments

Eine solche Arbeit – gerade wenn sie etwas länger andauert als üblich – ist nicht das Werk einer einzelnen Person. Es sind viele Menschen daran mittelbar oder unmittelbar beteiligt, denen ich danken möchte.

Fachlich sind hier vor allem zwei Personen hervorzuheben: Prof. John P. Burrows und Dr. Andreas Richter. Beiden möchte ich für ihre Geduld, die vielen Anregungen und nicht zuletzt für das trotz mancher Widrigkeiten angenehme Klima danken, die schließlich zum erfolgreichen Abschluß dieser Arbeit geführt haben. Andreas hat durch seine immer freundliche Art, verbunden mit überragender fachlicher Qualifikation erheblich zu der Arbeit beigetragen.

Prof. Otto Schrems kenne und schätze ich bereits seit meinem Einstieg in die Umweltphysik 1992 beim Alfred-Wegener-Institut Bremerhaven. Ihm danke ich für die Übernahme des Zweitgutachtens.

Eine lange gemeinsame Arbeit führt manchmal zum Aufbau von Freundschaften: Danke an Hilke Oetjen für viele Erlebnisse und für die mühsame Korrektur und Unterstützung meiner Versuche, die Arbeit auf Englisch zu schreiben.

Hier muss jetzt eine sehr lange Liste an Menschen folgen, die mich zumindest zeitweise in den letzten Jahren begleitet haben. Auch mit ihnen gab es spannende und meist auch schöne Momente, fachliche Diskussionen und Beiträge, private Zerstreuung, erfolgreiche Kampagnen, lange (Polar)Nächte, ... Einige haben auch direkt mit ihren Ergebnissen zu dieser Arbeit beigetragen.

Diese Liste kann niemals vollständig sein, sondern immer nur eine Auswahl und ich entschuldige mich schon jetzt bei denen, die nicht genannt worden sind:

- Die DOAS-Gruppe und ihre Ehemaligen: Silvia Schlieter, Michael Eisinger, Annette Ladstätter-Weißenmayer, Andreas Heckel, Marco Bruns, Thomas Medeke, Sixten Fietkau, Ping Wang, Oluyemi Afe, Hendrik Nüß, Marc Laue
- Der "Rest" des Instituts: Peter Spietz, Alexei Rozanov, Vladimir Rozanov, Lars Reichert, Maria Dolores 'Lola' Andrés-Hernández, Tilman Dinter, Tine Weinzierl, Marco Vountas, Björn-Martin Sinnhuber, Mark Weber, Heinrich Bovensmann, Stefan Noël, Klaus Bramstedt, Jörn Burkert, Sabine Packeiser, Susanne Themm, Heidemarie Krug, Birgit Teuchert, Jörn Bleck-Neuhaus, Justus Notholt, Heiko Schellhorn, Torsten Warneke, Voltaire Velazco
- Firma IMPRES, Bremen: Ingo Beninga, Wilfried Ruhe
- Firma LOT Oriel, Darmstadt: Olaf Koschützke
- Institut für Umweltphysik, Universität Heidelberg: Thomas Wagner, Irene Pundt, Claudia Hak
- IASB-BIRA, Brüssel, Belgien: Michel van Roozendael, François Hendrick, Ann-Carin VanDaele
- Alfred-Wegener-Institut: Roland Neuber, Peter von der Gathen, Andreas Herber, Mareile Wolff, Rolf Weller
- NILU, Kjeller, Norwegen: Bill Arlander (jetzt Patentamt Oslo), Geir Braathen (jetzt WMO), Kjersti Karlsen-Tørnkvist, Britt-Ann Kaastad-Høiskar, Kerstin Stebel, Aasmund Fahre Vik
- Forschungszentrum Karlsruhe: Gerd Hochschild, Jochen Gross
- Universidad de Los Andes, Mérida, Venezuela: Pedro Hofmann
- IFU Garmisch-Patenkirchen: Wolfgang Junkermann

- JRC, Ispra, Italien: Bo Larsen
- PSI, Villigen, Schweiz: André Prevot, Carlos Ordóñez
- CEA, Gif-sur-Yvette Cedex, Frankreich: Sophie Szopa, Didier Hauglustaine
- Max-Planck-Institut für Meteorologie, Hamburg: Martin Schultz
- SRON, Utrecht, Niederlande: Christina Tanzi
- KNMI, De Bilt, Niederlande: Ellen Brinksma, Mark Kroon
- INTA, Madrid, Spanien: Olga Puentera, Manuel Gil
- ALOMAR, Andenes, Norwegen: Michael Gausa
- NIWA, Lauder, Neuseeland: Karin Kreher, Paul Johnston
- BAS, Cambridge, England: Howard Roscoe
- University of Leicester: Gary Corlett, Paul Monks, Roland Leigh
- University of California, La Jolla, USA: Rainer Volkamer
- ... und alle Stationsingenieure und Stationsleiter an der Koldewey-Station sowie die Mitarbeiter der Kings Bay Company in Ny-Ålesund, Spitzbergen.

Allen Mitgliedern „meiner“ Feuerwehr Sudweyhe danke ich dafür, dass sie mir immer die notwendige Bodenhaftung verschafft haben.

Der herzlichste Dank gilt den Menschen, die sehr viel erdulden mussten, mitgelitten, mich in vielfältiger Form unterstützt und immer wieder aufgebaut haben: meiner Familie.

Liebe Gesine und lieber Hermann, ohne Eure Hilfe wäre vieles nicht möglich gewesen.

Liebe Mutter, lieber Vater, danke für all das Gute, was Ihr mir, aber auch Verena und den Kindern habt zukommen lassen.

Finn und Jan, durch Euch kam das Bewusstsein, was die wesentlichen Dinge im Leben sind.

Verena, Dir danke ich, dass Du zu mir gehalten hast. Ohne Deine Liebe hätte ich diese lange Zeit nicht durchgehalten.

Lebenslauf

Ich wurde am 1. November 1966 als viertes und letztes Kind von Heinrich und Irmgard Wittrock in Bremen geboren. Von 1972 bis 1976 habe ich die Grundschule Sudweyhe besucht. Es folgten bis zum Abitur im Jahr 1985 die Orientierungsstufe Lahausen von 1976 bis 1978 und ab 1978 der Gymnasialzweig der Kooperativen Gesamtschule Leeste.

Meinen Wehrdienst habe ich von 1985 bis 1986 an den Standorten Pinneberg und Visselhövede abgeleistet.

1986 nahm ich das Studium der Physik an der Universität Bremen auf. Die Schwerpunkte meines Studiums waren die Angewandte Optik sowie die Umweltphysik. Von 1992 bis 1994 habe ich als wissenschaftliche Hilfskraft am Alfred-Wegener-Institut in Bremerhaven gearbeitet und dort eine Diplomarbeit zum Thema „LIDAR-Untersuchungen der Arktischen Stratosphäre“ erstellt. Gutachter dieser Arbeit waren die Professoren Klaus Künzi und Otto Schrems.

Nach Abschluß des Studiums im Jahr 1994 habe ich 1995 die Arbeit in der DOAS-Gruppe im Institut für Umweltphysik der Universität Bremen unter der Leitung von Prof. John P. Burrows aufgenommen. Seitdem war ich unter anderem für den wissenschaftlichen Beitrag des Instituts für die EU-Projekte GODIVA, QUILT, FORMAT und RETRO verantwortlich. Die vorliegende Arbeit hat teilweise Eingang in die genannten Projekte gefunden.

Seit 1994 bin ich mit Verena Nullmeyer verheiratet. 1994 wurde unser erster Sohn Jan geboren, 2002 unser zweiter Sohn Finn.

Eidesstattliche Erklärung

Hiermit versichere ich, dass die Arbeit von mir und nur mit den angegebenen Quellen und Hilfsmitteln erstellt wurde. Inhaltlich entnommene Stellen sind entsprechend gekennzeichnet.

Bremen, den 3. Januar 2006

Folkard Wittrock

Bibliography

Abbot, D.S.; Palmer, P.I.; Martin, R.V.; Chance, K.V.; Jacob, D.J. and Guenther, A. (2003): *Seasonal and interannual variability of North American isoprene emissions as determined by formaldehyde column measurements from space*, Geophysical Research Letters 30 [17]. URL: <Go to ISI>://000185361100001

Afe, O.T. (2005): *Retrieval and observations of atmospheric BrO from SCIAMACHY nadir measurements*, Institute of Environmental Physics, University of Bremen, Bremen.

Afe, O.T.; Richter, A.; Sierk, B.; Wittrock, F. and Burrows, J.P. (2004): *BrO emission from volcanoes: A survey using GOME and SCIAMACHY measurements*, Geophysical Research Letters 31 [24]. URL: <Go to ISI>://000226133300002

Albrecht, T.; Notholt, J.; Wolke, R.; Solberg, S.; Dye, C. and Malberg, H. (2002): *Variations of CH_2O and C_2H_2 determined from groundbased FTIR measurements and comparison with model results*, Remote Sensing of Trace Constituents in the Lower Stratosphere, Troposphere and the Earth's Surface: Global Observations, Air Pollution and the Atmospheric Correction 29 [11], pp. 1713-1718. URL: <Go to ISI>://000177314200018

Aliwell, S.R.; Van Roozendael, M.; Johnston, P.V.; Richter, A.; Wagner, T.; Arlander, D.W.; Burrows, J.P.; Fish, D.J.; Jones, R.L.; Tornkvist, K.K.; Lambert, J.C.; Pfeilsticker, K. and Pundt, I. (2002): *Analysis for BrO in zenith-sky spectra: An intercomparison exercise for analysis improvement*, Journal of Geophysical Research-Atmospheres 107 [D14]. URL: <Go to ISI>://000178977300030

Allwine, G.; Lamb, B. and Westberg, H. (1992): *Cited in Fehsenfeld et al. (1992)*, Global Biogeochemical Cycles 6, pp. 389-430.

Anderson, L.G.; Lanning, J.A.; Barrell, R.; Miyagishima, J.; Jones, R.H. and Wolfe, P. (1996): *Sources and sinks of formaldehyde and acetaldehyde: an analysis of Denver's ambient concentration data*, Atmospheric Environment 30 [12], pp. 2113-2123.

Andreae, M.O. and Merlet, P. (2000): *Emission of Trace Gases and Aerosols from Biomass Burning*, Global Biogeochemical Cycles.

Arino, O.; Buongiorno, A. and Goryl, P. (1995): *Intercalibration of Avhrr and Atsr Data*, Calibration and Applications of Satellite Sensors for Environmental Monitoring 17 [1], pp. 29-38. URL: <Go to ISI>://A1995BD47G00004

Arlander, D.W.; Bruning, D.; Schmidt, U. and Ehhalt, D.H. (1995): *The Tropospheric Distribution of Formaldehyde during Tropoz-Ii*, Journal of Atmospheric Chemistry 22 [3], pp. 251-269. URL: <Go to ISI>://A1995TG71900002

Arpag, K.H.; Johnston, P.V.; Miller, H.L.; Sanders, R.W. and Solomon, S. (1994): *Observations of the Stratospheric Bro Column over Colorado, 40°N*, Journal of Geophysical Research-Atmospheres 99 [D4], pp. 8175-8181. URL: <Go to ISI>://A1994NH26300010

Baek, S.O. and Jenkins, R.A. (2004): *Characterization of trace organic compounds associated with aged and diluted sidestream tobacco smoke in a controlled atmosphere - Volatile organic compounds and polycyclic aromatic hydrocarbons*, Atmospheric Environment 38 [38], pp. 6583-6599.

Baez, A.P.; Padilla, H.G.; Garcia, R.M.; Belmont, R.D. and Torres Ma, D.C.B. (2004): *Measurements of carbonyls in a 13-story building*, Environmental Science and Pollution Research 11 [6], pp. 400-404.

Barret, B.; De Maziere, M. and Demoulin, P. (2003): *Retrieval and characterization of ozone profiles from solar infrared spectra at the Jungfraujoch (vol 108, pg , 2002)*, Journal of Geophysical Research-Atmospheres 108 [D12]. URL: <Go to ISI>://000184578700003

Beirle, S.; Platt, U.; Wenig, M. and Wagner, T. (2004): *Highly resolved global distribution of tropospheric NO_2 using GOME narrow swath mode data*, Atmospheric Chemistry and Physics 4, pp. 1913-1924. URL: <Go to ISI>://000224012400001

Boersma, K.F.; Eskes, H.J. and Brinksma, E.J. (2004): *Error analysis for tropospheric NO_2 retrieval from space*, Journal of Geophysical Research-Atmospheres 109 [D4]. URL: <Go to ISI>://000220216800004

Bogumil, K.; Orphal, J.; Homann, T.; Voigt, S.; Spietz, P.; Fleischmann, O.C.; Vogel, A.; Hartmann, M.; Kromminga, H.; Bovensmann, H.; Frerick, J. and Burrows, J.P. (2003): *Measurements of molecular absorption spectra with the SCIAMACHY pre-flight model: instrument characterization and reference data for atmospheric remote-sensing in the 230-2380 nm region*, Journal of Photochemistry and Photobiology a-Chemistry 157 [2-3], pp. 167-184. URL: <Go to ISI>://000182623100006

Boone, R.B. and Galvin, K.A. (2000): *Generalizing El Nino effects upon Maasai livestock using hierarchical clusters of vegetation patterns*, Photogrammetric Engineering & Remote Sensing 66 [6], pp. 737-744.

Bovensmann, H.; Burrows, J.P.; Buchwitz, M.; Frerick, J.; Noel, S.; Rozanov, V.V.; Chance, K.V. and Goede, A.P.H. (1999): *SCIAMACHY: Mission objectives and measurement modes*, Journal of the Atmospheric Sciences 56 [2], pp. 127-150. URL: <Go to ISI>://000078226000002

Bracher, A.U.; Kroon, B.M.A. and Lucas, M.I. (1999): *Primary production, physiological state and composition of phytoplankton in the Atlantic Sector of the Southern Ocean*, Marine Ecology-Progress Series 190, pp. 1-16. URL: <Go to ISI>://000084553000001

Brasseur, G.P.; Orlando, J.J.; Tyndall, G.S. and National Center for Atmospheric Research (U.S.) (1999): *Atmospheric chemistry and global change*, Topics in environmental chemistry, Oxford University Press, New York, ISBN: 0195105214 (cloth alk. paper).

Brewer, A.W.; McElroy, C.T. and Kerr, J.B. (1973): *Nitrogen dioxide concentrations in the atmosphere*, Nature 246, pp. 129-133.

Brinksma, E. (2005): *NO_2 in situ data, personal communication*

Brühl, C. and Crutzen, P. (1992): *Chemo-dynamical model of the atmosphere: Profile data base*, Mainz, Max-Plank-Institut für Chemie Mainz

Bruns, M. (2004): *NO_2 Profile Retrieval using Airborne Multiaxis Differential Optical Absorption Spectrometer (AMAXDOAS) Data*, Institute of Environmental Physics, University of Bremen, Bremen.

Bruns, M.; Buehler, S.A.; Burrows, J.P.; Heue, K.P.; Platt, U.; Pundt, I.; Richter, A.; Rozanov, A.; Wagner, T. and Wang, P. (2004): *Retrieval of profile information from airborne multiaxis UV-visible skylight absorption measurements*, Applied Optics 43 [22], pp. 4415-4426. URL: <Go to ISI>://000222934800018

Buchwitz, M.; de Beek, R.; Bramstedt, K.; Noel, S.; Bovensmann, H. and Burrows, J.P. (2004): *Global carbon monoxide as retrieved from SCIAMACHY by WFM-DOAS*, Atmospheric Chemistry and Physics 4, pp. 1945-1960. URL: <Go to ISI>://000224193100001

Buchwitz, M.; de Beek, R.; Burrows, J.P.; Bovensmann, H.; Warneke, T.; Notholt, J.; Meirink, J.F.; Goede, A.P.H.; Bergamaschi, P.; Korner, S.; Heimann, M. and Schulz, A. (2005): *Atmospheric methane and carbon dioxide from SCIAMACHY satellite data: initial comparison with chemistry and transport models*, Atmospheric Chemistry and Physics 5, pp. 941-962. URL: <Go to ISI>://000227793800004

Burkert, J.; Andres-Hernandez, M.D.; Reichert, L.; Meyer-Arnek, J.; Doddridge, B.; Dickerson, R.R.; Muhle, J.; Zahn, A.; Carsey, T. and Burrows, J.P. (2003): *Trace gas and radical diurnal behavior in the marine boundary layer during INDOEX 1999*, Journal of Geophysical Research-Atmospheres 108 [D8]. URL: <Go to ISI>://000182840200007

Burrows, J.P.; Buchwitz, M.; Eisinger, M.; Rozanov, V.V.; Richter, A.; Weber, M. and Ladstätter-Weißenmayer, A. (1997): *The Global Ozone Monitoring Experiment (GOME): Mission, Instrument Concept, and First Results (Ozone and NO_2)*, 3rd ERS Scientific Symposium, 17-21 March 1997, Space at the service of our Environment, Florence, Italy.

Burrows, J.P. and Chance, K.V. (1992): *S CIAMACHY and GOME : The scientific objectives*, Journal of Atmospheric Chemistry 1715, pp. 502-511.

Burrows, J.P.; Crutzen, P.J.; Harris, G.W.; Klemp, D.; Johnson, T.J.; Perner, D.; Wienhold, F.G. and Zenker, T. (1991): *Messung troposphärischer Spurengase mittels Dioden-Laser-Spektroskopie, BMFT Projekt-Nr. 0744112*, Bundesministerium für Forschung und Technologie

Burrows, J.P.; Dehn, A.; Deters, B.; Himmelmann, S.; Richter, A.; Voigt, S. and Orphal, J. (1998): *Atmospheric remote-sensing reference data from GOME: Part I. Temperature-dependent absorption cross-sections of NO_2 in the 231-794 nm range*, Journal of Quantitative Spectroscopy & Radiative Transfer 60 [6], pp. 1025-1031. URL: <Go to ISI>://000077024700009

Burrows, J.P.; Holzle, E.; Goede, A.P.H.; Visser, H. and Fricke, W. (1995): *Sciamachy - Scanning Imaging Absorption Spectrometer for Atmospheric Chartography*, Acta Astronautica 35 [7], pp. 445-451. URL: <Go to ISI>://A1995QX38100004

Burrows, J.P.; Richter, A.; Dehn, A.; Deters, B.; Himmelmann, S. and Orphal, J. (1999): *Atmospheric remote-sensing reference data from GOME - 2. Temperature-dependent absorption cross sections of O_3 in the 231-794 nm range*, Journal of Quantitative Spectroscopy & Radiative Transfer 61 [4], pp. 509-517. URL: <Go to ISI>://000078440200009

Burrows, J.P.; Weber, M.; Buchwitz, M.; Rozanov, V.; Ladstatter-Weissenmayer, A.; Richter, A.; DeBeek, R.; Hoogen, R.; Bramstedt, K.; Eichmann, K.U. and Eisinger, M. (1999): *The global ozone monitoring experiment (GOME): Mission concept and first scientific results*, Journal of the Atmospheric Sciences 56 [2], pp. 151-175. URL: <Go to ISI>://000078226000003

CamyPeyret, C.; Bergqvist, B.; Galle, B.; Carleer, M.; Clerbaux, C.; Colin, R.; Fayt, C.; Goutail, F.; NunesPinharanda, M.; Pommereau, J.P.; Hausmann, M.; Platt, U.; Pundt, I.; Rudolph, T.; Hermans, C.; Simon, P.C.; Vandaele, A.C.; Plane, J.M.C. and Smith, N. (1996): *Intercomparison of instruments for tropo-*

spheric measurements using differential optical absorption spectroscopy, Journal of Atmospheric Chemistry 23 [1], pp. 51-80. URL: <Go to ISI>://A1996TU21300004

Chameides, W.I. and Davis, D.D. (1983): *Aqueous phase source of formic acids in clouds*, Nature 304, pp. 427-429.

Chance, K.; Kurosu, T.P. and Sioris, C.E. (2005): *Undersampling correction for array detector-based satellite spectrometers*, Applied Optics 44 [7], pp. 1296-1304. URL: <Go to ISI>://000227459600022

Chance, K.; Palmer, P.I.; Spurr, R.J.D.; Martin, R.V.; Kurosu, T.P. and Jacob, D.J. (2000): *Satellite observations of formaldehyde over North America from GOME*, Geophysical Research Letters 27 [21], pp. 3461-3464. URL: <Go to ISI>://000165063000007

Chance, K.V.; Burrows, J.P.; D.Perner and Schneider, W. (1997): *Satellite measurements of atmospheric ozone profiles, including tropospheric ozone, from ultraviolet/visible measurements in the nadir geometry: a potential method to retrieve tropospheric ozone*, Journal of Quantitative Spectroscopy and Radiative Transfer 57 [4], pp. 467-476.

Chance, K.V. and Spurr, R.J.D. (1997): *Ring effect studies: Rayleigh scattering, including molecular parameters for rotational Raman scattering, and the Fraunhofer spectrum*, Applied Optics 36 [21], pp. 5224-5230. URL: <Go to ISI>://A1997XL47400044

Chen, D. and Brutsaert, W. (1998): *Satellite-sensed distribution and spatial patterns of vegetation parameters over a tallgrass prairie*, Journal of the Atmospheric Sciences 55 [7], pp. 1225-1238.

Chubachi, S. (1984): *Preliminary result of ozone observations at Syowa station from February 1982 to January 1983*, Mem. Natl. Inst. Polar Res. [Spec. Issue Jpn. 34], pp. 13-19.

Cicerone, R.J.; Stolarski, R.S. and Walters, S. (1974): *Stratospheric Ozone Destruction by Man-Made Chlorofluoromethanes*, Science 185 [4157], pp. 1165-1167.

Crawford, J.; Davis, D.; Chen, G.; Bradshaw, J.; Sandholm, S.; Kondo, Y.; Liu, S.; Browell, E.; Gregory, G.; Anderson, B.; Sachse, G.; Collins, J.; Barrick, J.; Blake, D.; Talbot, R. and Singh, H. (1997): *An assessment of ozone photochemistry in the extratropical western North Pacific: Impact of continental outflow during the late winter early spring*, Journal of Geophysical Research-Atmospheres 102 [D23], pp. 28469-28487. URL: <Go to ISI>://000071162700036

Crutzen, P.J. and Lovelock, J.E. (1983): *Atmospheric interactions; homogeneous gas reactions of C, N, and S containing compounds*, The major biogeochemical cycles and their interactions 21; pp. 67-114, Wiley & Sons, Chichester, United Kingdom.

Defries, R.S. and Townshend, J.R.G. (1999): *Global land cover characterization from satellite data: from research to operational implementation ?*, Global Ecology and Biogeography 8 [5], pp. 367-379. URL: <Go to ISI>://000085051400006

Deters, B.; Burrows, J.P.; Himmelmann, S. and Blindauer, C. (1996): *Gas phase spectra of HOBr and Br_2O and their atmospheric significance*, Annales Geophysicae-Atmospheres Hydrospheres and Space Sciences 14 [4], pp. 468-475. URL: <Go to ISI>://A1996UF50100010

Diallo, O. and Diouf, A. (1991): *AVHRR monitoring of savanna primary production in Senegal, West Africa: 1987-1988*, International Journal of Remote Sensing 12 [6], pp. 1259-1279.

Dieke, G.H. and Kistiakowsky, G.B. (1934): *The Structure of the Ultraviolet Absorption Spectrum of Formaldehyde*, Physical Review 45, pp. 4-28.

Dignon, J. and Logan, J. (1990): *Biogenic emissions of isoprene: A global inventory*, EOS, Transactions, American Geophysical Union 71, p. 1260.

Dinter, T. (2005): *Modellierung ozeanischer Rückstreuung unter Einbeziehung von Vibrations-Raman-Streuung und die Auswertung anhand von Satellitendaten*, Institut für Umweltphysik Universität Bremen, Bremen.

Dobson, G.M.B.; Harrison, D.N. and Lawrence, J. (1929): *Measurements of the amount of ozone in the Earth's atmosphere and its relation to other geophysical conditions*, Proc. R. Soc. London, Ser. A 122, pp. 456-486.

Eisinger, M. and Burrows, J.P. (1998): *Tropospheric sulfur dioxide observed by the ERS-2 GOME instrument*, Geophysical Research Letters 25 [22], pp. 4177-4180. URL: <Go to ISI>://000077019300019

Eisinger, M.; Richter, A.; LadstatterWeissenmayer, A. and Burrows, J.P. (1997): *DOAS zenith sky observations .1. BrO measurements over Bremen (53 degrees N) 1993-1994*, Journal of Atmospheric Chemistry 26 [1], pp. 93-108. URL: <Go to ISI>://A1997WY79600005

Erle, F.; Pfeilsticker, K. and Platt, U. (1995): *On the Influence of Tropospheric Clouds on Zenith-Scattered-Light Measurements of Stratospheric Species*, Geophysical Research Letters 22 [20], pp. 2725-2728. URL: <Go to ISI>://A1995TA64300012

ESA (1995): *The GOME Users Manual*, Bednarz, Ed, ESA Publication Division, Noordwijk, Netherlands.

Eskes, H.J. and Boersma, K.F. (2003): *Averaging kernels for DOAS total-column satellite retrievals*, Atmospheric Chemistry and Physics 3, pp. 1285-1291. URL: <Go to ISI>://000185141100002

Farman, J.C.; Gardiner, B.G. and Shanklin, J.D. (1985): *Large losses of total ozone in Antarctica reveal seasonal ClO_x/NO_x interaction*, Nature 315, pp. 207-210.

Ferlemann, F.; Camy-Peyret, C.; Fitzenberger, R.; Harder, H.; Hawat, T.; Osterkamp, H.; Schneider, M.; Perner, D.; Platt, U.; Vradelis, P. and Pfeilsticker, K. (1998): *Stratospheric BrO profiles measured at different latitudes and seasons: Instrument description, spectral analysis and profile retrieval*, Geophysical Research Letters 25 [20], pp. 3847-3850. URL: <Go to ISI>://000076502400028

Fietkau, S. (2006): *Messungen atmösphärischer Spurengase in Nairobi (1°S, 36°E)*, Institut für Umweltphysik, Universität Bremen, Bremen.

Finlayson-Pitts, B.J. and Pitts, J.N. (1986): *Atmospheric Chemistry: Fundamentals and Experimental Techniques*, John Wiley, New York.

Fischer, H.; de Reus, M.; Traub, M.; Williams, J.; Lelieveld, J.; de Gouw, J.; Warneke, C.; Schlager, H.; Minikin, A.; Scheele, R. and Siegmund, P. (2003): *Deep convective injection of boundary layer air into the lowermost stratosphere at midlatitudes*, Atmospheric Chemistry and Physics 3, pp. 739-745. URL: <Go to ISI>://000183559000001

Fish, D.J. and Jones, R.L. (1995): *Rotational Raman-Scattering and the Ring Effect in Zenith-Sky Spectra*, Geophysical Research Letters 22 [7], pp. 811-814. URL: <Go to ISI>://A1995QR15300018

Fleischmann, O.C.; Hartmann, M.; Burrows, J.P. and Orphal, J. (2004): *New ultraviolet absorption cross-sections of BrO at atmospheric temperatures measured by time-windowing Fourier transform spectroscopy*, Journal of Photochemistry and Photobiology a-Chemistry 168 [1-2], pp. 117-132. URL: <Go to ISI>://000224440000017

Folberth, G.A.; Hauglustaine, D.A.; Lathiere, J. and Brocheton, F. (2005): *Impact of biogenic hydrocarbons on tropospheric chemistry: results from a global chemistry-climate model*, Atmospheric Chemistry and Physics Discussions 5, pp. 10517–10612,.

Frankenberg, C.; Meirink, J.F.; van Weele, M.; Platt, U. and Wagner, T. (2005): *Assessing methane emissions from global space-borne observations*, Science 308 [5724], pp. 1010-1014. URL: <Go to ISI>://000229190700043

Fried, A.; Crawford, J.; Olson, J.; Walega, J.; Potter, W.; Wert, B.; Jordan, C.; Anderson, B.; Shetter, R.; Lefer, B.; Blake, D.; Blake, N.; Meinardi, S.; Heikes, B.; O'Sullivan, D.; Snow, J.; Fuelberg, H.; Kiley, C.M.; Sandholm, S.; Tan, D.; Sachse, G.; Singh, H.; Faloona, I.; Harward, C.N. and Carmichael, G.R. (2003): *Airborne tunable diode laser measurements of formaldehyde during TRACE-P: Distributions and box model comparisons*, Journal of Geophysical Research-Atmospheres 108 [D20]. URL: <Go to ISI>://000185651100005

Fromm, M.; Bevilacqua, R.; Servranckx, R.; Rosen, J.; Thayer, J.P.; Herman, J. and Larko, D. (2005): *Pyro-cumulonimbus injection of smoke to the stratosphere: Observations and impact of a super blowup in northwestern Canada on 3-4 August 1998*, Journal of Geophysical Research-Atmospheres 110 [D8]. URL: <Go to ISI>://000228897700001

Fromm, M.D. and Servranckx, R. (2003): *Transport of forest fire smoke above the tropopause by supercell convection*, Geophysical Research Letters 30 [10]. URL: <Go to ISI>://000183302500002

Frost, G.J.; Fried, A.; Lee, Y.N.; Wert, B.; Henry, B.; Drummond, J.R.; Evans, M.J.; Fehsenfeld, F.C.; Goldan, P.D.; Holloway, J.S.; Hubler, G.; Jakoubek, R.; Jobson, B.T.; Knapp, K.; Kuster, W.C.; Roberts, J.; Rudolph, J.; Ryerson, T.B.; Stohl, A.; Stroud, C.; Sueper, D.T.; Trainer, M. and Williams, J. (2002): *Comparisons of box model calculations and measurements of formaldehyde from the 1997 North Atlantic Regional Experiment*, Journal of Geophysical Research-Atmospheres 107 [D7-8]. URL: <Go to ISI>://000178894000014

Geiger, H.; Kleffmann, J. and Wiesen, P. (2002): *Smog chamber studies on the influence of diesel exhaust on photosmog formation*, Atmospheric Environment 36 [11], pp. 1737-1747.

Geogdzhayev, I.V.; Mishchenko, M.I.; Liu, L. and Remer, L. (2004): *Global two-channel AVHRR aerosol climatology: effects of stratospheric aerosols and preliminary comparisons with MODIS and MISR retrievals*, Journal of Quantitative Spectroscopy & Radiative Transfer 88 [1-3], pp. 47-59. URL: <Go to ISI>://000223415600007

Geogdzhayev, I.V.; Mishchenko, M.I.; Rossow, W.B.; Cairns, B. and Lacis, A.A. (2002): *Global two-channel AVHRR retrievals of aerosol properties over the ocean for the period of NOAA-9 observations and preliminary retrievals using NOAA-7 and NOAA-11 data*, Journal of the Atmospheric Sciences 59 [3], pp. 262-278. URL: <Go to ISI>://000173418300003

Golchert, S.H.W.; Buschmann, N.; Kleindienst, A.; Palm, M.; Schneider, N.; Jonch-Sorensen, H. and Notholt, J. (2005): *Starting long-term stratospheric observations with RAMAS at summit, Greenland*, Ieee Transactions on Geoscience and Remote Sensing 43 [5], pp. 1022-1027. URL: <Go to ISI>://000228672800011

Goloub, P. and Arino, O. (2000): *Verification of the consistency of POLDER aerosol index over land with ATSR-2/ERS-2 fire product*, Geophysical Research Letters 27 [6], pp. 899-902. URL: <Go to ISI>://000085868600041

Goode, J.G.; Yokelson, R.J.; Susott, R.A.; Babbitt, R.E.; Davies, M.A.; Hao, W.H. and Ward, D.E. (2000): *Measurements of Excess O_3, CO_2 , CO , CH_4 , C_2H_4 , C_2H_2 , HCN , NO , NH_3 , HCOOH , CH_3COOH , HCHO , and CH_3OH in 1997 Alaskan Biomass Burning Plumes by Airborne Fourier Transform Infrared Spectroscopy (AFTIR)*, Journal of Geophysical Research, p. submitted.

Goode, J.G.; Yokelson, R.J.; Susott, R.A. and Ward, D.E. (1999): *Trace gas emissions from laboratory biomass fires measured by open-path Fourier transform infrared spectroscopy: Fires in grass and surface fuels*, Journal of Geophysical Research-Atmospheres 104 [D17], pp. 21237-21245. URL: <Go to ISI>://000082690200002

Grainger, J.F. and Ring, J. (1962): *Anomalous Fraunhofer Line Profiles*, Nature 193, p. 762.

Greenblatt, G.D.; Orlando, J.J.; Burkholder, J. and Ravishankara, A.R. (1990): *Absorption Measurements of Oxygen between 330 and 1140 nm*, Journal of Geophysical Research 95, pp. 18577-18582.

Grutter, M.; Flores, E.; Andraca-Ayala, G. and Baez, A. (2005): *Formaldehyde levels in downtown Mexico City during 2003*, Atmospheric Environment 39 [6], pp. 1027-1034. URL: <Go to ISI>://000227200900005

Guenther, A. (2003): *Key species in land surface atmosphere interactions: Biogenic Volatile Organic Compounds*, iLEAPS meeting, Presentation

Guenther, A.; Hewitt, C.N.; Erickson, D.; Fall, R.; Geron, C.; Graedel, T.; Harley, P.; Klinger, L.; Lerdau, M.; Mckay, W.A.; Pierce, T.; Scholes, B.; Steinbrecher, R.; Tallamraju, R.; Taylor, J. and Zimmerman, P. (1995): *A Global-Model of Natural Volatile Organic-Compound Emissions*, Journal of Geophysical Research-Atmospheres 100 [D5], pp. 8873-8892. URL: <Go to ISI>://A1995QZ72400003

Guenther, A.; Karl, T.; Wiedinmyer, C.; Palmer, P.I. and Geron, C. (2005): *The Model of Emissions of Gases and Aerosols from Nature (MEGAN) Estimates of Global Isoprene Emissions*, Journal of Geophysical Research *in review*.

Hak, C. (2005): *Long-Path DOAS data from the FORMAT campaigns 2002 and 2003, personal communication*, Heidelberg, Institute of Environmental Physics

Hak, C.; Pundt, I.; Trick, S.; Kern, C.; Platt, U.; Dommen, J.; Ordonez, C.; Prevot, A.S.H.; Junkermann, W.; Astorga-Llorens, C.; Larsen, B.R.; Mellqvist, J.; Strandberg, A.; Yu, Y.; Galle, B.; Kleffmann, J.; Lorzer, J.C.; Braathen, G.O. and Volkamer, R. (2005): *Intercomparison of four different in-situ techniques for ambient formaldehyde measurements in urban air*, Atmospheric Chemistry and Physics 5, pp. 2881-2900. URL: <Go to ISI>://000232962900002

Hansen, M.C.; Defries, R.S.; Townshend, J.R.G. and Sohlberg, R. (2000): *Global land cover classification at 1km spatial resolution using a classification tree approach*, International Journal of Remote Sensing 21 [6-7], pp. 1331-1364. URL: <Go to ISI>://000086357700013

Hauf, T.; Schulte, P.; Alheit, R. and Schlager, H. (1995): *Rapid Vertical Trace Gas-Transport by an Isolated Midlatitude Thunderstorm*, Journal of Geophysical Research-Atmospheres 100 [D11], pp. 22957-22970. URL: <Go to ISI>://A1995TF79100017

Hauglustaine, D.A.; Hourdin, F.; Jourdain, L.; Filiberti, M.A.; Walters, S.; Lamarque, J.F. and Holland, E.A. (2004): *Interactive chemistry in the Laboratoire de Meteorologie Dynamique general circulation model: Description and background tropospheric chemistry evaluation*, Journal of Geophysical Research-Atmospheres 109 [D4]. URL: <Go to ISI>://000220216800003

Heckel, A. (2003): *Messungen troposphärischer Spurengase mit einem MAXDOAS-Instrument*, Institut für Umweltphysik, Universität Bremen, Bremen.

Heckel, A.; Richter, A.; Tarsu, T.; Wittrock, F.; Hak, C.; Pundt, I.; Junkermann, W. and Burrows, J.P. (2005): *MAX-DOAS measurements of formaldehyde in the Po-Valley*, Atmospheric Chemistry and Physics 5, pp. 909-918. URL: <Go to ISI>://000227793800001

Hedberg, E.; Kristensson, A.; Ohlsson, M.; Johansson, C.; Johansson, P.A.; Swietlicki, E.; Vesely, V.; Wideqvist, U. and Westerholm, R. (2002): *Chemical and physical characterization of emissions from birch wood combustion in a wood stove*, Atmospheric Environment 36 [30], pp. 4823-4837.

Hegels, E.; Crutzen, P.J.; Klupfel, T.; Perner, D. and Burrows, J.P. (1998): *Global distribution of atmospheric bromine-monoxide from GOME on earth observing satellite ERS-2*, Geophysical Research Letters 25 [16], pp. 3127-3130. URL: <Go to ISI>://000075462000019

Heikes, B.; Snow, J.; Egli, P.; D, O.S.; Crawford, J.; Olson, J.; Chen, G.; Davis, D.; Blake, N. and Blake, D. (2001): *Formaldehyde over the Central Pacific during PEM-Tropics B*, Journal of Geophysical Research D: Atmospheres 106 [23], pp. 32717-32731.

Heikes, B.; Snow, J.; Egli, P.; O'Sullivan, D.; Crawford, J.; Olson, J.; Chen, G.; Davis, D.; Blake, N. and Blake, D. (2001): *Formaldehyde over the central Pacific during PEM-Tropics B*, Journal of Geophysical Research-Atmospheres 106 [D23], pp. 32717-32731. URL: <Go to ISI>://000173479100072

Heikes, B.G.; Chang, W.N.; Pilson, M.E.Q.; Swift, E.; Singh, H.B.; Guenther, A.; Jacob, D.J.; Field, B.D.; Fall, R.; Riemer, D. and Brand, L. (2002): *Atmospheric methanol budget and ocean implication*, Global Biogeochemical Cycles 16 [4]. URL: <Go to ISI>://000181208700002

Hendrick, F.; Barret, B.; Van Roozendael, M.; Boesch, H.; Butz, A.; De Maziere, M.; Goutail, F.; Hermans, C.; Lambert, J.C.; Pfeilsticker, K. and Pommereau, J.P. (2004): *Retrieval of nitrogen dioxide stratospheric profiles from ground-based zenith-sky UV-visible observations: validation of the technique through correlative comparisons*, Atmospheric Chemistry and Physics 4, pp. 2091-2106. URL: <Go to ISI>://000224739400001

Hendrick, F.; Roozendael, M.V.; Kylling, A.; Petritoli, A.; Rozanov, A.; Sanghavi, S.; Schofield, R.; Friedeburg, C.v.; Wagner, T.; Wittrock, F.; Fonteyn, D. and Mazière, M.D. (2005): *Intercomparison exercise between different radiative transfer models used for the interpretation of ground-based zenith-sky and multi-axis DOAS observations*, Atmospheric Chemistry and Physics Discussions 5, pp. 7929-7964.

Ho, S.S.H. and Yu, J.Z. (2002): *Concentrations of formaldehyde and other carbonyls in environments affected by incense burning*, Journal of Environmental Monitoring 4 [5], pp. 728-733. URL: <Go to ISI>://000178925800025

Holton, J.R. (1992): *An introduction to dynamic meteorology*, Academic Press.

Holzinger, R.; Warneke, C.; Hansel, A.; Jordan, A.; Lindinger, W.; Scharffe, D.H.; Schade, G. and Crutzen, P.J. (1999): *Biomass burning as a source of formaldehyde, acetaldehyde, methanol, acetone, acetonitrile, and hydrogen cyanide*, Geophysical Research Letters 26 [8], pp. 1161-1164. URL: <Go to ISI>://000079793700040

Holzinger, R.; Williams, J.; Salisbury, G.; Klupfel, T.; de Reus, M.; Traub, M.; Crutzen, P.J. and Lelieveld, J. (2005): *Oxygenated compounds in aged biomass burning plumes over the Eastern Mediterranean: evidence for strong secondary production of methanol and acetone*, Atmospheric Chemistry and Physics 5, pp. 39-46. URL: <Go to ISI>://000226449200001

Hönninger, G. and Platt, U. (2002): *Observations of BrO and its vertical distribution during surface ozone depletion at Alert*, Atmospheric Environment 36 [15-16], pp. 2481-2489. URL: <Go to ISI>://000176614200003

Hoogen, R.; Rozanov, V.V. and Burrows, J.P. (1999): *Ozone profiles from GOME satellite data: Algorithm description and first validation*, Journal of Geophysical Research-Atmospheres 104 [D7], pp. 8263-8280. URL: <Go to ISI>://000079793600018

Huntrieser, H.; Heland, J.; Schlager, H.; Forster, C.; Stohl, A.; Aufmhoff, H.; Arnold, F.; Scheel, H.E.; Campana, M.; Gilge, S.; Eixmann, R. and Cooper, O. (2005): *Intercontinental air pollution transport from North America to Europe: Experimental evidence from airborne measurements and surface observations*, Journal of Geophysical Research-Atmospheres 110 [D1]. URL: <Go to ISI>://000226548200002

Jacobi, H.W.; Frey, M.M.; Hutterli, M.A.; Bales, R.C.; Schrems, O.; Cullen, N.J.; Steffen, K. and Koehler, C. (2002): *Measurements of hydrogen peroxide and formaldehyde exchange between the atmosphere and surface snow at Summit, Greenland*, Atmospheric Environment 36 [15-16], pp. 2619-2628. URL: <Go to ISI>://000176614200016

Johnston, P.V. (1996): *Studies on the I_0-effect*

Joiner, J.; Bhartia, P.K.; Cebula, R.P.; Hilsenrath, E.; Mcpeters, R.D. and Park, H. (1995): *Rotational Raman-Scattering (Ring Effect) in Satellite Backscatter Ultraviolet Measurements*, Applied Optics 34 [21], pp. 4513-4525. URL: <Go to ISI>://A1995RL12900042

Junkermann, W. (2003): *Aerosol and formaldehyde measurements during the FORMAT campaigns, personal communication*

Junkermann, W. and Stockwell, W.R. (1999): *On the budget of photooxidants in the marine boundary layer of the tropical South Atlantic*, Journal of Geophysical Research-Atmospheres 104 [D7], pp. 8039-8046. URL: <Go to ISI>://000079793600002

Kesselmeier, J.; Kuhn, U.; Wolf, A.; Andreae, M.O.; Ciccioli, P.; Brancaleoni, E.; Frattoni, M.; Guenther, A.; Greenberg, J.; Vasconcellos, P.D.; de Oliva, T.; Tavares, T. and Artaxo, P. (2000): *Atmospheric volatile organic compounds (VOC) at a remote tropical forest site in central Amazonia*, Atmospheric Environment 34 [24], pp. 4063-4072. URL: <Go to ISI>://000088818200002

Kesselmeier, J. and Staudt, M. (1999): *Biogenic volatile organic compounds (VOC): An overview on emission, physiology and ecology*, Journal of Atmospheric Chemistry 33 [1], pp. 23-88. URL: <Go to ISI>://000079722800002

Kinne, S.; Lohmann, U.; Feichter, J.; Schulz, M.; Timmreck, C.; Ghan, S.; Easter, R.; Chin, M.; Ginoux, P.; Takemura, T.; Tegen, I.; Koch, D.; Herzog, M.; Penner, J.; Pitari, G.; Holben, B.; Eck, T.; Smirnov, A.; Dubovik, O.; Slutsker, I.; Tanre, D.; Torres, O.; Mishchenko, M.; Geogdzhayev, I.; Chu, D.A. and Kaufman, Y. (2003): *Monthly averages of aerosol properties: A global comparison among models, satellite data, and AERONET ground data*, Journal of Geophysical Research-Atmospheres 108 [D20]. URL: <Go to ISI>://000186198500001

Koelemeijer, R.B.A.; de Haan, J.F. and Stammes, P. (2003): *A database of spectral surface reflectivity in the range 335-772 nm derived from 5.5 years of GOME observations*, Journal of Geophysical Research-Atmospheres 108 [D2]. URL: <Go to ISI>://000182894400006

Koelemeijer, R.B.A.; Stammes, P.; Hovenier, J.W. and de Haan, J.F. (2001): *A fast method for retrieval of cloud parameters using oxygen A band measurements from the Global Ozone Monitoring Experiment*, Journal of Geophysical Research-Atmospheres 106 [D4], pp. 3475-3490. URL: <Go to ISI>://000167155600012

Kormann, R.; Fischer, H.; de Reus, M.; Lawrence, M.; Bruhl, C.; von Kuhlmann, R.; Holzinger, R.; Williams, J.; Lelieveld, J.; Warneke, C.; de Gouw, J.; Heland, J.; Ziereis, H. and Schlager, H. (2003): *Formaldehyde over the eastern Mediterranean during MINOS: Comparison of airborne in-situ measurements with 3D-model results*, Atmospheric Chemistry and Physics 3, pp. 851-861. URL: <Go to ISI>://000183876300003

Kühl, S. (2005): *Quantifying Stratospheric Chlorine Chemistry by the Satellite Spectrometers GOME and SCIAMACHY*, Institute of Environmental Physics, University of Heidelberg, Heidelberg.

Kuhlmann, R.v. (2001): *Tropospheric Photochemistry of Ozone, its Precursors and the Hydroxyl Radical: A 3D-Modeling Study Considering Non-Methane Hydrocarbons*, Fachbereich Physik, Universtät Mainz, Mainz.

Kurosu, T. (2005): *Personal communication: CHOCHO observations by OMI*

Ladstätter-Weißenmayer, A.; Burrows, J.P.; Richter, A.; Wittrock, F.; Buchwitz, M.; Weber, M.; Eisinger, M. and Neuber, R. (1996): *Validation of GOME O_3 and NO_2 measurements in Bremen, Ny-Ålesund, and Neumayer*, GOME Geophysical Validation Campaign Proceedings - Final Results, 153-160, ESA-WPP 108, 24-26 January 1996, Frascati, Italy

Ladstätter-Weißenmayer, A.; Heland, J.; Kormann, R.; von Kuhlmann, R.; Lawrence, M.G.; Meyer-Arnek, J.; Richter, A.; Wittrock, F.; Ziereis, H. and Burrows, J.P. (2003): *Transport and build-up of tropospheric trace gases during the MINOS campaign: comparsion of GOME, in situ aircraft measurements and MATCH-MPIC-data*, Atmospheric Chemistry and Physics 3, pp. 1887-1902. URL: <Go to ISI>://000186392100004

Lathiere, J.; Hauglustaine, D.A. and Noblet-Ducoudre, N.D. (2005): *Past and future changes in biogenic volatile organic compound emissions simulated with a global dynamic vegetation model*, Geophys Res Lett 32.

Lee, S.C.; Li, W.M. and Ao, C.H. (2002): *Investigation of indoor air quality at residential homes in Hong Kong - Case study*, Atmospheric Environment 36 [2], pp. 225-237.

Lee, Y.N.; Zhou, X.; Kleinman, L.I.; Nunnermacker, L.J.; Springston, S.R.; Daum, P.H.; Newman, L.; Keigley, W.G.; Holdren, M.W.; Spicer, C.W.; Young, V.; Fu, B.; Parrish, D.D.; Holloway, J.; Williams, J.; Roberts, J.M.; Ryerson, T.B. and Fehsenfeld, F.C. (1998): *Atmospheric chemistry and distribution of formaldehyde and several multioxygenated carbonyl compounds during the 1995 Nashville/Middle Tennessee Ozone Study*, Journal of Geophysical Research D: Atmospheres 103 [D17], pp. 22,449-22,462.

Leer, B.V. (1977): *Towards the ultimate conservative difference scheme. Part IV: A new approach to numerical convection*, Journal of Computational Physics 23, pp. 276-299.

Leser, H.; Honninger, G. and Platt, U. (2003): *MAX-DOAS measurements of BrO and NO2 in the marine boundary layer*, Geophysical Research Letters 30 [10]. URL: <Go to ISI>://000183302300001

Lewis, A.C.; Carpenter, L.J. and Pilling, M.J. (2001): *Nonmethane hydrocarbons in Southern Ocean boundary layer air*, Journal of Geophysical Research-Atmospheres 106 [D5], pp. 4987-4994. URL: <Go to ISI>://000167482900022

Li, Z. and Kafatos, M. (2000): *Interannual variability of vegetation in the United States and its relation to El Nino/Southern Oscillation*, Remote Sensing of Environment 71 [3], pp. 230-247.

Logan, J.A.; Prather, M.J.; Wofsy, S.C. and McElroy, M.B. (1981): *Tropospheric Chemistry: A global Perspective*, Journal of Geophysical Research 86, pp. 7210-7254.

Lorenzen-Schmidt, H.; Wessel, S.; Unold, W.; Solberg, S.; Gernandt, H.; Stordal, F. and Platt, U. (1998): *Ozone measurements in the European Arctic during the ARCTOC 1995 campaign*, Tellus Series B-Chemical and Physical Meteorology 50 [5], pp. 416-429. URL: <Go to ISI>://000078421400002

Lutgens, F.K. and Tarbuck, E.J. (2001): *The atmosphere; an introduction to meteorology. 8 ed*, Prentice-Hall, Upper Saddle River, NJ, United States, ISBN: 0-13-087957-6.

Marbach, T.; Beirle, S.; Hollwedel, J.; Khokhar, F.; Platt, U. and Wagner, T. (2005): *Influence of the Vegetation Type on formaldehyde (HCHO) and Nitrogen oxide (NO_2) Tropospheric Emissions during Biomass Burning: Synergistic use of Satellite Observations*, Advanced Space Research submitted.

Marquard, L.C.; Wagner, T. and Platt, U. (2000): *Improved air mass factor concepts for scattered radiation differential optical absorption spectroscopy of atmospheric species*, Journal of Geophysical Research-Atmospheres 105 [D1], pp. 1315-1327. URL: <Go to ISI>://000084856600001

Martin, J.C.G.; Spietz, P.; Orphal, J. and Burrows, J.P. (2004): *Principal and independent components analysis of overlapping spectra in the context of multichannel time-resolved absorption spectroscopy*, Spectrochimica Acta Part a-Molecular and Biomolecular Spectroscopy 60 [11], pp. 2673-2693. URL: <Go to ISI>://000223526200036

Martin, R.V.; Chance, K.; Jacob, D.J.; Kurosu, T.P.; Spurr, R.J.D.; Bucsela, E.; Gleason, J.F.; Palmer, P.I.; Bey, I.; Fiore, A.M.; Li, Q.B.; Yantosca, R.M. and Koelemeijer, R.B.A. (2002): *An improved retrieval of tropospheric nitrogen dioxide from GOME*, Journal of Geophysical Research-Atmospheres 107 [D20]. URL: <Go to ISI>://000180466200100

Martin, R.V.; Jacob, D.J.; Chance, K.; Kurosu, T.P.; Palmer, P.I. and Evans, M.J. (2003): *Global inventory of nitrogen oxide emissions constrained by space-based observations of NO_2 columns*, Journal of Geophysical Research-Atmospheres 108 [D17]. URL: <Go to ISI>://000185361600003

Martin, R.V.; Parrish, D.D.; Ryerson, T.B.; Nicks, D.K.; Chance, K.; Kurosu, T.P.; Jacob, D.J.; Sturges, E.D.; Fried, A. and Wert, B.P. (2004): *Evaluation of GOME satellite measurements of tropospheric NO_2 and HCHO using regional data from aircraft campaigns in the southeastern United States*, Journal of Geophysical Research-Atmospheres 109 [D24]. URL: <Go to ISI>://000226027000005

Martinez, M.; Arnold, T. and Perner, D. (1999): *The role of bromine and chlorine chemistry for arctic ozone depletion events in Ny-Alesund and comparison with model calculations*, Annales Geophysicae-Atmospheres Hydrospheres and Space Sciences 17 [7], pp. 941-956. URL: <Go to ISI>://000081648000010

Medeke, T. (2006): *Validation von SCIAMACHY NO_2- Daten mit bodengebundenen DOAS- Messungen des Bremer DOAS- Messnetzes (BREDOM)*, Institut für Umweltphysik, Universität Bremen, Bremen.

Meller, R. and Moortgat, G.K. (2000): *Temperature dependence of the absorption cross sections of formaldehyde between 223 and 323 K in the wavelength range 225-375 nm*, Journal of Geophysical Research-Atmospheres 105 [D6], pp. 7089-7101. URL: <Go to ISI>://000086095000003

Meyer-Arnek, J.; Ladstätter-Weißenmayer, A.; Richter, A.; Wittrock, F. and Burrows, J.P. (2005): *A study of the trace gas columns O_3, NO_2 and HCHO over Africa in September 1997*, Faraday Discussions 130, pp. 387-405. URL: <Go to ISI>://000231804100023

Miller, H.L.; Weaver, A.; Sanders, R.W.; Arpag, K. and Solomon, S. (1997): *Measurements of Artic Sunrise Surface Ozone Depletion Events at Kangerlussuaq , Greenland (67 N , 51 W)*, Tellus 49.

Mishchenko, M.; Penner, J. and Anderson, D. (2002): *Global aerosol climatology project*, Journal of the Atmospheric Sciences 59 [3], pp. 249-249. URL: <Go to ISI>://000173418300001

Mishchenko, M.I.; Geogdzhayev, I.V.; Cairns, B.; Rossow, W.B. and Lacis, A.A. (1999): *Aerosol retrievals over the ocean by use of channels 1 and 2 AVHRR data: sensitivity analysis and preliminary results*, Applied Optics 38 [36], pp. 7325-7341. URL: <Go to ISI>://000084484400003

Mishchenko, M.I.; Geogdzhayev, I.V.; Liu, L.; Ogren, J.A.; Lacis, A.A.; Rossow, W.B.; Hovenier, J.W.; Volten, H. and Munoz, O. (2003): *Aerosol retrievals from AVHRR radiances: effects of particle nonsphericity and absorption and an updated long-term global climatology of aerosol properties*, Journal of Quantitative Spectroscopy & Radiative Transfer 79, pp. 953-972. URL: <Go to ISI>://000182647500031

Molina, J.M. and Rowland, F.S. (1974): *Stratospheric sink for chlorofluoromethanes: chlorine atom-catalysed destruction of ozone*, Nature 249, pp. 810-812.

Mount, G.H.; Sanders, R.W.; Schmeltekopf, A.L. and Solomon, S. (1987): *Visible spectroscopy at McMurdo Station , Antarctica . 1. Overview and daily variations of NO_2 and O_3 , Austral spring, 1986*, Journal of Geophysical Research 92, pp. 8320-8328.

Mueller, J.F. (1992): *Geographical distribution and seasonal variation of surface emissions and deposition velocities of atmospheric trace gases*, Journal of Geophysical Research 97, pp. 3787-3804.

Mueller, R.W.; Bovensmann, H.; Kaiser, J.W.; Richter, A.; Rozanov, A.; Wittrock, F. and Burrows, J.P. (2002): *Consistent interpretation of ground based and GOME BrO slant column data*, Remote Sensing of Trace Constituents in the Lower Stratosphere, Troposphere and the Earth's Surface: Global Observations, Air Pollution and the Atmospheric Correction 29 [11], pp. 1655-1660. URL: <Go to ISI>://000177314200009

Muller, M.D.; Kaifel, A.K.; Weber, M.; Tellmann, S.; Burrows, J.P. and Loyola, D. (2003): *Ozone profile retrieval from Global Ozone Monitoring Experiment (GOME) data using a neural network approach (Neural Network Ozone Retrieval System (NNORSY))*, Journal of Geophysical Research-Atmospheres 108 [D16]. URL: <Go to ISI>://000184998900002

Myhre, G.; Stordal, F.; Johnsrud, M.; Diner, D.J.; Geogdzhayev, I.V.; Haywood, J.M.; Holben, B.N.; Holzer-Popp, T.; Ignatov, A.; Kahn, R.A.; Kaufman, Y.J.; Loeb, N.; Martonchik, J.V.; Mishchenko, M.I.; Nalli, N.R.; Remer, L.A.; Schroedter-Homscheidt, M.; Tanre, D.; Torres, O. and Wang, M. (2005): *Intercomparison of satellite retrieved aerosol optical depth over ocean during the period September 1997 to December 2000*, Atmospheric Chemistry and Physics 5, pp. 1697-1719. URL: <Go to ISI>://000230453500002

Noël, S.; Buchwitz, M. and Burrows, J.P. (2004): *First retrieval of global water vapour column amounts from SCIAMACHY measurements*, Atmospheric Chemistry and Physics 4, pp. 111-125. URL: <Go to ISI>://000188775700001

Notholt, J.; Toon, G.; Stordal, F.; Solberg, S.; Schmidbauer, N.; Becker, E.; Meier, A. and Sen, B. (1997): *Seasonal variations of atmospheric trace gases in the high Arctic at 79 degrees N*, Journal of Geophysical Research-Atmospheres 102 [11D], pp. 12855-12861. URL: <Go to ISI>://A1997XG17900007

Notholt, J.; Toon, G.C.; Rinsland, C.P.; Pougatchev, N.S.; Jones, N.B.; Connor, B.J.; Weller, R.; Gautrois, M. and Schrems, O. (2000): *Latitudinal variations of trace gas concentrations in the free troposphere measured by solar absorption spectroscopy during a ship cruise*, Journal of Geophysical Research-Atmospheres 105 [D1], pp. 1337-1349. URL: <Go to ISI>://000084856600003

Noxon, J.F. (1975): *Nitrogen dioxide in the stratosphere and troposphere measured by ground-based absorption spectroscopy*, Science 189, pp. 547-549.

Nüß, H. (2005): *Verbesserung des troposphärischen NO_2-Retrievals aus GOME und SCIAMACHY-Daten*, Institut für Umweltphysik, Universität Bremen, Bremen.

Nyquist, H. (1928): *Certain topics in telegraph transmission theory*, Trans. AIEEE 47, pp. 617-644.

Oesterheld, M. and DiBella, C.M. (1998): *Relation between NOAA-AVHRR satellite data and stocking rate of rangelands*, Ecological Applications 8 [1], pp. 207-212.

Oetjen, H. (2002): *Messungen atmosphärischer Spurengase in Ny-Ålesund*, Institut für Umweltphysik, Universität Bremen, Bremen.

Olivier, J.G.J. and Berdowski, J.J.M. (2001): *Global emissions sources and sinks*, Berdowski; Guicherit and Heij, The Climate System, A. A. Balkema Publishers/Swets & Zeitlinger Publishers, Lisse, The netherlands.

Olivier, J.G.J.; Bouwman, A.F.; Vandermaas, C.W.M. and Berdowski, J.J.M. (1994): *Emission Database for Global Atmospheric Research (Edgar)*, Environmental Monitoring and Assessment 31 [1-2], pp. 93-106. URL: <Go to ISI>://A1994PL32500010

Ordonez, C. (2003): *Measurements of NO_2 and meteorological parameters during the FORMAT campaigns in 2002 and 2003, personal communication*

Orphal, J.; Perrin, A.; Flaud, J.M.; Smirnov, M.; Himmelmann, S.; Voigt, S. and Burrows, J.P. (2000): *New high-resolution analysis of the nu(3) band of the (NO_2)-N-15-O-16 isotopomer of nitrogen dioxide by Fourier transform spectroscopy*, Journal of Molecular Spectroscopy 204 [1], pp. 72-79. URL: <Go to ISI>://000165198700009

Palmer, P.I.; Jacob, D.J.; Chance, K.; Martin, R.V.; Spurr, R.J.D.; Kurosu, T.P.; Bey, I.; Yantosca, R.; Fiore, A. and Li, Q.B. (2001): *Air mass factor formulation for spectroscopic measurements from satellites: Application to formaldehyde retrievals from the Global Ozone Monitoring Experiment*, Journal of Geophysical Research-Atmospheres 106 [D13], pp. 14539-14550. URL: <Go to ISI>://000169903900026

Palmer, P.I.; Jacob, D.J.; Fiore, A.M.; Martin, R.V.; Chance, K. and Kurosu, T.P. (2003): *Mapping isoprene emissions over North America using formaldehyde column observations from space*, Journal of Geophysical Research-Atmospheres 108 [D6]. URL: <Go to ISI>://000182222800002

Palmer, P.I. and Shaw, S.L. (2005): *Quantifying global marine isoprene fluxes using MODIS chlorophyll observations*, Geophysical Research Letters 32 [9]. URL: <Go to ISI>://000229145300003

Perliski, L.M. and Solomon, S. (1993): *On the evaluation of air mass factors for atmospheric near-ultraviolet and visible absorption spectroscopy*, Journal of Geophysical Research 98, pp. 10363-10374.

Pfeilsticker, K.; Arlander, D.W.; Burrows, J.P.; Erle, F.; Gil, M.; Goutail, F.; Hermans, C.; Lambert, J.C.; Platt, U.; Pommereau, J.P.; Richter, A.; Sarkissian, A.; Van Roozendael, M.; Wagner, T. and Winterrath, T. (1999): *Intercomparison of the influence of tropospheric clouds on UV-visible absorptions detected during the NDSC intercomparison campaign at OHP in June 1996*, Geophysical Research Letters 26 [8], pp. 1169-1172. URL: <Go to ISI>://000079793700042

Pfeilsticker, K.; Erle, F.; Funk, O.; Marquard, L.; Wagner, T. and Platt, U. (1998): *Optical path modifications due to tropospheric clouds: Implications for zenith sky measurements of stratospheric gases*, Journal of Geophysical Research-Atmospheres 103 [D19], pp. 25323-25335. URL: <Go to ISI>://000076490200012

Pfeilsticker, K. and Platt, U. (1994): *Airborne Measurements during the Arctic Stratospheric Experiment - Observation of O3 and No2*, Geophysical Research Letters 21 [13], pp. 1375-1378. URL: <Go to ISI>://A1994NW30100048

Philips, K.J. (1992): *Guide to the Sun*, Cambridge University Press.

Platt, U. and Hausmann, M. (1994): *Spectroscopic Measurement of the Free-Radicals NO_3, BrO, IO, and OH in the Troposphere*, Research on Chemical Intermediates 20 [3-5], pp. 557-578. URL: <Go to ISI>://A1994NG54100014

Platt, U.; Marquard, L.; Wagner, T. and Perner, D. (1997): *Corrections for zenith scattered light DOAS*, Geophysical Research Letters 24 [14], pp. 1759-1762. URL: <Go to ISI>://A1997XL83700011

Platt, U. and Perner, D. (1980): *Direct measurements of atmospheric CH_2O , HNO_2 , O_2 , NO_2 and SO_2 by differential absorption in the near UV*, Journal of Geophysical Research 85, pp. 7453-7458.

Pope, R.M. and Fry, E.S. (1997): *Absorption spectrum (380-700 nm) of pure water .2. Integrating cavity measurements*, Applied Optics 36 [33], pp. 8710-8723. URL: <Go to ISI>://A1997YF88600025

Preston, K.E.; Jones, R.L. and Roscoe, H.K. (1997): *Retrieval of NO2 vertical profiles from ground-based UV-visible measurements: Method and validation*, Journal of Geophysical Research-Atmospheres 102 [D15], pp. 19089-19097. URL: <Go to ISI>://A1997XT10100022

Price, H.U.; Jaffe, D.A.; Cooper, O.R. and Doskey, P.V. (2004): *Photochemistry, ozone production, and dilution during long-range transport episodes from Eurasia to the northwest United States*, Journal of Geophysical Research-Atmospheres 109 [D23]. URL: <Go to ISI>://000222917000001

Pundt, I.; Mettendorf, K.U.; Laepple, T.; Knab, V.; Xie, P.; Losch, J.; Friedeburg, C.V.; Platt, U. and Wagner, T. (2005): *Measurements of trace gas distributions using Long-path DOAS-Tomography during the motorway campaign BAB II: experimental setup and results for NO_2*, Atmospheric Environment 39 [5], pp. 967-975. URL: <Go to ISI>://000226884000014

Rasmussen, R. and Khalil, M. (1988): *Isoprene over the Amazon basin*, Journal of Geophysical Research 93, pp. 1417-1421.

Rasmussen, R.A. and Went, F.W. (1965): *Volatile organic material of plant origin in the atmosphere*, Proc. Nat. Acad. Sci. 53, pp. 215-220.

Rathke, C.; Notholt, J.; Fischer, J. and Herber, A. (2002): *Properties of coastal Antarctic aerosol from combined FTIR spectrometer and sun photometer measurements*, Geophysical Research Letters 29 [23]. URL: <Go to ISI>://000181096700002

Renard, J.B.; Pirre, M.; Robert, C. and Huguenin, D. (1997): *OBrO Est-il Present Dans la Stratosphere?*, Sciences de la terre et des planetes 325, pp. 921-924.

Richter, A. (1997): *Absorptionsspektrospkopische Messungen stratosphärischer Spurengase über Bremen, 53° N*, Institute of Environmental Physics, University of Bremen, Bremen.

Richter, A. and Burrows, J.P. (2002): *Tropospheric NO2 from GOME measurements*, Remote Sensing of Trace Constituents in the Lower Stratosphere, Troposphere and the Earth's Surface: Global Observations, Air Pollution and the Atmospheric Correction 29 [11], pp. 1673-1683. URL: <Go to ISI>://000177314200012

Richter, A.; Burrows, J.P.; Nuss, H.; Granier, C. and Niemeier, U. (2005): *Increase in tropospheric nitrogen dioxide over China observed from space*, Nature 437 [7055], pp. 129-132. URL: <Go to ISI>://000231560400055

Richter, A.; Eisinger, M.; Ladstatter-Weissenmayer, A. and Burrows, J.P. (1999): *DOAS Zenith sky observations: 2. Seasonal variation of BrO over Bremen (53 degrees N) 1994-1995*, Journal of Atmospheric Chemistry 32 [1], pp. 83-99. URL: <Go to ISI>://000079289200005

Richter, A.; Eyring, V.; Burrows, J.P.; Bovensmann, H.; Lauer, A.; Sierk, B. and Crutzen, P.J. (2004): *Satellite measurements of NO_2 from international shipping emissions*, Geophysical Research Letters 31 [23]. URL: <Go to ISI>://000225878900001

Richter, A. and Wagner, T. (2001): *Diffuser plate structures and their influence on GOME slant columns*, Technical Note, http://www.iup.physik.uni-bremen.de/gome

Richter, A.; Wittrock, F.; Eisinger, M. and Burrows, J.P. (1998): *GOME observations of tropospheric BrO in northern hemispheric spring and summer 1997*, Geophysical Research Letters 25 [14], pp. 2683-2686. URL: <Go to ISI>://000074886300057

Richter, A.; Wittrock, F.; Ladstatter-Weissenmayer, A. and Burrows, J.P. (2002): *GOME measurements of stratospheric and tropospheric BrO*, Remote Sensing of Trace Constituents in the Lower Stratosphere, Troposphere and the Earth's Surface: Global Observations, Air Pollution and the Atmospheric Correction 29 [11], pp. 1667-1672. URL: <Go to ISI>://000177314200011

Ricotta, C. and Avena, G.C. (1998): *Fractal modelling of the remotely sensed two-dimensional net primary production pattern with annual cumulative AVHRR NDVI data*, International Journal of Remote Sensing 19 [12], pp. 2413-2418. URL: <Go to ISI>://000075502900013

Riedel, K.; Weller, R. and Schrems, O. (1999): *Variability of formaldehyde in the Antarctic troposphere*, Physical Chemistry Chemical Physics 1 [24], pp. 5523-5527. URL: <Go to ISI>://000085242400019

Robinson, E. and Robbins, R. (1968): *Sources, abundance and fate of gaseous atmospheric pollutants*, Stanford Research Institute, Menlo Park, California, PR-6757

Rodgers, C.D. (1976): *Retrieval of Atmospheric Temperature and Composition from Remote Measurements of Thermal Radiation*, Reviews of Geophysics and Space Physics 14 [4], pp. 609-624.

Rodgers, C.D. (1990): *Characterization and error analysis of profiles retrieved from remote sounding measurements*, Journal of Geophysical Research 95, pp. 5587-5595.

Rodgers, C.D. (1998): *Information content and optimisation of high spectral resolution remote measurements*, Remote Sensing: Inversion Problems and Natural Hazards 21 [3], pp. 361-367. URL: <Go to ISI>://000073538000001

Rodgers, C.D. (2000): *Inverse Methods for Atmospheric Sounding, Theory and Practise*, World Scientific Publishing, London.

Roscoe, H.K.; Fish, D.J. and Jones, R.L. (1996): *Interpolation errors in UV-visible spectroscopy for stratospheric sensing: implications for sensitivity, spectral resolution, and spectral range*, Applied Optics 35, pp. 428-432.

Roscoe, H.K.; Freshwater, R.A.; Wolfenden, R.; Jones, R.L.; Fish, D.J.; Harries, J.E.; South, A.M. and Oldham, D.J. (1994): *Using Stars for Remote-Sensing of the Earths Stratosphere*, Applied Optics 33 [30], pp. 7126-7131. URL: <Go to ISI>://A1994PN17900030

Roscoe, H.K.; Johnston, P.V.; Van Roozendael, M.; Richter, A.; Sarkissian, A.; Roscoe, J.; Preston, K.E.; Lambert, J.C.; Hermans, C.; Decuyper, W.; Dzienus, S.; Winterrath, T.; Burrows, J.; Goutail, F.; Pommereau, J.P.; D'Almeida, E.; Hottier, J.; Coureul, C.; Didier, R.; Pundt, I.; Bartlett, L.M.; McElroy, C.T.; Kerr, J.E.; Elokhov, A.; Giovanelli, G.; Ravegnani, F.; Premuda, M.; Kostadinov, I.; Erle, F.; Wagner, T.; Pfeilsticker, K.; Kenntner, M.; Marquard, L.C.; Gil, M.; Puentedura, O.; Yela, M.; Arlander, D.W.; Hoiskar, B.A.K.; Tellefsen, C.W.; Tornkvist, K.K.; Heese, B.; Jones, R.L.; Aliwell, S.R. and Freshwater, R.A. (1999): *Slant column measurements of O_3 and NO_2 during the NDSC intercomparison of zenith-sky UV-visible spectrometers in June 1996*, Journal of Atmospheric Chemistry 32 [2], pp. 281-314. URL: <Go to ISI>://000079328000003

Rothman, L.S.; Gamache, R.R.; Tipping, R.H.; Rinsland, C.P.; Smith, M.A.H.; Benner, C.D.; Devi, V.M.; Flaud, J.M.; Camy-Peyret, C.; Perrin, A.; Goldman, A.; Massie, S.T. and Brown, L.R. (1992): *The HITRAN molecular database editions 1991 and 1992*, J. Quant. Spectrosc. Radiat. Transfer 48, pp. 469-507.

Rottenberger, S.; Kuhn, U.; Wolf, A.; Schebeske, G.; Oliva, S.T.; Tavares, T.M. and Kesselmeier, J. (2004): *Exchange of short-chain aldehydes between Amazonian vegetation and the atmosphere*, Ecological Applications 14 [4 SUPPL.], pp. S247-S262.

Rottenberger, S.; Kuhn, U.; Wolf, A.; Schebeske, G.; Oliva, S.T.; Tavares, T.M. and Kesselmeier, J. (2005): *Formaldehyde and acetaldehyde exchange during leaf development of the Amazonian deciduous tree species Hymenaea courbaril*, Atmospheric Environment 39 [12], pp. 2275-2279. URL: <Go to ISI>://000228945400011

Row, L.W.; Hastings, D.A. and Dunbar, P.K. (1994): *Terrainbase worldwide digital terrain data. Release 1.0*, National Geophysical Data Center, Boulder

Rozanov, A. (2001): *A numerical Radiative Transfer Model for a Spherical Planetary Atmosphere: Combined Differential-Integral Approach involving the Picar Iterative Approximation*, Institute of Environmental Physics, University of Bremen, Bremen.

Rozanov, A.; Rozanov, V. and Burrows, J.P. (2001): *A numerical radiative transfer model for a spherical planetary atmosphere: combined differential-integral approach involving the Picard iterative approximation*, Journal of Quantitative Spectroscopy & Radiative Transfer 69 [4], pp. 491-512. URL: <Go to ISI>://000168073600008

Rozanov, A.; Rozanov, V. and Burrows, J.P. (2002): *Evaluation of the combined differential-integral approach for limb viewing geometry*, Remote Sensing of Trace Constituents in the Lower Stratosphere, Troposphere and the Earth's Surface: Global Observations, Air Pollution and the Atmospheric Correction 29 [11], pp. 1843-1848. URL: <Go to ISI>://000177314200038

Rozanov, A.V.; Rozanov, V.V. and Burrows, J.P. (2000): *Combined differential-integral approach for the radiation field computation in a spherical shell atmosphere: Nonlimb geometry*, Journal of Geophysical Research-Atmospheres 105 [D18], pp. 22937-22942. URL: <Go to ISI>://000089598000019

Rozanov, V.V.; Buchwitz, M.; Eichmann, K.U.; de Beek, R. and Burrows, J.P. (2002): *SCIATRAN - A new radiative transfer model for geophysical applications in the 240-2400 nm spectral region: The pseudo-spherical version*, Remote Sensing of Trace Constituents in the Lower Stratosphere, Troposphere and the Earth's Surface: Global Observations, Air Pollution and the Atmospheric Correction 29 [11], pp. 1831-1835. URL: <Go to ISI>://000177314200036

Rozanov, V.V.; Diebel, D.; Spurr, R.J.D. and Burrows, J.P. (1997): *GOMETRAN: A radiative transfer model for the satellite project GOME, the plane-parallel version*, Journal of Geophysical Research-Atmospheres 102 [D14], pp. 16683-16695. URL: <Go to ISI>://A1997XN38400020

Rudolph, J.; Fu, B.R.; Thompson, A.; Anlauf, K. and Bottenheim, J. (1999): *Halogen atom concentrations in the Arctic troposphere derived from hydrocarbon measurements: Impact on the budget of formaldehyde*, Geophysical Research Letters 26 [19], pp. 2941-2944. URL: <Go to ISI>://000082960700012

Sadourny, R. and Laval, K. (1984): *January and July performance of the LMD general circulation model*, Berger and Nicolis, New Perspectives in Climate Modeling pp. 173-197, Elsevier.

Sanderson, M.G. (2002): *Emission of Isoprene, Monoterpenes, Ethene and Propene by Vegetation - Description and Implementation in the STOCHEM Model*, Hadley Center, Meteorological Office

Sathyendranath, S. and Platt, T. (1998): *Ocean-color model incorporating transspectral processes*, Applied Optics 37 [12], pp. 2216-2227. URL: <Go to ISI>://000073148600004

Scheeren, H.A. (2003): *Reactive hydro- end chlorocarbons in the troposphere and lower stratosphere : sources, distributions, and chemical impact*, Universiteit Utrecht, Utrecht.

Schlieter, S. (2001): *Spurengasmessungen während der Nacht mittels Mondlichtspektroskopie im Vergleich mit Modellrechnungen*, Institut für Umweltphysik, Universität Bremen, Bremen.

Schlieter, S.; Bruns, M.; Eisinger, M.; Ladstätter-Weißenmayer, A.; Richter, A.; Wittrock, F. and Burrows, J.P. (1997): *Trace gas measurements in polar regions and midlatitudes in 1996/97 using the moon as a lightsource*, Polar stratospheric ozone 1997, Schliersee, Germany.

Schmidt, U. and Lowe, D.C. (1982): *Vertical profiles of formaldehyde in the troposphere (Eifel West Germany)*, Versino and Ott, Physical chemical behaviour of atmospheric pollutants Proc 2nd European symposium, Varese, 1981 pp. 377-386, 5 figs, 15 refs, Reidel for the EEC; EUR 7624.

Schofield, R.; Connor, B.J.; Kreher, K.; Johnston, P.V. and Rodgers, C.D. (2004): *The retrieval of profile and chemical information from ground-based UV-visible spectroscopic measurements*, Journal of Quantitative Spectroscopy & Radiative Transfer 86 [2], pp. 115-131. URL: <Go to ISI>://000221210000001

Shaw, S.L.; Chisholm, S.W. and Prinn, R.G. (2003): *Isoprene production by Prochlorococcus, a marine cyanobacterium, and other phytoplankton*, Marine Chemistry 80 [4], pp. 227-245. URL: <Go to ISI>://000181512200001

Shettle, P. and Fenn, R.W. (1976): *Models of the atmospheric aerosols and their optical properties*, AGARD Conference Proceedings on optical propagation in the atmosphere.

Simon, M.; Plummer, S.; Fierens, F.; Hoelzemann, J.J. and Arino, O. (2004): *Burnt area detection at global scale using ATSR-2: The GLOBSCAR products and their qualification*, Journal of Geophysical Research-Atmospheres 109 [D14]. URL: <Go to ISI>://000222780400001

Singh, H.B.; Salas, L.J.; Chatfield, R.B.; Czech, E.; Fried, A.; Walega, J.; Evans, M.J.; Field, B.D.; Jacob, D.J.; Blake, D.; Heikes, B.; Talbot, R.; Sachse, G.; Crawford, J.H.; Avery, M.A.; Sandholm, S. and Fuelberg, H. (2004): *Analysis of the atmospheric distribution, sources, and sinks of oxygenated volatile organic chemicals based on measurements over the Pacific during TRACE-P*, Journal of Geophysical Research-Atmospheres 109 [D15]. URL: <Go to ISI>://000221954000002

Sinnhuber, B.M.; Arlander, D.W.; Bovensmann, H.; Burrows, J.P.; Chipperfield, M.P.; Enell, C.F.; Friess, U.; Hendrick, F.; Johnston, P.V.; Jones, R.L.; Kreher, K.; Mohamed-Tahrin, N.; Muller, R.; Pfeilsticker, K.; Platt, U.; Pommereau, J.P.; Pundt, I.; Richter, A.; South, A.M.; Tornkvist, K.K.; Van Roozendael, M.; Wagner, T. and Wittrock, F. (2002): *Comparison of measurements and model calculations of stratospheric bromine monoxide*, Journal of Geophysical Research-Atmospheres 107 [D19]. URL: <Go to ISI>://000180428300066

Slemr, J.; Junkermann, W. and VolzThomas, A. (1996): *Temporal variations in formaldehyde, acetaldehyde and acetone and budget of formaldehyde at a rural site in southern Germany*, Atmospheric Environment 30 [21], pp. 3667-3676. URL: <Go to ISI>://A1996VD98700009

Slijkhuis, S.; Bargen, A.v.; Thomas, W. and Chance, K.V. (1999): *Calculation of Undersampling Correction Spectra for DOAS Spectral Fitting*, Atmospheric Measurements from Space. URL: http://elib.dlr.de/153

Solomon, S.; Schmeltekopf, A.L. and Sanders, R.W. (1987): *On the Interpretation of Zenith Sky Absorption Measurements*, Journal of Geophysical Research 92 [D7], pp. 8311-8319.

Spaulding, R.S.; Schade, G.W.; Goldstein, A.H. and Charles, M.J. (2003): *Characterization of secondary atmospheric photooxidation products: Evidence for biogenic and anthropogenic sources*, Journal of Geophysical Research-Atmospheres 108 [D8]. URL: <Go to ISI>://000182842900003

Stam, D.M.; Aben, I. and Helderman, F. (2002): *Skylight polarization spectra: Numerical simulation of the Ring effect*, Journal of Geophysical Research-Atmospheres 107 [D20]. URL: <Go to ISI>://000180466200073

Stohl, A.; Huntrieser, H.; Richter, A.; Beirle, S.; Cooper, O.R.; Eckhardt, S.; Forster, C.; James, P.; Spichtinger, N.; Wenig, M.; Wagner, T.; Burrows, J.P. and Platt, U. (2003): *Rapid intercontinental air pollution transport associated with a meteorological bomb*, Atmospheric Chemistry and Physics 3, pp. 969-985. URL: <Go to ISI>://000184098300001

Sumner, A.L.; Shepson, P.B.; Grannas, A.M.; Bottenheim, J.W.; Anlauf, K.G.; Worthy, D.; Schroeder, W.H.; Steffen, A.; Domine, F.; Perrier, S. and Houdier, S. (2002): *Atmospheric chemistry of formaldehyde in the Arctic troposphere at Polar Sunrise, and the influence of the snowpack*, Atmospheric Environment 36 [15-16], pp. 2553-2562. URL: <Go to ISI>://000176614200010

Tanskanen, A.; Arola, A. and Kujanpää, J. (2003): *Use of the moving time-window technique to determine surface albedo from the TOMS reflectivity data*, Proc. SPIE 4896, pp. 239-250.

Taylor, J.; Zimmermann, P. and Erickson, D. (1990): *A 3-D modelling study of the sources and sinks of atmospheric carbon monoxide*, CRES Work, Canberra, Aust. Nat. Univ., Pap. 199013

Tellmann, S.; Rozanov, V.V.; Weber, M. and Burrows, J.P. (2004): *Improvements in the tropical ozone profile retrieval from GOME-UV/Vis nadir spectra*, Trace Constituents in the Troposphere and Lower Stratosphere 34 [4], pp. 739-743. URL: <Go to ISI>://000223618200010

Thomas, W.; Hegels, E.; Slijkhuis, S.; Spurr, R. and Chance, K.I. (1998): *Detection of biomass burning combustion products in Southeast Asia from backscatter data taken by the GOME spectrometer*, Geophysical Research Letters 25 [9], pp. 1317-1320. URL: <Go to ISI>://000073414900008

Thompson, A.M. and Zafiriou, O. (1983): *Air-sea fluxes of transient atmospheric species*, Journal of Geophysical Research 88, pp. 6696-6708.

Tie, X.X.; Madronich, S.; Walters, S.; Edwards, D.P.; Ginoux, P.; Mahowald, N.; Zhang, R.Y.; Lou, C. and Brasseur, G. (2005): *Assessment of the global impact of aerosols on tropospheric oxidants*, Journal of Geophysical Research-Atmospheres 110 [D3]. URL: <Go to ISI>://000227065800004

Tiedke, M. (1989): *A comprehensive mass-flux scheme for cumulus parameterization in large scale models*, Monthly Weather Review, pp. 1779-1780.

Tornkvist, K.K.; Arlander, D.W. and Sinnhuber, B.M. (2002): *Ground-based UV measurements of BrO and OClO over Ny-Alesund during winter 1996 and 1997 and Andoya during winter 1998/99*, Journal of Atmospheric Chemistry 43 [2], pp. 75-106. URL: <Go to ISI>://000177722400001

Treffeisen, R.; Herber, A.; Strom, J.; Shiobara, M.; Yamagata, T.Y.; Holmen, K.; Kriews, M. and Schrems, O. (2004): *Interpretation of Arctic aerosol properties using cluster analysis applied to observations in the Svalbard area*, Tellus Series B-Chemical and Physical Meteorology 56 [5], pp. 457-476. URL: <Go to ISI>://000225463000007

Turner, D.; Baglio, J.; Pross, D.; Wones, A.; McVeety, B.; Vong, R. and Philips, D. (1991): *Climate change and isoprene emissions from vegetation*, Chemosphere 23, pp. 37-56.

van Aardenne, J.A.; Dentener, F.J.; Olivier, J.G.J.; Goldewijk, C.G.M.K. and Lelieveld, J. (2001): *A 1 degrees x 1 degrees resolution data set of historical anthropogenic trace gas emissions for the period 1890-1990*, Global Biogeochemical Cycles 15 [4], pp. 909-928. URL: <Go to ISI>://000172755300011

van der Werf, G.R.; Randerson, J.T.; Collatz, G.J. and Giglio, L. (2003): *Carbon emissions from fires in tropical and subtropical ecosystems*, Global Change Biology 9 [4], pp. 547-562. URL: <Go to ISI>://000182008600007

van der Werf, G.R.; Randerson, J.T.; Collatz, G.J.; Giglio, L.; Kasibhatla, P.S.; Arellano, A.F.; Olsen, S.C. and Kasischke, E.S. (2004): *Continental-scale partitioning of fire emissions during the 1997 to 2001 El Nino/La Nina period*, Science 303 [5654], pp. 73-76. URL: <Go to ISI>://000187710600035

Vandaele, A.C.; Fayt, C.; Hendrick, F.; Hermans, C.; Humbled, F.; Van Roozendael, M.; Gil, M.; Navarro, M.; Puentedura, O.; Yela, M.; Braathen, G.; Stebel, K.; Tornkvist, K.; Johnston, P.; Kreher, K.; Goutail, F.; Mieville, A.; Pommereau, J.P.; Khaikine, S.; Richter, A.; Oetjen, H.; Wittrock, F.; Bugarski, S.; Friess, U.; Pfeilsticker, K.; Sinreich, R.; Wagner, T.; Corlett, G. and Leigh, R. (2005): *An intercomparison campaign of ground-based UV-visible measurements of NO_2, BrO, and OClO slant columns: Methods of analysis and results for NO2*, Journal of Geophysical Research-Atmospheres 110 [D8]. URL: <Go to ISI>://000228897500007

Vandaele, A.C.; Hermans, C.; Fally, S.; Carleer, M.; Colin, R.; Merienne, M.F.; Jenouvrier, A. and Coquart, B. (2002): *High-resolution Fourier transform measurement of the NO_2 visible and near-infrared absorption cross sections: Temperature and pressure effects*, Journal of Geophysical Research-Atmospheres 107 [D18]. URL: <Go to ISI>://000180427400013

Vasilkov, A.P.; Joiner, J.; Gleason, J. and Bhartia, P.K. (2002): *Ocean Raman scattering in satellite backscatter UV measurements*, Geophysical Research Letters 29 [17]. URL: <Go to ISI>://000180397500018

Voigt, S.; Orphal, J.; Bogumil, K. and Burrows, J.P. (2001): *The temperature dependence (203-293 K) of the absorption cross sections of O_3 in the 230-850 nm region measured by Fourier-transform spectroscopy*, Journal of Photochemistry and Photobiology a-Chemistry 143 [1], pp. 1-9. URL: <Go to ISI>://000171214700001

Volkamer, R.; Molina, L.T.; Molina, M.J.; Shirley, T. and Brune, W.H. (2005): *DOAS measurement of glyoxal as an indicator for fast VOC chemistry in urban air*, Geophysical Research Letters 32 [8]. URL: <Go to ISI>://000228851300007

Volkamer, R.; Platt, U. and Wirtz, K. (2001): *Primary and secondary glyoxal formation from aromatics: Experimental evidence for the bicycloalkyl-radical pathway from benzene, toluene, and p-xylene*, Journal of Physical Chemistry A 105 [33], pp. 7865-7874. URL: <Go to ISI>://000170506700012

Volkamer, R.; Spietz, P.; Burrows, J. and Platt, U. (2005): *High-resolution absorption cross-section of glyoxal in the UV-vis and IR spectral ranges*, Journal of Photochemistry and Photobiology a-Chemistry 172 [1], pp. 35-46. URL: <Go to ISI>://000229059500005

von Savigny, C.; Kaiser, J.W.; Bovensmann, H.; Burrows, J.P.; McDermid, I.S. and Leblanc, T. (2005): *Spatial and temporal characterization of SCIAMACHY limb pointing errors during the first three years of the mission*, Atmospheric Chemistry and Physics 5, pp. 2593-2602. URL: <Go to ISI>://000232205200001

von Savigny, C.; Rozanov, A.; Bovensmann, H.; Eichmann, K.U.; Noel, S.; Rozanov, V.V.; Sinnhuber, B.M.; Weber, M. and Burrows, J.P. (2005): *The ozone hole breakup in September 2002 as seen by SCIAMACHY on ENVISAT*, Journal of the Atmospheric Sciences 62 [3], pp. 721-734. URL: <Go to ISI>://000228012100014

Vountas, M.; Richter, A.; Wittrock, F. and Burrows, J.P. (2003): *Inelastic scattering in ocean water and its impact on trace gas retrievals from satellite data*, Atmospheric Chemistry and Physics 3, pp. 1365-1375. URL: <Go to ISI>://000185621800002

Vountas, M.; Rozanov, V.V. and Burrows, J.P. (1998): *Ring effect: Impact of rotational Raman scattering on radiative transfer in earth's atmosphere*, Journal of Quantitative Spectroscopy & Radiative Transfer 60 [6], pp. 943-961. URL: <Go to ISI>://000077024700003

Wagner, T. (1999): *Satellite Observations of Atmospheric Halogen Oxides*, Institue of Environmental Physics, University of Heidelberg, Heidelberg.

Wagner, T.; Dix, B.; von Friedeburg, C.; Friess, U.; Sanghavi, S.; Sinreich, R. and Platt, U. (2004): *MAX-DOAS O_4 measurements: A new technique to derive information on atmospheric aerosols - Principles and information content*, Journal of Geophysical Research-Atmospheres 109 [D22]. URL: <Go to ISI>://000225430000004

Wagner, T.; Erle, F.; Marquard, L.; Otten, C.; Pfeilsticker, K.; Senne, T.; Stutz, J. and Platt, U. (1998): *Cloudy sky optical paths as derived from differential optical absorption spectroscopy observations*, Journal of Geophysical Research-Atmospheres 103 [D19], pp. 25307-25321. URL: <Go to ISI>://000076490200011

Wagner, T.; Otten, C.; Pfeilsticker, K.; Pundt, I. and Platt, U. (2000): *DOAS moonlight observation of atmospheric NO_3 in the Arctic winter*, Geophysical Research Letters 27 [21], pp. 3441-3444. URL: <Go to ISI>://000165063000002

Wagner, T. and Platt, U. (1998): *Satellite Mapping of Enhanced BrO Concentrations in the Troposphere*, Nature.

Wagner, V.; Schiller, C. and Fischer, H. (2001): *Formaldehyde measurements in the marine boundary layer of the Indian Ocean during the 1999 INDOEX cruise of the R/V Ronald H. Brown*, Journal of Geophysical Research-Atmospheres 106 [D22], pp. 28529-28538. URL: <Go to ISI>://000172355800036

Wang, P.; Richter, A.; Bruns, M.; Rozanov, V.V.; Burrows, J.P.; Heue, K.P.; Wagner, T.; Pundt, I. and Platt, U. (2005): *Measurements of tropospheric NO2 with an airborne multi-axis DOAS instrument*, Atmospheric Chemistry and Physics 5, pp. 337-343. URL: <Go to ISI>://000226907900002

Warneck, P. (1988): *Chemistry of the Natural Atmosphere*, Academic Press, San Diego.

Warneck, P. (2005): *Multi-phase chemistry of C-2 and C-3 organic compounds in the marine atmosphere*, Journal of Atmospheric Chemistry 51 [2], pp. 119-159. URL: <Go to ISI>://000232205300001

Wayne, R.P. (2000): *Chemistry of Atmospheres*, Oxford Science Publications.

Weller, R.; Schrems, O.; Boddenberg, A.; Gab, S. and Gautrois, M. (2000): *Meridional distribution of hydroperoxides and formaldehyde in the marine boundary layer of the Atlantic (48< degrees >N-35< degrees >S) measured during the Albatross campaign*, Journal of Geophysical Research D: Atmospheres 105 [11], pp. 14,401-14,412.

Went, F.W. (1960): *Organic matter in the atmosphere and its possible relation to petroleum formation*, Proc. Nat. Acad. Sci., pp. 212-221.

Wiedinmyer, C.; Friedfeld, S.; Baugh, W.; Greenberg, J.; Guenther, A.; Fraser, M. and Allen, D. (2001): *Measurement and analysis of atmospheric concentrations of isoprene and its reaction products in central Texas*, Atmospheric Environment 35 [6], pp. 1001-1013.

Wiedinmyer, C.; Greenberg, J.; Guenther, A.; Hopkins, B.; Baker, K.; Geron, C.; Palmer, P.I.; Long, B.P.; Turner, J.R.; Petron, G.; Harley, P.; Pierce, T.E.; Lamb, B.; Westberg, H.; Baugh, W.; Koerber, M. and Janssen, M. (2005): *Ozarks Isoprene Experiment (OZIE): Measurements and modeling of the ľsoprene volcano"*, Journal of Geophysical Research-Atmospheres 110 [D18]. URL: <Go to ISI>://000232179800004

Wilmouth, D.M.; Hanisco, T.F.; Donahue, N.M. and Anderson, J.G. (1999): *Fourier transform ultraviolet spectroscopy of the A (2)Pi(3/2) <- X (II3/2)-I-2 transition of BrO*, Journal of Physical Chemistry A 103 [45], pp. 8935-8945. URL: <Go to ISI>://000083724900005

Winterrath, T.; Kurosu, T.P.; Richter, A. and Burrows, J.P. (1999): *Enhanced O-3 and NO2 in thunderstorm clouds: Convection or production?*, Geophysical Research Letters 26 [9], pp. 1291-1294. URL: <Go to ISI>://000080122900027

Wittrock, F.; Altmeyer, H.; Bruns, M.; Laue, M.; Munderloh, K.; Richter, A.; Schlieter, S. and Burrows, J.P. (1999): *Measurements of Ozone, NO_2, BrO and OClO at different latitudes*, Stratospheric ozone 1999, Schliersee, Germany.

Wittrock, F.; Bruns, M.; Eisinger, M.; Ladstätter-Weißenmayer, A.; Richter, A.; Schlieter, S. and Burrows, J.P. (1997): *Measurements of atmospheric trace gases above Ny-Ålesund, Spitsbergen by zenith sky and GOME DOAS from 1995-1997*, Polar stratospheric ozone 1997, Schliersee, Germany.

Wittrock, F.; Eisinger, M.; Ladstätter-Weißenmayer, A.; Richter, A. and Burrows, J.P. (1995): *Ground-based UV/vis instruments of O_3, NO_2, BrO and OClO over Ny-Ålesund (79°N, 12°E)*, Polar stratospheric ozone, Schliersee, Germany.

Wittrock, F.; Eisinger, M.; Ladstätter-Weißenmayer, A.; Richter, A. and Burrows, J.P. (1996): *Ground-based UV/vis measurements of O3, NO2, OClO and BrO over Ny-Ålesund (79°N,12°E)*, XVIII Quadrennial Ozone Symposium, L'Aquila, Italy.

Wittrock, F.; Muller, R.; Richter, A.; Bovensmann, H. and Burrows, J.P. (2000): *Measurements of iodine monoxide (IO) above Spitsbergen*, Geophysical Research Letters 27 [10], pp. 1471-1474. URL: <Go to ISI>://000087062000012

Wittrock, F.; Oetjen, H.; Richter, A.; Fietkau, S.; Medeke, T.; Rozanov, A. and Burrows, J.P. (2004): *MAX-DOAS measurements of atmospheric trace gases in Ny-Alesund - Radiative transfer studies and their application*, Atmospheric Chemistry and Physics 4, pp. 955-966. URL: <Go to ISI>://000222321900002

Wittrock, F.; Richter, A. and Burrows, J.P. (1999): *Validation of GOME BrO and OClO Measurements in the Northern Hemisphere*, European Symposium on Atmospheric Measurements from Space.

Wittrock, F.; Richter, A.; Ladstätter-Weißenmayer, A. and Burrows, J.P. (2000): *Global Observations of Formaldehyde*, ERS-ENVISAT symposium, Gothenburg.

WMO (2003): *Scientific assessment of Ozone depletion: 2002. Persuant to Article 6 of the Montreal Protocol on substances that deplete the ozone layer*, Scientific assessment of ozone depletion ; 2002, World Meteorological Organization, Geneva, ISBN: 9280722611.

Yamanouchi, T.; Treffeisen, R.; Herber, A.; Shiobara, M.; Yamagata, S.; Hara, K.; Sato, K.; Yabuki, M.; Tomikawa, Y.; Rinke, A.; Neuber, R.; Schumachter, R.; Kriews, M.; Strom, J.; Schrems, O. and Gernandt, H. (2005): *Arctic Study of Tropospheric Aerosol and Radiation (ASTAR) 2000: Arctic haze case study*, Tellus Series B-Chemical and Physical Meteorology 57 [2], pp. 141-152. URL: <Go to ISI>://000228267600006

Yokelson, R.J.; Bertschi, I.T.; Christian, T.J.; Hobbs, P.V.; Ward, D.E. and Hao, W.M. (2003): *Trace gas measurements in nascent, aged, and cloud-processed smoke from African savanna fires by airborne Fourier transform infrared spectroscopy (AFTIR)*, Journal of Geophysical Research D: Atmospheres 108 [13], pp. SAF 14-1 - SAF 14-18.

Yokelson, R.J.; Goode, J.G.; Ward, D.E.; Susott, R.A.; Babbitt, R.E.; Wade, D.D.; Bertschi, I.; Griffith, D.W.T. and Hao, W.M. (1999): *Emissions of formaldehyde, acetic acid, methanol, and other trace gases from biomass fires in North Carolina measured by airborne Fourier transform infrared spectroscopy*, Journal of Geophysical Research-Atmospheres 104 [D23], pp. 30109-30125. URL: <Go to ISI>://000084399500003

Zhang, H.P.; Wang, L.Q. and Qin, G.W. (2005): *Grayanane diterpenoids from the leaves of Craiobiodendron yunnanense*, Bioorganic & Medicinal Chemistry 13 [17], pp. 5289-5298. URL: <Go to ISI>://000231341900035

Zhou, X.L. and Mopper, K. (1997): *Photochemical production of low-molecular-weight carbonyl compounds in seawater and surface microlayer and their air-sea exchange*, Marine Chemistry 56 [3-4], pp. 201-213. URL: <Go to ISI>://A1997WQ30000005

Zimmermann, P.R. (1979): *Determination of emission rates of hydrocarbons from indigenous species of vegetation in the Tampa/St. Petersburg Florida area*, Atlanta, Georgia, U.S. Environmental Protection Agency, Region IV, EPA/904/9-77/028